Space Charge Effects and Advanced Modelling for CERN Low Energy Machines

ÉCOLE POLYTECHNIQUE FÉDÉRALE DE LAUSANNE

PAR

Adrian OEFTIGER

acceptée sur proposition du jury:

Prof. R. Houdré, président du jury
Prof. L. Rivkin, Dr G. Rumolo, directeurs de thèse
Prof. O. Boine-Frankenheim, rapporteur
Dr A. Adelmann, rapporteur
Dr M. Meddahi, rapporteuse

EPFL

ÉCOLE POLYTECHNIQUE
FÉDÉRALE DE LAUSANNE

Suisse
2016

The important thing is not to stop questioning.
Curiosity has its own reason for existing.
One cannot help but be in awe
when he contemplates
the mysteries of eternity, of life,
of the marvelous structure of reality.
It is enough if one tries merely to comprehend
a little of this mystery every day.

— Albert Einstein

in the spirit of *the institute,*
the Basic Research Community for Physics

Acknowledgements

Firstly, I would like to express my sincere gratitude to my thesis director Prof. Leonid Rivkin and my CERN supervisor Dr. Giovanni Rumolo for supporting my Ph.D. study and to offer me the opportunity to contribute to research in the intriguing field of accelerator physics.

I would further like to thank my thesis committee – Prof. Oliver Boine-Frankenheim, Prof. Romuald Houdré, Dr. Andreas Adelmann and Dr. Malika Meddahi – for the useful comments on my thesis as well as the rich and diverse discussion of the topic during the oral examination.

I am indebted to the voluntary proofreaders of my thesis for their valuable feedback, notably to Dr. Shinji Machida, Dr. Simon Albright, Jason Aebischer, Agnes Jakab, Manuel Meyer, Steffen Pade, Ciprian Tomoiaga and Murtaza Tunio.

The inspiring environment at CERN has profoundly shaped me since I started the Ph.D. endeavour in May 2013. Numerous fruitful discussions with motivated colleagues from the ABP and the RF group stimulated fresh ideas and allowed me enlightening insights into beam dynamics topics beyond my own immediate research. Foremost I thank Dr. Kevin Li for always having an open door for me, sharing his expertise on collective effects and numerical simulation studies and inviting me to join him on developing PyHEADTAIL. I especially remember the fun during joint programming sessions with Michael Schenk and Stefan Hegglin. The exciting and lively discussions with Cedric Hernalsteens, Simon Hirlander and Malte Titze will always remain in my memories. Unforgotten remain also the sleepless and yet successful measurement nights in the CERN control centre with Dr. Hannes Bartosik and Dr. Frank Schmidt where I have learned so immensely much about the accelerators, their operation and the interrelation between all the beam dynamics variables – thank you! At this point, I wish to express my deepest gratitude to the operation crews of the PS Booster, the PS and the SPS: not only did the successful outcome of our measurements depend on your unconditional support, you also made me feel like part of the teams. I am thankful for the great brainstorming sessions with the ever-patient Dr. Guido Sterbini and Dr. Nicolas Mounet. Dr. Elias Métral and Dr. Simone Gilardoni always found time to discuss my ideas and point out on which details to focus, thanks to you I have frequently gained a new perspective on various aspects of my thesis project. Dr. Christian Carli and Dr. Heiko Damerau have been of invaluable help whenever I needed support on longitudinal beam dynamics. Thank you also

Acknowledgements

for taking me into the PS tunnel and explaining me the hardware details of the machine, Heiko. It has been a great pleasure to work with Dr. Giovanni Iadarola: your creativity often sparked new ideas and clever approaches to challenges, thank you Gianni! Never to be forgotten are the great times with the Wu Shu Kwan team around the dedicated Dr. Androula Alekou —cheers'n'bow!— and the energy I could draw from our training sessions which carried me through demanding times. I owe my deepest gratitude to Dr. Steven Hancock. You have been a wonderful mentor to me, Steve! I highly appreciate all the time you have generously spent introducing me to the machine systems and sharing your expertise on radio frequency (RF) topics, your contagious motivation which led the way to success, as well as your constructive and invaluable feedback on the papers and my thesis chapter. Thank you!

Throughout the time of my Ph.D. studies I have been blessed with deep, cheerful and supporting friendships. I especially wish to thank Sebastian Bott, Daniel Cámpora and Oliver Stein for always being there for me, be it in the highs or lows of this exciting period of my life. My shared house, Emilia Noyeres, has become like a family to me – I will always keep you in my heart!

This journey would not even have started without my parents. Thank you for always being there for me, asking the right questions and unconditionally supporting me. It seems like there might be interesting long-term consequences of betting that you could teach a two-year-old how to pronounce $E = mc^2$...

Geneva, October 2016   Adrian

Abstract

The strong space charge regime of future operation of CERN's circular particle accelerators is investigated and mitigation strategies are developed in the framework of the present thesis. The intensity upgrade of the injector chain of Large Hadron Collider (LHC) prepares the particle accelerators to meet the requirements of the High-Luminosity LHC project. Producing the specified characteristics of the future LHC beams imperatively relies on injecting brighter bunches into the Proton Synchrotron Booster (PSB), the downstream Proton Synchrotron (PS) and eventually the Super Proton Synchrotron (SPS). The increased brightness, i.e. bunch intensity per transverse emittance, entails stronger beam self-fields which can lead to harmful interaction with betatron resonances. Possible beam emittance growth and losses as a consequence thereof threaten to degrade the beam brightness. These space charge effects are partly mitigated by the upgrade of the PSB and PS injection energies. Nevertheless, the space charge tune spreads of the future injector beams are found to exceed the values reached by present LHC or other intense fixed target physics beams.

This thesis project comprises three key tasks: detailed modelling of space charge effects, measurement at the CERN machines and mitigation of space charge impact. Throughout the course of this thesis, the simulation tool PyHEADTAIL has been developed and extended to model 3D space charge effects in circular accelerators across the wide energy range from PSB to SPS. The implementation for hardware-accelerating GPU architectures enables extensive studies, especially when employing the self-consistent particle-in-cell algorithm. The implemented models have been benchmarked with analytical results for space charge beam dynamics. In particular, the spectra of quadrupolar pick-ups – which provide a direct measurement method for the space charge tune shift – have been simulated and compared with the derived theory. The space charge situation at the SPS injection plateau has been extensively investigated in the course of comprehensive measurement studies, resulting in the identification of an optimal working point region for the SPS. The interplay of space charge and the horizontal quarter-integer resonance has been scrutinised in measurement, theory and simulation. Last but not least, a new LHC beam type with a hollow longitudinal phase space distribution has been developed for the PSB and proved to substantially mitigate space charge impact on the PS injection plateau.

Keywords: particle accelerators physics, electrodynamics, beam dynamics, collective effects, space charge, particle-in-cell algorithm

List of Publications

The present thesis is based on work reported in the following papers:

1. G. Rumolo, H. Bartosik, H. Damerau, A. Findlay, S. Hancock, B. Mikulec, and A. Oeftiger [2014]. "Expected performance in the injectors at 25 ns without and with LINAC4". In: *RLIUP: Review of LHC and Injector Upgrade Plans*, pp. 17–24.

2. E. Métral, T. Argyropoulos, H. Bartosik, N. Biancacci, X. Buffat, J. F. E. Muller, W. Herr, G. Iadarola, A. Lasheen, K. Li, A. Oeftiger, T. Pieloni, D. Quartullo, G. Rumolo, B. Salvant, M. Schenk, E. Shaposhnikova, C. Tambasco, H. Timko, C. Zannini, A. Burov, D. Banfi, J. Barranco, N. Mounet, O. Boine-Frankenheim, U. Niedermayer, V. Kornilov, and S. White [2016]. "Beam Instabilities in Hadron Synchrotrons". In: *IEEE Transactions on Nuclear Science* 63.2, pp. 1001–1050.

3. A. Oeftiger, H. Bartosik, A. J. Findlay, S. Hancock, and G. Rumolo [2016]. "MD210 Note: Creation of Hollow Bunches in the PSB". in: *CERN ACC NOTE 2016-0045*.

4. A. Oeftiger, A. Aviral, R. D. Maria, L. Deniau, S. Hegglin, K. Li, E. McIntosh, and L. Moneta [2016]. "Space Charge Studies with High Intensity Single Bunch Beams in the CERN SPS". in: *International Particle Accelerator Conference (IPAC 2016)*, WEPOY044.

5. A. Oeftiger, H. Bartosik, A. Findlay, S. Hancock, and G. Rumolo [2016]. "Flat Bunches with a Hollow Distribution for Space Charge Mitigation". In: *International Particle Accelerator Conference (IPAC 2016)*, MOPOR023.

6. H. Bartosik, A. Oeftiger, M. Schenk, F. Schmidt, and M. Titze [2016]. "Improved Methods for the Measurement and Simulation of the CERN SPS Non-linear Optics". In: *International Particle Accelerator Conference (IPAC 2016)*, THPMR036.

7. H. Bartosik, A. Oeftiger, F. Schmidt, and M. Titze [2016]. "Space Charge Studies with High Intensity Single Bunch Beams in the CERN SPS". in: *International Particle Accelerator Conference (IPAC 2016)*, MOPOR021.

8. F. Schmidt, H. Bartosik, A. Huschauer, A. Oeftiger, M. Titze, G. Franchetti, J. Holmes, Y. Alexahin, J. Amundson, V. Kapin, and E. Stern [2016]. "Code Bench-marking for Long-term Tracking and Adaptive Algorithms". In: *ICFA Advanced Beam Dynamics Workshop on High-Intensity and High-Brightness Hadron Beams (HB 2016)*, WEAM1X01.

9. K. Li, H. Bartosik, G. Iadarola, A. Oeftiger, A. Passarelli, A. Romano, G. Rumolo, and M. Schenk [2016]. "Code Development for Collective Effects". In: *ICFA Advanced Beam Dynamics Workshop on High-Intensity and High-Brightness Hadron Beams (HB 2016)*, WEAM3X01.

10. A. Oeftiger and S. Hegglin [2016]. "Space Charge Modules for PyHEADTAIL". in: *ICFA Advanced Beam Dynamics Workshop on High-Intensity and High-Brightness Hadron Beams (HB 2016)*, MOPR025.

11. A. Oeftiger, S. Hancock, and G. Rumolo [2016]. "Space Charge Mitigation with Longitudinally Hollow Bunches". In: *ICFA Advanced Beam Dynamics Workshop on High-Intensity and High-Brightness Hadron Beams (HB 2016)*, MOPR026.

Contents

Contents

List of Figures

List of Tables

1 Introduction

With the first accelerated protons in CERN's Proton Synchrotron (PS) in 1959, the era of alternating gradient synchrotrons began. The foundation of this success story is the concept of *strong focusing* of particle beams. First conceived in 1950 and patented by Christofilos [1956], strong focusing has been independently established by Blewett [1952] and Courant, Livingston, and Snyder [1952]. The study by the latter led to the construction of the Alternating Gradient Synchrotron (AGS) at Brookhaven National Laboratory (BNL) in the U.S., which started up just a year after the PS at CERN. A few decades have passed since then, tremendous advances in the understanding of beam dynamics as well as in the development of new key technologies such as reliable superconducting magnets have been made. Yet the largest modern particle accelerators are still based on the same physics principles of the early synchrotrons proving the power and scalability of the concept.

1.1 Why Does CERN Want High Brightness Beams?

On how the Large Hadron Collider pushes the high-energy frontier in basic research...

In 2008 the first proton beams circulated around the Large Hadron Collider (LHC). Today, CERN's 27 km long synchrotron sketched in figure 1.1 accelerates proton beams up to 6.5 TeV. The two counter-circulating beams are then brought into collision in four locations. The resulting interaction products are continuously recorded by four detector collaborations for the purpose of fundamental particle physics research.

One of the dedicated goals of the particle physics experiments at the LHC is the investigation of the Higgs boson, a quantum excitation of the Brout-Englert-Higgs field. This field is of crucial importance in the Standard Model of particle physics (SM) because the mass of fermions and bosons, the elementary particles, is explained by interaction with it. Therefore, the verification of this mechanism by detecting the Higgs boson posed a long standing quest for experimental particle physics.

1

Figure 1.1 – The LHC and its surrounding geography in the valley of Geneva, Switzerland [Brice 2008]. The locations of the four major LHC experiments – ALICE, ATLAS, LHCb and CMS – are indicated along the ring.

Since its proposition in the 1960s it should take half a century to confirm the mechanism. In July 2012, the two general-purpose LHC experiment collaborations, A Toroidal LHC ApparatuS (ATLAS) and Compact Muon Solenoid (CMS), finally announced the discovery of a new particle: a scalar boson. In the meantime, the new particle has indeed been identified as a Higgs particle at a mass of around $m_H \approx 125\,\text{GeV}$, so far conforming with the properties predicted by the SM [ATLAS Collaboration and CMS Collaboration 2015]. The most exciting prospect of further investigation of the Higgs boson's properties is the possibility of unveiling new physics deviating from the otherwise extremely solid and well tested SM. To quote Rolf Heuer [2012], the Director General of CERN at the time of the discovery:

> "We have reached a milestone in our understanding of nature. The discovery of a particle consistent with the Higgs boson opens the way to more detailed studies, requiring larger statistics, which will pin down the new particle's properties, and is likely to shed light on other mysteries of our universe."

Even though the quest to find the Higgs particle has been successful, and most predictions

by the SM have been experimentally verified to great precision, there are many fundamental questions left open. Due to the expansion of our universe, cosmology predicts a Big Bang singularity some 13.82×10^9 years in the past [Ade 2015]. Extrapolating from the present towards the Big Bang, the temperature or energy density in the universe increases. At some point very close to the Big Bang, the processes in the universe are entirely microscopic and are governed by elementary particle physics – hence, our present macroscopic situation evolved from microscopic dynamics. This strong link between (macroscopic) cosmology and particle physics gives us a hint of what to expect from a satisfactory model of the microscopic elementary interactions. There are numerous reasons to believe in physics beyond the SM – as self-contained as it is, the model must be incomplete. Certain observations and facts, e.g. from cosmology, cannot be explained by it or are simply not included, such as:

1. the asymmetry between baryonic matter and antimatter,

2. the origin of dark matter,

3. the hierarchy problem (m_H is negligibly small compared to the Planck scale),

4. the gravitational force,

5. neutrino oscillations (which have already been experimentally verified).

Besides pushing the accuracies of the experimental verification of the SM predictions, the LHC experiments explore ever higher energies in single-particle collisions. CERN contributes to the investigation of physics beyond the SM either by excluding parameter ranges and hence guiding extended theoretical models that address these shortcomings by falsification, or by finding new particles and states of matter that give insight on new physics. For this endeavour, the LHC beams are pushing the boundaries on the high-energy research frontier.

Besides dedicated experiments at CERN's antimatter decelerator facility [Hangst 2014], a third LHC experiment collaboration named Large Hadron Collider beauty (LHCb) examines the violation of the CP (charge and parity conjugation) symmetry between particles and antiparticles. The SM can only account for a "weak" symmetry breaking (explaining e.g. quark flavour mixing) while the strong asymmetry between baryonic matter and antimatter cannot be fully explained. In a simple argument, if there were stars or galaxies made of antimatter we would observe very violent annihilation events in one of the numerous star collisions happening in the cosmos. The absence of such experimental evidence leads to the conclusion that our universe is mostly made of matter. At the same time, the Big Bang is believed to have produced equal amounts of matter and antimatter. If creation and annihilation of particles and antiparticles happened symmetrically, our universe would be a rather cheerless place filled with photons only. A plausible and compelling reason for the abundance of matter in our present universe is the violation of the CP symmetry leading to this baryogenesis [Wiese 2010]. Nevertheless, the exact mechanism remains a mystery and to date no preferred theory has been established. LHCb analyses rare particle interactions involving beauty quarks produced during collisions of the LHC proton beams that might shed a light on the CP violation mechanism in

weak interactions. First results on direct CP violation involving strange B_s^0 mesons have been reported in 2013 [Aaij 2013]. As a by-product, the collaboration has recently published the exciting first evidence of a pentaquark state involving five bound quarks instead of the usual three in baryons [Aaij 2015].

The electroweak symmetry breaking happens $\mathcal{O}\left(10^{-12}\,\text{s}\right)$ after the Big Bang. Its physics is now well established with the Nobel Prize awarded findings of the weak force carriers (the W and Z bosons) [Linglin 1983; Sadoulet 1983] as well as the Higgs boson [Aad et al. 2012; Chatrchyan et al. 2012]. After this electroweak phase transition, the quark epoch begins and free quarks and gluons fill the universe in a special state of matter called the quark-gluon plasma. Around $\mathcal{O}\left(10^{-5}\,\text{s}\right)$, the universe experiences the next phase transition when the quarks and gluons become bound in hadrons. From our present perspective in a much further cooled down universe, we only see these confined quark and gluon states such as protons, neutrons, pions etc. However, if we achieve very high energy densities, we can recreate the circumstances of asymptotically free quarks and gluons. This can in principle be achieved with lead-lead and proton-lead ion beam collisions at the LHC. The fourth largest of the LHC experiment collaborations, A Large Ion Collider Experiment (ALICE), dedicates its research programme to the detection and investigation of such quark-gluon plasmas. In 2013, they published first results on the phenomenon and have since reported peculiar properties of this ultra-hot state of matter. In 2015, a CMS analysis with further data from proton-lead collisions confirmed the existence and the fluid-like behaviour of the plasma [Khachatryan 2015].

The past two decades have brought forth many new insights in the thriving field of cosmology. In 1998, the Nobel Prize awarded finding that the expansion of our universe actually accelerates has put the concept of a cosmological constant back on the table [Perlmutter 1999; Riess et al. 1998]. It had once been introduced by Albert Einstein, ironically in an attempt to make the universe static, but later it had been abandoned in favour of a decelerating expanding universe based on the experimental evidence of the time. Today, quoting the latest precision measurements by the Planck mission [Ade 2015], we are left with an exciting puzzle: we know that the content of the present universe only consists to a $\Omega_b = 0.049$ fraction of luminous, baryonic matter. In other words, the entire contents of the SM only account for 4.9% of the mass-energy content of today's cosmos, the remaining 95.1% are of unknown nature. The acceleration of the expansion can be included into the dynamics dictated by the Friedmann equations by adding the aforementioned cosmological constant Λ. Present research in cosmology is yet to find the essence behind this "anti-gravitating", negative pressure constituent which makes for a good $\Omega_\Lambda = 0.686$ fraction of the content of our universe – the commonly used term dark energy somewhat lives up to its mystery. But equally so does the name for the remaining fraction of $\Omega_c = 0.265$: cold (i.e. non-relativistic) dark matter is another yet unknown constituent which is not part of the SM. Among other influences, it is thought to account for the anomaly in the radial frequency distribution of the rotation of galaxies which is observed to stay constant at large radii. The presently favoured hypothesis for the nature of dark matter is that it is made of (so far unknown) weakly interacting massive particles, i.e. the particles are expected to merely interact through gravity and the weak force. This is

where particle physics comes into play: the LHC collaborations (with the general-purpose experiments ATLAS and CMS leading the way) are actively searching for such dark matter candidates.

To round off the tour into intriguing "beyond-the-SM physics" investigated with the aid of the LHC particle beams, let us briefly address the hierarchy problem about why the Higgs mass is so low, which at the same time brings up the gravity subject. A hypothetical generic theory of everything would involve gravity as the fourth elementary force. The SM on the other hand only contains the triumvirate of the electromagnetic, the weak and the strong force as quantised theories. The hierarchy problem enters the discussion when addressing theories including gravitation.

To date, theoretical research has not brought forth a satisfactory and generally accepted model of quantum gravity. Quantitatively, the quantum nature of gravity is expected to play a significant role at the Planck scale, corresponding to a length of $\mathcal{O}\left(10^{-35}\,\text{m}\right)$ or, equivalently, an energy of $\mathcal{O}\left(10^{19}\,\text{GeV}\right)$ (below this energy or above this length, the classical theory of gravity, general relativity, provides a trustful model). While the LHC experiments at CERN are pushing on the upper energy limit of human created physics experiments, we are nevertheless talking about energies below $\mathcal{O}\left(10^{4}\,\text{GeV}\right)$. This is 15 orders of magnitude below the Planck scale showing that direct experimental investigation of gravitational quantum effects in particle collisions is not a realistic project.

How does this discussion relate to the mass of the Higgs boson? Due to the Brout-Englert-Higgs mechanism, we know that the Higgs particle's effective (experimentally measured) mass m_H is related to the weak gauge bosons' acquired masses and thus has to be found at the electroweak scale, $\mathcal{O}\left(10^{3}\,\text{GeV}\right)$, where it has indeed been experimentally detected. In a quantum field theory, a scalar boson's bare mass (i.e. the case of the Higgs particle) is subject to quantum loop corrections. The impact of these corrections scales with the largest relevant energy scale of the possible interactions described by the quantum field theory. Consequently, if we add gravity to create a theory of everything, the quantum corrections to the bare Higgs mass should be of the order of the Planck scale – which we know is huge. In order to then explain the small effective mass of the electroweak scale, one would have to postulate a heavy bare Higgs mass, which could in turn compensate these large quantum corrections in a precisely fine-tuned manner. Without any specific mechanism to explain such a cancellation this is considered quite unsatisfactory, hence the terminus of a hierarchy problem between the weak force and gravitation. A corresponding candidate for a theory of everything is expected to solve this issue in a natural way without unjustified fine-tuning of parameters.

A step towards this goal is the famous theory of supersymmetry which relates bosons and fermions in a fundamental symmetry. Supersymmetry is like a joker answering many open questions at once: the hierarchy problem, the flatness of our universe (which can be explained via cosmological inflation models based on supersymmetry), it might provide the weakly interacting massive particles as candidates for dark matter, lead to a precise unification of

the coupling parameters of the fundamental forces at high energies (which mismatch in SM extrapolations) and, finally, supersymmetry allows to include general relativity in models called supergravity. In order for the simplest supersymmetry models to solve the hierarchy problem, it is constrained to an energy range around the TeV scale. Hence, the LHC experiments are able to possibly detect or, conversely, to exclude a majority of plausible supersymmetric models. To date, the analysis of the first LHC research run between 2009 and 2013 has not brought forth any news on this side. Results from the second run taking place since 2015 are expected to indicate whether supersymmetry is realised in nature or not.

1.2   Introduction to Accelerator Physics

... and how the beam brightness contributes to this endeavour.

Many of these intriguing questions involve the Higgs making it an interesting study case for physics beyond the SM. Any measured deviation of the Higgs particle's characteristics from the SM predictions might lead us to new insights. For this purpose, the experiments need to collect as many statistics as possible. In technical terms, the event rate $R_{event} = \sigma_{event}\mathscr{L}$ of a specific interaction is determined by its event cross section σ_{event} and the operational accelerator variable $\mathscr{L}$ called instantaneous luminosity. The physics of the interaction gives σ_{event}. Consequently, one aims to maximise the integrated luminosity. The luminosity expresses the density of collision centres in the two counter-circulating colliding beams. Assuming short bunches in head-on collisions with a Gaussian transverse profile, we can write down a simple expression for the effective instantaneous luminosity of a single collision,

$$\mathscr{L} = \frac{N^2}{4\pi\sigma_x\sigma_y} f_{rev} \quad , \tag{1.1}$$

where f_{rev} denotes the revolution frequency of the circular collider, N the number of particles in each of the two identical colliding bunches (termed the intensity) and $\sigma_{x,y}$ the standard deviation of their horizontal and vertical Gaussian beam profiles (the r.m.s. beam widths) [Wiedemann 2007, equation (18.40)]. To be precise, the transverse beam size in accelerators is determined by two factors, the focusing strength of the machine and the inherent phase space density. The latter is a quantity of fundamental importance called the beam emittance whose lower limit is mainly determined by the injection quality across the machines of the accelerator complex. The normalised beam emittance $\epsilon_{x,y}$ is conceptually closely related to entropy, in a closed system it can only grow – therefore one aims to preserve it as much as possible from right after the particle source until the collider. In absence of further effects, the beam size simply relates to the emittance via $\sigma_{x,y} \propto \sqrt{\epsilon_{x,y}}$. We conclude that two important ingredients to increase R_{event} from the operational perspective of the particle accelerators are (i.) a small transverse normalised emittance $\epsilon_{x,y}$ and (ii.) a high intensity N.

Since the 1950s, particle colliders have been used as a powerful tool for experimental basic research in fundamental particle physics. In the meantime, particle accelerators have found

applications in widely varying fields. Exciting and rapidly developing fields range from nuclear physics research using neutron spallation e.g. for exploring nuclear waste treatment (cf. the new European Spallation Source in Denmark and Sweden) over synchrotron radiation production for condensed matter physics, biology and chemistry research (cf. the European XFEL project in Germany or the Swiss Light Source in Switzerland) through to industrial manufacturing processes (e.g. doping of semiconductors) and medical purposes (hadron cancer therapy). Synchrotrons play a leading role in most of these fields.

Many of these applications have in common the requirement for a high beam brightness, i.e. intensity per averaged transverse normalised emittance. With increasing beam density, the electromagnetic fields generated by the beam become stronger which in turn influences the motion of the particles. Beam distributions under these circumstances become subject to quite complex internal dynamics, hence making the self-consistent treatment and analysis of such *space charge* physics an interesting task. In particular, the periodic nature of the external focusing system, into which the beam is embedded in the case of circular accelerators, can give rise to intriguing beam dynamics and the impact on the operation of the particle accelerators can be significant. Space charge provides an upper limit on a machine's beam brightness, although not necessarily the most stringent one as there can be other harmful multi-particle related effects (involving e.g. the interaction with the beam surroundings such as the vacuum pipe). Nevertheless, the limitation by space charge usually plays a crucial role for certain parts of an accelerator complex, most prominently at the low-energy machines. Attempting to exceed this brightness limit can generate resonant beam motion and instabilities potentially resulting in (i.) emittance growth (increasing $\epsilon_{x,y}$ and hence $\sigma_{x,y}$) and (ii.) beam losses (which decreases N). Furthermore, such losses may also activate the machine and lead to remnant radiation doses. To conclude, efforts to maximise the beam brightness are bounded by a maximum value established by direct space charge effects.

1.3   Space Charge Matters

Space charge knocks on the door...

The veterans among the synchrotrons, the initially mentioned AGS at BNL and the PS at CERN, continue to deliver beams to the downstream accelerators. The PS has gone from delivering beam intensities of $\mathcal{O}\left(10^{10}\right)$ to the present 3×10^{13} protons per pulse (ppp) [Burnet et al. 2011], cf. figure 1.2. During the more than five decades of operation, these synchrotrons have been upgraded several times to push space charge limitations. The PS upgrades include the construction of the Proton Synchrotron Booster (PS Booster) completed in 1972, which raised the kinetic injection energy of the PS to 800 MeV from the previous 50 MeV from the Linear Accelerator (LINAC). The PS Booster pushed the space charge limit at injection into the PS to 10^{13} ppp resulting in a quick increase of the peak intensity after 1972 in figure 1.2). Shortly after, in 1978, LINAC2 has been built to replace LINAC1 which resulted again in an intensity jump. With the decision to build the LHC, the requirements for the PS became more

stringent in terms of beam densities. It became crucial to conserve the normalised emittance throughout the PS cycle, which has been subject to blow-up due to space charge effects. In 1999, the PS Booster extraction energy has been raised to 1.4 GeV to counter space charge which is most critical around the injection energy.
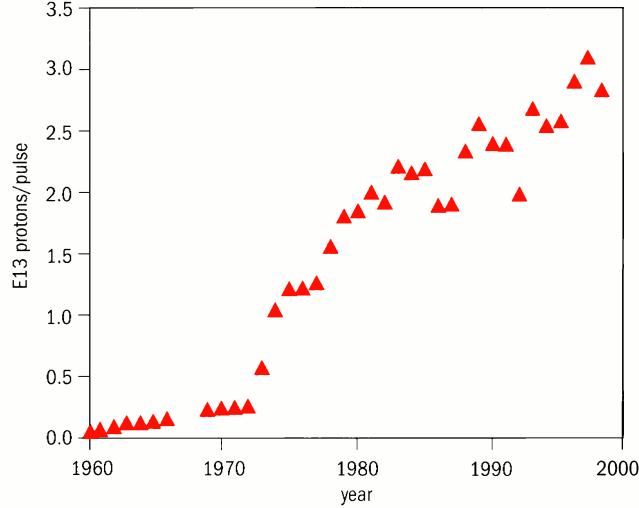
Figure 1.2 – Annual PS peak intensity in protons per pulse from 1960 till 2000 [PS Staff 1999].

With the increasing demands on brightness, the understanding of space charge dynamics and its effects on the beam has significantly advanced. In 1999, the University of Maryland in the U.S. even designed and constructed an electron ring called UMER solely for the purpose of beam dynamics research on how to push the brightness limits further. The goal is to accelerate an extremely intensive, space charge dominated beam by crossing dangerous betatron resonances quickly enough not to affect the beam quality [Kishek et al. 2000].

There have been various milestones throughout the history of space charge research in circular accelerators. After the invention of the strong focusing principle in the 1950s, non-linear resonances have been thoroughly investigated in view of the new design of alternating-gradient synchrotrons – to note the remarkable work of Schoch [1958]. A solid foundation for the self-consistent description and analytic treatment of the space charge problem has been laid by Kapchinsky and Vladimirsky [1959]. Kapchinsky and Vladimirsky constructed an equilibrium beam distribution for a coasting (longitudinally constant) beam taking into account the linear self-fields of the beam as well as the periodic focusing fields. Equilibrium here refers to the distribution remaining stationary (i.e. time-independent) exhibiting no growth or redistribution (in the absence of resonance phenomena). For this distribution, all particles turn out to move at exactly one frequency. This is closely related to the fact that the distribution function f_{KV} is a singular hyper-shell in 4D transverse phase space reading $f_{KV} = \delta\left(\mathcal{H}_\perp - \mathcal{H}_0\right)$ in terms of the Hamiltonian $\mathcal{H}_\perp$ governing the transverse motion ($\mathcal{H}_0$ is a fixed value) and the Dirac delta function δ. The so-called Kapchinskij-Vladimirskij (KV) distribution is uniform in the transverse $x - y$ plane and gives rise to linear self-fields over the beam cross-section.

To date, it seems to be the only known equilibrium distribution to the space charge problem being subject to periodic linear focusing. Kapchinsky and Vladimirsky also introduced the *envelope equations* (also known as the KV equations) which describe the time evolution of the KV equilibrium distribution.

The powerful concept of the envelope equations has later been extended first to beam distributions of circular symmetry by Gluckstern [1970] and then to general elliptical symmetry by Lapostolle [1971] and Sacherer [1971] even in full 3D for bunched beams (but without the existence of a KV-like equilibrium solution), provided that the KV distribution's semi-axes in the equation are replaced by corresponding r.m.s. values of the general beam distribution. A central and fundamental result from this work is that r.m.s. equivalent beam distributions can be compared to the corresponding KV distribution dynamics, which can largely be solved analytically. We will treat the envelope equations in section 2.2.2.

The envelope equations allow to draw fundamental conclusions on the beam stability regarding collective effects. In this context, Hofmann, Laslett, et al. [1983] found that the KV distribution is more susceptible to instabilities than more realistic distributions due to its singular δ-function nature. Their work established regions of instability for certain envelope modes by investigating perturbations about the equilibrium state. Their efforts are continued by Chen and Davidson [1994] who examine mis-matched KV distributions without the previously employed linear approximation. The beam envelope oscillations are found to possibly become subject to non-linear resonances which are related to the instabilities found before and which can give rise to beam halo formation and emittance growth.

Later, a criterion has been established to distinguish between unstable KV typical modes – which occur in theory and simulations of KV beams and are not found in realistic distributions that decrease monotonically from the centre – and modes in principle occurring in all kinds of distributions [Hofmann, Franchetti, et al. 2003]. The KV specific instabilities are explained to be non-physical as they are "negative energy" modes, i.e. one needs to take away energy from the distribution to make it become unstable. Instead, it is the positive energy modes (requiring energy to be added to the beam to become unstable) which are the dynamically relevant ones shared by the KV and more realistic distributions: they turn out to be dangerous for machine operation when excited due to betatron resonances. In the KV case, they can be analytically solved for exact periodic focusing – realistic distributions can then be compared via the r.m.s. equivalence principle.

... making numerical simulation software become a crucial tool...

Since the space charge problem is in general not analytically solvable for real accelerator layouts (which are not exact periodic focusing), one often employs numerical simulation tools to obtain quantitative results. S. M. Lund, Kikuchi, and Davidson [2009] gave an extensive review on this subject. The conventional algorithm of choice for self-consistent space charge simulations is the particle-in-cell approach in which a macro-particle beam distribution is spread on a regular grid and the beam self-fields are calculated solving the Poisson equation via finite difference techniques. This strategy originates from plasma physics [Hockney and Eastwood 1988].

The transverse self-fields of the beam counteract the applied strong focusing of the external magnetic fields in synchrotrons – resulting in a reduction of the oscillation frequencies. The more realistic case of Gaussian normal beam distributions exhibits non-linear self-fields as opposed to the KV case. Figure 1.3 compares the horizontal electric field in the beam frame of a round coasting beam (with a constant line density in the longitudinal plane) in the CERN Super Proton Synchrotron (SPS) machine for a Gaussian transverse distribution and the r.m.s. equivalent uniform distribution: the KV distribution produces the linear radial electric field of figure 1.3a with the beam edge clearly visible, while the Gaussian normal distribution gives rise to the non-linear field of figure 1.3b. The peak electric fields of both distributions are of comparable values but the slope of the linear part around to the origin is *twice* as large for the Gaussian distribution as compared to the KV one.

(a) Linear E_x of a uniform distribution.   (b) Non-linear E_x of a Gaussian distribution.
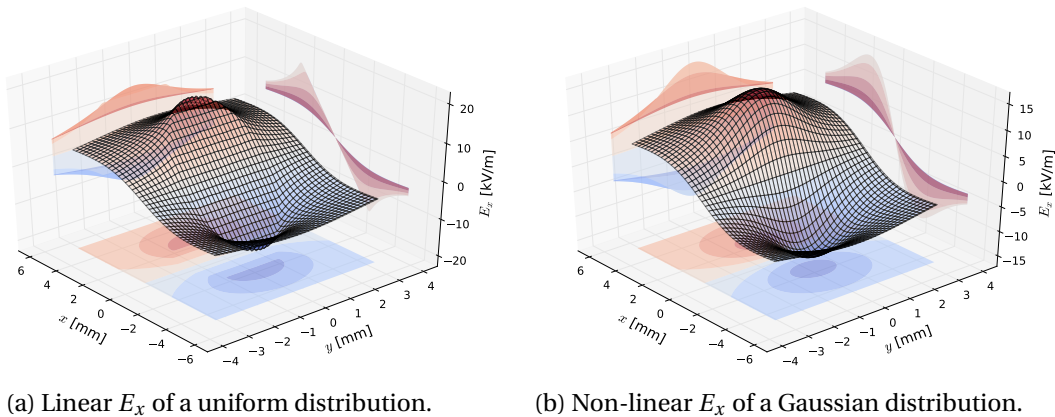
Figure 1.3 – The horizontal electric fields E_x of two r.m.s.-equivalent transverse distributions obtained via a particle-in-cell (PIC) algorithm are plotted across the transverse plane of the round SPS beams.

... to analyse the impact of betatron resonances...

Synchrotrons are circular particle accelerators employing strong periodic electromagnetic fields to focus and guide electrically charged particles. The principle of strong focusing

confines the particles in the transverse plane perpendicular to the direction of motion. To this end one arranges quadrupolar magnets in a regular lattice as illustrated in figure 1.4, whose quadratic potentials form a chain of harmonic oscillator systems for the beam. A particle travelling along the accelerator exhibits sinusoidal motion due to the alternating field gradients. The strength of the magnetic currents in principle determines the design number of oscillation periods a particle undergoes during one ring revolution. In the transverse plane, one speaks of the so-called (bare machine) betatron tunes.

Figure 1.4 – A regular alignment of quadrupole magnets following the principle of strong focusing [KEK, Japan 2013].

The beams often circulate for hundreds of thousands of revolutions around the accelerator ring. Due to the nature of the system, ever-present small field errors recur periodically for the beam. In mathematical terms, these field errors show up in the quasi-harmonic system as a sinusoidal driving term with an amplitude of the field error multipole order. In a simple picture, a single particle in a synchrotron which is subject to a localised magnet imperfection experiences a perturbative kick once each turn. If the oscillation phase of this very particle advances by a harmonic of 2π or a low-order fraction thereof, the particle is repetitively kicked into the same direction. Correspondingly, the particle may gain in energy as the amplitude of its motion increases resonantly. This dangerous effect is commonly referred to as a betatron resonance. The single particle being only subject to the external magnetic fields oscillates at the betatron tunes (Q_x, Q_y) (also called the working point) and becomes resonant when

$$m_1 Q_x + m_2 Q_y = n \quad \text{for} \quad m_1, m_2, n \in \mathbb{Z} \tag{1.2}$$

is met, where the integers $|m_1| + |m_2|$ determine the resonance order and n its harmonic. Betatron resonances can lead to serious beam degradation in terms of transverse beam size growth (emittance blow-up) which may as well result in beam losses as particles hit the machine aperture.

Since synchrotrons often consist of a certain number of periodically repeating sections, one speaks of the super-periodicity of a machine. Consider e.g. the CERN PS machine with a super-periodicity of 10. The PS lattice comprises 50 symmetric pairs of combined function magnets which provide the alternating gradient quadrupole fields for the strong focusing. Recent studies have shown a strong impact of the vertical quarter-integer resonance located near to the operational tunes at $Q_y = 6.25$. The resonance affects high intensity beams in terms of considerable losses [Wasef et al. 2013], which have been related to the structural composition of the PS lattice [Gilardoni et al. 2014; Machida 2014; Wasef 2014]. In fact, harmonics of the PS super-periodicity 10 can drive what is called a parametric structure resonance. At high beam intensities, these systematic betatron resonances can have an even stronger impact than the aforementioned generic resonances excited by local magnet imperfections due to the increased periodicity.

The identified structure resonance in the PS is not observed to have an impact for low intensity beams. Much on the contrary, the beam losses scale with the brightness of the beam, which entails that the resonance mechanism is based on the presence of considerable beam self-fields (it is said to be space charge driven). In a transversely Gaussian normal distributed particle beam, the particles oscillating at amplitudes much larger than the standard deviation of the transverse beam distribution are called the *beam halo*. They act much like test particles feeling the beam self-field as an external field while not contributing by themselves. These halo particles can be lost when interacting resonantly with the beam core and a resonance. This has e.g. been observed for the PS structure resonance in self-consistent space charge simulations for halo particles at large synchrotron amplitudes in the longitudinal plane [Machida 2014; Wasef 2014] when the vertical bare tune is located slightly above $Q_y = 6.25$.

The *beam core*, on the other hand, is also strongly affected by space charge effects, its envelope dynamics follow to a certain extent the r.m.s. equivalent KV distribution as outlined before. A qualitative difference is the dependence of the phase advance on the transverse amplitude in the Gaussian case due to the non-linear self-fields. Particles at different amplitudes oscillate at different tunes inducing a tune spread across the beam which is shown in the tune histogram example for the PS plotted in figure 1.5. In fact, the extent of the Gaussian tune spread is twice as large as the space charge tune shift of the equivalent KV beam, which is closely related to the previously noted slope of the electric field around the beam core. The tune spread is known to be responsible for a much weaker resonance response of a Gaussian beam (in terms of r.m.s. emittance blow-up) as compared to the equivalent KV beam. At the same time, the space charge modified resonance conditions can lead to emittance blow-up becoming dependent on the transverse amplitude. This is not possible in the linear KV case, where the whole beam distribution oscillates at the same frequency, all particles are shifted from the bare machine
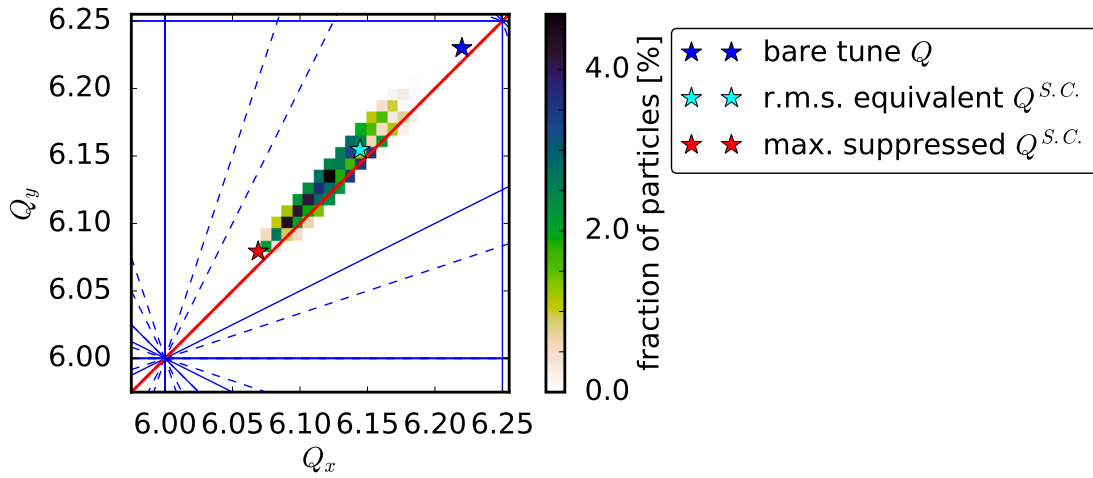
Figure 1.5 – Tune diagram with the tune spread of a transversely Gaussian distributed coasting round PS beam of high brightness. The maximal tune shift of the spread Q^{SC} is twice as large as for the r.m.s. equivalent KV beam.

tune Q_0 to the same space charge depressed tune $Q^{\text{SC}} = Q_0 - \Delta Q^{\text{KV}}$.

R. Baartman [1998] clarified this amplitude dependence feature in the context of coherent (collective mode) and incoherent (single-particle) resonance conditions and demonstrated numerical simulations with KV and Gaussian distributions for a coasting beam. Figure 1.6 shows simulation results from an intensity scan at a fixed bare tune of $Q_0 = 2.45$. The one-dimensional third-order $3Q = 7$ betatron resonance is slowly crossed from above by increasing the space charge strength (artificially) via the beam intensity. The abscissa shows the r.m.s. equivalent space charge shifted tune $Q^{\text{SC}} = Q_0 - \Delta Q^{\text{KV}}$ which decreases with increasing intensity. The plot has therefore to be understood as that space charge increases from the right towards the left, the curves evolve from high to low Q^{SC}. The graph shows three different types of curves:

1. in green crosses: the r.m.s. beam size of the simulated equivalent KV distribution, which shows a sharp increase where the beam envelope meets the coherent symmetric third-order mode resonance condition,

2. in thin coloured lines: by fixing a transverse amplitude (i.e. emittance), the fraction of the distribution contained within this amplitude is plotted, and

3. in black plus symbols: the transverse amplitude (in units of the fraction of therein contained particles) at which the respective oscillating particles meet the incoherent single-particle resonance condition $3Q^{\text{SC}} = 7$ with their space charge depressed tunes.

It is worth to spend some moments on understanding this plot as it illustrates the fundamental difference and transition between the collective nature of the core and the single-particle behaviour of the halo under the influence of space charge.
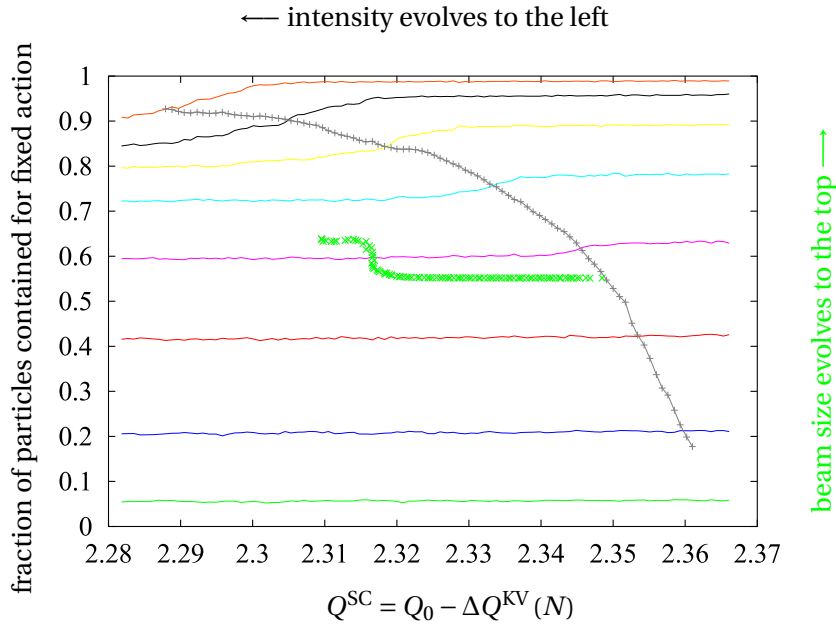
Figure 1.6 – The core and halo response to a betatron resonance [R. Baartman 1998]. The curves are explained in detail in the text.

The KV distribution shows only the collective response which happens exactly at the space charge shifted resonant tune $Q^{SC} = 2.31667$. The envelope resonates in the sextupolar symmetric mode, the particles are excited to larger single-particle emittances and the r.m.s. beam size correspondingly increases. In the Gaussian case we have the core-halo distinction. Small amplitude particles in the beam core are represented by the thin lines in the lower part of the plot. For all particle fractions below 0.5, these core particles show no considerable excitation in response to the sextupolar driving term in the simulation – the fixed transverse amplitude curves contain the same amount of particles irrespective of the space charge strength. These particles can satisfy the incoherent single-particle resonance condition (where the black plus symbols intersect e.g. with the blue and red line) and are not affected by it. On the other hand, if we approach large transverse amplitudes, the halo particles start to become excited exactly where the incoherent resonance condition is met (following the black plus symbols to the left). Therefore, the fixed amplitudes lose a fraction of the particles contained within them, and the curves drop.

R. Baartman reported a "dramatic emittance increase" for the resonating particles "along with an appearance of an m-fold symmetric island structure" (where $m = 3$ for the sextupolar driving term in this simulation). These halo particles experience the electromagnetic fields of the core as an external space charge force which mainly depends on the number of particles in the core and not so much on the shape of it.

In total, R. Baartman observed the r.m.s. width of the whole Gaussian distribution to increase centred around the same space charge shifted tune as the equivalent KV distribution (note the

dropping fraction of particles per fixed amplitude). This relationship between the Gaussian and the uniform KV distribution, both having the same ΔQ^{KV} (which is *half* the Gaussian maximal tune shift), illustrates Sacherer's central theorem regarding the r.m.s. equivalence of beams. We will come back to this during our SPS experiments on the fourth-order resonance in chapter 4.

1.4 Motivation, Goals and Outline for This Thesis

> *... for the present upgrade scenario of the CERN accelerator complex.*

As pointed out earlier, the LHC requires quite small beam emittances to be provided by the injectors. In fact, the plans to upgrade the current LHC – the High Luminosity LHC (HL-LHC) project [Apollinari et al. 2015] – to increase its discovery potential pose even tighter constraints: it is foreseen to increase the luminosity through several measures, among them increasing the intensity by nearly a factor 2 with respect to the presently delivered $N \approx 1.2 \times 10^{11}$ protons per bunch (p/b) to 2.3×10^{11} p/b [Arduini et al. 2014]. At the same time, the normalised transverse emittances are constrained to $\epsilon_{x,y} = 2.08\,\mathrm{mm\,mrad}$ which is approximately what the standard 72 bunch per PS batch scheme currently provides. In summary, the beam brightness (intensity per emittance) is to be increased by at least a factor 2.

Figure 1.7 presents a schematic overview of the CERN accelerator complex. The LHC is supplied with protons from a series of injector machines: starting from the LINAC2, the four PS Booster rings are filled with a multi-turn injection scheme. In the nominal LHC filling scheme (the "72 bunch scheme"), two subsequent batches of PS Booster beams are injected into the PS. This requires a full basic cycle during which the four bunches of the first batch wait at injection energy until the second batch of another two bunches arrives. During the 3 basic periods long PS cycle, radio frequency (RF) gymnastics splits the beam into a total of 72 bunches which are then injected into the SPS. Up to four of these PS batches are to be accommodated in the SPS making the injection plateau take $(4 - 1) \times 3$ basic cycles until the machine is filled and the acceleration ramp begins. Finally, the SPS delivers up to 12 of these bunch trains to fill the LHC with up to 2808 bunches in total.

In order to satisfy the demanding HL-LHC requirements, the whole LHC injector chain needs to be prepared and upgraded as well. The corresponding LHC Injectors Upgrade (LIU) project has been summarised in the LIU Technical Design Report [Damerau et al. 2014]. The doubled beam brightness is challenging for the PS and the SPS injection plateau during which space charge could blow up the transverse emittances. To meet the design HL-LHC parameters, the various LHC injectors have been assigned beam loss and emittance growth budgets [Bartosik, Argyropoulos, et al. 2014] which are summarised in table 1.1.

In the present accelerator configuration with LINAC2, the LHC beams are produced in the PS Booster at a constant beam brightness, which is mainly determined by the multi-turn injection
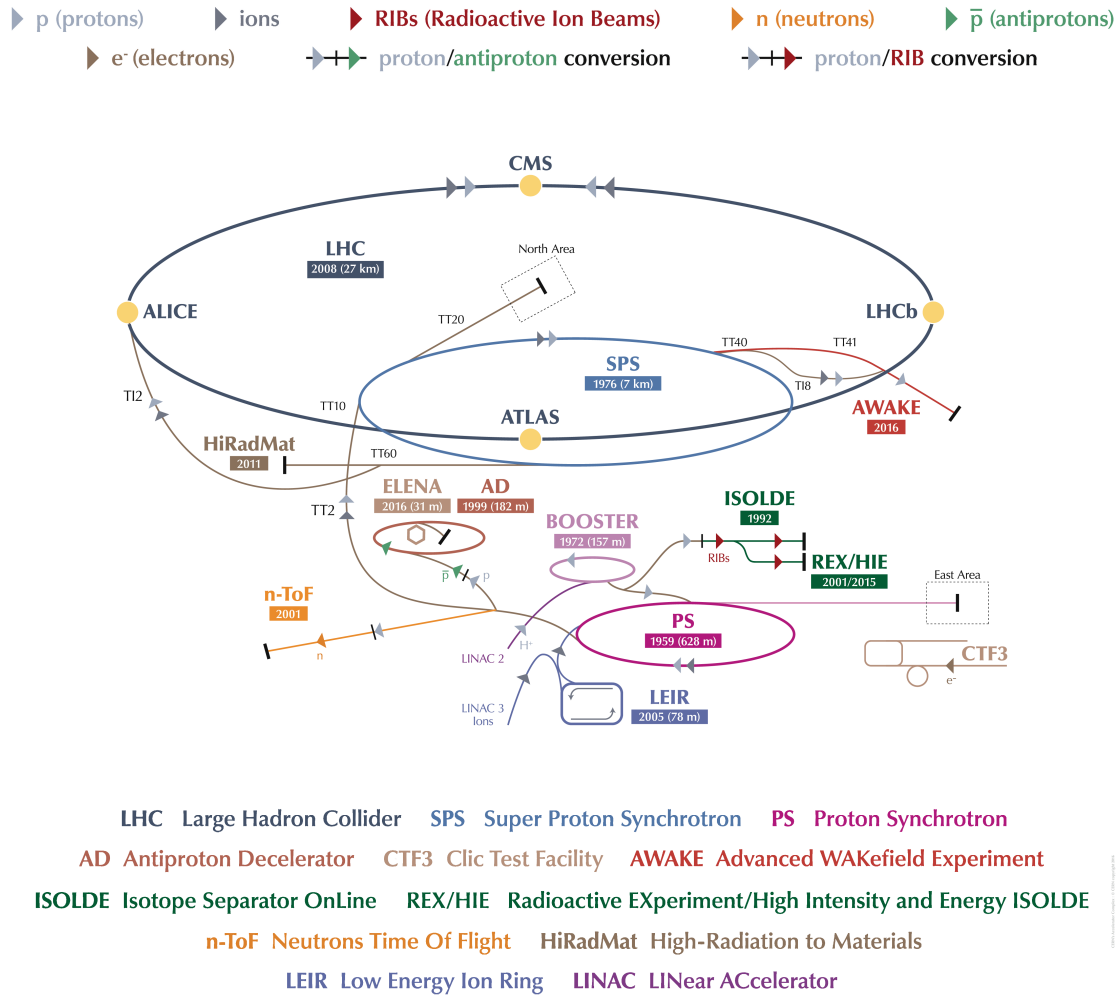
Figure 1.7 – Scheme of the present accelerator complex at CERN [De Melis 2016, modified].

process and space charge effects in the low-energy part of the cycle. With LINAC4, the PS Booster kinetic injection energy will be raised to $E_{kin} = 160\,\mathrm{MeV}$ from the present $50\,\mathrm{MeV}$. The space charge tune shift depends on the inverse energy by $\Delta Q^{SC} \propto 1/(\beta\gamma^2)$. Following the argument of the r.m.s. equivalence of beams with respect to space charge, one can compare the beams on the basis of equal space charge tune shifts. Correspondingly, one expects to achieve double beam brightness at the same overall space charge tune spread [Rumolo, Bartosik, et al. 2014] by compensating the injection energy increase. The H^- charge-exchange injection will allow to paint the transverse emittances to obtain tailored values as opposed to the current multi-turn mechanism where the brightness is fixed.

With these high brightness beams injected into the PS using the nominal filling scheme, the first of the two batches can suffer from direct space charge while waiting for the second batch. Hence, the anticipated impact during the injection plateau will have to be mitigated. The afore-mentioned structure resonance limits the operational PS tunes to below $Q_y < 6.25$.

Table 1.1 – LHC Injectors Upgrade beam loss and emittance growth budgets over the whole machine cycle [Bartosik, Argyropoulos, et al. 2014, table 1].

machine	beam loss $(N_0 - N)/N_0$	emittance growth $(\epsilon - \epsilon_0)/\epsilon_0$
PS Booster	5%	5%
PS	5%	5%
SPS	10%	10%
total	19%	21%

Experimental studies at the current kinetic injection energy of $E_{\mathrm{kin}} = 1.4\,\mathrm{GeV}$ show a Gaussian tune spread estimate of $|\Delta Q_y^{\mathrm{SC}}| = 0.31$ to be compatible with the allocated budget [ibid.]. Beams exceeding this brightness limit suffer from emittance growth due to the beam core interacting with the vertical integer resonance. The PS injection plateau essentially poses a major bottleneck of the injector chain in view of the HL-LHC beam parameters. As the main counter-measure, the PS injection energy is increased as well – for the third time in its history – to $E_{\mathrm{kin}} = 2\,\mathrm{GeV}$. Further possible counter-measures to comply with the assigned budget are investigated [ibid.].

The HL-LHC high brightness beams also suffer from emittance growth in the SPS at the present operational machine tunes as they are exposed to strong space charge during the 10.8 s long injection plateau. Preliminary working point studies below $Q_y < 20.25$ conducted in 2012 with very bright beams identified a maximum acceptable space charge tune spread of $|\Delta Q_y^{\mathrm{SC}}| = 0.21$ for the SPS [Bartosik, Argyropoulos, et al. 2014].

The space charge limits assessed in the CERN machines have been determined empirically and a deeper understanding of their origin is of importance. The higher brightness of future LHC beams will naturally lead to a situation in which most of the LHC beams will be limited by space charge both in the PS and in the SPS. In view of the upgrade of the CERN machines, it becomes crucial to fully understand the beam evolution under a strong space charge regime and to relax the present constraints. The LIU project with the outlined space charge issues defines the context for the present Ph.D. thesis project titled "Space Charge Effects and Advanced Modelling for CERN Low Energy Machines". As sketched in figure 1.8, the goals of the thesis are three-fold: (1) development of a detailed 3D *model* of space charge forces with the application of high-performance computing techniques, as well as the integration into a suitable particle tracking tool to carry out systematic studies (in close interaction with the next two topics); (2) *measuring* of space charge impact in the critical machines under various experimental conditions to understand the beam behaviour; and (3) *mitigation* of the beam quality degradation inflicted by space charge to reach the LIU beam parameter targets.
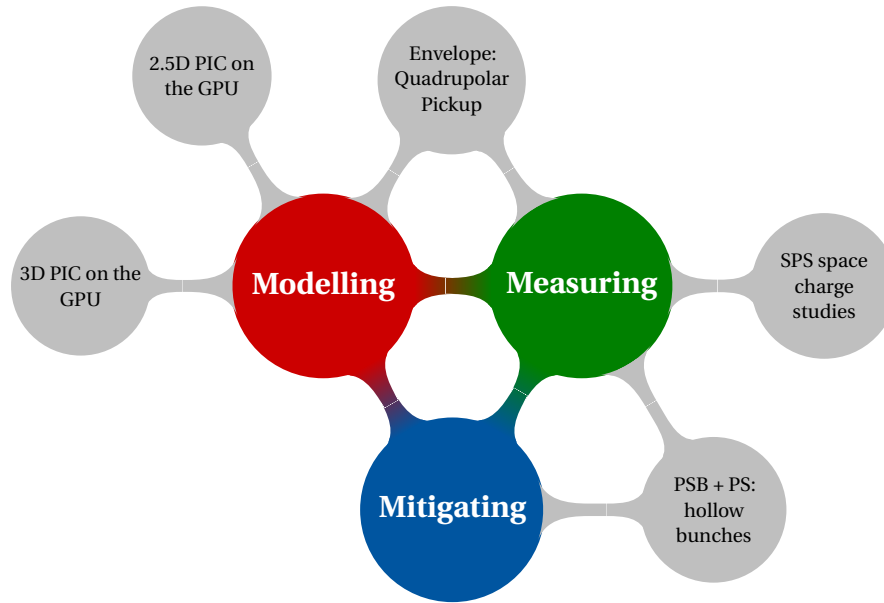
Figure 1.8 – Sketch of the core tasks for this Ph.D. thesis project.

The work and results of the Ph.D. project are presented in this thesis. After an introduction to the key concepts of beam dynamics in chapter 2, where collective space charge dynamics is treated on the basis of the envelope equations, the structure of the thesis follows the outlined three key tasks. In chapter 3 we introduce PyHEADTAIL, a collective beam dynamics simulation software developed at CERN to which constitutive contributions have been made throughout the course of the thesis. We focus on our developed space charge suite with a number of implemented models, viz. an effective longitudinal 1D model, a semi-analytical transverse 2D model based on assuming Gaussian normal distributions, a 2.5D self-consistent PIC Poisson solver which assumes relativistic beams and a full 3D PIC Poisson solver which can be used for CERN's low-energy circular accelerators as it does not assume relativistic beams. The development involved high-performance computing techniques in terms of Graphics Processing Unit (GPU)-accelerated computing, a key ingredient to make studies with the 3D space charge model feasible. Space charge simulations have been carried out with PyHEAD-TAIL to compare the collective envelope modes of a KV and a Gaussian distribution with the theoretical expectation. The relation to quadrupolar pick-ups and possible measurements of the envelope oscillations are discussed.

Chapter 4 presents the measurements of the SPS space charge situation based on an extensive working point scan with high brightness beams in the lower left half-integer quadrant of the tune diagram. The identification of ideal future working points complying with the assigned beam loss and emittance growth budgets is followed by a thorough analysis of their loss behaviour. Finally, a study of the identified harmful horizontal fourth-order resonance by driving with localised octupole magnets explores the interaction of the SPS beams with space charge. Numerical simulations with PyHEADTAIL complement the understanding of the

findings.

Last but not least, we present a mitigation strategy for the space charge issues on the PS plateau in chapter 5. We investigate the creation of hollow longitudinal phase space distributions in the PS Booster as a counter-measure for the space charge impact during the PS injection plateau. The creation mechanisms are investigated both via numerical simulations with the aid of PyHEADTAIL as well as the experimental implementation in the CERN machines. The subsequent improvements on the PS situation are studied in detailed space charge experiments.

Following the concluding chapter 6, which discusses the outlook and possible future applications of the developed work, the appendix covers the details of the hollow bunch creation mechanism in the PS Booster.

2 Relevant Concepts of Beam Dynamics

We consider a homogeneous collection of one kind of charged particles, e.g. protons, which are sent through a storage ring at momentum p_0. Figure 2.1 illustrates the employed Frenet-Serret curvilinear coordinate system. The ideal path of the particles, the *reference orbit*, is parametrised with the path length s and periodic with the ring circumference $C = 2\pi R$. The local orthonormal coordinate system (x, y, z) moves with the particles, whose motion is described with respect to s as the independent variable. The coordinates x, y and z respectively denote the horizontal (normal), vertical (binormal) and longitudinal (tangential) offset from the reference orbit for a given s and are measured in meter units in the laboratory frame. Conventionally, x points outwards from the ring centre and s increases clockwise. We consider planar machines in the $x - z$ plane without any torsion along the reference orbit. The local (horizontal) curvature radius of the reference orbit is denoted with $\rho_0(s)$.

(a) Particle bunch in the laboratory frame.   (b) Frenet-Serret coordinates.
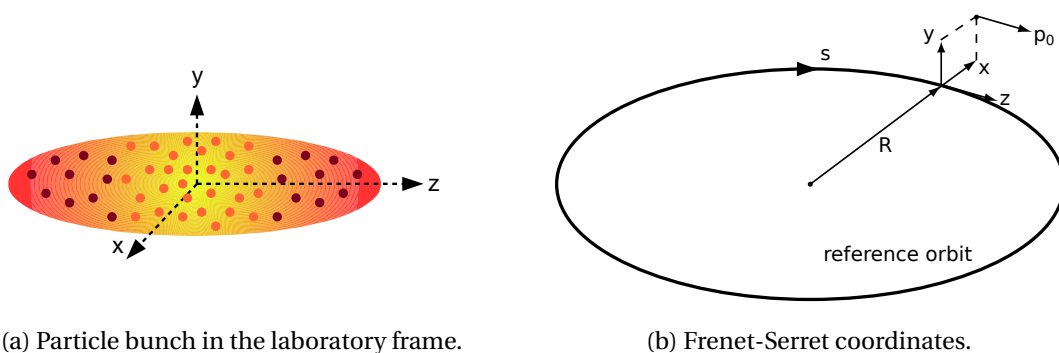
Figure 2.1 – A bunch of particles with the local coordinate system (x, y, z) for the horizontal, vertical and longitudinal plane, respectively.

The oscillatory motion of the particles around the reference orbit in the machine comprises several influences. Magnets and radio frequency (RF) systems in the machine guide, focus, accelerate and stabilise the particle beam; their effect is commonly referred to as *single-particle dynamics*. The influence of other particles from within the beam itself or the ionised rest gas in the vacuum chamber is summarised under the term *collective effects*.

We will first revise the most important concepts in single-particle dynamics due to the applied external electromagnetic fields before we turn to the self-fields of the beam and the corresponding space charge effects on the beam dynamics. The chapter is based on the materials covered by Lee [2004], S. Lund [2015], and Wiedemann [2007].

2.1 Single-particle Dynamics Due To External Fields

The particles of mass m_p move at relativistic velocity $\mathbf{v}$ and carry an electric charge q. The beam of particles is steered by using electric and magnetic fields $\mathbf{E}$ and $\mathbf{B}$ in the vacuum. The Lorentz force

$$\mathbf{F}_L = q\left(\mathbf{E} + \mathbf{v} \times \mathbf{B}\right) \tag{2.1}$$

indicates that electric fields $\mathbf{E}$ can be applied to accelerate the particles into the direction of motion. In contrast, magnetic fields $\mathbf{B}$ act orthogonal to the direction of motion and can thus be exploited to deflect particles.

In synchrotrons, particle beams are usually *paraxial*: the transverse velocities v_x, v_y are very small compared to the longitudinal velocity $v_z \approx v_0$,

$$v_x \ll v_z \quad \text{and} \quad v_y \ll v_z \quad . \tag{2.2}$$

As a consequence, static magnetic fields $\mathbf{B} = \nabla \times \mathbf{A}$ mainly have a strong deflecting effect when involving v_z, i.e. for the transverse plane. Here it shall therefore suffice to consider vector potentials of the form

$$\mathbf{A} = (0, 0, A_z) \tag{2.3}$$

where $A_z = A_z(x, y)$. Conversely, electric fields $\mathbf{E} = -\nabla V$ are most useful in the longitudinal plane and we restrict the discussion to scalar potentials $V = V(z, s)$.

The equilibrium of centripetal and Lorentz force yield the transverse bending radii $\rho_{x,y}$ of a particle trajectory under the influence of such a purely transverse magnetic field $\mathbf{B} = \nabla \times \mathbf{A} = (B_x, B_y, 0)$:

$$F_{\text{centrip.}} = F_L \implies \frac{m_p \gamma v^2}{\rho_{x,y}} = q\left|v_z B_{y,x}\right| \quad , \tag{2.4}$$

where B_y determines ρ_x and B_x determines ρ_y and we have used the paraxial beam approximation $v^2 \approx v_z^2$. With the particle momentum $p = \gamma m v$ and dropping subscripts, we find the expression

$$|B\rho| = \frac{p}{q} \quad , \tag{2.5}$$

which defines the *beam rigidity* $B\rho$ depending on a specific momentum p.

Magnet multipole strengths k_i are conventionally defined independent of p. Starting from the bending radius, which is generated by the corresponding magnetic field, we expand in the multipole components of the field. For the horizontal plane, we obtain

$$
\frac{1}{\rho_x} = \frac{q}{p} B_y
$$

$$
= \underbrace{k_1}_{\text{dipole}} - \underbrace{k_2 x}_{\text{quadrupole}} + \underbrace{k_{s2} y}_{\text{skew quadrupole}} + \underbrace{\frac{1}{2} k_3 x^2}_{\text{sextupole}} + \underbrace{k_{s3} xy}_{\text{skew sextupole}} + \mathcal{O}(3) \quad , \tag{2.6}
$$

and an analogous version in y for the vertical plane. The skew components are indicated by a subscript 's' and refer to the nth multipole field rotated by $\pi/(2n)$ compared to the upright field.

2.1.1 Transverse Betatron Motion

Bending magnets are used to guide the particles on a circular trajectory around the ring. Their dipolar vertical magnetic fields $B_y = \frac{p}{q} k_1$ curve the reference orbit leading to the local bending radius $\rho_0(s)$ (with $\rho_0(s) = \infty$ where dipolar fields vanish).

In the transverse $x - y$ plane, particles may be injected off the reference orbit with non-zero coordinates x, y and/or non-zero momenta $x' = dx/ds$, $y' = dy/ds$. Synchrotrons confine beams based on the *strong focusing* principle: particles are made to oscillate around the reference orbit with quasi-harmonic motion. To this end, one makes use of quadrupole magnets, which are periodically arranged with alternating polarities. The quadrupolar magnetic fields

$$
B_x = \frac{p}{q} k_2 y \quad \text{and} \quad B_y = -\frac{p}{q} k_2 x \tag{2.7}
$$

bend particles towards the reference orbit in the focusing plane and simultaneously away from the orbit in the other, the defocusing plane. Conventionally, a quadrupole magnet with positive strength $k_2 > 0$ focuses in the horizontal plane and is hence referred to as a *focusing quadrupole*.

Consider now a periodic *linear lattice*, i.e. a regular arrangement of dipole and quadrupole magnets in the ring layout. We will often refer to this set-up as a periodic focusing channel. The transverse motion of particles with momentum p_0 is governed by a system of linear second-order ordinary differential equation (ODE),

$$
\frac{d^2}{ds^2} \begin{pmatrix} x(s) \\ y(s) \end{pmatrix} + \underbrace{\begin{pmatrix} K_x(s) & K_{xy}(s) \\ K_{xy}(s) & K_y(s) \end{pmatrix}}_{\doteq K(s)} \begin{pmatrix} x(s) \\ y(s) \end{pmatrix} = 0 \quad , \tag{2.8}
$$

where all quadrupolar field components are collected in the matrix $K(s)$. The matrix compo-

nents $K_x(s), K_{xy}(s), K_y(s)$ are functions depending on the path length s and are periodic in the circumference C (often even in smaller periodically repeating sections). The off-diagonal terms K_{xy} represent the coupling between the horizontal and the vertical plane.

The solutions are known as the betatron motion of particles, a quasi-harmonic oscillation around the closed orbit. Since the focusing $K(s)$ is periodic in s, one can use *Floquet theory* to solve (2.8). For demonstration purposes, let us consider the decoupled horizontal equation with $K_{xy} = 0$,

$$\frac{d^2 x}{ds^2} + K_x(s) x = 0 \quad , \tag{2.9}$$

also known as the (homogeneous) *Hill's equation*. We can write the two linearly independent solutions as

$$x(s) = A_x w_x(s) e^{i\psi_x(s)} \quad \text{and} \quad x^\star(s) = A_x w_x(s) e^{-i\psi_x(s)} \quad , \tag{2.10}$$

where A_x is a constant, $w_x(s)$ the betatron amplitude function and $\psi_x(s)$ the phase advance function. To solve (2.9), w_x and ψ_x need to satisfy

$$\frac{d^2 w_x}{ds^2} + K_x(s) w_x - \frac{1}{w_x^3} = 0 \qquad \text{and} \tag{2.11a}$$

$$\frac{d\psi_x}{ds} = \frac{1}{w_x^2} \quad . \tag{2.11b}$$

According to the Floquet theorem, the betatron amplitude exhibits the same periodicity as $K_x(s)$ for a stable lattice. Equation (2.11a) entails that w_x can never change sign, as the barrier term $1/w_x^3$ prevents w_x from reaching zero. Conventionally, the betatron amplitude is chosen to be positive, $w_x(s) > 0$. The non-linear ODEs (2.11) are usually solved numerically for a given lattice design with focusing $K(s)$ by employing iterative algorithms in computer programs like MAD-X [Accelerator Beam Physics Group 2016].

Once we have found $w_x(s)$ and $\psi_x(s)$, the horizontal transfer map for the linear lattice between two locations s_1, s_2 can be expressed as the matrix

$$\mathcal{M}_{s_1 \to s_2} = \begin{pmatrix} \sqrt{\beta_{x2}} & 0 \\ -\frac{\alpha_{x2}}{\sqrt{\beta_{x2}}} & \frac{1}{\sqrt{\beta_{x2}}} \end{pmatrix} \begin{pmatrix} \cos(\Delta\psi_x) & \sin(\Delta\psi_x) \\ -\sin(\Delta\psi_x) & \cos(\Delta\psi_x) \end{pmatrix} \begin{pmatrix} \frac{1}{\sqrt{\beta_{x2}}} & 0 \\ \frac{\alpha_{x2}}{\sqrt{\beta_{x2}}} & \sqrt{\beta_{x2}} \end{pmatrix} \tag{2.12}$$

such that horizontal phase space evolves as

$$\begin{pmatrix} x \\ x' \end{pmatrix}_{s=s_2} = \mathcal{M}_{s_1 \to s_2} \begin{pmatrix} x \\ x' \end{pmatrix}_{s=s_1} \quad . \tag{2.13}$$

The phase advance between the two locations has been denoted by $\Delta\psi_x \doteq \psi_x(s_2) - \psi_x(s_1)$ and we have introduced the *Twiss parameters* β_x and α_x which depend on w_x and its derivative

$w'_x = d w_x / d s$:

$$\beta_x(s) \doteq w_x^2(s) \tag{2.14a}$$

$$\alpha_x(s) \doteq -w_x(s) w'_x(s) \equiv -\frac{1}{2} \frac{d\beta_x}{ds} \quad . \tag{2.14b}$$

The third Twiss parameter γ_x depends on the two others and is defined as

$$\gamma(s) \doteq \frac{1}{w_x^2(s)} + \left(w'_x(s)\right)^2 \equiv \frac{1 + \alpha_x^2(s)}{\beta_x(s)} \quad . \tag{2.14c}$$

The solution (2.12) to the betatron equation of motion (2.9) is an equivalent real valued linear combination of the general amplitude-phase solutions (2.10), the explicit orbit reads

$$x(s) = A_x \sqrt{\beta_x(s)} \cos(\psi(s) + \psi_0) \tag{2.15a}$$

$$x'(s) = A_x \frac{\alpha_x(s)}{\sqrt{\beta_x(s)}} \cos(\psi(s) + \psi_0) - A_x \frac{1}{\sqrt{\beta_x(s)}} \sin(\psi(s) + \psi_0) \tag{2.15b}$$

with the two integration constants or initial conditions A_x and ψ_0. The matrix $\mathcal{M}_{s_1 \to s_2}$ essentially constitutes a rescaling to the constant part A_x of the amplitude in $x - x'$ phase space, a subsequent phase rotation by $\Delta\psi_x$ and finally a transformation stretching the phase space back to the local Twiss parameters at s_2.

Linear betatron motion is integrable and Hill's equation can be derived from the transverse betatron Hamiltonian

$$\mathcal{H}_\perp(x, y, x', y'; s) = \frac{x'^2}{2} + \frac{y'^2}{2} + \frac{1}{2} K_x(s) x^2 + K_{xy}(s) x y + \frac{1}{2} K_y(s) y^2 \tag{2.16}$$

which carries rad^2 units as $x' = \partial x / \partial s \equiv p_x / p_0$.

A classic harmonic oscillator with $K(s) = $ const conserves energy. This is not the case for betatron oscillations (2.10) where the magnetic fields along s can pump energy in and out of the transverse plane. Nonetheless, there are invariants of motion. By rearranging and squaring equations (2.15), we construct the *Courant-Snyder invariant,*

$$\widetilde{\epsilon}_x^2 = \left(\frac{x(s)}{w_x(s)}\right)^2 + \left(w_x(s) x'(s) - w'_x(s) x(s)\right)^2 = \text{const} \quad , \tag{2.17}$$

which can be expressed in terms of the Twiss parameters as

$$\widetilde{\epsilon}_x^2 = \gamma_x x^2 + 2\alpha_x x x' + \beta_x x'^2 \quad . \tag{2.18}$$

In fact, the Courant-Snyder invariant corresponds to the constant part of the transverse amplitude $\widetilde{\epsilon}_x = A_x^2$ and may be referred to as the *single-particle emittance* (or sometimes the "action" $2J_x$).

The discussed concepts apply to the vertical plane in the same fashion. In summary, the betatron amplitude of a particle consists of the two separate influences, on the one hand the constant initial condition (from injection) expressed by $\widetilde{\epsilon}_{x,y}$ and on the other hand the s dependent focusing by the machine expressed by $\beta_{x,y}(s)$. The Twiss parameters $\left(\beta_{x,y}(s), \alpha_{x,y}(s), \gamma_{x,y}(s)\right)$ hence effectively describe how the machine shapes the beam. We will come back to $\beta(z)$ in the space charge discussion as the undepressed *beam envelope* for the case of vanishing space charge.

The phase advance around the whole ring in units of 2π given by the machine optics is an important quantity called the *bare machine tune*,

$$Q_{x,y} = \psi_{x,y}(C) = \oint \frac{ds}{\beta_{x,y}(s)} \quad . \tag{2.19}$$

So far, we have described the betatron motion of particles with design momentum p_0. Particles may move at slightly different momentum p than the design momentum p_0. We therefore expand the factor q/p entering the equations of motion via the magnetic fields (2.6) as

$$\frac{q}{p} = \frac{q}{p_0}(1-\delta) + \mathcal{O}(\delta^2) \tag{2.20}$$

to first order in the *momentum deviation* from p_0,

$$\delta \doteq \frac{p - p_0}{p_0} \quad . \tag{2.21}$$

Off-momentum particles are consequently bent more or less in the respective magnetic field. This introduces a coupling between the transverse and the longitudinal phase space.

The effect of dipolar magnetic fields on off-momentum particles is called *dispersion* and leads to a modified effective radius at which a particle circulates through the ring. As we consider a planar ring in the $x - z$ plane, we obtain an added inhomogeneity in the horizontal Hill equation,

$$\frac{d^2 x}{ds^2} + K_x(s)x = \frac{\delta}{\rho_0(s)} \quad . \tag{2.22}$$

Since the ODE is linear, the general solution consists of a superposition of the betatron solution (2.15a), henceforth referred to as $x_\beta(s)$, and a particular solution x_{disp},

$$x(s) = x_\beta(s) + x_{\mathrm{disp}}(s) \quad \text{with} \quad x_{\mathrm{disp}}(s) = D_x(s)\delta \quad . \tag{2.23}$$

The *dispersion function* $D_x(s)$ satisfies the inhomogeneous ODE

$$\frac{d^2 D_x}{ds^2} + K_x(s)D_x = \frac{1}{\rho_0(s)} \quad . \tag{2.24}$$

Equivalently to the Twiss functions resp. $w_x(s)$, $D_x(s)$ exhibits the same periodicity as $K_x(s)$.

The focusing by the quadrupolar magnetic fields is subject to *chromatic aberration* for particles travelling at $\delta \neq 0$. This introduced quadrupolar field error

$$\Delta K_{x,y} = K_{x,y}\delta + \mathcal{O}(\delta^2) \tag{2.25}$$

changes the betatron tune of a particle to first order in the momentum deviation δ by

$$\Delta Q_{x,y} = \underbrace{\left(\frac{-1}{4\pi} \oint \beta_{x,y} K_{x,y} ds\right)}_{\doteq Q'_{x,y,\text{natural}}} \delta \quad . \tag{2.26}$$

As chromaticity $Q'_{x,y}$ is defined by the change of the tune with the momentum,

$$Q'_{x,y} \doteq \frac{\Delta Q_{x,y}}{\delta} \quad , \tag{2.27}$$

equation (2.26) describes the natural chromaticity of the machine. $Q'_{x,y,\text{natural}}$ is always negative since higher momentum particles with $\delta > 0$ are less deflected compared to the design focusing $K(s)$.

A beam as a collection of many particles features a certain width in the transverse plane. For a vertical Gaussian distribution, the r.m.s. beam size reads

$$\sigma_y^2(s) = \left\langle y^2(s)\right\rangle_\perp - \left\langle y(s)\right\rangle_\perp^2 = \beta_y(s)\left\langle \widetilde{\epsilon}_y\right\rangle_\perp \doteq \beta_y(s)\epsilon_{y,\text{geo}} \tag{2.28}$$

where $\langle\cdot\rangle_\perp$ denotes the transverse expectation value over all particles. We have defined the vertical geometric r.m.s. beam emittance $\epsilon_{y,\text{geo}}$ which can be defined as the statistical quantity

$$\epsilon_{y,\text{geo}} \doteq \sqrt{\left\langle y^2\right\rangle_\perp \left\langle y'^2\right\rangle_\perp - \left\langle yy'\right\rangle_\perp^2 - \left\langle y\right\rangle_\perp^2 \left\langle y'^2\right\rangle_\perp - \left\langle y^2\right\rangle_\perp \left\langle y'\right\rangle_\perp^2 + 2\left\langle yy'\right\rangle_\perp \left\langle y\right\rangle_\perp \left\langle y'\right\rangle_\perp} \quad . \tag{2.29}$$

In the case of $\left\langle y\right\rangle_\perp = \left\langle y'\right\rangle_\perp = 0$, this expression reduces to

$$\epsilon_{y,\text{geo}} = \sqrt{\left\langle y^2\right\rangle_\perp \left\langle y'^2\right\rangle_\perp - \left\langle yy'\right\rangle_\perp^2} \quad . \tag{2.30}$$

The geometric emittance shrinks when the beam is accelerated. In synchrotrons, this shrinking is happening adiabatically. This "adiabatic damping" can be taken into account by defining the *normalised beam emittance*

$$\epsilon_y \doteq \beta\gamma\epsilon_{y,\text{geo}} \quad . \tag{2.31}$$

Without filamentation or dynamical effects e.g. from resonances and neglecting multi-particle effects, ϵ_y remains constant during acceleration. In the horizontal plane, the beam size needs to take into account the dispersive effect which broadens the distribution.

The horizontal position of a particle (2.23) consists of the independent sum of two random variables: x_β as the betatron motion and $x_{\text{disp}} = D_x \delta$ as the dispersion contribution depending on the andomly distributed momentum deviation δ. By looking at the ensemble of particles, we can therefore express the resulting horizontal distribution as a convolution of the normalised distribution functions of both x_β and x_{disp}, which we denote f_β and f_{disp}, respectively. A normalised distribution function integrates to unity over the entire domain. The dispersion distribution relates to the normalised momentum distribution f_δ via

$$f_{\text{disp}}(x) = \frac{f_\delta\left(x/D_x\right)}{|D_x|} \quad . \tag{2.32}$$

Finally, the horizontal distribution $p(x)$ yields

$$p(x) = \int_{-\infty}^{\infty} dx'\, f_\beta(x - x') f_{\text{disp}}(x') \tag{2.33}$$

which corresponds to the beam profile one measures at a given time. We can evaluate the r.m.s. beam width of $p(x)$ as a sum of the respective variances of f_β and f_δ. Given the variance of the betatron distribution equivalently to (2.28) with the horizontal normalised r.m.s. emittance ϵ_x (cf. (2.31)),

$$\sigma_{x_\beta}^2 = \frac{\beta_x \epsilon_x}{\beta \gamma} \quad , \tag{2.34}$$

and the variance of the momentum deviation distribution, δ_{rms}^2, the horizontal r.m.s. beam width in the presence of dispersion at the location s of the profile measurement reads

$$\sigma_x^2(s) = \beta_x(s) \frac{\epsilon_x}{\beta \gamma} + D_x^2(s) \delta_{\text{rms}}^2 \quad . \tag{2.35}$$

This statement is in general true if and only if x_β and δ are independent random variables (otherwise covariances enter the expression) with σ_x, δ_{rms} and ϵ_x strictly being r.m.s. quantities.

2.1.2 Longitudinal Dynamics

In synchrotrons, RF cavities provide longitudinal focusing. A particle crossing the gap of an RF cavity at a phase φ is subject to the electric potential

$$V(\varphi) = \hat{V} \sin\left(\varphi + \Delta \varphi\right) \tag{2.36}$$

for a given RF phase offset $\Delta \varphi$ and for $\hat{V}$ the maximal amplitude of the RF voltage oscillating at frequency f_{RF}. The RF phase φ relates to the longitudinal beam offset z via

$$\varphi = -\frac{hz}{R} \quad , \tag{2.37}$$

(modulo 2π). The effective machine radius has been denoted by $R = C/(2\pi)$. The harmonic h of the RF frequency f_{RF} with respect to the revolution frequency of the beam,

$$f_{rev} = \frac{\beta c}{C} \quad , \tag{2.38}$$

is given by

$$h \doteq \frac{f_{RF}}{f_{rev}} \quad . \tag{2.39}$$

For a synchrotron to work "synchronous", the harmonic of the principle RF system needs to be an integer. Phase feedback loops are often employed to align the main RF phase to the centre-of-gravity phase of the beam. The RF wave (2.36) then leads to phase focusing of the beam around the synchronous phase φ_s. For $h > 1$ one can accommodate several bunches of particles in the circular accelerator, each spaced by C/h.

Let us follow the particle motion close to the synchronous phase assuming a stationary situation with no acceleration on average. Fixing the principle RF reference phase at $\Delta\varphi = \pi$, a particle arriving at the RF cavity ahead of the $z = 0$ synchronous particle sitting at $\Delta\varphi$, i.e. at $\varphi < \Delta\varphi$ ($z > 0$), traverses a negative potential difference across the gap and becomes decelerated. In contrast, particles arriving at $\varphi > \Delta\varphi$ ($z < 0$) become accelerated. In addition, particles at positive momentum offset $\delta > 0$ travel around the accelerator ring faster than particles at reference momentum $\delta = 0$ at sufficiently low energies below transition energy $\gamma < \gamma_{tr}$. Therefore, they will arrive ahead of the synchronous particle at some point and be decelerated until the opposite situation is reached and they are accelerated from behind the synchronous particle. The particles are thus subject to a net focusing effect, their motion is confined around a stable fix point at $\Delta\varphi$ (for sufficiently small synchrotron amplitudes).

Suppose now the principal RF cavity to pulse at a non-vanishing synchronous phase $\Delta\varphi = \pi - \varphi_s < \pi$. A bunch of particles arriving at the cavity with its centre-of-gravity phase $\langle\varphi\rangle$ aligned with the RF reference phase $\langle\varphi\rangle = \Delta\varphi$ experiences a net acceleration because its kinetic energy increases with

$$\Delta E_{kin} = q\hat{V}\sin(\varphi_s) \quad . \tag{2.40}$$

The dispersion effect from the dipole bending magnets leads to a difference in the path length around the accelerator for particles of different momentum deviations δ. This effect is commonly referred to as (first-order) momentum compaction. To first order in δ we can define the momentum compaction factor α_c via the individual path difference ΔC_i as

$$\frac{\Delta C_i}{C} \doteq \alpha_c\delta \equiv \delta \oint ds \, \frac{D_x(s)}{\rho_0(s)} \quad . \tag{2.41}$$

At a specific beam velocity β, this increase in path length will outweigh the gain in arrival time

for a $\delta > 0$ particle. This happens at the transition energy γ_{tr}, where all particles arrive at the same time like the synchronous particle (and therefore phase focusing will be lost). By looking at the revolution period $T = C/(\beta c)$, we find the individual particle time offset ΔT_i related to the individual velocity offset $\Delta \beta_i$ via

$$\frac{\Delta T_i}{T} = \frac{\Delta C_i}{C} - \frac{\Delta \beta_i}{\beta} \quad . \tag{2.42}$$

From (2.41) with the differential of β expressed with respect to δ we obtain the expression

$$\frac{\Delta T_i}{T} = \underbrace{\left(\alpha_c - \frac{1}{\gamma^2} \right)}_{\doteq \eta} \delta \quad , \tag{2.43}$$

which defines the first-order slippage factor

$$\eta \doteq \alpha_c - \frac{1}{\gamma^2} \quad . \tag{2.44}$$

With the definition of the transition energy as the critical Lorentz factor

$$\gamma_{\text{tr}} \doteq \frac{1}{\sqrt{\alpha_c}} \tag{2.45}$$

we can therefore relate a negative slippage factor $\eta < 0$ to the regime below transition energy, $\gamma < \gamma_{\text{tr}}$, and vice versa a positive slippage factor $\eta > 0$ to the regime above transition energy, $\gamma > \gamma_{\text{tr}}$. In order to maintain phase focusing above transition, where the longer paths $\Delta C_i > 0$ for $\delta > 0$ particles leads to delayed instead of advanced arrival at the RF cavity, the principal reference RF phase needs to be aligned at $\Delta \varphi = \varphi_s$ (instead of $\Delta \varphi = \pi - \varphi_s$ below transition). The arrival time ΔT_i relates to the longitudinal position offset Δz of the particle via

$$\Delta T_i = -\beta c \Delta z \quad . \tag{2.46}$$

We have finally gathered all necessary ingredients to describe the synchrotron motion by a discrete map from one turn to the next in terms of the pair of conjugate variables $(z, \Delta p = \delta p_0)$. For a single-harmonic RF system with one cavity giving a kick at one location, the RF reference phase corresponds to the synchronous phase (with the π offset depending on the phase stability)

$$\Delta \varphi = \begin{cases} \pi - \varphi_s & , \gamma < \gamma_{\text{tr}} \\ \varphi_s & , \gamma > \gamma_{\text{tr}} \end{cases} \quad . \tag{2.47}$$

The longitudinal coordinate z measures the offset relative to the location of the synchronous

particle. The synchrotron map then reads

$$\Delta p|_{n+1} = \Delta p|_n + \frac{q\hat{V}}{\beta c} \left[\sin\left(\frac{hz|_n}{R} + \Delta\varphi \right) - \sin\left(\Delta\varphi \right) \right] \quad , \tag{2.48}$$

$$z|_{n+1} = z_n + \eta\left(\frac{\Delta p|_{n+1}}{p_0} \right) \frac{\Delta p|_{n+1}}{p_0} C \quad . \tag{2.49}$$

One can extend this one-turn map to include multi-harmonic RF systems with cavities at different locations in the ring each with respective configurations $(h_i, \hat{V}_i, \Delta\varphi_i)$ by adding the corresponding kicks in Δp interleaved by drifts in z over the respective length $L \le C$.

Since the synchrotron period is usually on the order of $\mathcal{O}(10)$ to $\mathcal{O}(1000)$ turns, one can describe the effect of the sinusoidal RF kick smoothly spread out across the ring via the non-linear longitudinal Hamiltonian

$$\mathcal{H}_{\parallel}(z, \Delta p; t) = -\frac{1}{2}\eta\beta c \frac{\Delta p^2}{p_0(t)} + \frac{q}{2\pi} \frac{\hat{V}(t)}{h} \left[\cos\left(\frac{hz}{R} + \Delta\varphi(t) \right) + \sin\left(\Delta\varphi(t) \right) \frac{hz}{R} \right] \quad . \tag{2.50}$$

For accelerated bunches, the momentum $p_0(t)$ and thus $\beta(t)$ and $\eta(t)$ change with time t, the independent parameter of $\mathcal{H}_{\parallel}$. The RF parameters $\hat{V}(t)$ and $\varphi(t)$ may be modified with time. We exploit this in chapter 5 to modify the longitudinal phase space distribution.

The non-linear Hamiltonian landscape imprinted on phase space by (2.50) is separated into two distinct regions by a separatrix: outside the separatrix particles move unbound (and are usually lost at the machine aperture in the case of acceleration because the horizontal offset increases with the momentum offset due to dispersion), while inside the separatrix particles follow bound, periodic motion according to the phase focusing. The area inside the separatrix is commonly referred to as the RF bucket.

The longitudinal equation of motion derived from the Hamiltonian (2.50) yields

$$\frac{d^2 z}{d t^2} + \frac{\eta\beta c q \hat{V}}{p_0 C} \left[\sin\left(\frac{hz}{R} + \Delta\varphi(t) \right) - \sin\left(\Delta\varphi(t) \right) \right] = 0 \quad . \tag{2.51}$$

Linearising the potential term in (2.51) around the stable fix point at $z = R\Delta\varphi(t)/h$ yields

$$\sin\left(\frac{hz}{R} + \Delta\varphi(t) \right) = \sin\left(\frac{hz}{R} \right) \cos\left(\Delta\varphi(t) \right) + \cos\left(\frac{hz}{R} \right) \sin\left(\Delta\varphi(t) \right)$$

$$= \frac{hz}{R} \cos\left(\Delta\varphi(t) \right) + \mathcal{O}\left(z^2 \right) \tag{2.52}$$

and we obtain the ODE for linearised synchrotron motion,

$$\frac{d^2 z}{d t^2} + \underbrace{\frac{h\eta\beta c q \hat{V}}{p_0 C R} \cos\left(\Delta\varphi(t) \right)}_{\doteq (2\pi f_{s,0})^2} z = 0 \quad , \tag{2.53}$$

which describes harmonic oscillation at the linear synchrotron frequency $f_{s,0}$. The ratio to the revolution frequency $f_{\text{rev}} = \beta c / C$ finally gives the expression for the linear synchrotron tune

$$Q_{s,0} = \frac{f_{s,0}}{f_{\text{rev}}} = \sqrt{\frac{q\hat{V}h\eta\cos(\Delta\varphi)}{2\pi p_0 \beta c}} \tag{2.54}$$

for particles oscillating close to the RF bucket centre around the stable fix point.

2.2 Direct Space Charge Dynamics

We now turn our attention to the multi-particle aspect of beams. When describing the motion of a distribution of particles, one conventionally distinguishes between two categories of motion. The independent oscillations of a single particle within the beam are referred to as *incoherent* motion. The individual betatron amplitude, phase and frequency can usually not be observed in instruments installed in particle accelerators[1]. We normally assume the parameters to be randomly distributed over all particles. The incoherent picture plays a central role in the previously discussed single-particle beam dynamics effects. Modelling the motion of beam halo particles in the electromagnetic fields of an intense beam also relies on the incoherent description.

As opposed to the individual particles, the statistical moments of the confined beam distribution are accessible e.g. by electric pick-ups. Two electrodes installed on opposite sides of the vacuum tube, for example, can yield the dipolar moment of the beam in the spanned plane by subtraction of their signals. The base-band tune measurement system (BBQ) is based on this principle: it gives the frequency of the beam centroid (i.e. the dipolar beam moment, which is the mean value of the distribution) relating to the betatron tune. Likewise, higher-order beam moments can be measured with more electrodes using a corresponding combination of their signals. In section 3.5, we discuss measuring the quadrupolar beam moment (i.e. the standard deviation) associated with the envelope oscillations of the beam with a Quadrupolar Pick-up (QPU) structure. The evolution of the statistical moments is referred to as the *coherent* motion of the beam, which always involves many particles moving with strong phase correlation. In contrast, incoherent motion of the particles is independent of the phase – thus it is possible that all particles actually oscillate while the beam as a whole remains static in the statistical sense. The distinction between incoherent and coherent motion is illustrated on the example of a swing as well as a coasting beam in figure 2.2.

The lowest (zero-order or monopole) moment of a beam distribution $f(x, y, z, x', y', \delta; s)$ gives its normalisation,

$$1 = \int d^6\zeta \, f(\zeta; s) \tag{2.55}$$

---

[1]with the exception of Schottky pick-up electrodes which can measure the incoherent frequency spread of an unbunched beam (cf. e.g. Schindl [1999])
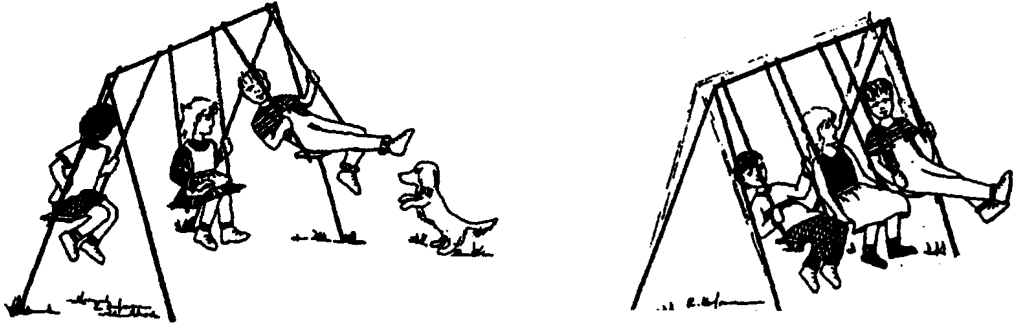
(a) Incoherent motion of a swing.

(b) Coherent (dipolar) motion of a swing.
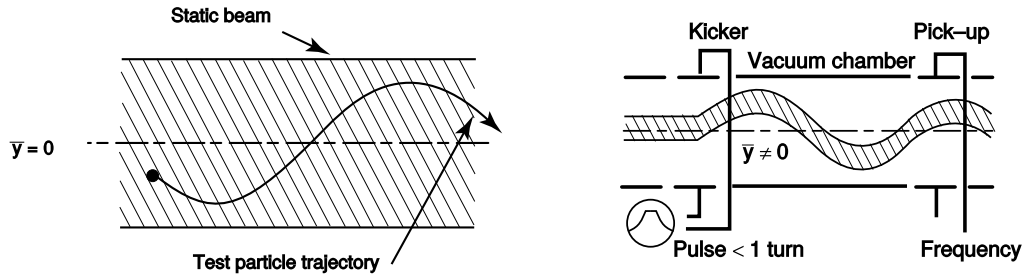
(c) Incoherent motion of a particle in a static beam.

(d) Coherent dipolar motion of the whole beam.

Figure 2.2 – The distinction between incoherent and coherent motion (courtesy of Zotter [1998, figure 3] as well as Schindl [1999, figures 9 and 10]).

with $\zeta \doteq (x, y, z, x', y', \delta)$ the vector of all six phase space coordinates and the integration domain covering the entire phase space.

The first-order (dipole) moment of any generalised coordinate or momentum $u = \zeta_i$ is equivalent to the expectation value with respect to f and has already been introduced as $\langle \cdot \rangle$, it reads

$$\langle u \rangle (s) = \int d^6\zeta \, u f(\zeta; s) \quad . \tag{2.56}$$

Any higher nth-order statistical moment u_n is then expressed with respect to the mean value (i.e. the beam centroid) and amounts to

$$u_n(s) = \int d^6\zeta \, (u - \langle u \rangle)^n f(\zeta; s) \quad . \tag{2.57}$$

The moment u_n can in principle consist of a combination of ζ_i and it evolves along s. We already denoted the quadrupolar moment (i.e. the variance) by $\sigma_{x,y}^2$ and identified σ with the r.m.s. beam size.

The collective nature of a beam expresses in the coherent modes that can be excited. The

dipolar mode has already been depicted in figure 2.2d. Pictorially, the beam distribution is contracted to a point and behaves exactly like a single particle which, if excited e.g. by a dipolar kicker magnet, oscillates about the reference orbit. In free space, the oscillation frequency amounts to the bare machine tune as the beam centroid is subjected to the restoring force of the magnetic fields from the quadrupole magnets. However, the beam is usually confined within a conducting vacuum tube and also the magnet poles are located at a finite distance to the beam. The correspondingly induced currents in the vacuum tube walls and the magnet poles due to the electromagnetic beam fields affect the evolution of the beam distribution. This effect is referred to as *indirect space charge* and it influences the coherent motion of the beam from the dipolar order on. The dipolar coherent oscillation of the beam centroid can consequently be detuned, entailing that the measured betatron frequency in a BBQ pick-up yields a tune shifted below the bare machine tune. In this context, one often encounters the notion of a coherent tune shift, hence omitting the "dipole" connotation. For further details on indirect space charge, we refer to the textbook by Chao [1993]. Here it may suffice to mention that appropriate models for the dipolar and quadrupolar influence of indirect space charge (and beam-wall impedance interactions) via the wake function formalism are included in the beam dynamics simulation software PyHEADTAIL at CERN, which we introduce in chapter 3.

In this thesis, we concentrate on the *direct space charge* forces, their modelling and effect on beams. Direct space charge addresses the interaction of the beam particles with the electromagnetic fields generated by the beam distribution itself. The dipolar beam moment does not exhibit any influence from direct space charge since the internal structure of the beam is integrated out. Only from the quadrupole moment on, the so-called "beam envelope", the distribution plays a role and so does direct space charge in affecting coherent motion. The next sections summarise important concepts for space charge based on the treatment by R. Baartman [1998], S. Lund [2015], and Reiser [2008].

2.2.1 On the Incoherent Tune Shift

Transverse Space Charge

The KV distribution is of major importance in analytical space charge calculations as it is the only known transverse equilibrium distribution in a periodic focusing channel (the longitudinal distribution is translation invariant, the beam is coasting). Kapchinsky and Vladimirsky [1959] worked out the nature of this distribution which is given by

$$f_{KV} = \delta \left(\mathcal{H}_\perp - \mathcal{H}_0 \right) \tag{2.58}$$

where $\mathcal{H}_\perp$ is the transverse Hamiltonian (e.g. the betatron Hamiltonian (2.16) without space charge yet) and $\mathcal{H}_0$ a fixed value thereof which all particles assume due to the Dirac function δ. For the linear betatron Hamiltonian, (2.58) entails that all particles have the same Hamiltonian value $\mathcal{H}_0$ and hence their oscillation evolves with the same phase advance $\psi_{x,y}(s)$. In other words, all particles exhibit the same betatron tune $Q_{x,y}$. Now we include the intensity effects

of the KV beam at particle charge q and constant longitudinal line charge density $\lambda = $ const.

In general, the electromagnetic fields created by any time dependant charge distribution $\rho(x, y, z; t)$ have to satisfy the Maxwell equations,

$$\nabla \cdot \mathbf{E} = \frac{\rho}{\epsilon_0} \tag{2.59a}$$

$$\nabla \times \mathbf{E} = -\frac{\partial \mathbf{B}}{\partial t} \tag{2.59b}$$

$$\nabla \cdot \mathbf{B} = 0 \tag{2.59c}$$

$$\nabla \times \mathbf{B} = \mu_0 \mathbf{j} + \frac{1}{c^2} \frac{\partial \mathbf{E}}{\partial t} \tag{2.59d}$$

In the beam rest frame, the paraxial nature of synchrotron beams (2.2) entails that the magnetic fields $\mathbf{B}$ are negligibly small: the particles move at very slow relative velocities and the electric Coulomb interaction is by far the dominant effect. We will exploit this electrostatic nature of the beam self-fields in the rest frame for the space charge modelling in chapter 3. Most importantly, the transverse electric field can be written in terms of a potential $\phi = \phi(x, y, z; t)$,

$$\mathbf{E}_\perp = -\nabla_\perp \phi \quad , \tag{2.60}$$

leading to a conservative space charge force field. The Maxwell equations for this electrostatic scenario reduce to the Poisson equation

$$\Delta \phi = -\frac{\rho}{\epsilon_0} \tag{2.61}$$

with the Laplace operator $\Delta = \nabla^2 = \partial^2/\partial x^2 + \partial^2/\partial y^2 + \partial^2/\partial z^2$. If we Lorentz transform to the laboratory frame for the beam moving at a certain kinetic energy

$$E_{\text{kin}} = (\gamma - 1) m_p c^2 \quad , \tag{2.62}$$

the beam becomes a current $j = \rho \beta c$ generating a corresponding transverse magnetic field $\mathbf{B}$. Using the longitudinal vector potential $\mathbf{A} = (0, 0, A_z)$ discussed around (2.3), $\mathbf{B}$ directly relates to the beam potential ϕ via

$$\mathbf{B} = \nabla \times \mathbf{A} \quad , \tag{2.63}$$

$$A_z = \frac{\beta}{c} \phi \quad . \tag{2.64}$$

We can extend the betatron Hamiltonian (2.16) for the transverse motion of a particle by including the beam self-fields as

$$\mathcal{H}_\perp = \frac{x'^2}{2} + \frac{y'^2}{2} + \frac{1}{2} K_x(s) x^2 + K_{xy}(s) xy + \frac{1}{2} K_y(s) y^2 + \frac{q}{\beta \gamma^2 p_0 c} \phi(x, y, z; s) \tag{2.65}$$

where the potential ϕ is determined by the evolving beam charge distribution $\rho(s)$ via the

Poisson equation. The notion of *self-consistency* enters the arena, since the motion of the particles may change the beam distribution which in turn determines the beam self-fields and hence the particle motion.

The crucial ingredients to the importance of the KV distribution are, firstly, its equilibrium nature in a periodic focusing $K(s)$ and, secondly, its linear transverse electromagnetic fields (within the beam distribution). This allows for fundamental analytic insight into the collective nature of particle beams and has been a gold mine for space charge research since the pioneering work by Kapchinsky and Vladimirsky [1959]. The transverse potential of the KV distribution entering in (2.65) is quadratic and thus preserves the harmonic oscillator nature of the transverse betatron Hamiltonian (2.16) even in the presence of space charge. Correspondingly, the equations of motion for the transverse particles coordinates $\mathbf{x}_\perp = (x, y)^T$,

$$\frac{d^2 \mathbf{x}_\perp}{ds^2} + K(s)\mathbf{x}_\perp = \frac{q}{\beta\gamma^2 p_0 c}\mathbf{E}_\perp \quad , \tag{2.66}$$

remain completely linear within the beam cross-section as $\mathbf{E} \propto (\mathbf{x} - \langle\mathbf{x}\rangle)$. The reason why the KV distribution (2.58) has a quadratic potential and therefore linear self-fields lies in the beam geometry. At any point s, the transverse spatial projection of this singular hyper-shell phase space distribution f_{KV} becomes an elliptical disk of uniform density,

$$\rho(x, y; s) = \begin{cases} \dfrac{\lambda}{\pi a b} & , \dfrac{(x - \langle x\rangle)^2}{a^2} + \dfrac{(y - \langle y\rangle)^2}{b^2} \leq 1 \\ 0 & , \text{else} \end{cases} \tag{2.67}$$

with horizontal semi-axis $a = a(s)$ and vertical semi-axis $b = b(s)$. The detailed derivation of $\rho_\perp$ is straightforward starting from (2.58) by employing (2.65), cf. e.g. S. Lund [2015]. The particles in the KV distribution all travel at the same betatron amplitude and thus periodically traverse the transverse plane from one beam edge to the other. The space charge force is linear across the whole distribution owing to the linear electric and magnetic self-fields $\mathbf{E}$ and $\mathbf{B}$ generated by the ellipse, which are easily computed to amount to

$$\mathbf{E}_{\mathrm{KV}} = \frac{\lambda}{\pi\epsilon_0(a+b)}\left(\frac{x - \langle x\rangle}{a}, \frac{y - \langle y\rangle}{b}, 0\right) \tag{2.68a}$$

$$\mathbf{B}_{\mathrm{KV}} = \frac{\mu_0 \lambda\beta c}{\pi(a+b)}\left(-\frac{y - \langle y\rangle}{b}, \frac{x - \langle x\rangle}{a}, 0\right) \tag{2.68b}$$

within the beam edges. The longitudinal fields vanish due to the symmetry $\partial/\partial z = 0$. The corresponding quadratic potential of the KV distribution solving the Poisson equation yields

$$\phi_{\mathrm{KV}} = -\frac{\lambda}{2\pi\epsilon_0}\left[\frac{(x - \langle x\rangle)^2}{a(a+b)} + \frac{(y - \langle y\rangle)^2}{b(a+b)}\right] + \text{const} \quad . \tag{2.69}$$

Since all particles exhibit the same Hamiltonian value in the singular KV distribution, we are

now in the position to compute their betatron tune including the space charge effect. The linear self-fields (2.68) can be understood to contribute to the externally applied focusing force $K(s)$ in the equations of motion (2.66). Assume vanishing machine coupling for now, $K_{xy}(s) = 0$. Defining the *space charge perveance* as

$$K^{\mathrm{SC}} \doteq \frac{q\lambda}{2\pi\epsilon_0 \beta\gamma^2 p_0 c} \quad, \tag{2.70}$$

the single particle equations of motion (2.66) yield for the horizontal plane

$$\frac{d^2 x}{ds^2} + K_x(s)x = \frac{2K^{\mathrm{SC}}}{a(a+b)}(x - \langle x \rangle) \quad, \tag{2.71}$$

and an equivalent equation for the vertical plane by exchanging $x \leftrightarrow y$ and $a \leftrightarrow b$. We obtain the beam centroid motion by taking the expectation value $\langle \cdot \rangle$ over both sides,

$$\frac{d^2}{ds^2}\langle x \rangle + K_x(s)\langle x \rangle = 0 \quad. \tag{2.72}$$

This reflects the independence of the beam centroid motion from direct space charge, which we mentioned before when introducing the beam moments: the K^{SC} term vanishes for the dipolar coherent motion and the restoring force (determining the betatron tune) only comes from the external fields. We can now subtract (2.72) from (2.71) to finally obtain the incoherent motion of a particle with respect to the beam centroid:

$$\frac{d^2}{ds^2}(x - \langle x \rangle) + \left[K_x(s) - \frac{2K^{\mathrm{SC}}}{a(a+b)} \right](x - \langle x \rangle) = 0 \quad. \tag{2.73}$$

Therefore, linear transverse space charge forces lead to a defocusing effect as the space charge restoring force term carries a negative sign. The incoherent betatron tune of the single particles Q^{SC} thus appears shifted by ΔQ^{KV} from the bare machine tune. Again, as all particles in the KV distribution oscillate at the same Hamiltonian value $\mathcal{H}_0$, the incoherent space charge tune shift ΔQ^{KV} shifts all particles to the same tune. Having also the same betatron amplitudes, the particles only differ by their uniformly distributed phases.

If we assume a continuous focusing channel, i.e. $K_x(s) = \mathrm{const}$ and $K_y(s) = \mathrm{const}$, it follows directly from (2.19) that

$$K_x = \frac{1}{\beta_x^2} = \frac{Q_x^2}{R^2} \tag{2.74a}$$

$$K_y = \frac{1}{\beta_y^2} = \frac{Q_y^2}{R^2} \tag{2.74b}$$

for $R = C/(2\pi)$ the effective machine radius. (2.74) is also referred to as the *smooth ring*

approximation, $Q_{x,y}$ are the bare machine tunes. From (2.73) we then obtain

$$\left(Q_x^{\text{SC}}\right)^2 = Q_x^2 - \frac{2K^{\text{SC}}R^2}{a(a+b)} \quad , \tag{2.75}$$

where a, b are the *equilibrium* semi-axes. Neglecting quadratic terms in

$$\Delta Q_x^{\text{KV}} \doteq Q_x^{\text{SC}} - Q_x \quad , \tag{2.76}$$

we find the horizontal incoherent space charge tune shift in the smooth approximation for a KV distribution to amount to

$$\Delta Q_x^{\text{KV}} = -\frac{K^{\text{SC}}R^2}{a(a+b)Q_x} \tag{2.77}$$

(and likewise for the vertical plane).

In the general case where the betatron functions vary around the ring, we can treat the space charge restoring force term in (2.73) as a distributed quadrupolar gradient error similar to the natural chromaticity in expression (2.26). The beam sizes may vary around the ring, $a = a(s)$ and $b = b(s)$, depending on the local focusing $K(s)$. The KV space charge tune shift then evaluates to the expression

$$\Delta Q_x^{\text{KV}} = \frac{1}{4\pi} \oint ds\, \Delta K\, \beta_x(s) = \frac{K^{\text{SC}}}{2\pi} \oint ds\, \frac{\beta_x(s)}{a(s)[a(s)+b(s)]} \quad , \tag{2.78}$$

which immediately reduces to (2.77) for the smooth approximation (2.74).

We can apply the concept of the incoherent tune shift to a more realistic distribution. The thermal distribution

$$f(\mathcal{H}_\perp) = \exp\left(-\frac{\mathcal{H}_\perp}{\mathcal{H}_0}\right) \tag{2.79}$$

describes the transverse planes of beams in the injector chain of the LHC. It reduces to a Gaussian normal distribution if the space charge term in (2.65) becomes small (i.e. approaching the case of the pure betatron Hamiltonian (2.16)). The electric field of such a Gaussian distributed beam is non-linear which leads to an amplitude dependency of the tune shift. Therefore, we encounter an *incoherent tune spread* among all particles. The largest tune shifts are encountered for particles at small amplitudes remaining in the centre of the beam because the potential ϕ is largest here.

Suppose a transverse Gaussian charge density function

$$\rho(x, y) = \frac{\lambda}{2\pi\sigma_x\sigma_y} \exp\left(-\frac{x^2}{2\sigma_x^2} - \frac{y^2}{2\sigma_y^2}\right) \tag{2.80}$$

with r.m.s. widths (standard deviations) σ_x and σ_y. The electric fields generated by this charge

distribution (in the laboratory frame) read

$$
E_u = \frac{\lambda}{4\pi\epsilon_0} u \int\limits_0^\infty dt \, \frac{\exp\left(-\frac{x^2}{2\sigma_x^2+t} - \frac{y^2}{2\sigma_y^2+t}\right)}{(\sigma_u^2 + t)\sqrt{(\sigma_x^2 + t)(\sigma_y^2 + t)}}
$$
(2.81)

for $u = x, y$ [Wiedemann 2007, equation (18.31)]. The particles at small transverse amplitudes in the bunch centre mainly see the linear part of (2.81), whose linearisation yields

$$
E_u = \frac{\lambda}{4\pi\epsilon_0} u \underbrace{\int\limits_0^\infty \frac{dt}{(\sigma_u^2 + t)\sqrt{(\sigma_x^2 + t)(\sigma_y^2 + t)}}}_{= \frac{2}{\sigma_x(\sigma_x + \sigma_y)}} + \mathcal{O}\left(u^3\right)
$$

$$
= \frac{\lambda}{2\pi\epsilon_0} \frac{u}{\sigma_u(\sigma_x + \sigma_y)} + \mathcal{O}\left(u^3\right) \quad .
$$
(2.82)

Plugging this electric field into the equations of motion (2.66) leads to

$$
\frac{d^2}{ds^2}\left(x - \langle x \rangle\right) + \left[K_x(s) - \frac{K^{\mathrm{SC}}}{\sigma_u(\sigma_x + \sigma_y)}\right]\left(x - \langle x \rangle\right) = 0 \quad .
$$
(2.83)

Similarly to (2.78), we can derive the maximum tune shift in the Gaussian distribution from this linearised space charge restoring force term to be

$$
\Delta Q_x^{\mathrm{SC}} = \frac{K^{\mathrm{SC}}}{4\pi} \oint ds \, \frac{\beta_x(s)}{\sigma_x(s)[\sigma_x(s) + \sigma_y(s)]} \quad .
$$
(2.84)

As we have noted in the introductory chapter in the context of figure 1.3, the electric field of a Gaussian distribution features twice the linear slope in the centre as the r.m.s. equivalent KV distribution. The latter can be found by computing the r.m.s. width of the respective horizontal and vertical projection of the KV distribution yielding the relations

$$
a = 2\sigma_x \quad ,
$$
(2.85a)
$$
b = 2\sigma_y \quad .
$$
(2.85b)

Substituting this into the KV electric field expression (2.68a) we indeed find it to amount to half of the linearised Gaussian electric field (2.82) for the same σ_x, σ_y. The maximum tune shift in the Gaussian direct space charge tune spread (indicated throughout by superscript 'SC') correspondingly becomes twice as large as the r.m.s. equivalent KV tune shift,

$$
\max\left\{\Delta Q_{x,y}^{\mathrm{SC}}\right\} = 2\,\Delta Q_{x,y}^{\mathrm{KV}} \quad .
$$
(2.86)

So far, we have discussed longitudinally constant line densities, i.e. coasting beams. We can

extend the notion of the tune spread to bunched beams: for the synchrotrons at CERN the synchrotron periods are much longer than the betatron periods or, in other words, the time scale of the longitudinal motion is much slower than the transverse motion. Consequently, the betatron tune shift depends on the local line density $\lambda = \lambda(z)$. Reinserting the definition of the space charge perveance into (2.84) yields the generalised expression

$$\Delta Q_{x,y}^{\text{SC}}(z) = -\frac{q\lambda(z)}{8\pi^2\epsilon_0 m_p c^2 \beta^2 \gamma^3} \oint ds \frac{\beta_{x,y}(s)}{\sigma_{x,y}(s)\left(\sigma_x(s) + \sigma_y(s)\right)} \quad . \tag{2.87}$$

Longitudinal Space Charge

Longitudinal space charge in a bunch leads to defocusing (focusing) in the longitudinal plane when the machine is operated below (above) transition energy (2.45). The linear synchrotron tune (2.54) becomes depressed (increased) by

$$Q_S^2 = Q_{S,0}^2 + \frac{3}{4z_m^3} \frac{Nq^2\eta R^2 g}{4\pi\epsilon_0 \beta\gamma^2 p_0 c} \tag{2.88}$$

for a parabolic distribution of half-width z_m [Chao 1993, equation (1.47)]. The geometry factor g is discussed in more detail in section 3.2.1. If we assume a Gaussian instead of a parabolic distribution and we linearise the space charge force, we obtain an equivalent expression with a different form factor,

$$Q_S^2 = Q_{S,0}^2 + \frac{1}{\sqrt{2\pi}\sigma_z^3} \frac{Nq^2\eta R^2 g}{4\pi\epsilon_0 \beta\gamma^2 p_0 c} \quad , \tag{2.89}$$

where σ_z denotes the r.m.s. bunch length.

2.2.2   Envelope Equations and Coherent Quadrupolar Tune Shift

After the discussion of the incoherent tunes, we now proceed to the transverse coherent motion of the beam distribution. Suppose a coasting beam with a transverse distribution of elliptic symmetry,

$$\rho = \rho\left(\chi\right) \quad \text{for} \quad \chi \doteq \frac{x^2}{r_x^2} + \frac{y^2}{r_y^2}, \tag{2.90}$$

where $r_x = \sigma_x, r_y = \sigma_y$ mark the r.m.s. beam widths in the horizontal and vertical plane, respectively.

We investigate the evolution of the second-order moments r_x, r_y. According to (2.57), one has

$$r_x = \sqrt{\langle x^2 \rangle_\perp - \langle x \rangle_\perp^2} \quad , \tag{2.91a}$$

$$r_y = \sqrt{\langle y^2 \rangle_\perp - \langle y \rangle_\perp^2} \tag{2.91b}$$

with $\langle \cdot \rangle_\perp$ the transverse expectation value. Denoting $r_x' = dr_x/ds$, the first derivative of (2.91) along the design path length s gives

$$r_x' = \frac{\langle xx' \rangle_\perp - \langle x \rangle_\perp \langle x' \rangle_\perp}{r_x} \quad , \tag{2.92a}$$

$$r_y' = \frac{\langle yy' \rangle_\perp - \langle y \rangle_\perp \langle y' \rangle_\perp}{r_y} \tag{2.92b}$$

and the second derivative correspondingly evaluates to

$$r_x'' = -\frac{\left(\langle xx' \rangle_\perp - \langle x \rangle_\perp \langle x' \rangle_\perp \right)^2}{r_x^3} + \frac{\langle xx'' \rangle_\perp - \langle x \rangle_\perp \langle x'' \rangle_\perp + \langle x'^2 \rangle_\perp - \langle x' \rangle_\perp^2}{r_x} \quad ,$$

$$= -\frac{\epsilon_{x,\text{geo}}^2}{r_x^3} + \frac{\langle xx'' \rangle_\perp - \langle x \rangle_\perp \langle x'' \rangle_\perp}{r_x} \tag{2.93a}$$

where in the second line the statistical (geometrical i.e. non-normalised) r.m.s. emittance expression (2.29) has been substituted. Likewise, we obtain for the vertical plane

$$r_y'' = -\frac{\epsilon_{y,\text{geo}}^2}{r_y^3} + \frac{\langle yy'' \rangle_\perp - \langle y \rangle_\perp \langle y'' \rangle_\perp}{r_y} \quad . \tag{2.93b}$$

The coherent dipolar motion $\langle x'' \rangle_\perp = d^2 \langle x \rangle_\perp /ds^2$ and $\langle y'' \rangle_\perp = d^2 \langle y \rangle_\perp /ds^2$ is independent of direct space charge as we found in equation (2.72). Substituting (2.72) as well as the single particle equations of motion (2.66) into (2.93) yields

$$r_x'' + K_x r_x - \frac{\epsilon_{x,\text{geo}}^2}{r_x^3} - \frac{q}{\beta \gamma^2 p_0 c} \frac{\langle x E_x(x, y) \rangle_\perp}{r_x} = 0 \quad , \tag{2.94a}$$

$$r_y'' + K_y r_y - \frac{\epsilon_{y,\text{geo}}^2}{r_y^3} - \frac{q}{\beta \gamma^2 p_0 c} \frac{\langle y E_y(x, y) \rangle_\perp}{r_x} = 0 \quad . \tag{2.94b}$$

In the case of no space charge, i.e. vanishing self-fields $E_{x,y}(x, y) = 0$, we recover the equation of motion (2.11a) for the betatron amplitude function with the identification

$$w_{x,y}(s) \equiv \frac{r_{x,y}(s)}{\sqrt{\epsilon_{x,y,\text{geo}}}} \quad . \tag{2.95}$$

The linear beam self-fields of the KV distribution enabled Kapchinsky and Vladimirsky to

derive a self-consistent set of equations for the beam evolution from (2.94), the so-called *enve-lope equations.* The crucial point is that this system of equations is closed and does not lead to higher than second-order moment terms related to the evolution of the system. As pointed out in the introduction, the applicability of these KV equations to general monotonically decreasing distributions has been realised first by Gluckstern [1970] (for circular symmetry) and then by Sacherer [1971] (for general elliptic distributions). However, in the general monotonically decreasing distribution case the beam self-fields $E_{x,y}$ need not be (and usually are not) linear. Consequently, higher than second-order moments may influence the time evolution which can be absorbed in the now non-conserved r.m.s. emittances $\epsilon_{x,y,\text{geo}} = \epsilon_{x,y,\text{geo}}(s)$. The enve-lope equations involving only second-order r.m.s. moments are hence no longer a closed set of equations. If the r.m.s. emittances vary sufficiently slowly though, the coherent quadrupolar envelope modes can still be extracted from (2.94) for a general distribution.

We need to evaluate the expectation values $\langle xE_x(x,y)\rangle_\perp$ and $\langle yE_y(x,y)\rangle_\perp$. This is now where the elliptic symmetry of the charge distribution (2.90) comes in. For a monotonically decreasing $\rho = \rho(\chi)$ we have

$$\frac{d\rho}{d\chi} \leq 0 \quad , \quad \chi \geq 0 \quad . \tag{2.96}$$

Sacherer [ibid.] then proved the relation

$$\langle xE_x(x,y)\rangle_\perp = \frac{\lambda}{4\pi\epsilon_0} \frac{r_x}{r_x + r_y} \quad , \tag{2.97a}$$

$$\langle yE_y(x,y)\rangle_\perp = \frac{\lambda}{4\pi\epsilon_0} \frac{r_y}{r_x + r_y} \quad . \tag{2.97b}$$

Substituting (2.97) into (2.94) then finally leads to the r.m.s. envelope equations

$$r_x'' + K_x(s)r_x - \frac{\epsilon_{x,\text{geo}}^2}{r_x^3} - \frac{K^{\text{SC}}}{2(r_x + r_y)} = 0 \quad , \tag{2.98a}$$

$$r_y'' + K_y(s)r_y - \frac{\epsilon_{y,\text{geo}}^2}{r_y^3} - \frac{K^{\text{SC}}}{2(r_x + r_y)} = 0 \tag{2.98b}$$

where we have replaced the space charge perveance $K^{\text{SC}} = \text{const}$ expression (2.70). The envelope equations are a coupled set of equations for the evolution of the transverse r.m.s. beam widths $r_{x,y} = \sigma_{x,y}$ along the design path length s. We derived the envelope equations in the absence of any lattice coupling, $K_{xy} = 0$. In this case, the space charge term provides the only coupling between the transverse planes. In the presence of lattice coupling, $K_{xy}(s)r_y$ enters the left hand side of (2.98a) and likewise $K_{xy}(s)r_x$ on the left of (2.98b).

Let us investigate the envelope oscillations $r_{x,y}(s)$ for a smoothly approximated ring (2.74)

with $K_{x,y}(s) = $ const. The condition for a stationary or matched distribution reads

$$r''_{x,y}(s) = 0 \quad \overset{(2.98)}{\Longrightarrow} \quad r'_{x,y}(s) = 0 \quad , \tag{2.99}$$

i.e. the matched r.m.s. envelopes $r_{x,\mathrm{m}}$ and $r_{y,\mathrm{m}}$ simply remain constant under the continuous focusing. They satisfy the coupled quartic equations

$$\frac{Q_x^2}{R^2} r_{x,\mathrm{m}} - \frac{\epsilon_{x,\mathrm{geo}}^2}{r_{x,\mathrm{m}}^3} - \frac{K^{\mathrm{SC}}}{2(r_{x,\mathrm{m}} + r_{y,\mathrm{m}})} = 0 \quad , \tag{2.100a}$$

$$\frac{Q_y^2}{R^2} r_{y,\mathrm{m}} - \frac{\epsilon_{y,\mathrm{geo}}^2}{r_{y,\mathrm{m}}^3} - \frac{K^{\mathrm{SC}}}{2(r_{x,\mathrm{m}} + r_{y,\mathrm{m}})} = 0 \tag{2.100b}$$

for constant bare betatron tunes $Q_{x,y}$, given r.m.s. emittances and constant space charge perveance.

Consider now a small perturbation about these equilibrium envelopes

$$r_x = r_{x,\mathrm{m}} + \delta r_x \quad \text{and} \tag{2.101a}$$

$$r_y = r_{y,\mathrm{m}} + \delta r_y \quad , \tag{2.101b}$$

where $\delta r_x \ll r_{x,\mathrm{m}}$ and $\delta r_y \ll r_{y,\mathrm{m}}$. Their coupled linearised equations of motion follow from (2.98) by plugging in (2.100a) while neglecting terms from $\mathcal{O}\left(\delta r^2\right)$ on:

$$\delta r''_x + \left(\frac{3\epsilon_{x,\mathrm{geo}}^2}{r_{x,\mathrm{m}}^4} + \frac{K^{\mathrm{SC}}}{2(r_{x,\mathrm{m}} + r_{y,\mathrm{m}})^2} + \frac{Q_x^2}{R^2} \right) \delta r_x = -\frac{K^{\mathrm{SC}}}{2(r_{x,\mathrm{m}} + r_{y,\mathrm{m}})^2} \delta r_y \quad , \tag{2.102a}$$

$$\delta r''_y + \left(\frac{3\epsilon_{y,\mathrm{geo}}^2}{r_{y,\mathrm{m}}^4} + \frac{K^{\mathrm{SC}}}{2(r_{x,\mathrm{m}} + r_{y,\mathrm{m}})^2} + \frac{Q_y^2}{R^2} \right) \delta r_y = -\frac{K^{\mathrm{SC}}}{2(r_{x,\mathrm{m}} + r_{y,\mathrm{m}})^2} \delta r_x \quad . \tag{2.102b}$$

Equations (2.102) can equivalently be expressed in terms of the matrix equation

$$\frac{d^2}{ds^2} \begin{pmatrix} \delta r_x \\ \delta r_y \end{pmatrix} = - \underbrace{\begin{pmatrix} \kappa_x & \kappa_{\mathrm{SC}} \\ \kappa_{\mathrm{SC}} & \kappa_y \end{pmatrix}}_{\doteq (\kappa)} \cdot \begin{pmatrix} \delta r_x \\ \delta r_y \end{pmatrix} \tag{2.103}$$

where we have defined the diagonal matrix entries as

$$\kappa_{x,y} \doteq \frac{3\epsilon_{x,y,\mathrm{geo}}^2}{r_{x,y,\mathrm{m}}^4} + \frac{Q_{x,y}^2}{R^2} + \kappa_{\mathrm{SC}} \tag{2.104}$$

and the symmetric off-diagonal matrix entries as

$$\kappa_{\mathrm{SC}} \doteq \frac{K^{\mathrm{SC}}}{2(r_{x,\mathrm{m}} + r_{y,\mathrm{m}})^2} \quad . \tag{2.105}$$

The geometrical r.m.s. emittances in the diagonal matrix entries can be eliminated by using the matching condition (2.100a) giving

$$\kappa_x = 4\frac{Q_x^2}{R^2} - \frac{2r_{x,\mathrm{m}} + 3r_{y,\mathrm{m}}}{r_{x,\mathrm{m}}}\kappa_{\mathrm{SC}} \quad , \tag{2.106a}$$

$$\kappa_y = 4\frac{Q_y^2}{R^2} - \frac{3r_{x,\mathrm{m}} + 2r_{y,\mathrm{m}}}{r_{y,\mathrm{m}}}\kappa_{\mathrm{SC}} \quad . \tag{2.106b}$$

Now, sufficiently small excursions $\delta r_{x,y}$ can be described by the coupled harmonic oscillator differential equation (2.103). We can determine the corresponding two independent eigenmodes of the coherent quadrupolar oscillation by diagonalising the symmetric matrix (κ). To this end, we have to solve for the roots $\kappa_\pm$ of the characteristic polynomial

$$\det\begin{pmatrix} \kappa_x - \kappa_\pm & \kappa_{\mathrm{SC}} \\ \kappa_{\mathrm{SC}} & \kappa_y - \kappa_\pm \end{pmatrix} = \kappa_\pm^2 - \kappa_\pm(\kappa_x + \kappa_y) + (\kappa_x\kappa_y - \kappa_{\mathrm{SC}}^2) \overset{!}{=} 0 \quad . \tag{2.107}$$

The eigenvalues $\kappa_\pm$ are related to the coherent quadrupolar tunes $Q_\pm$ by

$$\kappa_\pm = \frac{Q_\pm^2}{R^2} \quad . \tag{2.108}$$

Solving (2.107) for $Q_\pm$ hence yields

$$Q_\pm^2 = \frac{R^2}{2}\left[\kappa_x + \kappa_y \pm \sqrt{4\kappa_{\mathrm{SC}}^2 + (\kappa_y - \kappa_x)^2}\right] \tag{2.109}$$

and we have $Q_+ \geq Q_-$. For vanishing space charge $\kappa_{\mathrm{SC}} = 0$ we recover that the envelopes oscillate with twice the bare tune as the diagonal matrix entries reduce to $\kappa_x = 4Q_x^2/R^2$ and $\kappa_y = 4Q_y^2/R^2$. In the finite space charge case $\kappa_{\mathrm{SC}} > 0$, the envelope tunes become depressed by space charge: reinserting the definitions of the (κ) matrix entries yields the full expression for the quadrupolar mode tunes,

$$Q_\pm^2 = 2(Q_x^2 + Q_y^2) - \frac{K^{\mathrm{SC}}R^2}{(r_{x,\mathrm{m}} + r_{y,\mathrm{m}})^2}\left[1 + \frac{3}{4}\left(\frac{r_{y,\mathrm{m}}}{r_{x,\mathrm{m}}} + \frac{r_{x,\mathrm{m}}}{r_{y,\mathrm{m}}}\right) \mp \frac{\sqrt{1 + D^2}}{2}\right] \quad , \tag{2.110}$$

where we have introduced the *coupling parameter*

$$D \doteq \frac{\kappa_y - \kappa_x}{2\kappa_{\mathrm{SC}}} = 4\frac{K_y - K_x}{K^{\mathrm{SC}}}(r_{x,\mathrm{m}} + r_{y,\mathrm{m}})^2 + \frac{3}{2}\left(\frac{r_{y,\mathrm{m}}}{r_{x,\mathrm{m}}} - \frac{r_{x,\mathrm{m}}}{r_{y,\mathrm{m}}}\right) \quad . \tag{2.111}$$

Along with the eigenmode tunes $Q_\pm$ we retrieve an expression for the (unnormalised) eigenvectors,

$$\delta r_\pm = \delta r_x + \left(D \pm \sqrt{1 + D^2}\right)\delta r_y \quad . \tag{2.112}$$

Both are orthogonal to each other, $\langle \delta r_+, \delta r_- \rangle = 0$. In fact, depending on the coupling strength,

the normalised eigenvectors appear rotated with respect to the horizontal and vertical coordinate axes by

$$
\begin{pmatrix} \delta r_+ \\ \delta r_- \end{pmatrix} = \begin{pmatrix} \cos(\alpha) & -\sin(\alpha) \\ \sin(\alpha) & \cos(\alpha) \end{pmatrix} \cdot \begin{pmatrix} \delta r_x \\ \delta r_y \end{pmatrix} \quad .
\tag{2.113}
$$

The coupling parameter D determines the angle α of the rotation from the horizontal and vertical coordinate axes into the eigensystem of the modes via

$$
\begin{aligned}
\tan(\alpha) &= \frac{1}{2\kappa_{\mathrm{SC}}} \left[\kappa_y - \kappa_x + \sqrt{4\kappa_{\mathrm{SC}}^2 + (\kappa_y - \kappa_x)^2} \right] \\
&= D + \sqrt{1 + D^2} \quad .
\end{aligned}
\tag{2.114}
$$

There are two important limit cases for the quadrupolar modes:

1. negligible coupling $|D| \to \infty$ and
2. maximal coupling $D = 0$.

Negligible Coupling Limit $|D| \gg 1$

We can expand the factor $\sqrt{1 + D^2} \approx |D|$ in the previous expressions. The two eigenvectors $\delta r_\pm$ from (2.112) lie in the horizontal and vertical plane. For $D > 0$, the vertical plane dominates the horizontal plane: either the beam sizes are fixed and approximately round and we find $Q_y > Q_x$, or instead the bare machine tunes are fixed at a finite difference and the vertical beam size needs to be much larger than the horizontal beam size, $r_{y,\mathrm{m}} > r_{x,\mathrm{m}}$. The case $D > 0$ in (2.112) results in δr_+ identifying with δr_y since $D + \sqrt{1 + D^2} \approx 2D \gg 1$ and likewise δr_- with δr_x because $D - \sqrt{1 + D^2} \approx 0 \ll 1$.

$D < 0$ entails the opposite case with the horizontal plane dominating the vertical plane, one encounters the relations $\delta r_+ \leftrightarrow \delta r_x$ and $\delta r_- \leftrightarrow \delta r_y$. Correspondingly, the phase α between the eigensystem and the original coordinate system rotates by $\pi/2$ from $D \to -\infty$ to $D \to \infty$.

The approximation $\sqrt{1 + D^2} \approx |D|$ also decouples expression (2.110) for the coherent quadrupolar mode tunes. By substituting back the definition of D, we find for $D > 0$

$$
Q_+^2 = 4Q_y^2 - \frac{K^{\mathrm{SC}} R^2}{(r_{x,\mathrm{m}} + r_{y,\mathrm{m}})^2} \left[1 + \frac{3 r_{x,\mathrm{m}}}{2 r_{y,\mathrm{m}}} \right] \quad ,
\tag{2.115a}
$$

$$
Q_-^2 = 4Q_x^2 - \frac{K^{\mathrm{SC}} R^2}{(r_{x,\mathrm{m}} + r_{y,\mathrm{m}})^2} \left[1 + \frac{3 r_{y,\mathrm{m}}}{2 r_{x,\mathrm{m}}} \right] \quad .
\tag{2.115b}
$$

For $D < 0$, the indices $x \leftrightarrow y$ are again exchanged.

Maximal Coupling Limit $D = 0$

For the fully coupled case, the eigenmode system is rotated by $\alpha = \pi/4$ with respect to the coordinate system: the normalised eigenvectors amount to

$$\delta r_+ = \frac{\delta r_x + \delta r_y}{2} \quad , \tag{2.116a}$$

$$\delta r_- = \frac{\delta r_x - \delta r_y}{2} \quad . \tag{2.116b}$$

The corresponding envelope tunes become

$$Q_+^2 = 2(Q_x^2 + Q_y^2) - \frac{K^{SC}R^2}{2(r_{x,m} + r_{y,m})^2}\left[1 + \frac{3}{2}\left(\frac{r_{y,m}}{r_{x,m}} + \frac{r_{x,m}}{r_{y,m}}\right)\right] \quad , \tag{2.117a}$$

$$Q_-^2 = 2(Q_x^2 + Q_y^2) - \frac{K^{SC}R^2}{2(r_{x,m} + r_{y,m})^2}\left[3 + \frac{3}{2}\left(\frac{r_{y,m}}{r_{x,m}} + \frac{r_{x,m}}{r_{y,m}}\right)\right] \quad . \tag{2.117b}$$

For negligible space charge $K^{SC} = 0$, the envelope frequencies would be exactly identical. As soon as we have space charge decoupling, the mode tunes depart with $Q_- < Q_+$. In fact, the symmetric mode entails that both δr_x and δr_y oscillate in phase. Along with this goes a change in the density which leads to the higher frequency, therefore the symmetric mode is often called "breathing" mode. The antisymmetric mode consists of δr_x and δr_y oscillating in anti-phase and is often referred to as the quadrupolar mode, the density of the distribution remains constant.

For a stationary round beam with equal transverse emittances, the continuous focusing is necessarily isotropic and we define

$$\begin{cases} r_m \doteq r_{x,m} \equiv r_{y,m} \quad , \\ \epsilon_{geo} \doteq \epsilon_{x,geo} \equiv \epsilon_{y,geo} \quad , \\ K \doteq K_x \equiv K_y \quad . \end{cases} \tag{2.118}$$

The difference between the two oscillation frequencies becomes evident from the restoring forces in the equations of motion in the eigensystem:

$$\delta r_+'' + \left(\frac{3\epsilon_{geo}^2}{r_m^4} + \frac{K^{SC}}{8r_m^2} + K\right)\delta r_+ = 0 \quad \longrightarrow \text{breathing mode} \quad , \tag{2.119a}$$

$$\delta r_-'' + \left(\frac{3\epsilon_{geo}^2}{r_m^4} + \phantom{\frac{K^{SC}}{8r_m^2}} K\right)\delta r_- = 0 \quad \longrightarrow \text{quadrupolar mode} \quad . \tag{2.119b}$$

2.2.3   Relation of Coherent Quadrupolar Modes to Incoherent Tune Shift

It is of interest to relate the incoherent KV space charge depressed tune to the coherent quadrupolar mode tunes: in section 3.5, we discuss how measuring the coherent envelope oscillations with a QPU can provide the not directly measurable incoherent r.m.s. equivalent KV tune shifts as useful quantities to indicate the space charge strength. The physical observables are hence

1. the two coherent quadrupolar mode tunes $Q_\pm$,
2. the bare machine tunes $Q_{x,y}$, and
3. the ratio ξ between the equilibrium r.m.s. beam sizes,

where we define the beam size ratio as

$$\xi \doteq \frac{r_{y,\mathrm{m}}}{r_{x,\mathrm{m}}} \quad . \tag{2.120}$$

The off-diagonal matrix terms κ_{SC} represent the space charge coupling strength independently of the plane. For convenience, let

$$\Lambda \doteq -\kappa_{\mathrm{SC}} R^2$$
$$= -\frac{K^{\mathrm{SC}} R^2}{2(r_{x,\mathrm{m}} + r_{y,\mathrm{m}})^2} \quad . \tag{2.121}$$

Now, the sum of the envelope mode tunes (2.110) provides an expression removing the coupling parameter term,

$$Q_+^2 + Q_-^2 = 4\left(Q_x^2 + Q_y^2\right) - \frac{K^{\mathrm{SC}} R^2}{2(r_{x,\mathrm{m}} + r_{y,\mathrm{m}})^2} \left[4 + 3\left(\frac{r_{y,\mathrm{m}}}{r_{x,\mathrm{m}}} + \frac{r_{x,\mathrm{m}}}{r_{y,\mathrm{m}}}\right)\right] \quad . \tag{2.122}$$

Based on this expression, the space charge quantity Λ can directly be related to the aforementioned observables via

$$\Lambda \equiv \frac{Q_+^2 + Q_-^2 - 4(Q_x^2 + Q_y^2)}{4 + 3\xi + 3/\xi} \quad . \tag{2.123}$$

The parameter Λ also appears in the incoherent tune expressions: we use (2.85) to replace the KV beam edges with the corresponding r.m.s. values $a = 2r_{x,\mathrm{m}}$ and $b = 2r_{y,\mathrm{m}}$ in the smooth approximation expression (2.75) (which does not neglect quadratic terms yet) for the incoherent KV space charge tunes $Q_{x,y}^{\mathrm{SC}}$,

$$\left(Q_x^{\mathrm{SC}}\right)^2 = Q_x^2 - \frac{K^{\mathrm{SC}} R^2}{2r_{x,\mathrm{m}}(r_{x,\mathrm{m}} + r_{y,\mathrm{m}})} \quad , \tag{2.124a}$$

$$\left(Q_y^{\mathrm{SC}}\right)^2 = Q_y^2 - \frac{K^{\mathrm{SC}} R^2}{2r_{y,\mathrm{m}}(r_{x,\mathrm{m}} + r_{y,\mathrm{m}})} \quad . \tag{2.124b}$$

With the definition (2.76) of the incoherent tune shift, we can finally express $\Delta Q_{x,y}^{\mathrm{KV}}$ in terms of Λ (i.e. the observables) via the exact relation

$$\Delta Q_x^{\mathrm{KV}}\left(\Delta Q_x^{\mathrm{KV}} + 2Q_x\right) = (1+\xi)\Lambda \quad , \tag{2.125a}$$

$$\Delta Q_y^{\mathrm{KV}}\left(\Delta Q_y^{\mathrm{KV}} + 2Q_y\right) = (1+1/\xi)\Lambda \quad . \tag{2.125b}$$

Neglecting quadratic terms, we recover (2.77) in terms of Λ:

$$\Delta Q_x^{\mathrm{KV}} = -\frac{K^{\mathrm{SC}}R^2}{4r_{x,\mathrm{m}}(r_{x,\mathrm{m}} + r_{y,\mathrm{m}})Q_x}$$
$$= \frac{1+\xi}{2Q_x}\Lambda \quad , \tag{2.126a}$$

$$\Delta Q_y^{\mathrm{KV}} = -\frac{K^{\mathrm{SC}}R^2}{4r_{y,\mathrm{m}}(r_{x,\mathrm{m}} + r_{y,\mathrm{m}})Q_y}$$
$$= \frac{1+1/\xi}{2Q_y}\Lambda \quad . \tag{2.126b}$$

Consider the limit case of negligible coupling with $|D| \gg 1$, say $D > 0$. From (2.115) it follows for the vertical plane

$$\underbrace{Q_+^2 - 4Q_y^2}_{\approx (Q_+ - 2Q_y)4Q_y} = \Lambda\left[1 + \frac{3r_{x,\mathrm{m}}}{2r_{y,\mathrm{m}}}\right]$$
$$= \left(2 + \frac{r_{x,\mathrm{m}}}{(r_{x,\mathrm{m}} + r_{y,\mathrm{m}})}\right)\underbrace{\left[\left(Q_y^{\mathrm{SC}}\right)^2 - Q_y^2\right]}_{\approx 2\Delta Q_y^{\mathrm{KV}}Q_y} \quad , \tag{2.127}$$

and an equivalent expression with Q_- for the horizontal plane. For $D < 0$, the indices x and y need to be exchanged.

Assuming a small incoherent KV tune shift and correspondingly small quadrupolar mode shift with respect to twice the bare tune (the undepressed envelope tune) leads to the expression

$$\Delta Q_y^{\mathrm{KV}} = \frac{Q_+ - 2Q_y}{\frac{1}{2}\left(3 - \frac{r_{y,\mathrm{m}}}{r_{x,\mathrm{m}} + r_{y,\mathrm{m}}}\right)} \quad . \tag{2.128}$$

This off-coupling result has been quoted e.g. in Chanel [1996] for LEAR experiments at CERN or in Hofmann, Bar, et al. [1998] for SIS18 experiments at GSI – we discuss further details in section 3.5.

Last but not least, consider the case of full coupling with $D = 0$ and a round beam as in (2.118). The isotropic focusing gives the same bare betatron tunes $Q_0 \doteq Q_{x,y}$. The incoherent KV tune

shift $\Delta Q^{\text{KV}} = Q^{\text{SC}} - Q_0$ is determined from (2.124) as

$$\left(Q^{\text{SC}}\right)^2 - Q_0^2 = -\frac{K^{\text{SC}} R^2}{4 r_{\text{m}}^2} \quad . \tag{2.129}$$

From (2.117), the breathing and quadrupolar mode can be linked to ΔQ^{KV} via the exact expressions

$$\underbrace{Q_+^2 - 4Q_0^2}_{\approx (Q_+ - 2Q_0)4Q_0} = -2 \frac{K^{\text{SC}} R^2}{4 r_{\text{m}}^2} \tag{2.130a}$$

$$= 2 \underbrace{\left[(Q^{\text{SC}})^2 - Q_0^2\right]}_{\approx 2\Delta Q^{\text{KV}} Q_0} \quad ,$$

$$\underbrace{Q_-^2 - 4Q_0^2}_{\approx (Q_- - 2Q_0)4Q_0} = -3 \frac{K^{\text{SC}} R^2}{4 r_{\text{m}}^2} \tag{2.130b}$$

$$= 3 \underbrace{\left[(Q^{\text{SC}})^2 - Q_0^2\right]}_{\approx 2\Delta Q^{\text{KV}} Q_0} \quad .$$

Correspondingly, for small ΔQ^{KV} and likewise a small envelope mode shift we obtain the relation of the two modes to the incoherent KV tune shift as

$$Q_+ = 2Q_0 - |\Delta Q^{\text{KV}}| \quad , \tag{2.131a}$$

$$Q_- = 2Q_0 - \frac{3}{2} |\Delta Q^{\text{KV}}| \quad . \tag{2.131b}$$

2.3 Space Charge and Betatron Resonances

Betatron resonances in conjunction with coherent modes have been studied intensely in the past, and detailed treatments can be found e.g. in R. Baartman [1998], Hofmann, Franchetti, et al. [2003] and Ng [2006]. Here we briefly outline the qualitative concepts.

In the previous sections, we have derived the coherent dipolar equation of motion (2.72) where direct space charge did not influence the dipolar tune. This is closely connected to Newton's third law stating that for all action there is an equal and opposite reaction – thus, the sum of the space charge forces of all particles repelling each other via the Coulomb force needs to vanish. Now, the dipolar motion of the beam centroid can become resonantly excited by dipole field errors (in the absence of indirect space charge effects) if the bare betatron tune in either the horizontal or vertical plane satisfies the integer resonance condition

$$Q_{x,y}^{\text{dip.coh.}} = Q_{x,y} = n \quad \text{for} \quad n \in \mathbb{N} \quad . \tag{2.132}$$

For the next order we have treated the coherent quadrupolar modes in depth, whose frequen-

cies are indeed depressed by direct space charge through the beam self-fields. These modes can become resonantly excited by quadrupolar field errors if one of the two envelope tunes matches an integer:

$$Q_\pm = n \quad \text{for} \quad n \in \mathbb{N} \quad . \tag{2.133}$$

For vanishing space charge, the quadrupolar modes oscillate at twice the bare machine tunes. In the presence of gradient errors, resonance therefore occurs at half-integer bare betatron tunes. In the presence of space charge, the detuning of the quadrupolar modes leads to shifted resonance conditions with respect to the bare betatron tune.

For a round beam far off the coupling resonance at split betatron tunes, say $D \gg 1$ (i.e. $Q_y > Q_x$ and $\delta r_+ \leftrightarrow \delta r_y$), (2.128) leads to

$$Q_+ = 2Q_y - \frac{5}{4}|\Delta Q_y^{\mathrm{KV}}| \quad , \tag{2.134a}$$

$$Q_- = 2Q_x - \frac{5}{4}|\Delta Q_x^{\mathrm{KV}}| \quad . \tag{2.134b}$$

Consequently, (2.133) can be satisfied for two different resonance conditions in terms of the bare machine tunes Q_x, Q_y:

$$Q_x - \frac{5}{8}|\Delta Q_x^{\mathrm{KV}}| = \frac{n_1}{2} \quad , \tag{2.135a}$$

$$Q_y - \frac{5}{8}|\Delta Q_y^{\mathrm{KV}}| = \frac{n_2}{2} \quad . \tag{2.135b}$$

The factor two in the denominator comes from the resonance order ("quadrupolar" corresponds to the second order moment) and the two integer numbers $n_1, n_2 \in \mathbb{N}$ represent the harmonics for the two (decoupled) quadrupolar modes. Hence, we obtain a half-integer resonance condition for the bare machine tunes $Q_{x,y}$ subtracted by the r.m.s. equivalent KV tune shifts multiplied by the factor 5/8 coming from the space charge depression of the envelope modes. Note that these factors change depending on the coupling parameter D. Furthermore, this resonance condition applies to any monotonically decreasing beam distribution (2.96) for whom the corresponding r.m.s. equivalent KV tune shifts $\Delta Q_{x,y}^{\mathrm{KV}}$ are calculated. Expressing the coherent resonance condition in terms of the incoherent tune shift comes merely from a notational convenience point of view because the space charge strength of beams is often characterised by the r.m.s. equivalent $\Delta Q_{x,y}^{\mathrm{KV}}$. This does not involve *incoherent* space charge dynamics. As a last remark, $\Delta Q_{x,y}^{\mathrm{KV}}$ can be related to the tune spread of the r.m.s. equivalent Gaussian beam distribution by a factor two, cf. (2.86).

For a round beam on the coupling resonance ($D = 0$), i.e. at equal bare machine tunes $Q_0 = Q_x = Q_y$, (2.131) provides the resonance condition in terms of Q_0 and the incoherent KV space

charge tune shift ΔQ^{KV} via

$$Q_0 - \frac{1}{2}|\Delta Q^{\text{KV}}| = \frac{n_1}{2} \quad , \tag{2.136a}$$

$$Q_0 - \frac{3}{4}|\Delta Q^{\text{KV}}| = \frac{n_2}{2} \quad . \tag{2.136b}$$

The harmonic $n_1 \in \mathbb{N}$ and factor 1/2 refer to the symmetric (breathing) mode resonance and the harmonic $n_2 \in \mathbb{N}$ and factor 3/4 refer to the antisymmetric (quadrupolar) mode resonance. As we see, the quadrupolar factors indeed change depending on D.

R. Baartman [1998] reviewed exactly this topic and generalised the one- and two-dimensional coherent resonances for higher orders. In the one-dimensional case, the general space charge depressed betatron resonance condition reads

$$m(Q_0 + C_{mk}\Delta Q^{\text{KV}}) = n \quad \text{for} \quad m, n \in \mathbb{N} \quad , \tag{2.137}$$

where the matrix C_{mk} has indices m (coinciding with the resonance order here) for the azimuthal and k for the radial mode. For spherical symmetry reasons, odd k only appear with odd m while even k require even m.

Hofmann [1998] treated the two-dimensional resonance case for general anisotropic beams, i.e. different transverse emittances and different continuous focusing strengths (i.e. bare tunes) have been covered including up to octupolar order. For round beams, R. Baartman provided the corresponding values of C_{mk}, which we quote in table 2.1. Note our previously derived results for $C_{11} = 0$ from (2.132) and for $C_{22} \in \{1/2, 3/4\}$ from (2.136). Further work by Hofmann, Franchetti, et al. [2003] with (non-KV) beam simulations revealed that mainly the diagonal modes with $m = k$ play a role in space charge dynamics of r.m.s. equivalent realistic beam distributions.

Table 2.1 – Coherent mode coefficients for the incoherent KV tune shift appearing in the two-dimensional space charge depressed betatron resonance condition (2.137) [R. Baartman 1998, table 2].

	dipolar	quadrupolar	sextupolar	octupolar
	$m = 1$	2	3	4
$k = 1$	0			
2		1/2, 3/4		
3	3/4, 5/4		3/4, 11/12	
4		7/8, 5/4		13/16, 7/8, 31/32

3 Modelling of Space Charge

The circular accelerators at CERN produce beams of various intensities. The number of protons per bunch ranges from $\mathcal{O}\left(10^9\right)$ for the LHC probe and pilot beams to up to $\mathcal{O}\left(10^{12}\right)$ for the fixed target beams. With higher intensities per bunch, the "collective effects" play an increasingly important role in the beam dynamics. Detailed simulation models become crucial to quantitatively assess the impact of such multi-particle interactions [Métral, Argyropoulos, et al. 2016]. Relevant effects originate from the beam self-fields (direct space charge), induced wall currents (impedances), beam-beam lensing for colliding beams, as well as electron clouds. Mitigation of their harmful impact may proceed through countermeasures such as enhancing Landau damping by exploiting the detuning with amplitude from octupole magnets, using active damper feedback systems or electron lenses etc. Such concepts are explored, established and understood in wide parameter scans with the aid of simulation codes.

Instabilities triggered by collective effects and resonances can take some time in the circular accelerators to evolve, which reflects in simulations by the need of covering several thousands or even hundreds of thousands of ring revolutions. Especially the self-consistent treatment of direct space charge as a continuous phenomenon requires a fine resolution of the machine into many small segments over which the effect is integrated: the particles interact with the beam self-fields everywhere around the ring while the local field strength depends on the transverse beam size. At the same time, the strong focusing in synchrotrons as well as dispersion effects continuously change the beam size as figure 3.1 illustrates for a high-brightness beam example in the SPS.

3.1 N-body Simulations and Macro-particle Models

Particle beams can be treated as an evolving N-body system. The system of $6N$ ordinary differential equations describing the particle motion is readily solved by numerical integration over discrete time steps. Modelling the beams with the real number of particles while simulating over many turns (where each turn may well have to be resolved into hundreds or thousands of integration steps) often becomes computationally prohibitive. In order to
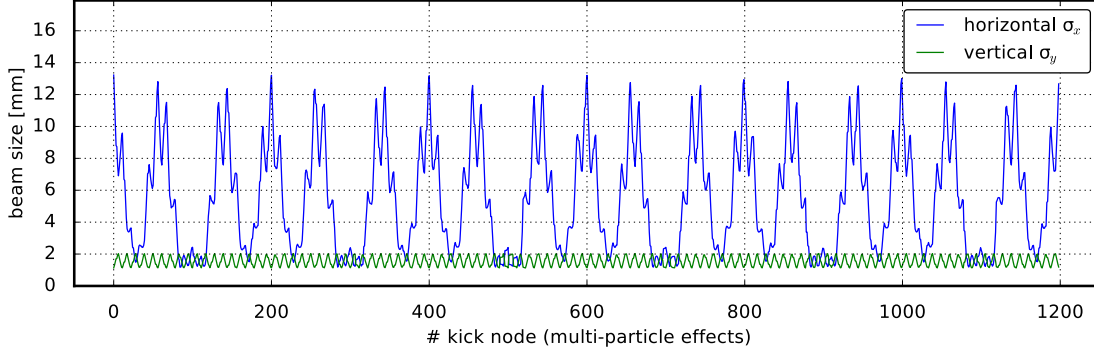
Figure 3.1 – Transverse beam sizes around the SPS ring (using the "Q20" optics, cf. chapter 4) for a low-emittance beam. The SPS ring has been split into 1200 nodes to sufficiently resolve the beam size for space charge simulations.

make long-term simulation studies feasible, one employs so-called macro-particle models by representing the N real particles by $N_{m.p.}$ macro-particles. Each macro-particle stands for a group of $N/N_{m.p.}$ real particles and correspondingly carries a larger charge $q \cdot N/N_{m.p.}$ and mass $m_p \cdot N/N_{m.p.}$. The motion of these macro-particles in the synchrotron may be described by a split Hamiltonian

$$\mathcal{H} = \mathcal{H}_{\text{tracking}} + \mathcal{H}_{\text{interaction}} \quad . \tag{3.1}$$

The tracking part $\mathcal{H}_{\text{tracking}}$ describes the single-particle motion due to the applied external electromagnetic fields, while $\mathcal{H}_{\text{interaction}}$ covers the multi-particle interactions. This allows to construct simulation codes which advance the macro-particles around the ring by alternately solving the single-particle and multi-particle dynamics.

Let $\{f, g\}$ denote the Poisson bracket

$$\{f, g\} \doteq \sum_{i=1}^{3} \left(\frac{\partial f}{\partial q_i} \frac{\partial g}{\partial p_i} - \frac{\partial f}{\partial p_i} \frac{\partial g}{\partial q_i} \right) \tag{3.2}$$

for two smooth functions f, g, the generalised coordinates q_i and their respective canonically conjugate momenta p_i. The Lie operator

$$:\mathcal{H}: \doteq \{\mathcal{H}, \cdot\} \tag{3.3}$$

then expresses the time evolution of a Hamiltonian system,

$$\frac{d}{ds} = \frac{\partial}{\partial s} + \{\cdot, \mathcal{H}\} = \frac{\partial}{\partial s} - :\mathcal{H}: \quad . \tag{3.4}$$

Consequently, we can write the Hamiltonian equations of motion for the phase space coordi-

nates $\zeta = (q_i, p_i)_{i=1..3}$ of the macro-particles as

$$\frac{d\zeta}{ds} = \{\zeta, \mathcal{H}\} = -:\mathcal{H}:\zeta \quad , \tag{3.5}$$

which is formally solved by the Lie map

$$\zeta(s_0 + \Delta s) = e^{-\Delta s:\mathcal{H}:}\zeta(s_0) \quad . \tag{3.6}$$

To lowest order in the Baker-Campbell-Hausdorff operator splitting, the phase space coordinates ζ of the macro-particles can be pushed forward over a distance Δs by

$$\zeta(s_0 + \Delta s) = e^{-\Delta s:\mathcal{H}_{\text{interaction}}:} e^{-\Delta s:\mathcal{H}_{\text{tracking}}:} \zeta(s_0) \quad . \tag{3.7}$$

The splitting of the original Lie map into two subsequent Lie maps corresponds to the aforementioned alternating integration of single-particle and multi-particle dynamics.

A major project of this Ph.D. thesis comprises the contribution to the development and establishment of a 6D macro-particle simulation code for synchrotrons named PyHEADTAIL with focus on the implementation of various space charge models. The software and its applications have been presented in papers and conferences [Li et al. 2016; Métral, Argyropoulos, et al. 2016; Oeftiger 2015; Oeftiger and Hegglin 2016].

Each macro-particle of a PyHEADTAIL beam is described by the 6D set of coordinates

$$\zeta = (x, x', y, y', z, \delta) \quad , \tag{3.8}$$

where x denotes the horizontal offset from the reference orbit, y the vertical offset, $x' = p_x/p_0$ and $y' = p_y/p_0$ the corresponding transverse normalised momenta for $p_0 = \gamma m_p \beta c$ the total beam momentum (p_x and p_y are the conjugate momenta to x and y, respectively), z denotes the longitudinal offset from the synchronous particle in the laboratory frame and $\delta = (p_z - p_0)/p_0$ the relative momentum deviation. In the case of beam acceleration, p_0 slowly changes which leads to adiabatic damping of the transverse phase space. PyHEADTAIL correspondingly shrinks the transverse momenta x', y' to conserve the underlying symplectic nature of the integration of motion.

In the transverse plane, PyHEADTAIL models the single-particle motion $e^{-\Delta s:\mathcal{H}_{\text{tracking}}:}$ by means of the transverse betatron matrix (with expression (2.12) for the horizontal and vertical plane as blocks along the diagonal of a 6×6 unit matrix), which represents the optics of the accelerator expressed in terms of the Twiss parameters. In order to take into account non-linear single-particle detuning effects such as chromaticity and detuning with amplitude (introduced e.g. by octupole fields), we adjust the phase advance $\psi_{x,y}(s) = \psi_{x,y}(x, y, \delta; s)$ for each macro-particle (the corresponding change in each macro-particle's momentum deviation to conserve the symplectic nature of the integration of motion is neglected as it is only a tiny longitudinal effect). For a given tracking step over an unperturbed phase advance $\Delta\psi_{x,y}$, the detuned

phase advance hence consists of

$$\psi_{x,y}(x,y,\delta;s+\Delta s) = \psi_{x,y}(s) + \Delta\psi_{x,y} + \Delta\psi_{x,y,\text{chroma}}(\delta) + \Delta\psi_{x,y,\text{oct}}(x,y) \quad . \tag{3.9}$$

Denote the normalised chromaticity of order i by

$$\left(\xi_{x,y}\right)_i = \frac{Q_{x,y}^{(i)}}{Q_{x,y}} \quad . \tag{3.10}$$

In the case of up to nth order chromaticity, the detuning is then implemented as

$$\Delta\psi_{\text{chroma}}(\delta) = \sum_{i=1}^{n} \frac{\xi_i \Delta\psi}{i!} \delta^i \quad , \tag{3.11}$$

thus distributing the chromatic effect proportionally to the phase advance between the inter-action points. The octupolar detuning with amplitude is distributed over the ring in the same way. The local optics functions (Twiss parameters) $\left(\alpha_{x,y}, \beta_{x,y}, \gamma_{x,y}\right)$ determine the "action" (i.e. half the single-particle emittance (2.18)) of a macro-particle,

$$J_x = \frac{1}{2}\left(\gamma_x x^2 + 2\alpha_x x x' + \beta_x x'^2\right) \quad \text{and} \tag{3.12a}$$

$$J_y = \frac{1}{2}\left(\gamma_y y^2 + 2\alpha_y y y' + \beta_y y'^2\right) \quad . \tag{3.12b}$$

Denoting the relative octupolar detuning strengths (the *anharmonicities*) as $\left(a_{x,x}, a_{x,y} = a_{y,x}, a_{y,y}\right)$, the detuning with amplitude amounts to

$$\begin{pmatrix} \Delta\psi_{x,\text{oct}} \\ \Delta\psi_{y,\text{oct}} \end{pmatrix} = \begin{pmatrix} a_{x,x} & a_{x,y} \\ a_{x,y} & a_{y,y} \end{pmatrix} \begin{pmatrix} J_x \Delta\psi_x \\ J_y \Delta\psi_y \end{pmatrix} \quad . \tag{3.13}$$

Chromaticity and octupolar detuning with amplitude are the most significant off-momentum and non-linear single-particle effects contributing to the tune spread.

In the longitudinal plane, the motion can be treated either linearly or with sinusoidal kicks modelling the passage of (possibly multi-harmonic) RF cavities according to (2.48). Most of the collective effect models in PyHEADTAIL including space charge are based on "beam slices" which represent longitudinally binned subsets of the macro-particle distribution. The particle density per slice is determined by nearest-grid-point (NGP) interpolation (i.e. lowest order).

3.2 PyHEADTAIL Space Charge Models

The self-fields of particle beams superpose the electromagnetic fields applied by magnets and RF cavities in synchrotrons. The corresponding space charge effects lead to defocusing in the transverse plane and focusing (defocusing) in the longitudinal plane for operation above (below) transition energy. For non-linear beam distributions, space charge results in a tune

spread which makes it an important factor e.g. when investigating betatron resonances or the influence of Landau damping on instabilities.

In the following we present the implemented space charge models, viz.

1. a line density derivative model for the longitudinal plane,

2. a semi-analytical Bassetti-Erskine model (based on the assumption of a two-dimensional Gaussian normal distribution) for the transverse plane (iteratively for each slice),

3. a so-called "2.5D" model based on a PIC algorithm which self-consistently solves the electromagnetic forces of the transverse distributions for each slice separately (thus accounting for varying longitudinal distributions such as in bunched beams), as well as

4. a 3D PIC model solving the full particle distribution to obtain the electromagnetic forces in all three planes.

3.2.1 Longitudinal Model

When the longitudinal electric beam field is much weaker than the RF focusing (which is usually the case at CERN's synchrotrons), the beam is said to be "emittance-dominated". In terms of the envelope equations (2.98) – which can equivalently be formulated in 1D for the longitudinal plane –, the emittance term ϵ^2/r^3 is larger than the space charge term K^{SC}/r. As a consequence, the longitudinal beam profile of a matched (i.e. stationary) bunch distribution is primarily determined by the RF bucket shape and the amount to which it is filled by the particles. Longitudinal space charge mainly affects the synchrotron tunes of the particles and does not significantly contribute to the beam profile. For such emittance-dominated beams, the longitudinal electric field depends on the local line density $\lambda(z)$.

Beams in CERN's circular accelerators typically exhibit very long bunch lengths in comparison to the vacuum tube radius r_p. For a perfectly conducting vacuum tube, the electric field lines enter the wall perpendicularly. In other words, the induced image currents compress the free space electric field lines. For an ellipsoidal bunch with uniform distribution having transverse radius r_b and longitudinal semi-axis z_m, this results in a non-linear suppression of the otherwise linear electric field along the bunch. Figure 3.2 sketches the corresponding bending of the field lines in the vacuum tube depending on how far the wall is located from the local beam edge.

We base the longitudinal space charge model of PyHEADTAIL on the extensive theoretical analysis in Reiser [2008, chapter 5]. Conceptually, the space charge forces are computed by describing the actual distribution with a linear equivalent field which includes the image effects in terms of an averaged geometry factor. Furthermore, the local electric field at a given bunch slice is derived from the local line density derivative, which encodes the information of how many particles are pushing from the slices towards the head compared to the slices towards the tail of the bunch for a given location in z.
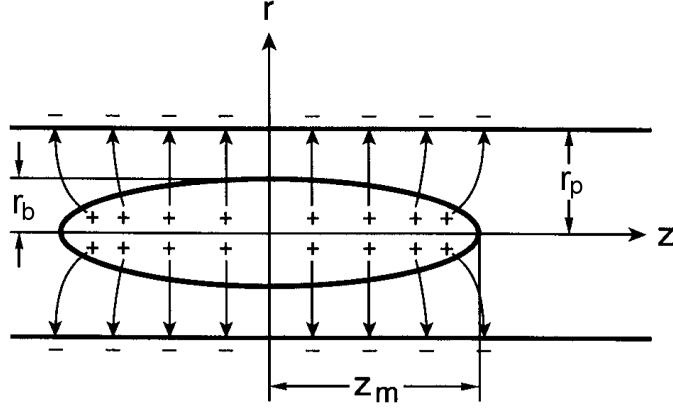
Figure 3.2 – The electric field lines of an ellipsoidal bunch in a perfectly conducting cylindrical vacuum tube enter the wall perpendicularly [Reiser 2008, figure 5.13].

We start our calculation in the *beam frame*, where we can neglect the relative motion of the particles and therefore the magnetic fields. Afterwards we Lorentz boost to the *laboratory frame* to relate to quantities such as λ which are expressed in laboratory coordinates. The electrostatic potential ϕ of the beam self-field in the beam frame consists of the free space potential, ϕ_{free}, as well as the image contribution from the perfectly conducting boundary conditions, ϕ_{im},

$$\phi = \phi_{\text{free}} + \phi_{\text{im}} + \phi_0 \quad , \tag{3.14}$$

where the constant ϕ_0 can be chosen such as to have vanishing potential $\phi(r_p, z) = 0$ at the boundary. The potential ϕ has to satisfy the Poisson equation

$$\Delta\phi = -\frac{\rho}{\epsilon_0} \quad . \tag{2.61}$$

In order to derive the said linear equivalent field expression, we will start from a uniform distribution giving rise to such a linear electric field. Consider the aforementioned transversely rotationally symmetric ellipsoidal bunch. The charge over the ellipsoid volume $4\pi r_b^2 z_m/3$ is uniformly distributed, hence the density ρ is constant reading

$$\rho(r, z) = \begin{cases} \rho_0 = \frac{qN}{4\pi r_b^2 z_m/3} & , r < r_b \text{ and } z < z_m \\ 0 & , \text{ else} \end{cases} \quad . \tag{3.15}$$

Its longitudinal projection along the ellipsoidal bunch, i.e. the corresponding line charge density, is of parabolic form amounting to

$$\lambda(z) = \frac{3}{4}\frac{qN}{z_m}\left(1 - \frac{z^2}{z_m^2}\right) \quad . \tag{3.16}$$

The solution to equation (2.61) then depends on the beam aspect ratio,

$$\chi \doteq \sqrt{1 - \frac{r_b^2}{z_m^2}} \quad . \tag{3.17}$$

The free space solution inside the bunch splits into the parabolic radial and longitudinal parts [Reiser 2008, equation (5.350b)],

$$\phi_{\text{free}}(r, z) = -\frac{\rho_0}{4\epsilon_0} \left[\left(1 - \frac{r_b^2}{2z_m^2} g_0 \right) r^2 + \frac{r_b^2}{z_m^2} g_0 z^2 \right] \quad . \tag{3.18}$$

Here, $g_0 = g_0(\chi)$ denotes the free space *geometry factor* accounting for the bunch shape of the ellipsoid, it is defined by

$$g_0(\chi) \doteq \frac{2}{\chi^2} \left(\frac{1}{2\chi} \ln \left(\frac{1+\chi}{1-\chi} \right) - 1 \right) \quad . \tag{3.19}$$

We are now in the position to express the linear longitudinal free space electric field of the ellipsoid (in the beam frame) in terms of the geometry factor and the derivative of the parabolic line density as

$$E_z^{\text{beam}}(z) = -\frac{\partial \phi_{\text{free}}(r, z)}{\partial z} = \frac{g_0}{4\pi\epsilon_0} \underbrace{\left[\frac{3qN}{4z_m} \frac{2z}{z_m} \right]}_{=-\frac{d\lambda}{dz}} \tag{3.20}$$

$$= -\frac{g_0}{4\pi\epsilon_0} \frac{d\lambda(z)}{dz} \quad . \tag{3.21}$$

By Lorentz boosting to the laboratory frame, we pick up a γ^{-2} factor from $z_m \mapsto \gamma z_m$ (in the line charge density denominator) and the longitudinal derivative $d/dz \mapsto \gamma^{-1} d/dz$. Thus, the longitudinal electric field (3.20) transforms to

$$E_z(z) = -\frac{g_0}{4\pi\epsilon_0 \gamma^2} \frac{d\lambda(z)}{dz} \quad . \tag{3.22}$$

This expression for the 3D ellipsoid may now serve as the equivalent electric field when generalising (i.) to include the perfect conducting boundary conditions via ϕ_{im} and (ii.) to general bunch profiles. By averaging over the bunch distribution one can approximate this general case with an equivalent field. In particular, this model identifies the mean value of the real electric field $\langle z E_z^{\text{real}}(z) \rangle_z$ (which includes the non-linear image effects) with the corresponding analytical expression for the parabolic distribution with the generalised geometry factor g, which then absorbs the image field contributions.

The careful analysis by Reiser [ibid.] compared self-consistent numerical simulations with ellipsoidal bunches for various χ and r_p/r_b ratios. The conclusion qualitatively distinguishes between three regions: region 1 with $z_m \lesssim r_p$, region 2 with $r_p \leq z_m \leq 3r_p$ and region 3 with

$3r_p < z_m$. The latter is the relevant one for the CERN synchrotrons with the main result being that the geometry factor g becomes independent of the aspect ratio χ and can be approximated by [Reiser 2008, equation (5.365)]

$$g(z = 0) = 2\ln\left(\frac{r_p}{r_b}\right) \quad , \tag{3.23a}$$

$$g \approx 0.67 + 2\ln\left(\frac{r_p}{r_b}\right) \quad . \tag{3.23b}$$

The ratio between the beam radius and the vacuum tube radius determines how much the geometry factor would vary along the bunch (compare e.g. the 0.67 offset from the averaged geometry factor to the expression for the centre of the bunch). As a further remark, Reiser [ibid., chapter 6] also discusses the case of two parallel conducting plates with distance $2r_p$, for which the logarithmic term in the geometry factor becomes

$$2\ln\left(\frac{r_p}{r_b}\right) \mapsto 2\ln\left(\frac{4r_p}{\pi r_b}\right) \quad . \tag{3.24}$$

As an interesting side note, Hancock, Lindroos, and Koscielniak [2000] have implicitly determined the g-factor to a value around 2 via longitudinal phase space tomography measurements including space charge effects in CERN's PS Booster machine at very low energies.

In PyHEADTAIL, we have implemented this so-called $\lambda'(z)$ model for general beam distributions. The space charge forces in the longitudinal plane are readily computed by plugging in the general geometry factor (3.23b) as well as the actual $\lambda(z)$ (calculated from the accumulated macro-particle numbers per slice) into the equivalent field expression (3.22),

$$F_z(z) \equiv \frac{dp_z}{dt}(z) = qE_z^{\text{equiv}}(z) = -q\frac{g}{4\pi\epsilon_0\gamma^2}\frac{d\lambda(z)}{dz} \quad . \tag{3.25}$$

Consequently, integrating $F_z(z)$ over a finite Δs gives the longitudinal kick

$$\begin{aligned}\Delta\delta &= \frac{\Delta p_z}{p_0} = \frac{F_z(z)}{p_0}\frac{\Delta s}{\beta c} \\ &= -\frac{qg}{4\pi\epsilon_0\beta^2\gamma^3 m_p c^2}\frac{d\lambda(z)}{dz}\Delta s \quad . \end{aligned} \tag{3.26}$$

In order to validate the longitudinal model, we follow the linear synchrotron motion of particles in the bucket centre during numerical simulations of varying intensities. The simulations have been carried out for the PS Booster at extraction energy $E_{\text{kin}} = 1.4\,\text{GeV}$ (which is below transition) always starting from the same Gaussian phase space distributions with a very small r.m.s. longitudinal emittance of $\epsilon_z = 0.3\,\text{eVs}$. We used 1×10^6 macro-particles and 400 slices and we evaluate the simulation for 100 synchrotron periods. The Fourier spectrum yields the actual synchrotron frequency of the particles which is changes with the intensity due to space charge effects. Below transition, longitudinal space charge acts against the RF phase focusing and hence depresses the synchrotron frequency. Figure 3.3 shows the decrease of the linear

synchrotron tune with intensity.

As the intensity increases, the bunch additionally becomes mismatched because the RF bucket (to which it is matched) gets squeezed when the phase focusing is cancelled by the beam fields below transition. Therefore, the distribution oscillates with a quadrupolar mode resulting in an oscillating bunch length σ_z. The theoretical prediction from equation (2.89) takes into account the actual average bunch length and is plotted in blue in figure 3.3. The corresponding average bunch lengths are shown in the lower panel.
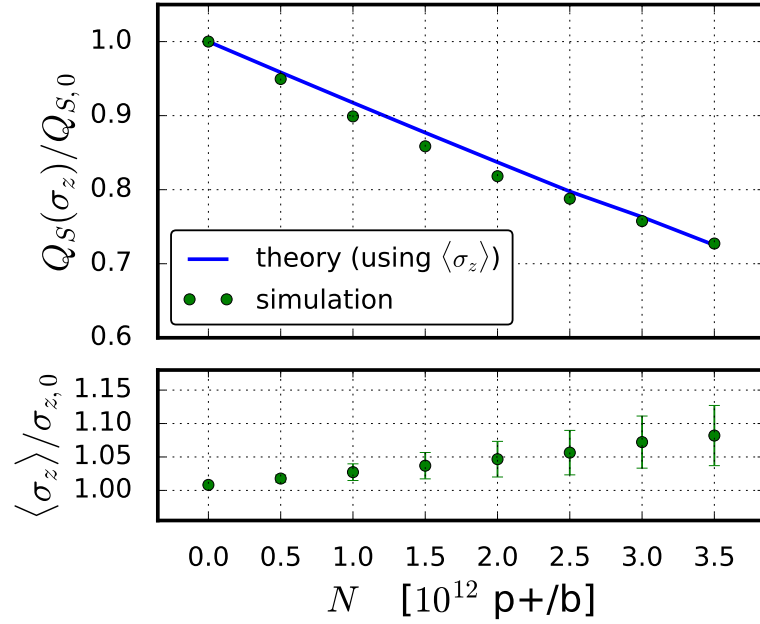
Figure 3.3 – Depression of the linear synchrotron tune $Q_{S,0}$ with stronger space charge as the intensity increases. The lower plot shows the corresponding average r.m.s. bunch length σ_z along with the standard deviation of the quadrupolar oscillation.

3.2.2 Transverse Semi-analytic Gaussian Model

In the beam rest frame, a two-dimensional Gaussian charge density function (2.80) generates the electric fields

$$E_u = \frac{\lambda}{4\pi\epsilon_0} u \int_0^\infty dt \frac{\exp\left(-\frac{x^2}{2\sigma_x^2+t} - \frac{y^2}{2\sigma_y^2+t}\right)}{(\sigma_u^2+t)\sqrt{(\sigma_x^2+t)(\sigma_y^2+t)}} \tag{2.81}$$

for $u = x, y$. Solving this integral numerically for many macro-particle positions (x, y) is computationally very expensive. Bassetti and Erskine [1980] proposed a substitution for this integral in the context of beam-beam interaction simulations in particle colliders , which

allows to express the electric fields in terms of the complex-valued Faddeeva function $w(x+iy)$,

$$E_y + i E_x = \frac{\lambda}{2\epsilon_0 \sqrt{2\pi(\sigma_x^2 - \sigma_y^2)}}$$
$$\left[w\left(\frac{x + iy}{\sqrt{2(\sigma_x^2 - \sigma_y^2)}} \right) - \exp\left(-\frac{x^2}{2\sigma_x^2} - \frac{y^2}{2\sigma_y^2} \right) w\left(\frac{x\frac{\sigma_y}{\sigma_x} + iy\frac{\sigma_x}{\sigma_y}}{\sqrt{2(\sigma_x^2 - \sigma_y^2)}} \right) \right]$$

(3.27)

given $\sigma_x > \sigma_y$ (otherwise exchange $x \leftrightarrow y$). Numerical evaluation of the beam electric fields is much more rapid using this expression, which is often referred to simply as the "Bassetti-Erskine" formula. The Faddeeva function is defined for a complex number z as

$$w(z) \doteq \exp\left(-z^2 \right) \left[1 + \frac{2i}{\sqrt{\pi}} \int_0^z dt \, \exp\left(t^2 \right) \right] \quad .$$

(3.28)

Several efficient implementations of algorithms calculating the Faddeeva function have been reviewed [Oeftiger, Aviral, et al. 2016]. On this basis, we have implemented a Bassetti-Erskine space charge model for the transverse plane in PyHEADTAIL. The beam widths σ_x and σ_y are evaluated slice-wise to compute the space charge forces along the bunch for each slice separately. When $\sigma_x \approx \sigma_y$, the denominators in (3.27) diverge and numerical accuracy becomes affected. Therefore, we evaluate the round beam formula when the beam widths are sufficiently close,

$$E_r(r) = \frac{\lambda}{2\pi\epsilon_0} \frac{1 - \exp\left(-\frac{r^2}{2\sigma_r^2} \right)}{r} \quad .$$

(3.29)

All electric fields so far have been expressed in the beam frame. In order to apply them to the coordinates in PyHEADTAIL, we need to Lorentz boost the fields to the laboratory frame. All in all, the space charge forces pick up a factor γ^{-2} as in the longitudinal case before. The line charge density in the laboratory frame becomes $\lambda \mapsto \lambda/\gamma$ which compensates the γ factor in the transverse electric field transforming to $E_u \mapsto \gamma E_u$. At the same time, the Lorentz boost generates an azimuthal magnetic field contribution to the electric field. In laboratory frame quantities, the transverse magnetic field components read

$$B_x = -\frac{\beta}{c} E_y \quad ,$$

(3.30a)

$$B_y = \frac{\beta}{c} E_x \quad ,$$

(3.30b)

$$B_z = 0 \quad .$$

(3.30c)

Their contribution to the Lorentz force partly compensates the transverse electric field:

$$F_x = q(E_x - \beta c B_y) = q(1 - \beta^2)E_x = q\frac{E_x}{\gamma^2} \quad , \tag{3.31a}$$

$$F_y = q(E_y + \beta c B_x) = q(1 - \beta^2)E_y = q\frac{E_y}{\gamma^2} \quad . \tag{3.31b}$$

Finally, the transverse space charge forces integrated over a finite Δs yield the kicks

$$\begin{aligned}\Delta u' = \frac{\Delta p_u}{p_0} &= \frac{F_u(x,y)}{p_0}\frac{\Delta s}{\beta c} \\ &= \frac{q}{p_0}\frac{E_u(x,y)}{\gamma^2}\frac{\Delta s}{\beta c}\end{aligned} \tag{3.32}$$

with the Bassetti-Erskine electric field expression (3.27) (or the round beam expression (3.29) in case of $\sigma_x \approx \sigma_y$).

3.2.3 Particle-in-cell Model

In order to account for general (not necessarily Gaussian normal) macro-particle distributions when calculating the beam fields, we have to resolve the actual distribution: PIC algorithms model space charge self-consistently [Hockney and Eastwood 1988]. In order to compute the kicks, the macro-particle distribution is first interpolated to nodes of a regular mesh (particle-to-mesh or "P2M" step), then the charge distribution on the mesh is solved for the potential and consequently the force (solve step), and finally the force is interpolated back to the particles (mesh-to-particles or "M2P" step). Figure 3.4 explains the principle of the PIC algorithm for a 2D transverse particle distribution on a slice. A separate library has been developed named PyPIC to encapsulate the various PIC algorithm implementations.

In synchrotrons, the relative momenta between the particles are usually much smaller than p_0. This can be exploited when solving the Maxwell equations by Lorentz boosting to the beam rest frame, where we neglect the relative particle motion and correspondingly only have to deal with an electrostatic problem. Before the P2M step, we Lorentz boost from the co-moving laboratory frame $(x, y, z)_{\text{lab}}$ to the beam rest frame

$$(\tilde{x}, \tilde{y}, \tilde{z})_{\text{beam}} = (x, y, \gamma z)_{\text{lab}} \quad . \tag{3.33}$$

Correspondingly, the bunch becomes much longer, the mesh is then constructed in the beam frame. In PyPIC we have implemented a linear spatial cloud-in-cell (CIC) interpolation, i.e. the shape function of the macro-particles is a constant Heaviside step function over the diameter of a cell. In principle, higher order shape functions as discussed in Hockney and Eastwood [ibid., section 5-3-4] result in better error behaviour of the particle-in-cell algorithm: unphysical energy increase of the particles (also called grid heating) due to the finite mesh size and non-symplectic integration of motion can lead to artificial emittance growth with an impact on the long-term predictability of the simulation. Hockney and Eastwood find
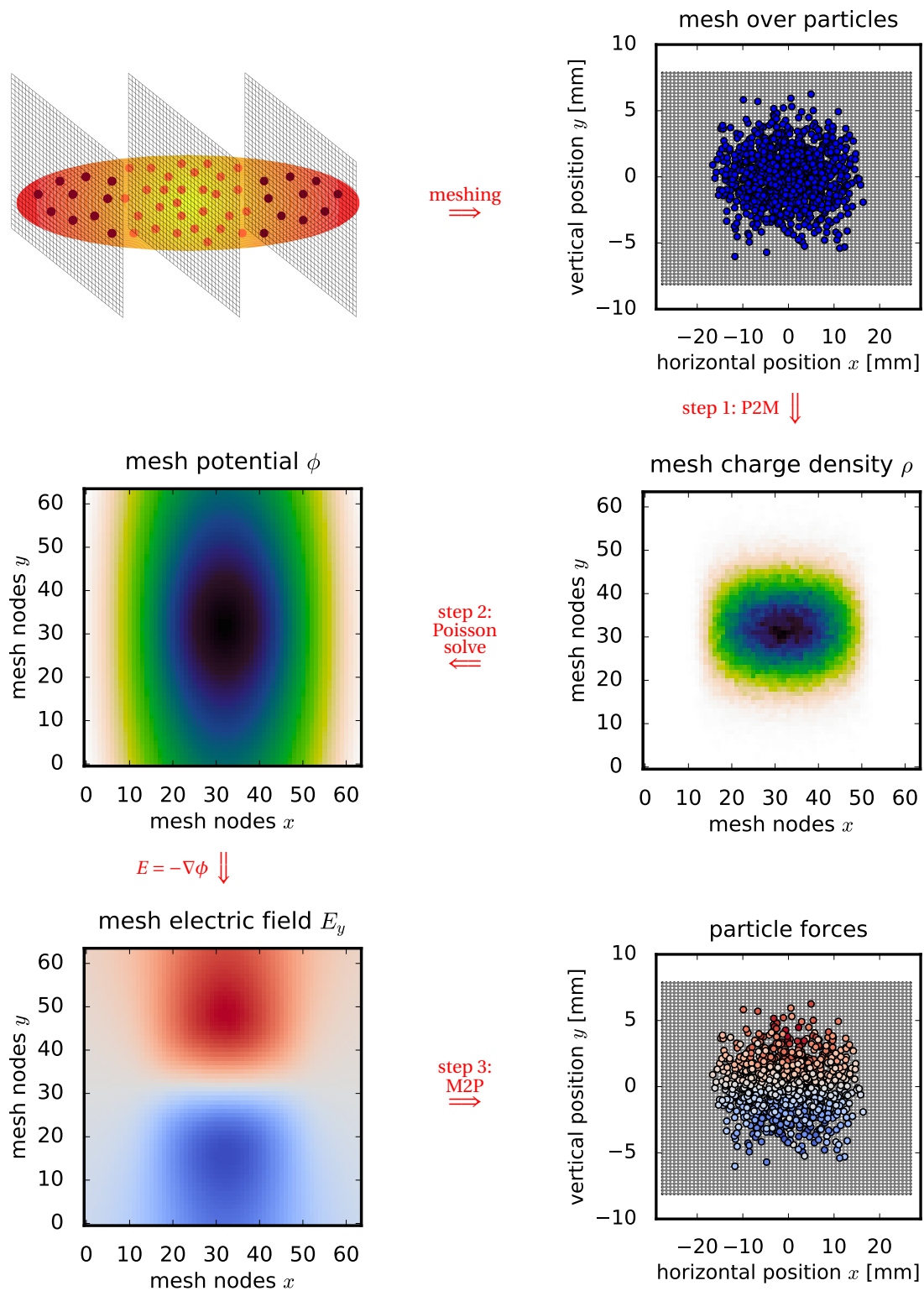
Figure 3.4 – Principle of particle-in-cell algorithm for a 2.5D slice-by-slice example.

higher-order interpolation functions to significantly reduce the grid heating effect for a given mesh size.

With the resulting mesh charge density ρ, we are ready to solve the discrete version of the 2D or 3D Poisson equation,

$$\Delta\phi = -\frac{\rho}{\epsilon_0} \quad , \tag{2.61}$$

on the mesh for the mesh potential ϕ.

To this end, we implemented several Poisson solvers in both 2.5D (i.e. slice-by-slice 2D transverse solving) and full 3D variants. The solvers cover finite difference (FD) approaches with direct matrix solving via QR or LU decomposition (with Dirichlet or arbitrary boundary conditions) and Green's function methods (with free space or rectangular boundary conditions) exploiting the Fast Fourier Transform (FFT) algorithm.

The FD implementations construct a sparse Poisson matrix A with a first-order nearest-neighbour stencil. In case of the LU decomposition $A = LU$, the sparse lower and upper triangle matrices L, U are then precomputed at set-up. At each solve step, the linear matrix equation $LU\phi = -\rho/\epsilon_0$ is solved given the respective vector ρ containing the mesh charge density of all nodes. This approach is extremely efficient on the CPU in conjunction with the KLU algorithm [Davis and Palamadai Natarajan 2010] if the Poisson matrix remains constant over many solve steps [Iadarola et al. 2015]. Therefore, e.g. matrix element indices for the boundary conditions should not change due to a differently shaped boundary, otherwise the LU decomposition needs to be recomputed which is computationally expensive. The QR decomposition is slower but numerically more stable than the LU decomposition (cf. e.g. Geist and Romine [1988]), hence it may serve as a reference to cross-check the results. Finite difference equations always require boundary conditions which can be advantageous if indirect space charge effects from the vacuum tube need to be taken into account. If the transverse beam sizes are rather small compared to the vacuum tube, the mesh can become prohibitively large though. In this case, the following method may be more appropriate.

Another approach to solve equation (2.61) is to use the free space Green's functions G in $D=2$ dimensions (for $\mathbf{x} = (\tilde{x}, \tilde{y})_{\text{beam}}$),

$$\phi(\mathbf{x}) = \frac{1}{4\pi\epsilon_0} \int d^2\widehat{\mathbf{x}} \quad G(\mathbf{x} - \widehat{\mathbf{x}}) \, \rho(\widehat{\mathbf{x}}) \tag{3.34a}$$

with

$$G(\mathbf{x} - \widehat{\mathbf{x}}) = -\frac{1}{2}\ln\left(|\mathbf{x} - \widehat{\mathbf{x}}|^2\right) \quad , \tag{3.34b}$$

resp. in $D=3$ dimensions (for $\mathbf{x} = (\tilde{x}, \tilde{y}, \tilde{z})_{\text{beam}}$),

$$\phi(\mathbf{x}) = \frac{1}{8\pi\epsilon_0} \int d^3\widehat{\mathbf{x}} \quad G(\mathbf{x} - \widehat{\mathbf{x}}) \, \rho(\widehat{\mathbf{x}}) \tag{3.34c}$$

with

$$G(\mathbf{x} - \widehat{\mathbf{x}}) = \frac{1}{\sqrt{|\mathbf{x} - \widehat{\mathbf{x}}|^2}} \quad . \tag{3.34d}$$

We apply Hockney's trick where the domain of the Green's function is doubled by cyclical expansion in each dimension [Hockney and Eastwood 1988]. The explicit expressions are obtained by mirroring the Green's function while the mesh charge density ρ vanishes across the extension, cf. e.g. Qiang et al. [2006, equations (7-10)]. The hence achieved periodicity over the whole new domain allows to make use of the computationally very effective FFT algorithm for the convolution (3.34). The potential in the expanded region of the domain will be wrong after the convolution but as it is irrelevant we can discard it.

In principle, the Green's function needs to be evaluated on a square (cuboid) mesh with equal distances in all directions. In the transverse plane, aspect ratios may be large due to the betatron function ratio and additional dispersion effects. To the least in the 3D case, the aspect ratio of the transverse with respect to the longitudinal plane will certainly be large and thus require many mesh points to cover the whole distribution – which may become computationally heavy. Therefore, we make use of the integrated Green's functions (IGF) $\widehat{G}$. IGF conceptually include the aspect ratio into the discrete Green's function by integrating over each cell assuming ρ to be constant across the cell. This approximation has to be kept in mind when choosing the mesh size. Let $h_{x,y,z}$ denote the mesh sizes in horizontal, vertical and longitudinal direction, respectively, and $N_{x,y,z}$ the corresponding number of mesh cells per dimension. For the (i,j)-indexed mesh cell centred at $(\tilde{x}_i, \tilde{y}_j)$, the open boundary $D = 2$ effective potential can be written

$$\phi(\tilde{x}_i, \tilde{y}_j) = \frac{h_x h_y}{2\pi\epsilon_0} \sum_{i'=1}^{2N_x} \sum_{j'=1}^{2N_y} \widehat{G}(\tilde{x}_i - \tilde{x}_{i'}, \tilde{y}_j - \tilde{y}_{j'}) \rho(\tilde{x}_{i'}, \tilde{y}_{j'}) \quad , \tag{3.35}$$

where the IGF is computed via

$$\widehat{G}(\tilde{x}_i - \tilde{x}_{i'}, \tilde{y}_j - \tilde{y}_{j'}) = \int_{\tilde{x}_{i'} - h_x/2}^{\tilde{x}_{i'} + h_x/2} dx \int_{\tilde{y}_{j'} - h_y/2}^{\tilde{y}_{j'} + h_y/2} dy \, G(\tilde{x}_i - x, \tilde{y}_j - y) \quad . \tag{3.36}$$

Note that the discrete convolution runs over twice the number of mesh cells in each direction as required for the cyclic domain expansion. The integration can be carried out analytically with the indefinite integral expression

$$\int dy \int dx \ln(x^2 + y^2) = -3xy + x^2 \arctan(y/x) + y^2 \arctan(x/y) + xy \ln(x^2 + y^2) \quad , \tag{3.37}$$

cf. Qiang, Furman, and Ryne [2004, equations (56-58)].

Equivalently, the $D = 3$ effective potential

$$\phi\left(\tilde{x}_i, \tilde{y}_j, \tilde{z}_k\right) = \frac{h_x h_y h_z}{4\pi\epsilon_0} \sum_{i'=1}^{2N_x} \sum_{j'=1}^{2N_y} \sum_{k'=1}^{2N_z} \widehat{G}(\tilde{x}_i - \tilde{x}_{i'}, \tilde{y}_j - \tilde{y}_{j'}, \tilde{z}_k - \tilde{z}_{k'}) \rho(\tilde{x}_{i'}, \tilde{y}_{j'}, \tilde{z}_{k'}) \tag{3.38}$$

has the corresponding IGF

$$\widehat{G}(\tilde{x}_i - \tilde{x}_{i'}, \tilde{y}_j - \tilde{y}_{j'}, \tilde{z}_k - \tilde{z}_{k'}) = \int\limits_{\tilde{x}_{i'}-h_x/2}^{\tilde{x}_{i'}+h_x/2} dx \int\limits_{\tilde{y}_{j'}-h_y/2}^{\tilde{y}_{j'}+h_y/2} dy \int\limits_{\tilde{z}_{k'}-h_z/2}^{\tilde{z}_{k'}+h_z/2} dz\, G(\tilde{x}_i - x, \tilde{y}_j - y, \tilde{z}_k - z) \quad . \tag{3.39}$$

The three-dimensional $\widehat{G}$ can again be expressed in closed form, cf. Qiang et al. [2007, equation (2)].

The Fourier transform of the IGF, $\mathscr{F}\widehat{G}$, is computed at set-up time and stored until the mesh is changed. At each solve step, $\mathscr{F}\widehat{G}$ is multiplied by the Fourier transformed mesh charge density ρ and the result inversely Fourier transformed to yield the potential,

$$\phi = \mathscr{F}^{-1}\left[(\mathscr{F}\widehat{G}) \cdot (\mathscr{F}\rho)\right] \quad . \tag{3.40}$$

The FFT convolution approach is much more efficient at a complexity of $\mathscr{O}(n \log n)$ than computing the convolution integral in real space with $\mathscr{O}(n^2)$, where n denotes the total number of mesh nodes. Using this method with the FFTW implementation on the CPU [Frigo and Johnson 2005] takes less than twice as long as the KLU direct solving approach mentioned before [Iadarola et al. 2015].

After the potential ϕ has been determined on the mesh, the electric mesh fields $\tilde{\mathbf{E}}$ in the beam frame are computed as

$$\tilde{\mathbf{E}} = -\nabla\phi \tag{3.41}$$

via a numerical first-order finite difference gradient implementation. Finally, the electric fields are interpolated back to the macro-particles (M2P) and Lorentz boosted back to the laboratory frame,

$$(E_x, E_y, E_z)_{\text{lab}} = \left(\gamma\tilde{E}_x, \gamma\tilde{E}_y, \tilde{E}_z\right)_{\text{beam}} \quad . \tag{3.42}$$

The Lorentz forces for each macro-particle include the magnetic fields arising when transforming to the laboratory frame,

$$(B_x, B_y, B_z)_{\text{lab}} = \left(-\beta E_y/c, \beta E_x/c, 0\right)_{\text{lab}} \tag{3.43}$$

$$\implies (F_x, F_y, F_z)_{\text{lab}} = q\left(\frac{\tilde{E}_x}{\gamma}, \frac{\tilde{E}_y}{\gamma}, \tilde{E}_z\right)_{\text{beam}} \quad . \tag{3.44}$$

A necessary condition for total charge and momentum conservation is to use identical inter-

polation functions and order at both the P2M as well as the M2P step [Hockney and Eastwood 1988, section 5-3-3]. As a side note, the usual straightforward interpolation functions can be the source of noise and grid heating effects in the traditional PIC approach. Recently, symplectic algorithms have been derived to solve these issues [Qin et al. 2015], which can be interesting for long-term simulations over many turns since the symplectic nature implies a finite bound on the energy error.

Figure 3.5 shows the PIC computed electric field of a coasting beam with a KV distribution in the transverse plane for the SPS. For $\lambda = 5.1\,\text{C/m}$ and beam edges at $r_x = 2.5\,\text{mm}$ and $r_y = 1.6\,\text{mm}$, the maximal electric field at the beam edge analytically gives

$$E_x = \frac{\lambda}{\pi\epsilon_0} \frac{1}{r_x + r_y} = 15.2\,\text{kV/m} \quad , \tag{3.45}$$

which matches the result from the PIC algorithm in the 3D graph.
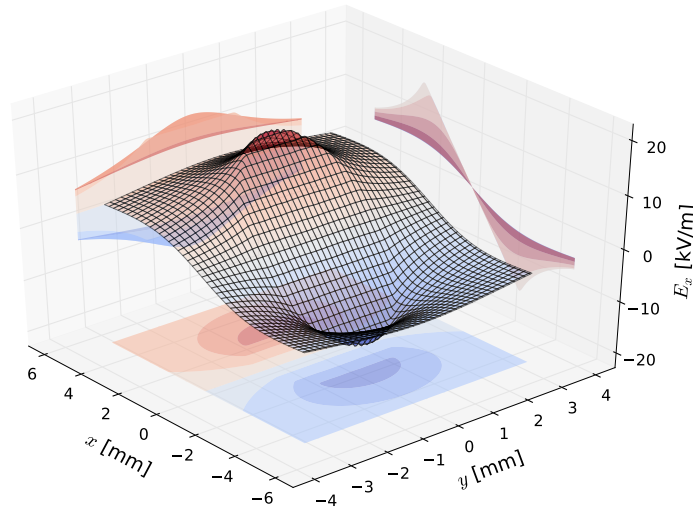
Figure 3.5 – Horizontal electric field of a KV beam in the SPS.

3.3 GPU High-performance Computing

PyHEADTAIL has been made available for GPU high-performance computing. The library PyCUDA provides an interface for GPU memory stored arrays that adopts the API of the standard Python library for scientific computing, NumPy, hence making large portions of the code easily applicable to both NumPy arrays and GPUArrays [Klöckner et al. 2012]. To make the GPU usage in PyHEADTAIL as transparent and flexible as possible for GPU users, Hegglin [2016] developed a context management system to switch between GPU and CPU contexts. Algorithms for the GPU need to make use of the pronounced parallel hardware structures and therefore often differ from serial CPU algorithms. The context managers switch between implemented algorithms e.g. for the bunch distribution statistics. For the GPU implementa-

tions it is therefore of crucial importance to have access to the underlying CUDA [Nickolls et al. 2008] API from Python which is fully provided by PyCUDA. Implementing and calling custom CUDA kernels is flexible and straight forward from the Python top layer. Besides the NumPy array API and the CUDA access, the third important ingredient to PyHEADTAIL on the GPU is the incorporation of effective GPU computing libraries such as cuFFT [NVIDIA 2016a], cuSOLVER [NVIDIA 2016b], cuSPARSE [NVIDIA 2016c] and Thrust [N. Bell and J. Hoberock 2011]. We achieve this partly via the Python binding library scikit-cuda [Givon 2016] and partly via self-implemented interfaces using `ctypes`.

Single-particle physics and hence the tracking modules of PyHEADTAIL profit tremendously from parallelisation. Since the particle motion can be integrated independently, the speed-up scales almost linearly with the available number of computing cores. The study reported in Oeftiger [2016] achieves $\mathcal{O}(100)$ speed-up for longitudinal tracking parallelised on the GPU (an NVIDIA Tesla C2075 in this case, cf. table 3.2). This is not necessarily the case for multi-particle interaction which may depend on exchanging information between the computing cores. Such algorithms then rely on the available memory bandwidth of the respective hardware accelerator. The speed-up of parallelising the mesh-particle conversion steps of the PIC algorithm, for example, is affected by the memory latency and specially tailored parallelisation techniques become important.

For the PyHEADTAIL space charge suite we have developed a GPU version of PyPIC. The performance bottlenecks appear very differently during the aforementioned three particle-in-cell steps P2M, solve and M2P when comparing runtime profiles between the CPU and GPU versions. Figure 3.6 shows the fraction of time spent on both architectures during each step for quadratically increasing transverse mesh sizes given a fixed number of macro-particles. Comparing the GPU cuFFT 3D Fourier transform performance to the CPU FFTW on a mesh of size $(16, 32, 64)$ gives a speed-up of up to $S = 35.8$, comparing to the standard NumPy FFT extension even reaches $S = 65.5$. We used an NVIDIA K40m GPU (specifications in table 3.2) and a single 2.3 GHz Intel Xeon E5-2630 (v1) CPU core (specifications in table 3.1 for this comparison. This explains why the solve step with the free space FFT-based Green's function Poisson solver does not have such a significant impact on the overall timing during the PIC algorithm on the GPU, while it essentially marks the bottleneck on the CPU.

Effectively, the particle deposition on the mesh is the most performance critical part in the GPU PIC algorithm. We have implemented an atomic deposition algorithm, in which a CUDA thread for each particle is launched which locks the memory location of the respective mesh node charge from access by other threads, reads the memory value, adds to it and then stores the updated value. With this approach, we observed a rather slow performance for large macro-particle numbers as memory bank conflicts and thread stalls can happen for both the software-emulated 64-bit and the hardware-accelerated 32-bit `atomicAdd` variants. This finding is especially pronounced in the 3D case where each particle updates eight surrounding mesh nodes (instead of four in the 2D case). The problem decreased when using less macro-particles for a given mesh size – however, to achieve a good resolution for the electric fields, at

(a) CPU implementation.

(b) GPU implementation.
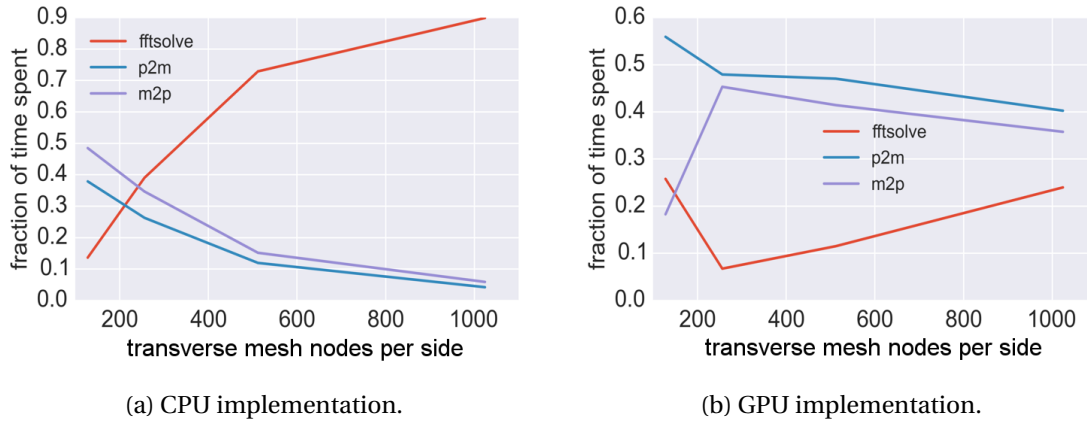
Figure 3.6 – Timing proportions between the P2M, solve and M2P step for the FFT-based 2.5D Poisson solver vs. number of mesh nodes per transverse side [Oeftiger and Hegglin 2016]. The number of macro-particles is fixed to 5×10^5 and only one slice has been used (for multiple slices the average timing for the GPU solve step reduces further due to concurrent solving of several slices).

least 10 macro-particles per cell are required [Hockney and Eastwood 1988].

To address this issue, we implemented a sorted deposition particle-in-cell algorithm [Ahnert, Demidov, and Mulansky 2014]. In this approach, the macro-particle coordinate arrays are first sorted by their cell IDs, for which we used the Thrust library with its `sort_by_key` functions. Subsequently, a thread is launched for each cell which loops through the particles within this cell to construct guard cell charge densities. In a third step, a kernel merges the four (2D) resp. eight (3D) guard meshes to the final mesh charge density ρ array. We achieved a speed-up of $S = 3.5$ for the mesh size $(64, 64, 32)$ and 1×10^6 macro-particles when comparing the sorted deposition to the double precision `atomicAdd` deposition (both on the GPU). In addition, the M2P step profits from the sorted arrays since global GPU memory is accessed in a coalesced manner: the kernel call on unsorted arrays takes 25% longer than on sorted arrays. Further approaches to address the memory bank conflicts (such as using L1 caching) have been investigated e.g. for SYNERGIA by Lu and Amundson [2014] and for ELEGANT by Pogorelov, Amyx, and Messmer [2011] and Pogorelov, Amyx, Balasalle, et al. [2012].

For the 2.5D case, the transverse Poisson equations can be solved for all slices in parallel. Since the cuFFT calls for each slice work with small arrays compared to the GPU memory size, the cuFFT batch-solving works very effectively. All in all, we achieved overall PIC speed-ups of up to $S = 13.2$ compared to the scalar CPU. Figure 3.7 shows how the GPU usage becomes increasingly beneficial for larger mesh sizes at a fixed number of 5×10^5 macro-particles. Also increasing the number of macro-particles scales less than linearly for the relevant parameter range as opposed to the CPU. These results allow the GPU accelerated space charge simulations to access much higher resolutions and increase the validity of simulations (also over longer time scales for larger mesh sizes and higher macro-particle

numbers).

A typical numerical scenario for the 2.5D model would be to integrate the motion of 1×10^6 macro-particles on a mesh of 20 slices and 128×128 transverse nodes. Our fastest CPU version (with the KLU algorithm) takes 152 ms to compute the space charge interaction over the whole bunch. For the GPU, the same numerical parameters take 110 ms. However, the beneficial scaling on the GPU allows to increase the transverse mesh size fourfold to 256×256 and use twice the number of macro-particles at the expense of 134 ms for the entire space charge interaction. This is still less than the original scalar CPU timing, which would (in the best case) linearly increase for the eightfold higher resolution.

In the 3D case, the solve step completely dominates the P2M and M2P steps on the CPU. Simulations for circular accelerators which supposedly cover thousands of revolutions and more become very costly. Here, the GPU approach becomes most valuable because the solve step takes less than a third of the total process. The additional FFT computation along the longitudinal direction adds on the 10% level to the overall GPU timing – on the CPU, instead, the timing increases by more than an order of magnitude. Therefore, the GPU acceleration renders the self-consistent 3D space charge model cost-effective and hence makes elaborate long-term studies possible.
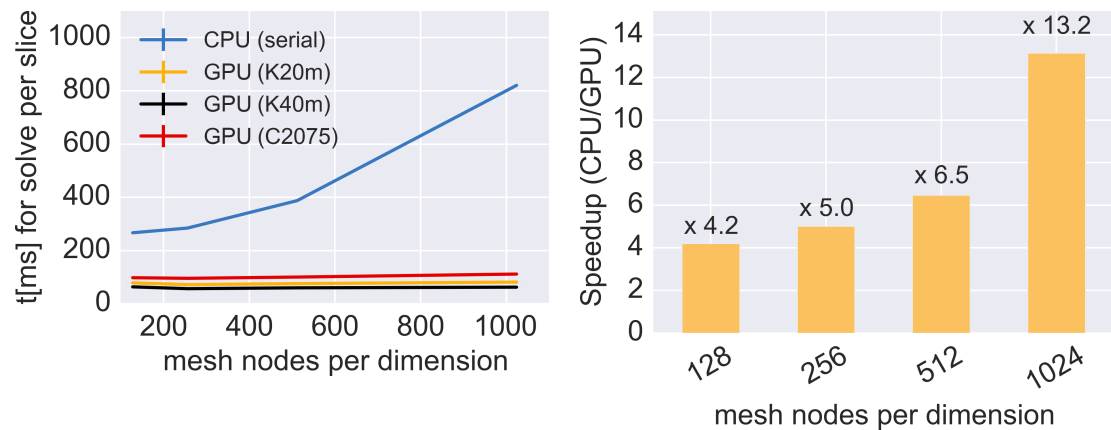
(a) Comparing various architectures.

(b) NVIDIA K40m GPU vs. single Intel Xeon E5-2630 CPU.

Figure 3.7 – Overall 2.5D PIC speed-up achieved (for a single slice) vs. number of mesh nodes per transverse dimension [Oeftiger and Hegglin 2016].

CPU	2× Intel Xeon E5-2630 (v1)
CPU cores	2 × 6
RAM	256 GB DDR3
CPU clock rate	2.30 GHz
CPU L3 cache	15 MB
instruction set	Intel AVX
performance (32bit floats)	0.1 TFLOPS

Table 3.1 – Relevant CPU machine specifications.

NVIDIA GPU model	Tesla C2075	Tesla K20m	Tesla K40m
GPU DDR5 RAM	5.3 GB	5.1 GB	12.3 GB
GPU clock rate	1.15 GHz	0.7 GHz	0.75 GHz
CUDA cores	448	2496	2880
CUDA computing capability	2.0	3.5	3.5
performance (32bit floats)	1.0 TFLOPS	3.5 TFLOPS	4.3 TFLOPS

Table 3.2 – Relevant GPU machine specifications.

3.4 Comparison Between Space Charge Models

The transverse semi-analytic model assumes Gaussian distributions in both the horizontal and the vertical plane. If the actual distribution deviates from a Gaussian, equation (3.27) only represents an approximation. This needs to be kept in mind especially in the presence of dispersion: even if the betatron distributions are of Gaussian nature, the momentum distribution may deviate from a Gaussian. Consequently, its contribution to the transverse profiles renders the whole profile non-Gaussian.

Figure 3.8 depicts an $N = 2 \times 10^{11}$ SPS bunch with a horizontal normalised emittance of $\epsilon_x = 0.84\,\text{mm}\,\text{mrad}$ and a very large longitudinal r.m.s. emittance of $\epsilon_z = 0.42\,\text{eVs}$. Since the RF bucket acceptance amounts to $0.68\,\text{eVs}$, the matched longitudinal thermal phase space distribution is deformed compared to a bi-Gaussian due to the RF bucket non-linearities. Given a dispersion of $D_x = 7.96\,\text{m}$, this non-Gaussian momentum distribution reflects in the evidently non-Gaussian horizontal beam profile plotted in blue in figure 3.8a. The r.m.s. equivalent Gaussian distribution is plotted in red as a comparison. Now, the latter gives rise to the corresponding electric field of the Bassetti-Erskine model space charge model which is plotted in green in figure 3.8b and which is used to compute the space charge force for the (blue) macro-particle distribution. Figure 3.8b also shows the real horizontal electric field of the central slice of the macro-particle distribution calculated with the 2.5D PIC model (depicted in orange) and the 3D PIC model (depicted in blue). Firstly, both 2.5D and 3D computed fields agree very closely, numerically they differ on the fifth significant figure – this means that the relativistic approximation (on which the 2.5D model is based) is indeed

well satisfied for SPS bunches of lengths in the same order of magnitude. Secondly, the PIC computed fields clearly show their maximum at an approximately 20% larger horizontal position compared to the Bassetti-Erskine based (Gaussian) field peak. This also leads to a different slope in the linear field part around the bunch centre. An interesting consequence resulting from this fact is the larger maximum incoherent betatron space charge tune shift in the Gaussian (green curve) case compared to the realistic PIC case (strongest space charge depression happens for particles in the core, which hence experience the linear part of E_x while their tune shift ΔQ_x^{SC} scales with the constant slope α of this linear $E_x \approx \alpha x$).
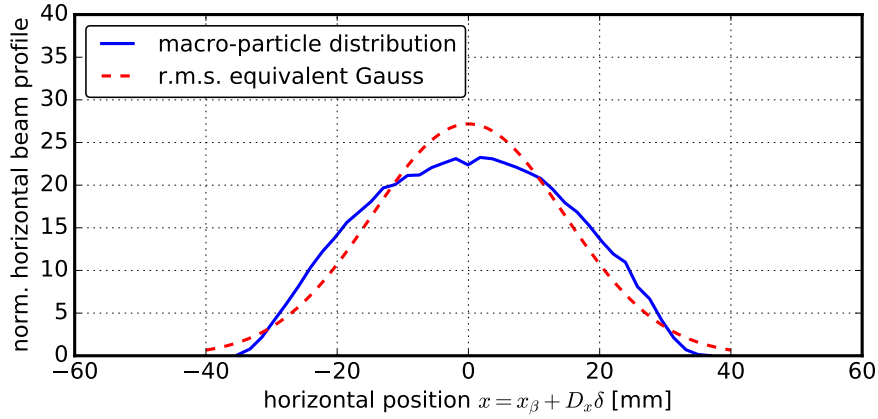
(a) Beam profile and Gaussian r.m.s. equivalent for central beam slice (with 1×10^6 macro-particles distributed over 32 slices).
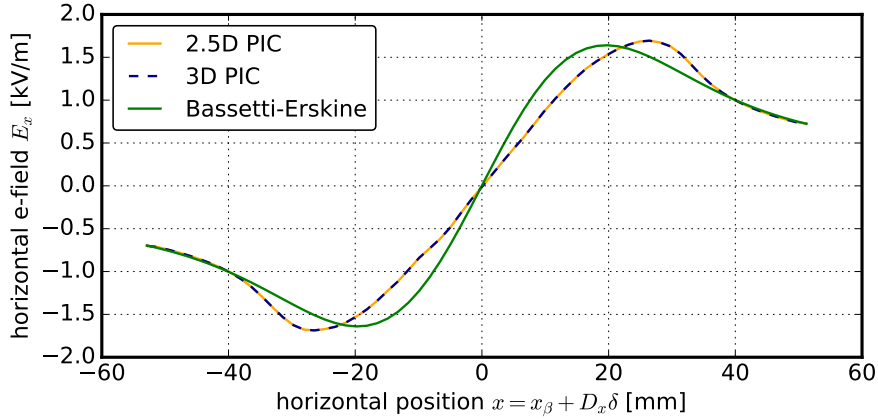
(b) Corresponding horizontal electric field in the central slice from the PIC and the (Gaussian) Bassetti-Erskine model.

Figure 3.8 – Large ϵ_z entail non-Gaussian momentum distributions which affect the horizontal distribution via dispersion.

In order to compare the longitudinal $\lambda'(z)$ from the first section to the longitudinal component of the 3D PIC model, we refer to the same SPS beam at injection energy with $\gamma = 27.72$. Figure 3.9 shows the longitudinal kicks obtained from the $\lambda'(z)$ model for a circular vacuum tube (for which the geometry factor amounts to $g = 5.25$, compare this to $g_0 = 6.36$ in free space).

The Gaussian beam has been divided into 32 slices which is few for the NGP interpolation, correspondingly the $\lambda'(z)$ model kicks appear step-like. In order not to violate momentum conservation, the interpolation order needs to be the identical for the initial binning of the particles into slices (in order to calculate the line density and its derivative based on the slices) and for the final application of the calculated space charge force to the particles [Hockney and Eastwood 1988, section 5-3-3]. Hence, if we use lowest-order NGP interpolation for the slice model, we should apply the same principle and use the calculated kick per slice for all particles over the whole slice without applying higher-order interpolation. One often uses large numbers (hundreds to thousands) of slices in longitudinal simulations which minimises the discrete step distance between slices.
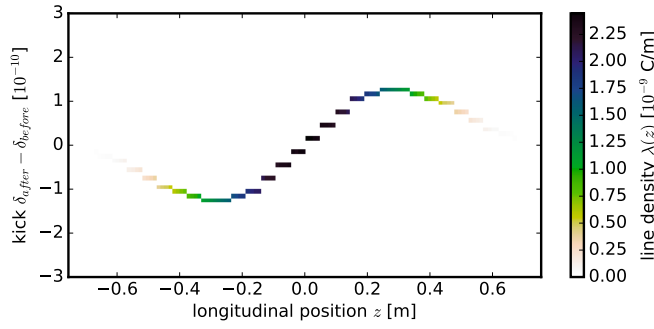
Figure 3.9 – Longitudinal space charge kicks vs. position employing the $\lambda'(z)$ model for 32 slices of an SPS beam at injection (assuming an $r_p = 5\,\text{cm}$ round vacuum tube boundary).

The 3D PIC model also calculates the longitudinal space charge forces for the distribution along the bunch. For open boundary conditions (i.e. free space), figure 3.10 shows the longitudinal kicks of a 3D Gaussian distributed macro-particle distribution. The longitudinal mesh here comprises 32 nodes. We can compare the result to the longitudinal 1D model from section 3.2.1, where we also used 32 slices for the kicks depicted in figure 3.9. The first-order cloud-in-cell (CIC) scheme we implemented for our PIC interpolation function makes the kicks much smoother across the bunch as compared to the zero-order NGP interpolation from the PyHEADTAIL slicing model, which made the $\lambda'(z)$ model kicks appear step-like. What is more, the $\lambda'(z)$ model of figure 3.9 includes the indirect space charge suppression of E_z from the non-linear interaction with the vacuum tube. This effect is not included in the open boundary 3D PIC model, hence the space charge kicks are larger in figure 3.10. Finally, the 3D model resolves the proper longitudinal field for varying transverse amplitudes, while the 1D model averages over the transverse distribution leading to the constant term of 0.67 (instead of the often cited axial value of 1 in the literature for zero transverse offset in the rigid ellipsoid) in the generalised geometry factor expression (3.23b). The varying longitudinal field at different transverse amplitudes leads to a spread of the longitudinal kicks in the 3D case around the averaged value used in the 1D model.
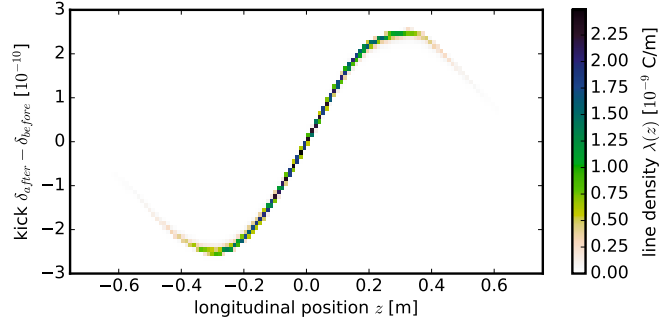
Figure 3.10 – Longitudinal space charge kicks vs. position employing the 3D PIC model for 32 longitudinal mesh nodes along the same SPS beam from figure 3.9.

3.5 Quadrupolar Pick-Ups and Envelope Simulations

The collective nature of a distribution of particles in a beam comprises coherent modes which can be observed in the moments of the beam distribution. Direct space charge influences the coherent mode frequency from the quadrupolar order on: in the transverse plane, the defocusing nature of space charge results in a frequency lowering. Therefore, we can make use of this information contained in the quadrupolar coherent mode which can be observed via the second (quadrupolar) moment of the beam to determine the space charge strength. Take a set-up of four electrodes azimuthally regularly arranged in $\pi/2$ distances as illustrated in figure 3.11. The transverse quadrupolar beam moment can be measured by summing the two horizontal electrode signals L (for left) and R (for right) as well as the two vertical signals T (for top) and B (for bottom) and then subtracting the two planes as in $(L+R)-(T+B)$. If the beam centroid is offset from the reference orbit, the beam performs dipolar coherent motion and the dipolar beam moment also adds to the final signal:

$$P_{\mathrm{QPU}} \propto \langle x^2 \rangle - \langle y^2 \rangle = \sigma_x^2 - \sigma_y^2 + \langle x \rangle^2 - \langle y \rangle^2 \quad . \tag{3.46}$$

(In fact, the dipolar contribution to the signal can be evaluated and removed as $L - R$ gives the horizontal beam position $\langle x \rangle$ and, likewise, $T - B$ the vertical beam position $\langle y \rangle$.)

The oscillations of the r.m.s. beam envelopes $\sigma_{x,y}$ can thus be recorded by this Quadrupolar Pick-up (QPU) set-up as to extract the quadrupolar mode frequency from a spectral analysis of its signal P_{QPU}. For bunched beams, longitudinal motion can result in synchrotron side-bands in the frequency spectrum if there is non-vanishing dispersion at the location of the QPU. It is to be emphasised that the frequency signal of the QPU relies on an envelope mismatch which can be either given by the (typically rapidly decaying) quadrupolar injection oscillations originating from an injection mismatch of the beam or via excitation by means of a quadrupolar kicker magnet.

The QPU method is non-destructive to the beam which makes it an intriguing method for the parasitic determination of the transverse emittances. It is important to note that the

75
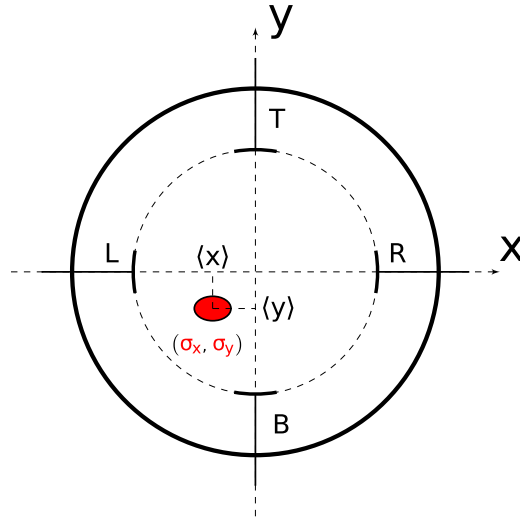
Figure 3.11 – Layout of the QPU set-up with the four electrodes T (top), B (bottom), L (left) and R (right) to measure the quadrupolar coherent beam modes [Singh et al. 2014, modified version of figure 1]. The beam is sketched in red at a centroid offset $\langle x \rangle, \langle y \rangle$.

measurement of the statistical quadrupolar moment of the beam distribution strictly relates to the statistical r.m.s. emittance, no further information on the beam shape (such as tails etc.) can be extracted. Since we are interested in assessing space charge impact to minimise emittance growth, we actually care for the r.m.s. emittance in any case (for the sake of Sacherer's r.m.s. equivalence principle). The emittance determination via the quadrupolar beam moment can avoid suffering from the (possibly large) systematic errors on the local optics parameters, which is inherent to other beam emittance determination methods such as wire scanning. By using at least two QPUs at two different locations, one can determine the two transverse emittances as well as the local Twiss parameters from the time evolution of P_{QPU}: the quadrupolar beam moment (depending on the r.m.s. beam sizes) can be directly related to the r.m.s. emittances via $\sigma_x^2 = \beta_x \epsilon_x / (\beta \gamma)$ or, in the presence of dispersion, via expression (2.35). This time-domain technique has been further developed in the Ph.D. thesis of Jansson [2001]. The work included an advanced design of a magnetic quadrupolar pick-up using four wire loops to measure the radial magnetic component of the beam instead of the four electrodes, two prototypes of which have successfully been operated at the PS. The advantage of the magnetic pick-up design lies in the absence of the monopole contribution to the signal P_{QPU} as opposed to electric pick-ups where the mere beam intensity (as the zero-order monopole beam moment) gives the largest signal contribution, which consequently needs to be subtracted from the time domain signal in order to extract the quadrupolar moment information. The motivation behind this method focused on identifying emittance growth from injection mismatch from the optics parameters.

In the presence of considerable space charge now, we can instead proceed via the frequency domain. The quadrupolar (envelope) mode frequencies $Q_\pm$ are shifted downwards from twice

the bare betatron tunes due to space charge defocusing. As we derived in the theory chapter, they relate to the incoherent KV space charge tune shift via expression (2.110).

The idea of measuring space charge impact via QPU set-ups has been mentioned already quite early in the history of space charge research by Hardt [1966] in the context of the derivation of the coherent resonance condition for the space charge shifted betatron resonances. In the 1990s, first experimental studies at CERN and GSI have investigated the QPU concept for space charge related issues. In both cases, quadrupolar kicker magnets have been used to excite the beams and measure the quadrupolar beam transfer functions. For the LEAR experiment, Chanel [1996] used the off-resonance equation (2.128). Also during the experiment at the heavy-ion synchrotron SIS-18 experiment at GSI, the betatron machine tunes have been sufficiently far apart for decoupled envelope modes [Hofmann, Bar, et al. 1998].

In order to apply this concept to CERN's PS and SPS, we have to take into account the proximity of their working points to the coupling difference resonance (the fourth-order $2Q_x - 2Q_y = n$ Montague resonance). The PS is in fact operated in this regime (presently around $Q_x \approx 6.22$ and $Q_y \approx 6.23$) to maximise the coupling between the two planes by exploiting the space charge coupling in conjunction with powering the skew quadrupoles in order to maximally suppress dangerous head-tail beam instabilities [Métral, Rumolo, et al. 2007]. Also the SPS working point exhibits fractional tunes of $q_x \approx 0.13$ and $q_y \approx 0.18$ (and equal integer tunes). Consequently, we need to employ the general envelope mode formula (2.110).

The model on which these envelope mode formulae are based assumes coasting beams, a uniform transverse KV distribution, smooth ring approximation (i.e. continuous focusing around the machine) and no off-momentum effects such as dispersion and chromaticity. We quantitatively discuss the behaviour of the envelope mode tunes for the SPS and the PS cases in the following paragraphs on the basis of numerical values.

Figures 3.12 and 3.13 illustrate the SPS situation for realistic beam parameters. The transverse normalised r.m.s. emittances amount to $\epsilon_{x,y} = 1.25\,\text{mm mrad}$. In figure 3.12, the constant beam line charge density is equivalent to $N = 1.2 \times 10^{11}$ over a hypothetical total bunch length of $4\sigma_z = 0.92\,\text{m}$, while the vertical betatron tune Q_y is scanned in the vicinity of the fixed horizontal betatron tune $Q_x = 20.13$. The graph 3.12a demonstrates the mode behaviour close to the fully coupled case of the round beam. At tunes above $Q_y > 20.16$ or below $Q_y < 20.10$, the mode frequency essentially approaches the dashed asymptotic off-resonance approximation (2.115). At $Q_x = Q_y = 20.13$ we encounter the fully coupled case, where the mode frequencies coincide with the on-resonance expression (2.117).

Figure 3.12b then depicts the approaching of the full coupling. For betatron tunes $Q_y \ll Q_x$ towards the left side of both plots, the eigenvectors of the envelope oscillation given by expression (2.112) lie in the horizontal and vertical plane as they are completely decoupled. The upper mode (the Q_+ tune in green) oscillates in the horizontal direction and the lower mode (the Q_- tune in blue) in the vertical direction. With respect to this convention, we define the rotation angle of the eigenmodes to approach zero value. The rotation angle's

arctangent scaling with the tune is plotted in turquoise in figure 3.12b. At full coupling the eigenmodes are rotated by 45° and then towards $Q_y \gg Q_x$ the horizontal and vertical plane identification with the two modes exactly swaps with respect to $Q_y \ll Q_x$, correspondingly the angle approaches 90°. The coupling parameter D from expression (2.111) vanishes at $Q_x = Q_y$ for the round beam. At $D = \pm 1$ we are halfway rotated from the full coupling to the decoupled case with a rotation angle of 22.5° resp. 67.5°. Finally, we see that at $|D| > 2$ we approach the asymptotic off-resonance case directly corresponding to the initially mentioned tune regions above $Q_y > 20.16$ and below $Q_y < 20.10$. In this region, it is safe to use the off-resonance approximation (2.115) while below $|D| < 2$ one should use the general expression (2.110). This reasoning applies in general for $|D| \gg 1 \implies$ off-resonance while from the order of D on towards 0 one requires the general expression.

In figure 3.13, we fix the working point at $Q_x = 20.13$ and $Q_y = 20.145$. Then we scan the intensity N with respect to the same $4\sigma_z = 0.92$ m interval as before. In figure 3.13a we start on the left from zero space charge at twice the bare machine tunes. Initially, the tunes are far from coupling as the incoherent space charge tune shift is negligibly small compared to the betatron tune split. Consequently, the modes follow the off-resonance asymptotes plotted in dashed lines of green and blue colour. Towards high intensities, the envelope modes converge towards the symmetric and antisymmetric on-resonance modes plotted in dashed orange lines. At an intensity of around $N = 1.25 \times 10^{11}$, we observe the largest distance of the actual envelope tunes from the intersecting asymptotes. Figure 3.13b demonstrates that the coupling parameter becomes $D = 1$ at this distinctive intensity – this is a general feature of the analytic expressions. We see how D approaches zero value for high intensities while the mode tunes approach the orange on-resonance asymptotes, while on the other side D diverges to infinity when space charge vanishes (i.e. the space charge perveance in the denominator of D in (2.111) becomes zero).

Figures 3.14 and 3.15 show the analogous situation for realistic beam parameters in the PS machine. The constant line charge density in figure 3.14 corresponds to an intensity of $N = 1.6 \times 10^{11}$ for a fixed reference longitudinal interval of $4\sigma_z = 49.4$ m equivalent to a 180 ns total bunch length. The normalised transverse r.m.s. emittances amount to 2.5 mm mrad. The horizontal tune is fixed at $Q_x = 6.22$ while the vertical tune varies around Q_x. For the line density scan (represented by the intensity with regard to the same fixed $4\sigma_z$ reference interval) presented in figure 3.15, we fix the working point at $Q_x = 6.22$ and $Q_y = 6.23$. This time, the distinctive $D = 1$ coupling strength is reached at $N = 0.7 \times 10^{12}$. This broad coupling region around the equal-tune region goes hand in hand with the previously mentioned operational strategy of maximally coupling the beams in the transverse plane to avoid head-tail instabilities.

This analysis of envelope modes is based on uniform KV beams. According to the r.m.s. equivalence principle, we expect the same modes for any elliptically symmetric beam distribution with a monotonically decreasing density at the same r.m.s. beam width. In particular, the discussion applies to the Gaussian-type transverse distributions in the real machine. The
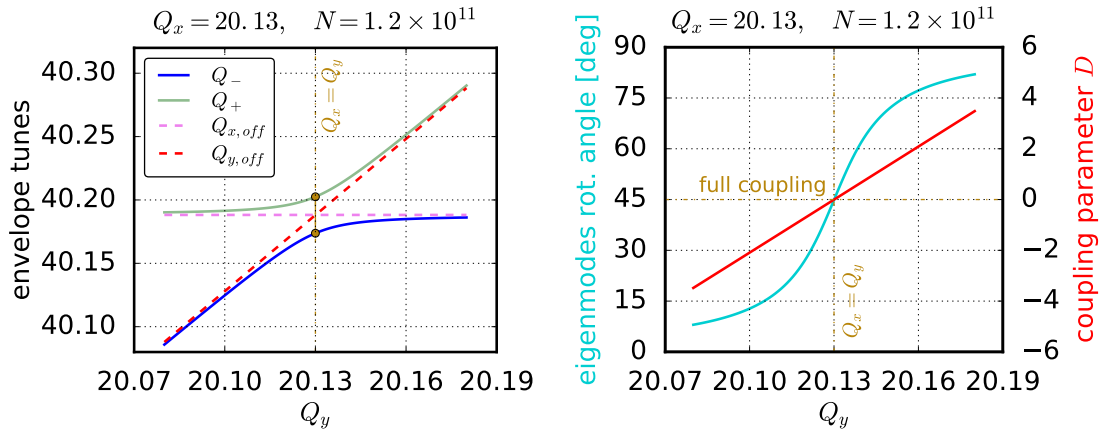
(a) Envelope tunes vs. vertical betatron tune (the dashed asymptotes are the off-resonance expressions while the two golden dots come from the on-resonance expression).

(b) Rotation angle of the mode eigenvector (in turquoise) and coupling parameter (in red) vs. vertical betatron tune.

Figure 3.12 – Envelope modes during a vertical tune scan at fixed $Q_x = 20.13$ for a coasting SPS beam with intensity $N = 1.2 \times 10^{11}$ and normalised transverse emittances $\epsilon_{x,y} = 1.25\,\mathrm{mm\,mrad}$.
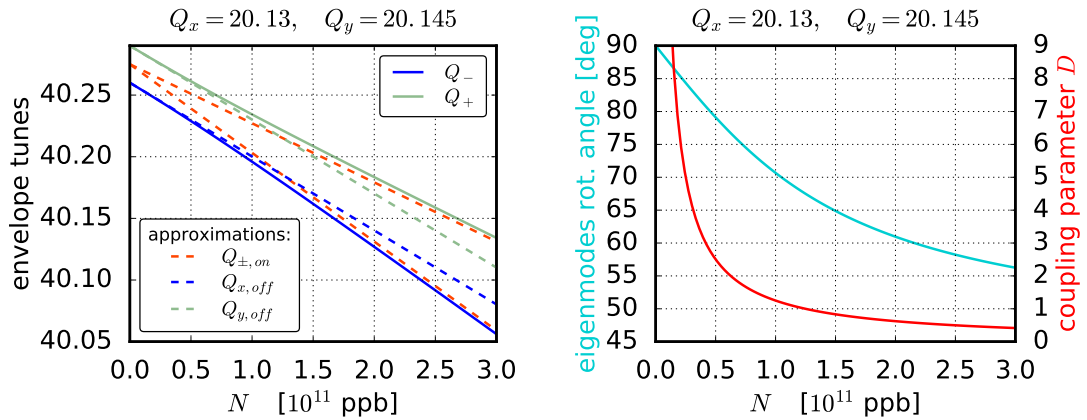
(a) Envelope tunes vs. bunch intensity (the dashed asymptotes are the off- and on-resonance expressions).

(b) Rotation angle of the mode eigenvector (in turquoise) and coupling parameter (in red) vs. bunch intensity.

Figure 3.13 – Envelope modes during an intensity scan at fixed $Q_x = 20.13$ and $Q_y = 20.145$ for a coasting SPS beam with normalised transverse emittances $\epsilon_{x,y} = 1.25\,\mathrm{mm\,mrad}$.
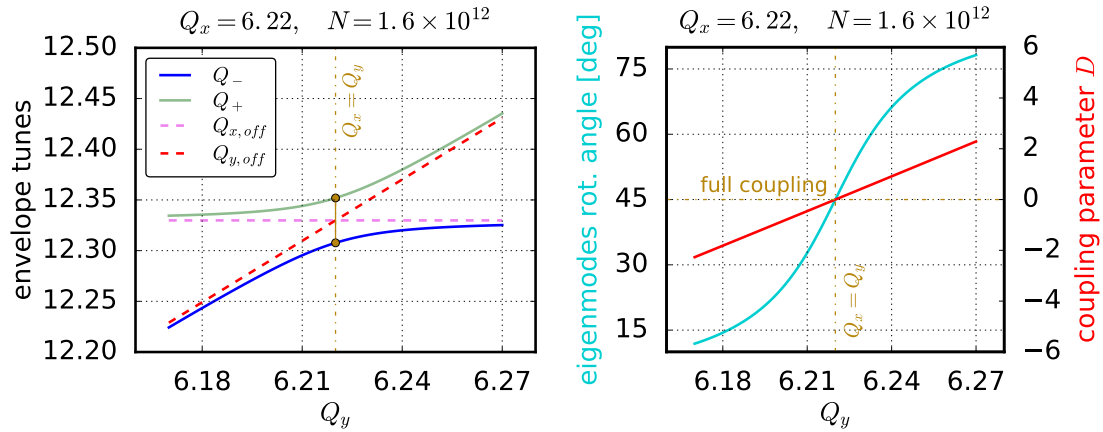
(a) Envelope tunes vs. vertical betatron tune (the dashed asymptotes are the off-resonance expressions while the two golden dots come from the on-resonance expression).

(b) Rotation angle of the mode eigenvector (in turquoise) and coupling parameter (in red) vs. vertical betatron tune.

Figure 3.14 – Envelope modes during a vertical tune scan at fixed $Q_x = 6.22$ for a coasting PS beam with intensity $N = 1.6 \times 10^{12}$ and normalised transverse emittances $\epsilon_{x,y} = 2.5\,\mathrm{mm\,mrad}$.
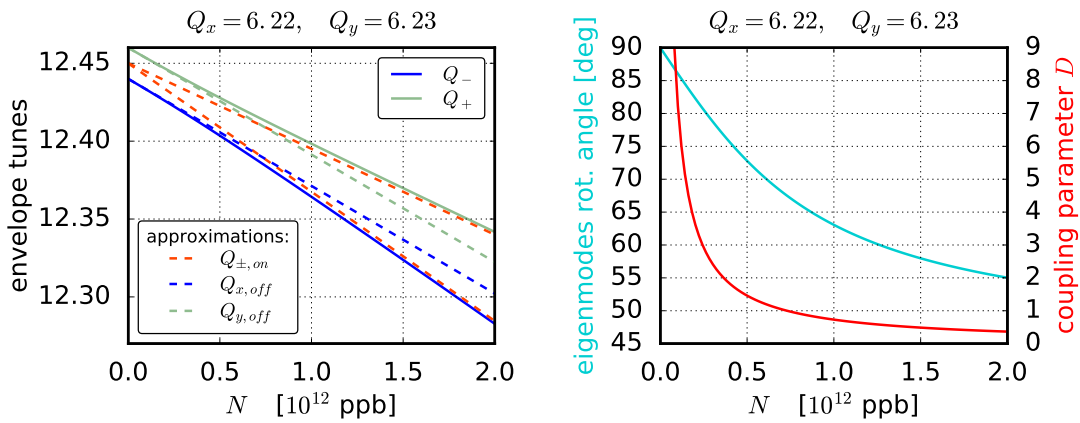
(a) Envelope tunes vs. bunch intensity (the dashed asymptotes are the off- and on-resonance expressions).

(b) Rotation angle of the mode eigenvector (in turquoise) and coupling parameter (in red) vs. bunch intensity.

Figure 3.15 – Envelope modes during an intensity scan at fixed $Q_x = 6.22$ and $Q_y = 6.23$ for a coasting PS beam with normalised transverse emittances $\epsilon_{x,y} = 2.5\,\mathrm{mm\,mrad}$.

quadrupolar coherent modes should therefore be observable in the frequency spectrum of P_{QPU} at the above envelope tunes. The goal is then to extract the KV space charge tune shifts from the two envelope modes via expression (2.125) – or rather, in conjunction with the beam current transformer (BCT) yielding the beam intensity, to extract the transverse beam size ratio (and hence the emittances).

3.5.1 PyHEADTAIL Simulations of Envelope Oscillations

We will now check these relations between the envelope mode tunes $Q_{\pm}$, the (r.m.s. equivalent) KV space charge tune shift ΔQ^{KV}, and the relevant beam parameters (the line charge density $\lambda = N/(4\sigma_z)$ and the normalised transverse emittances $\epsilon_{x,y}$) with the aid of PyHEADTAIL space charge simulations for transverse macro-particle distributions of uniform KV nature and also as a cross-check the r.m.s. equivalent Gaussian distribution. The simulations are set up equivalently to the theoretical assumptions, i.e. switching off synchrotron motion, no non-linear effects in the transverse plane (besides possibly space charge itself) and applying continuous focusing at constant betatron functions $\beta_x = \beta_y \approx 16\,\mathrm{m}$ (with no dispersion) using the corresponding values of the PS machine. We model the machine to be entirely decoupled. In fact, due to the smooth approximation, the beta functions are directly determined by the respective betatron tune via

$$\beta_{x,y} = \frac{R}{Q_{x,y}} \tag{3.47}$$

where $R = 100\,\mathrm{m}$ denotes the effective PS radius. We employ the 2.5D PIC space charge model for one beam slice containing all the macro-particles, which resembles the coasting beam situation from the theory. Consequently, we self-consistently solve the transverse beam fields permitting the evolution of the coherent modes. We use 1×10^6 macro-particles on a fixed transverse $x - y$ grid of 128×128 mesh nodes. The macro-particle distributions are initiated with transverse normalised emittances of $\epsilon_{x,y} = 2.5\,\mathrm{mm}$. The matched beam sizes are then determined from the non-linear matching condition of the envelope equations by finding roots to the coupled quartic functions (2.100a). The initial noise in the macro-particle distributions due to the random number generation process provides enough "mismatch" in order to observe the envelope oscillations in $\sigma_{x,y}$ – no further quadrupolar mismatch is required. The intensities values will again refer to the reference bunch length interval of $4\sigma_z = 49.4\,\mathrm{m}$, i.e. N determines the line charge density λ and hence the space charge perveance K^{SC}. We use a prime number of $n_{\mathrm{segments}} = 211$ kick nodes unevenly distributed around the circumference to avoid numerical artefacts which are equivalent to low-order structure resonances due to "lattice symmetries" from the distribution of space charge interaction points in the continuous focusing of the smoothly approximated ring (cf. e.g. Kesting and Franchetti [2015]).

Figure 3.16 presents the simulation details for a KV macro-particle distribution for the working point $Q_x = 6.22$ and $Q_y = 6.23$ with a "bunch" intensity of $N = 1.2 \times 10^{12}$. The matched transverse beam sizes amount to $2\sigma_x = 8.41\,\mathrm{mm}$ and $2\sigma_y = 8.40\,\mathrm{mm}$, hence the beam is

round (which is expected from quasi-isotropic focusing and equal emittances). At these beam parameters, the KV space charge tune shift gives $\Delta Q^{KV} = 0.022$. Correspondingly, the coupling strength yields $D = 1.84$ indicating a fair distance to the coupling resonance. Figure 3.16a shows the oscillating transverse beam widths (evaluated at each kick node). The relevant part of their spectrum is plotted in figure 3.16b, extracted via a FFT over 256 turns. We see two peaks in each transverse plane, one of which has a much larger amplitude than the other. This corresponds to the asymptotic decoupled case where the Q_- mode oscillates purely along the horizontal direction and the Q_+ mode along the vertical direction. For $|D| \gg 1$, the small peaks would vanish entirely while here they effectively show the small but non-vanishing coupling between the planes.

(a) Envelope oscillations during 256 turns.

(b) Envelope tune spectrum with two evident peaks at the theoretically expected frequencies.
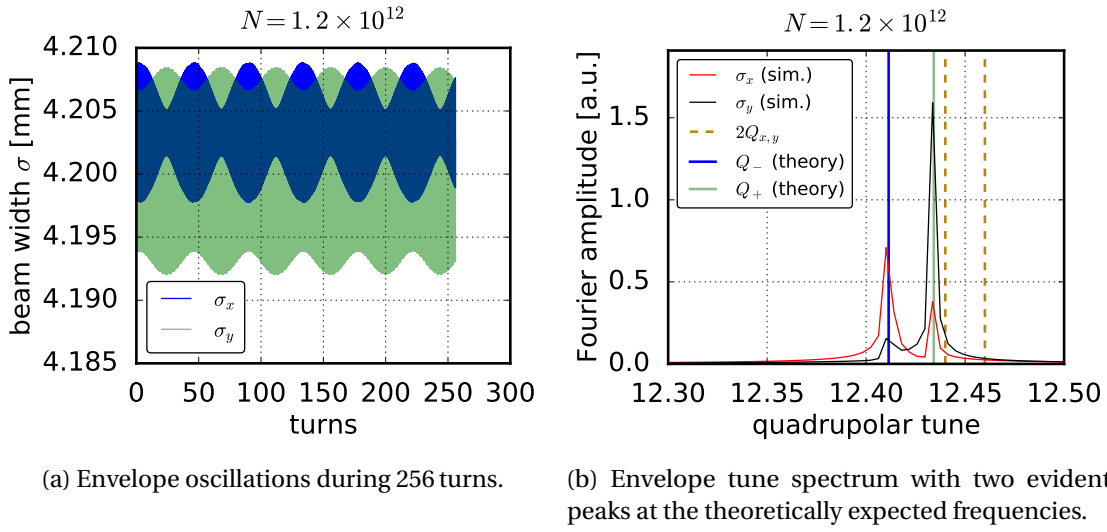
Figure 3.16 – Envelope oscillations for a KV distribution with tune shift $\Delta Q^{KV} = 0.022$ at transverse betatron tunes $Q_x = 6.22$ and $Q_y = 6.23$. With the approximately round beam of $2\sigma_x \approx 2\sigma_y \approx 8.4\,\text{mm}$, the coupling strength amounts to $D = 1.84$.

The same KV distributed macro-particles are presented in figure 3.17 for vanishing coupling at equal betatron tunes $Q_x = Q_y = 6.22$. The completely isotropic focusing with $\beta_x \equiv \beta_y$ entails equal transverse matched beam sizes for the equal emittances (for $Q_y = 6.23$ the matched beam sizes were slightly different). Correspondingly, we observe the envelopes to oscillate about the same equilibrium value $2\sigma_x = 2\sigma_y = 8.41\,\text{mm}$. The FFT spectrum in figure 3.17b shows the two quadrupolar mode peaks of the r.m.s. beam sizes exactly at the theoretically predicted coherent mode tunes $Q_\pm$. Since the transverse planes are fully coupled, the spectra show identical mode amplitudes in both planes. In fact, we observe the symmetric breathing mode Q_+ to dominate over the antisymmetric quadrupole mode Q_-. This can be traced to the initial conditions of the statistical noise of the macro-particle distribution: the envelope oscillations are plotted in figure 3.17c for the initial turn. We see that both σ_x and σ_y oscillate in phase which means the symmetric breathing mode has been launched as an initial condition. As a cross-check we extract the incoherent tunes with a SUSSIX analysis [Bartolini and Schmidt 1998] from the recorded particle motions and we observe all frequencies to be located exactly

at the space charge shifted KV betatron tune.
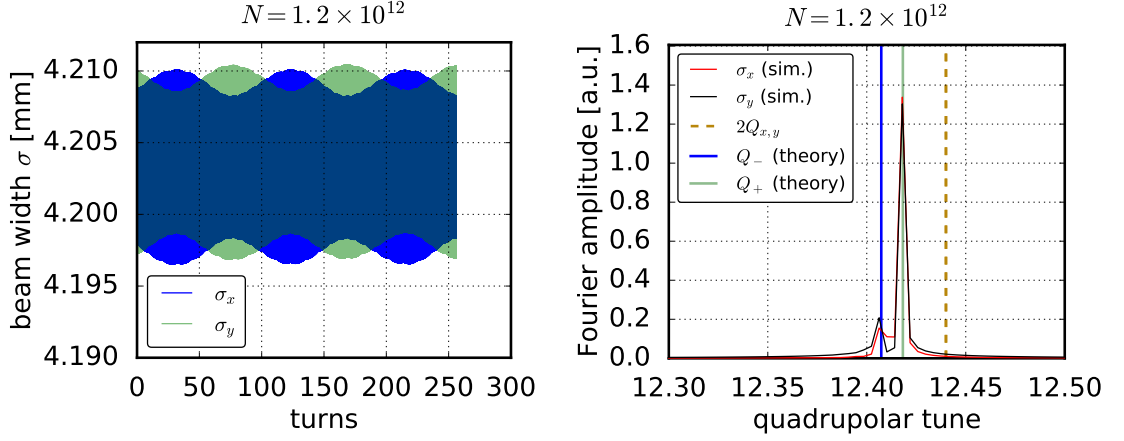
(a) Envelope oscillations during 256 turns.

(b) Envelope tune spectrum with two evident peaks at the theoretically expected frequencies.
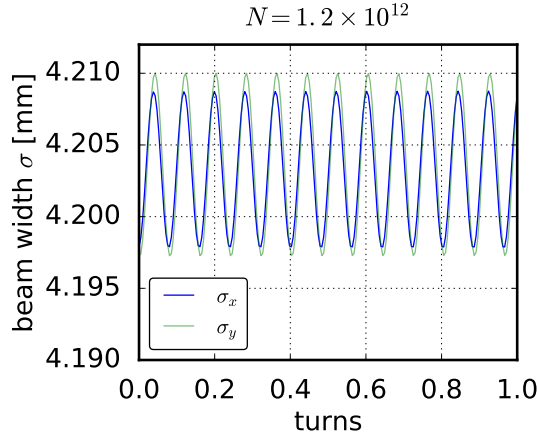
(c) Envelope oscillations during the first turn.

Figure 3.17 – Envelope oscillations for a KV distribution with tune shift $\Delta Q^{\mathrm{KV}} = 0.022$ at transverse betatron tunes $Q_x = Q_y = 6.22$. The round beam of size $2\sigma_x = 2\sigma_y = 8.41\,\mathrm{mm}$ is hence subject to full coupling at $D = 0$.

We have run this initial KV macro-particle distribution with the same random generator seed for various vertical bare machine tunes Q_y between $6.20\ldots6.24$. At $Q_y = 6.22$ we cross the coupling resonance as we have round beams $\epsilon_x = \epsilon_y$ and we keep the horizontal bare tune fixed at $Q_x = 6.22$ (this was precisely the case depicted in figure 3.17). In figure 3.18a we present the two envelope tunes extracted from the spectrum of each of the simulations (by using SUSSIX). The theoretical two envelope modes are calculated using the expression (2.110) with the average of the envelope equilibrium values a, b over the tune scan (these equilibrium values vary a bit due to the vertical betatron function scaling with the vertical tune, $\beta_y = R/Q_y$). The space charge perveances K^{SC} remain constant during the tune scan,

the situation is equivalent to figure 3.14.
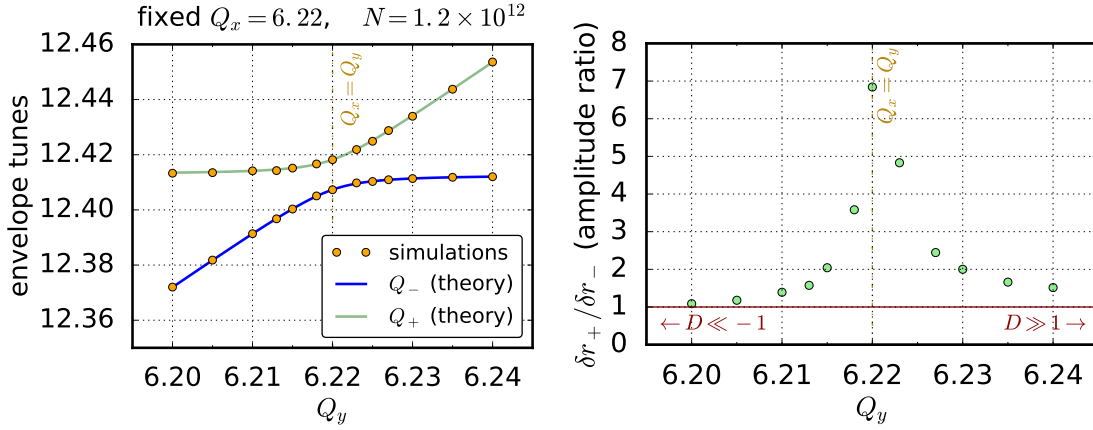
(a) Envelope tunes $Q_\pm$ vs. vertical betatron tune (cf. figure 3.14).

(b) Fourier coefficient ratio of Q_+ over Q_- (i.e. the amplitudes $\delta r_+ / \delta r_-$ of both envelope modes) vs. vertical betatron tune.
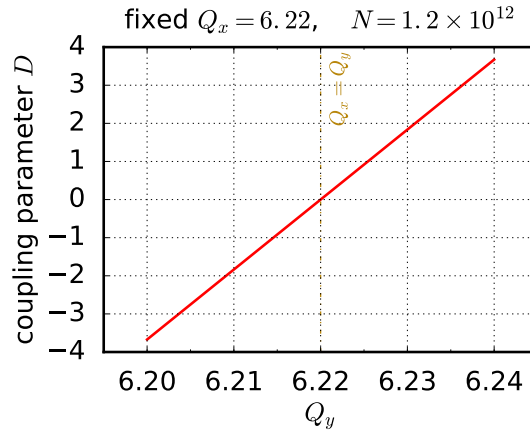
(c) Coupling parameter vs. vertical betatron tune.

Figure 3.18 – Simulation results showing envelope modes during a vertical tune scan at fixed $Q_x = 6.22$ for a coasting PS beam with intensity $N = 1.2 \times 10^{12}$ and normalised transverse emittances $\epsilon_{x,y} = 2.5$ mm mrad.

Next, we show the ratio of the two envelope mode amplitudes in figure 3.18b, which we determined by the respective Fourier coefficients. We had pointed out the peak ratio between the modes Q_+ and Q_- (respectively extracted from the largest peaks in the σ_x, σ_y spectra), for the two separately shown spectra on-resonance (figure 3.17b) and towards off-resonance (figure 3.16b for coupling parameter $D \approx 2$). For $D = 0$, the Q_+ oscillation corresponds to the symmetric in-phase breathing mode whose peak is seven times higher than the anti-symmetric anti-phase quadrupolar mode's peak – equally in both the σ_x and σ_y spectrum. Remind that we start from the same initial macro-particle distribution (with the random generated generalised coordinates and momenta arrays merely scaled to have $a = 2\sigma_{x,\text{random-generator}}$

and $b = 2\sigma_{y,\text{random-generator}}$ solve the matching conditions (2.100a)) for all simulations: consequently, we always have the same initial conditions of the horizontal and vertical excursions $\delta r_x \approx \delta r_y \approx 0.01\,\text{mm}$ (where $\delta r_x = 2\sigma_x|_{\text{turn}=0} - a$ and likewise $\delta r_y = 2\sigma_y|_{\text{turn}=0} - b$). At $D = 0$, the two transverse planes are fully coupled and this initial condition therefore launches the breathing mode. In contrast, $|D| \gg 1$ entails that the horizontal and vertical plane decouple and the envelope modes oscillate along x and y separately. For $r_x = r_y$, we therefore expect equal footing for the $Q_\pm$ peak amplitudes, or in other words, the ratio between the Fourier coefficients is expected to approach unity as in figure 3.18b (towards the red line). In fact, the curve is slightly skew since the initial conditions are not exactly symmetric (r_x and r_y actually differ on the order of 10% and the initial derivatives of $\sigma_{x,y}$ are not exactly vanishing, cf. figure 3.17c). Figure 3.18c shows the coupling parameter D for the various simulations scanning the vertical betatron tune Q_y.

Finally, we compare to a more realistic transverse Gaussian distribution. The results for an off-resonance case are illustrated in figure 3.19 for $Q_x = 6.22$ and $Q_y = 6.23$. The beam exhibits half the space charge perveance as the discussed KV case before since we have set $N = 0.6 \times 10^{12}$. Correspondingly, the Gaussian tune spread should theoretically amount to $\Delta Q^{\text{SC,spread}} = 0.022$ while the r.m.s. equivalent KV tune shift yields $\Delta Q^{\text{KV}} = \Delta Q^{\text{SC,spread}}/2 = 0.011$ according to the halved space charge perveance. Since the electric field of the Gaussian normal macro-particle distribution leads to non-linear space charge forces, we can now observe fluctuating amplitudes of the envelope oscillations in figure 3.19a. The FFT spectrum in figure 3.19b is not as clean as in the KV case any more (during the analysed 512 turns). Still, the two quadrupolar mode peaks are identifiable and they are located exactly at the frequencies of the r.m.s. equivalent KV distribution, as expected from theory in accordance with the r.m.s. equivalence principle. From figure 3.19e we see that the incoherent tune spread of the particles indeed reaches to the theoretically calculated $\Delta Q^{\text{SC,spread}}$. We have indicated the r.m.s. equivalent KV tune shift as a turquoise star, which features the *same* coherent space charge depressed modes as this Gaussian beam. As a last cross-check of our PIC space charge model, we have a look at the beam centroid motion which comes from an initial offset due to the noise originating from the randomly generated macro-particle distribution. The first two turns are plotted in figure 3.19f. We note that the beam centroid motion remains unaffected by all the direct space charge dynamics as expected. The first moment of the beam distribution (i.e. the mean value) averages out the beam self-fields. Consequently, the dipolar coherent beam motion does not feel the non-linear electric field of the Gaussian distribution and is subject only to the linear continuous focusing. Its amplitude and frequency (being equal to the betatron tunes) remain constant corresponding to perfect harmonic oscillatory motion. (In reality, the dipolar coherent motion would be affected by indirect space charge effects from the induced currents in the vacuum tube walls. We have not taken this effect into account in our model here.)

These simulations set the grounds for the experimental observation of the envelope modes with a QPU in the PS (and in the SPS if a corresponding QPU arrangement can be set up which is currently under preparation). Further simulations may be extended to include synchrotron
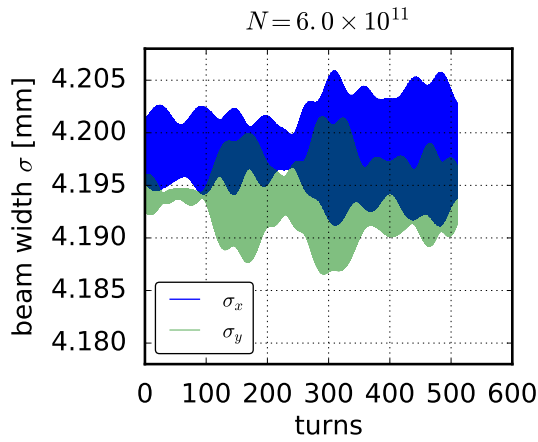
(a) Envelope oscillations during 512 turns.
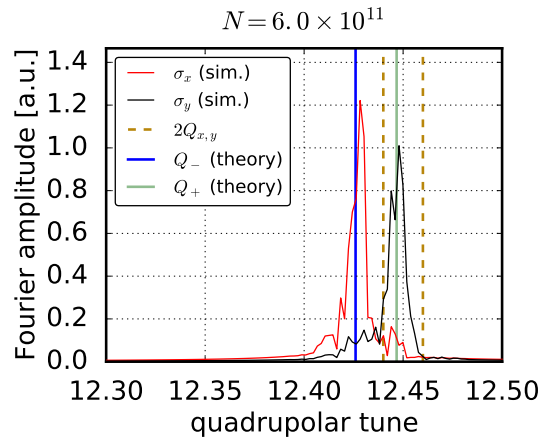
(b) Envelope tune spectrum with two peaks at the theoretically expected frequencies.
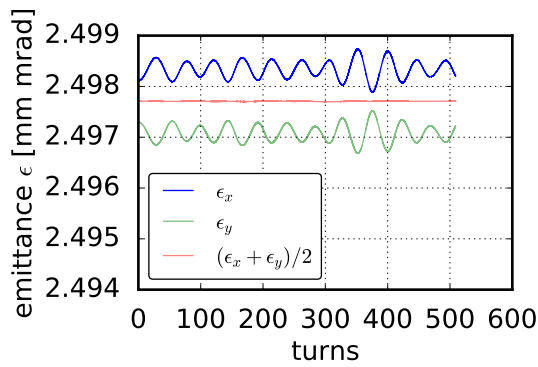
(c) Small emittance fluctuations between the planes.
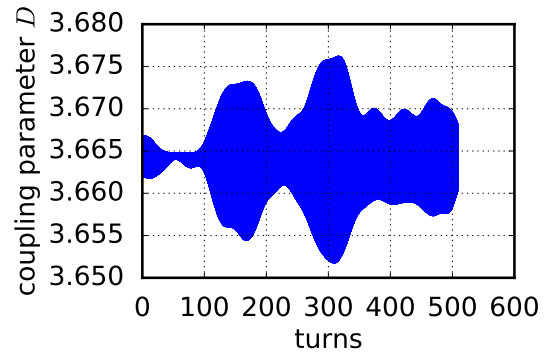
(d) The coupling strength oscillates around $D = 3.66$ with the oscillation of the beam sizes.
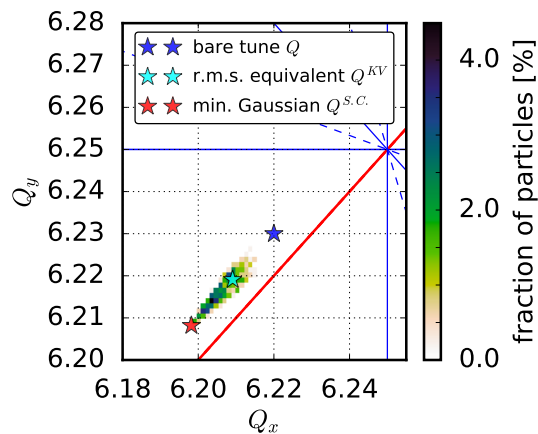
(e) Incoherent tune footprint of the Gaussian distribution.
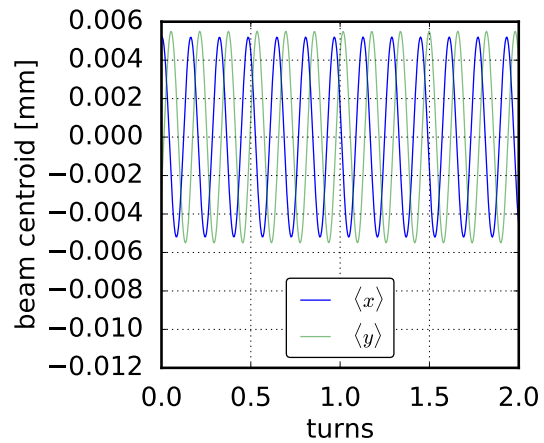
(f) Dipolar beam centroid motion during the first two turns.

Figure 3.19 – Envelope oscillations for a Gaussian distribution with r.m.s. equivalent KV tune shift $\Delta Q^{\mathrm{KV}} = 0.011$ at transverse betatron tunes $Q_x = 6.22$ and $Q_y = 6.23$. With the approximately round beam of $2\sigma_x \approx 2\sigma_y \approx 8.4\,\mathrm{mm}$, the coupling strength amounts to $D = 3.66$.

motion and off-momentum effects to study these influences within a scenario closer to the real machine situation. A similar numerical experiment set-up determining the space charge depressed quadrupolar mode tunes has been used by R. A. Baartman, D'yachkov, and F. W. Jones [1999] in order to validate their simulation space charge model.

4 Measurements: SPS Studies

The SPS is the last accelerator in the LHC injector chain. In the nominal LHC beam scenario with 25 ns spacing between subsequent bunches, the SPS receives four injections from the upstream PS. Each of these injected batches consists of 72 bunches such that the SPS accumulates a train of 288 bunches before the beam is accelerated and finally extracted into the downstream LHC.

The PS requires three basic periods of 1.2 s each to prepare these 72 bunches. Consequently, the total SPS injection plateau needs to cover 9 basic periods, i.e. $3 \times 3 \times 1.2 \, s = 10.8 \, s$ before acceleration, as figure 4.1 depicts. During this time, the already injected bunches can suffer from various collective effects.
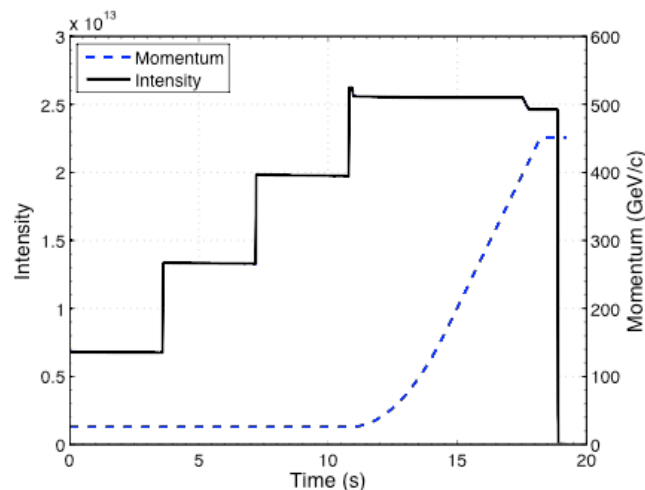
Figure 4.1 – The SPS cycle for LHC-type 25 ns beams [Bartosik 2013].

The nominal SPS optics operates at the working point $(Q_x, Q_y) = (26.13, 26.18)$, often referred to as the "Q26 optics". Studies with high-intensity LHC single bunches revealed severe performance limitations owing to transverse mode coupling instabilities [Salvant 2010]. An improved version of the SPS optics has been established to overcome this intensity limitation,

the "low transition energy optics" or simply the "Q20 optics" [Bartosik 2013]. A major change of this improved optics model are the lower integer tunes with the operational working point becoming $(Q_x, Q_y) = (20.13, 20.18)$. Being the default operational configuration since 2012 [Papaphilippou et al. 2013], the Q20 optics is the starting point for further studies aiming to improve the performance of high brightness LHC beams for future operation. Presently, the SPS provides the LHC with 25 ns beams at an intensity of $N \approx 1.2 \times 10^{11}$ p/b and transverse normalised emittances of $\epsilon_{x,y} \approx 2.6$ mm mrad.

In view of the HL-LHC project, the beam intensity at SPS extraction shall be increased by almost a factor two to $N = 2.3 \times 10^{11}$ p/b while slightly smaller normalised transverse emittances of $\epsilon_{x,y} = 2.1$ mm mrad are required [Arduini et al. 2014]. To reach these parameters, the LIU project assigns to the SPS an emittance growth budget of 10% along with a beam loss budget of 10% (RLIUP report by Bartosik, Argyropoulos, et al. [2014]), cf. table 1.1.

The increase in intensity causes space charge to become a possible threat. Considering an r.m.s. bunch length of $\sigma_t = 0.75$ ns and an r.m.s. momentum deviation of $\sigma_\delta = 1.5 \times 10^{-3}$, the Gaussian direct space charge tune spreads of the future high brightness beams amount to $\Delta Q_{x,y}^{\mathrm{SC}} = (-0.11, -0.2)$ according to expression (2.87). This estimation assumes the same production scheme in the PS as in present operation to obtain the same longitudinal parameters as today at SPS injection. The fractional tunes of the working point $(Q_x, Q_y) = (20.13, 20.18)$ are quite low and are observed to result in a strong impact of the integer resonance, which can lead to emittance growth as the bunch centre becomes resonantly excited by magnetic field errors.

In order to focus on how space charge affects the high brightness beams during the long injection plateau, the influence from other multi-bunch collective effects such as electron cloud interaction needs to be suppressed during a dedicated study. This can be achieved by studying single bunch beams. A first investigation of the working point environment around the Q20 tunes [ibid.] led to the conclusion that beams with a Gaussian tune spread of up to $|\Delta Q_y^{\mathrm{SC}}| = 0.21$ can be accepted by the SPS by optimising the working point. The study considered working points below the regular vertical fourth-order resonance $4Q_y = 81$.

Following the preliminary exploration, a systematic tune scan covering a large area of the tune diagram around the present operational working point has been carried out in the course of this thesis. The goal is to identify the optimal SPS working point region in terms of space charge given the constraints of the HL-LHC beam parameters while using the Q20 optics configuration. The transverse emittance growth and the beam losses are measured for each working point repeatedly for many shots. In a second step, a possible working point candidate is chosen from the optimal region and investigated under varying space charge conditions. The aim is to understand the beam behaviour for different intensities and transverse emittances when fixing either the brightness or the emittances while varying the other. The results of this extended study have been published [Bartosik, Oeftiger, Schmidt, et al. 2016].

Finally, we examine the interaction with a purposely excited resonance both from an exper-

imental and simulation perspective. The fourth-order $4Q_x = 81$ resonance is driven with a single octupole magnet that is strongly powered. Comparing the behaviour between low and high intensity beams when moving the horizontal tune across the resonance quantitatively unfolds the involved space charge dynamics. This scenario then allows for benchmarking with the simulation space charge models.

Throughout this chapter, the indicated transverse tunes (Q_x, Q_y) refer to the coherent dipolar tunes measured with the base-band tune measurement system (the BBQ). In the experiments, we adjusted the quadrupole magnets until the BBQ FFT spectrum displayed the coherent tunes as indicated. Zannini [2013] established an extensive impedance model for the SPS. In fact, the SPS impedance gives rise to a considerable intensity dependent coherent detuning in the vertical plane as figure 4.2 illustrates. The horizontal plane on the other hand remains unaffected [ibid., figure 4.8]. The impedance model relates the coherent dipolar tunes given throughout this chapter to the bare machine working point. At $N = 2 \times 10^{11}$, for example, the bare vertical machine tune lies about 0.03 above the measured coherent tune.
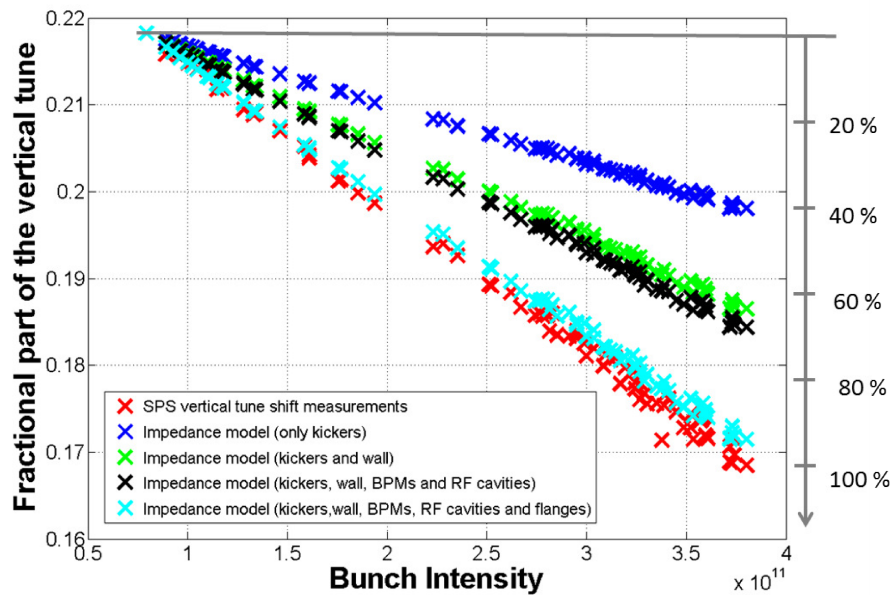
Figure 4.2 – Vertical coherent dipolar tune shift vs. bunch intensity with a measurement uncertainty of $\mathcal{O}(10^{-4})$ (Bartosik, Iadarola, et al. [2014, figure 1], cf. also Zannini [2013, figure 4.6]).

4.1   Tune Diagram for High-Brightness Beams

For the systematic tune scan, we use a dedicated machine development (MD) SPS cycle and measure the beam conditions at the beginning of the injection plateau (labelled 'in') and again 3 s later (labelled 'out'). This time span corresponds to about 130 000 turns. The relevant experiment parameters have been listed in table 4.1. The transverse tunes are adjusted before

the beam is injected and remain constant for each shot. The bunches prepared by the PS have smaller transverse emittances than required for the HL-LHC project but the intensity is also slightly lower. Correspondingly, the reached Gaussian space charge tune spread of $\Delta Q_{x,y}^{\text{SC}} = (-0.10, -0.18)$ is close to the situation for future beams. Hence, the experiment conditions are expected to give good predictions in terms of the space charge behaviour for the HL-LHC beams.

The bunch length has been extracted from the wall current monitor measurement after filamentation (i.e. when the quadrupolar injection oscillations have ceased). The r.m.s. momentum deviation σ_δ has been calculated from the RF parameters and the measured r.m.s. bunch length σ_t by assuming Hamiltonian equivalence in expression (2.50), i.e. assuming a longitudinally matched beam while neglecting intensity effects.

Table 4.1 – Experiment parameters in the SPS for the systematic tune scan.

parameter name	symbol	value
PS extracted intensity	N	$(2.0 \pm 0.1) \times 10^{11}\,\text{p/b}$
PS extracted horizontal normalised emittance	ϵ_x	$0.84\,\text{mm mrad} \pm 10\%$
PS extracted vertical normalised emittance	ϵ_y	$1.1\,\text{mm mrad} \pm 10\%$
r.m.s. bunch length	σ_t	$(0.836 \pm 0.008)\,\text{ns}$
r.m.s. momentum deviation	σ_δ	$(1.76 \pm 0.02) \times 10^{-3}$
total energy	E_{tot}	$26\,\text{GeV}$
measured chromaticity	(Q_x', Q_y')	$(7.5, 3.5)$
scanned horizontal tunes	Q_x	$20.12\ldots20.30$
scanned vertical tunes	Q_y	$20.16\ldots20.44$
Gaussian space charge tune spread	$\Delta Q_{x,y}^{\text{SC}}$	$(-0.10, -0.18)$
r.m.s. equivalent KV tune shift	$\Delta Q_{x,y}^{\text{KV}}$	$(-0.05, -0.09)$
RF voltage fundamental	V_{RF}	$4.5\,\text{kV}$
synchrotron period	Q_S^{-1}	$66\,\text{turns}$
fundamental harmonic	h	4620
SPS circumference	C	$2\pi \cdot 1100\,\text{m}$
transition energy	γ_{tr}	18.02

The linear wire scanners `BWS.51731.H_LIN` and `BWS.52171.V_LIN` are used to record the horizontal and vertical beam profiles, respectively. Due to hardware limitations, only one wire scanner can be used at a time. Therefore we are forced to measure each transverse plane separately over several shots and evaluate each working point statistically. We chose to repeat each plane measurement five times and hence record ten shots per working point.

Figure 4.3 illustrates the measurements and evaluations made for each working point. The beam intensity N is recorded along the cycle with the beam current transformer (BCT): the

plot in the top left shows the variation in N over the ten shots. The beam loss is determined by averaging the BCT curve within the shaded green regions resulting in N_{in} (between 100 ms and 200 ms) and N_{out} (between 3000 ms and 3100 ms). We hence evaluate

$$\text{beam loss} \doteq \frac{N_{in} - N_{out}}{N_{in}} \quad . \tag{4.1}$$

The loss plot in the lower left indicates a linear dependency with intensity. The overall beam loss of a working point is evaluated by extrapolating the ten beam loss measurements to a reference intensity of $N_{ref} = 2 \times 10^{11}$, which is indicated by the green lines.
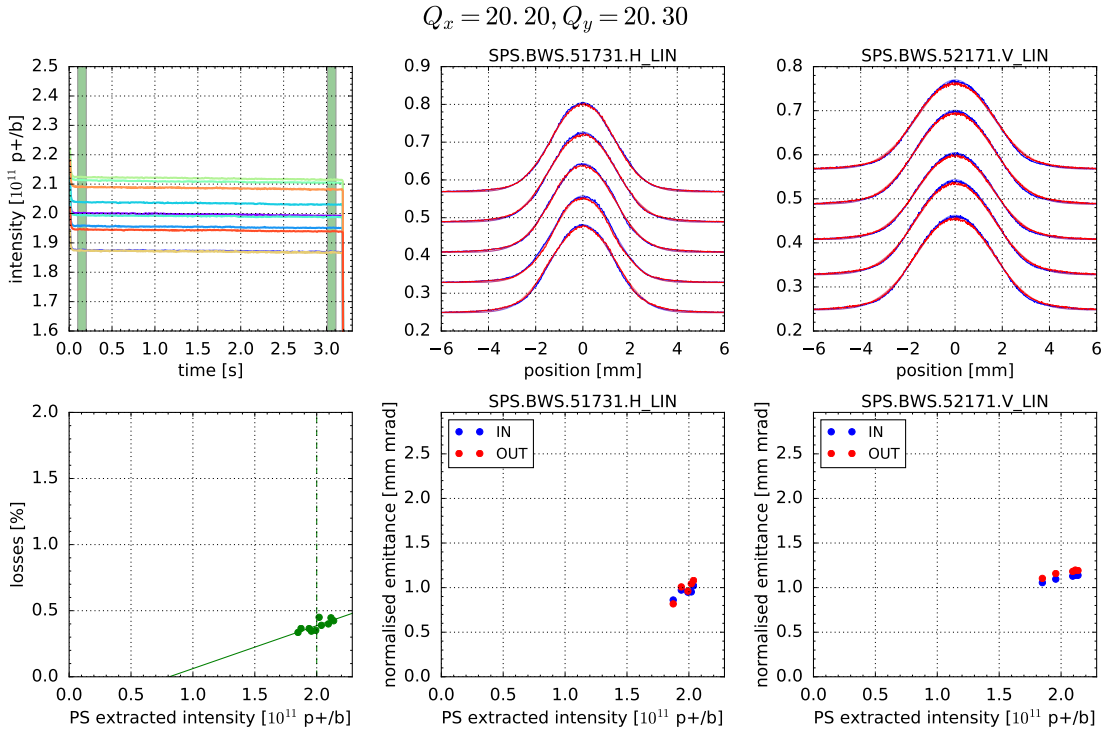
Figure 4.3 – Example evaluation for the coherent dipolar tunes $Q_x = 20.20$, $Q_y = 20.30$: measured intensity from BCT curves and extracted normalised emittances from wire scanner profiles.

The horizontal and vertical beam profiles at the 'in' and 'out' references are plotted in the top centre and top right graph, respectively, along with their Gaussian fits: blue represents the 'in' and red the 'out' profiles. The transverse emittances are extracted from each beam profile by assuming Gaussian distributed beams. The residuals of the Gaussian fits to almost all profiles are sufficiently small to justify the Gaussian distribution assumption. In the horizontal plane, equation (2.35) is employed to determine the emittance taking into account the dispersion of about $D_x \approx -0.5$ m at the location of BWS.51731.H_LIN. Since we vary the transverse tunes, the betatron and dispersion functions change slightly for a fixed location such as the wire scanners. Comparing the measured horizontal emittance in the PS and the SPS for the same beam reveals a clear tune dependency. Therefore, the SPS MAD-X optics model has been evaluated for

each of the scanned tunes to determine the correct dispersion function at `BWS.51731.H_LIN` [Bartosik, Oeftiger, Schmidt, et al. 2016]. After this correction, the measured horizontal emittances did match between PS extraction and SPS injection. The emittance blow-up has been defined as the emittance growth between 'in' and 'out' measurements,

$$\text{emittance blow-up} \doteq \frac{\epsilon_{\text{out}} - \epsilon_{\text{in}}}{\epsilon_{\text{in}}} \quad . \tag{4.2}$$

The overall transverse normalised emittances (and blow-up) for each working point have then been determined by averaging the respective five measurements.

Figure 4.4 summarises the beam loss and emittance blow-up for the tested tune diagram region. The black cross markers indicate the measured points. The tune diagram also contains the resonance lines up to fourth order, where the solid lines indicate regular and the dashed lines skew resonances. We observe that the relative beam losses and the transverse emittance blow-up complement each other in certain regions. The regions in blue are preferred while red indicates a critical region.

We identify two regions with enhanced losses:

$(20.25, 20.25)$: up to 5% losses within the 3 s would linearly scale to 18% losses for the whole injection plateau. This can be traced to the concurrence of several coherent resonance conditions, mainly the two octupole resonances $4Q_x = 81$ and $4Q_y = 81$ as well as the Montague coupling resonance $2Q_x - 2Q_y = 0$.

$(20.33, 20.33)$: we have not extended our measurements beyond $Q_x = 20.30$ but the measurements in the vicinity of this working point already indicate the overlapping sextupole resonances. We observe up to 7% beam loss.

Remarkably, the horizontal quarter-integer resonance $4Q_x = 81$ prints a clear trace over the whole scanned region in contrast to the absence of the vertical counterpart. Note that we have not measured directly on top of the respective resonant tunes. The third-order resonance $Q_x + 2Q_y = 61$ also appears through the loss pattern along the resonant tunes, the more other resonances overlap with it the stronger.

On the other hand, losses of less than 1% are obtained in the remaining part of the tested area in the tune diagram. The BCT curves show linearly decreasing intensities. This allows to extrapolate to the 10.8 s injection plateau for the LHC-type cycles, for which these losses would remain within 4%.

The transverse emittance blow-up shows a negative value around the lossy region $(20.25, 20.25)$ where the beam profiles are decimated due to the strong loss. As soon as the tunes approach the integer resonances in each transverse plane we observe blow-up. This is indeed separately the case for each respective plane, the blow-up shows up vertically only when approaching $Q_y = 20$ and likewise in the horizontal case when approaching $Q_x = 20$. In general, the transverse emittance also grows when having passed the fourth-order $4Q_x = 81$ resonance
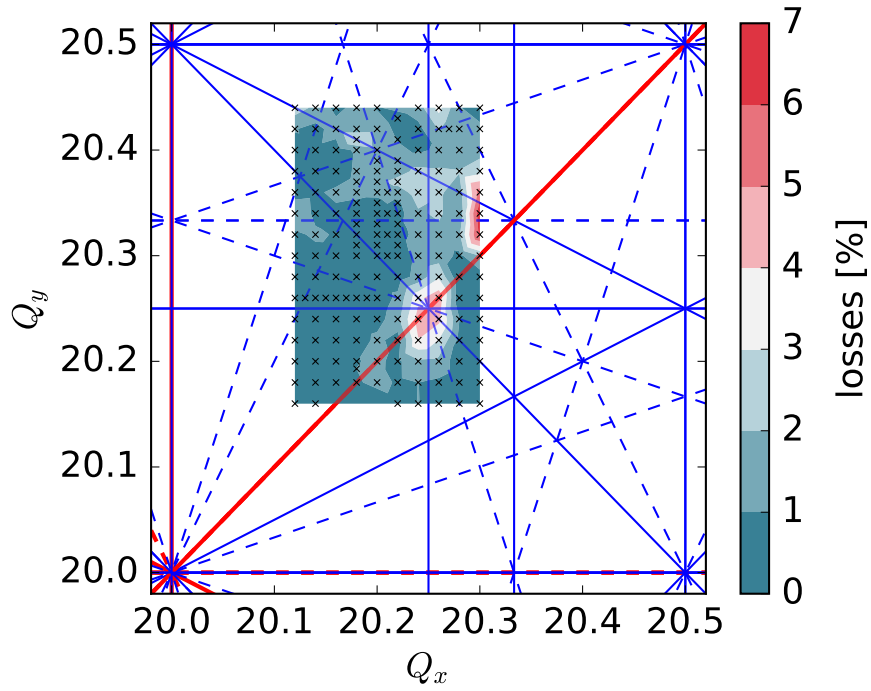
(a) Relative beam losses
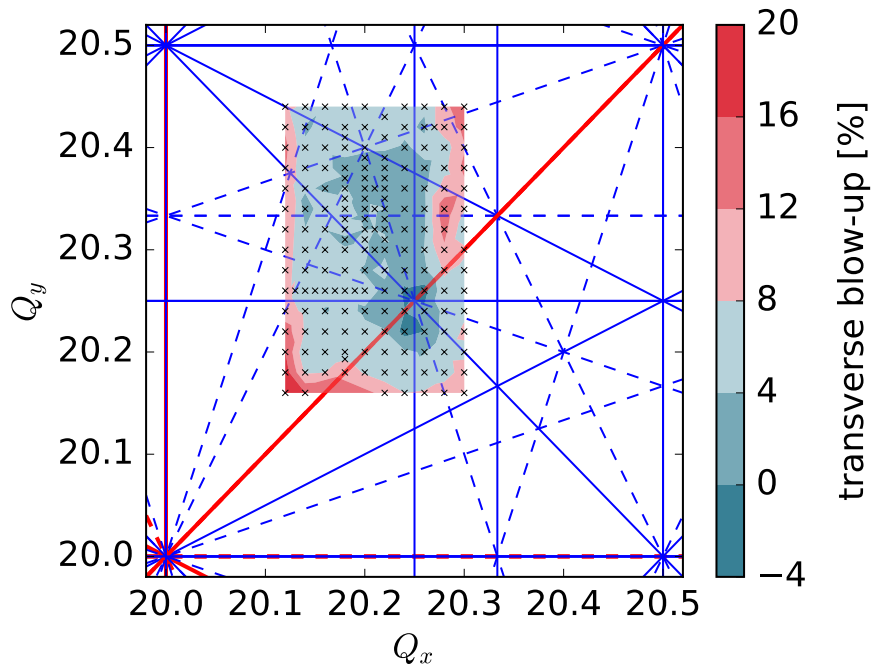
(b) Transverse emittance blow-up

Figure 4.4 – Tune diagrams with the scanned region and resonance lines up to 4$^{\text{th}}$ order.

and moving towards the regular third-order $3Q_x = 61$ resonance. This feature will be analysed in more detail in section 4.3 when purposely exciting the fourth-order resonance.

Overall, the transverse emittance blow-up is quite small given that a good part of it might come from the wire scanner as the wire traverses the beam. This contribution is foreseen to be analysed in future studies.

In summary, taking into account both the loss and the emittance blow-up perspective, the region around the coherent dipolar tunes $(20.22, 20.30)$ looks most interesting. Beam loss remains below 1% and the transverse emittance blow-up is bounded by 4%. Figure 4.5 shows the resulting beam brightness, which is defined by

$$\text{brightness} \doteq \frac{N}{(\epsilon_x + \epsilon_y)/2} \quad . \tag{4.3}$$

This definition of the beam brightness is motivated by its proportionality to the incoherent tune shift (cf. e.g. the maximum Gaussian tune spread extent (2.87)) as a measure of space charge strength.
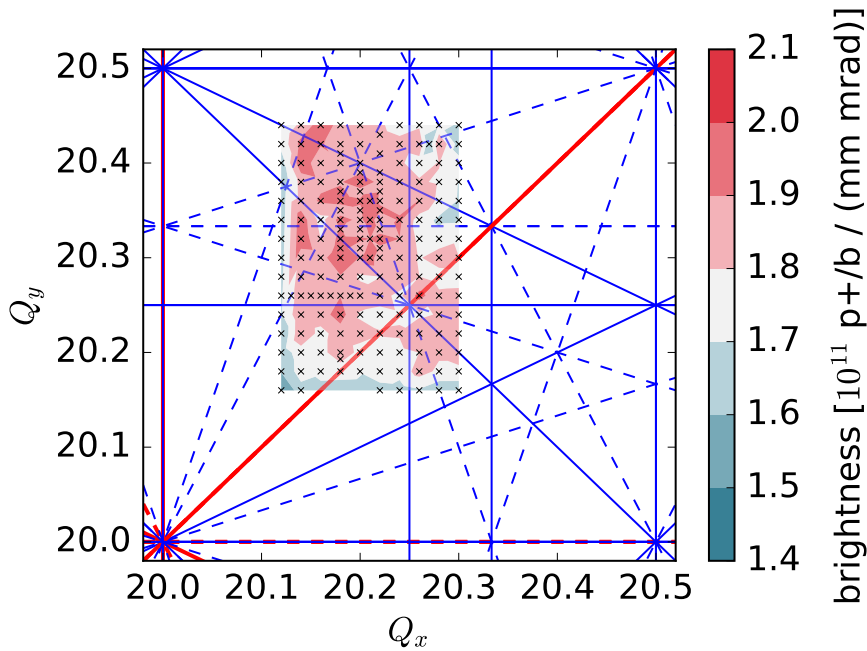
Figure 4.5 – Tune diagram with the brightness shown for the scanned region and resonance lines up to 4${}^{\text{th}}$ order.

4.2   Beam Loss Analysis for Optimal Working Point Region

We have identified an optimal tune region in the lower left quadrant for integer tunes of 20 using beams with a fixed intensity and transverse emittances. In the following two experiments, we explore how the beam losses depend on the transverse beam size and on the space charge strength. In each experiment, we keep one of the two parameters fixed while varying the other in order to isolate the nature and reason of the beam losses.

4.2.1   Constant Brightness

In order to analyse the beam loss behaviour for a range of emittances, we operate at the coherent tunes $(Q_x, Q_y) = (20.22, 20.31)$ (at $N = 2 \times 10^{11}$) and try to keep the brightness and therefore the space charge tune spread constant by varying N and $\epsilon_{x,y}$ by the same amounts. The space charge dynamics should hence remain unchanged as we scan the transverse beam size. Consequently the variation of beam losses is expected to solely come from the varying transverse beam size. As we scan the betatron beam sizes over a factor 2, we reach transverse emittances of 2.5 mm mrad. The corresponding beam brightness during our experiment amounts to half the brightness achieved during the large tune scan in the previous section.

The PS Booster provides the SPS with beams through the PS. The characteristics of the arriving beams in the SPS are already largely determined at the PS Booster. To be precise, the intensity of the resulting single bunch beams is given by two influences: firstly, the amount of turns injected from the LINAC2 during the multi-turn injection into the PS Booster, and secondly, the longitudinal acceptance bottle neck in conjunction with controlled longitudinal blow-up. In contrast to the latter, the former also influences the transverse emittances as the transverse beam size directly depends on the corresponding LINAC2 pulse length. For multi-bunch beams, this has been studied in detail under the conclusion that the PS Booster extracted $\epsilon_{x,y}$ depend linearly on the number of injected turns [Rumolo, Bartosik, et al. 2014, figure 1].

We make use of this mechanism and scan the SPS transverse emittances by varying the number of injected turns. Figure 4.6a shows the obtained horizontal and vertical normalised emittances versus the intensity for our single-bunch beam. The empirical quadratic fits show a slight non-linear behaviour in the inclination of the emittance curves. The brightness has been determined from the inverse slope of the transverse emittance fit and is plotted in figure 4.6b. As we can see, the brightness remains shortly below 1×10^{17} p/b/(mrad). The curve exhibits a drop at low intensities where figure 4.6a reveals much less inclination of the emittance curve. In fact, we inject less than one turn from the LINAC2 beam for these low intensities – hence the transverse normalised emittances of the LINAC2 beam itself define a lower boundary of $\epsilon_{in} \gtrsim 0.5$ mm mrad. The brightness curve also shows a descent at the high intensity end tracing back to a non-linear emittance blow-up.

Finally, the loss pattern as the main result is presented in figure 4.6c. For this plot, the intensity curves of each shot have been fit linearly to extract the relative beam loss. The transverse

emittance figures for each shot on the abscissa have been computed via the emittance fits from figure 4.6a with the corresponding 1σ confidence values. Above $\epsilon_{in} > 0.75\,\mathrm{mm\,mrad}$, the relative beam loss increases linearly with the initial transverse emittance, i.e. the beam size, at a slope of $(2.26 \pm 0.15)\,\%/(\mathrm{mm\,mrad})$. Extrapolating the linear fit, we would find vanishing beam loss around $\epsilon_{in} = (0.37 \pm 0.12)\,\mathrm{mm\,mrad}$.

For comparison: the conditions of the large tune scan experiment from the previous section provided beams of $\epsilon_{x,y} \approx 1\,\mathrm{mm\,mrad}$ (cf. the detailed measurements for $(Q_x, Q_y) = (20.20, 20.30)$ in figure 4.3). The losses we measured here thus confirm the value of 1% from the previous experiment.

A striking feature of the loss pattern is the observed strong beam loss below an initial normalised transverse emittance of $\epsilon_{in} < 0.75\,\mathrm{mm\,mrad}$. As pointed out at the outset of this chapter, the coherent vertical tune shift due to the beam-coupling impedance in the SPS results in a linearly decreasing coherent Q_y as the intensity N increases [Bartosik, Iadarola, et al. 2014]. Since we did not adjust the programmed bare vertical machine tune during the intensity scan (which is the usual procedure for default machine operation), the coherent tune indeed varies as the base-band tune measurements in figure 4.6d illustrate. Here, the coherent centroid motion (measured without additionally exciting the beam) has been Fourier transformed to obtain the coherent tune. The extrapolated machine tune at $N = 0$ lies around $Q_y \approx 20.345$. In the various plots of figure 4.6, the shaded orange region indicates where the losses start. Interestingly, this coincides with where the coherent vertical tune crosses the third-order $3Q_y = 61$ resonance at $N = 0.65 \times 10^{11}$ corresponding to the emittance of $\epsilon_{in} = 0.75\,\mathrm{mm\,mrad}$.

At the same time, the Gaussian space charge tune spread in figure 4.6f drops considerably within the orange region due to the lower achieved brightness. The values of ΔQ^{SC} have been computed from the empirical quadratic emittance fits and the r.m.s. bunch lengths in figure 4.6e. The latter have been determined by fitting the rising flanks of the longitudinal profiles after the longitudinal quadrupolar injection oscillations have damped. We only fit the rising flanks of the profile because the longitudinal bunch shape signal becomes asymmetric due to the transfer function of the signal chain.

The 1σ confidence bands in figure 4.6f take into account statistic uncertainties in σ_z and σ_δ. Due to the lower space charge tune spread at low intensities, the halo particles at large transverse amplitudes (which experience the lowest incoherent tune shift) oscillate much closer to the bare machine tune compared to the same transverse amplitudes at high intensities. Considering only direct space charge, the incoherent resonance condition of the $3Q_y = 61$ resonance (at these large transverse amplitudes) is hence satisfied for a larger part of the beam at low intensities than at high intensities. This may account for the observed strong beam loss.

Future work to clarify the influence of the coherent dipolar tune might include an experiment with varying vertical machine tunes such that the $3Q_y = 61$ resonance is crossed at different beam intensities. Comparing the resulting loss pattern between two beam variants with once

(a) Transverse emittance vs. intensity

(b) Brightness (from emittance fits) vs. intensity

(c) Relative beam losses vs. transverse emittance

(d) Coherent vertical tune vs. intensity

(e) R.m.s. bunch length vs. intensity

(f) Gaussian space charge tune spread vs. intensity
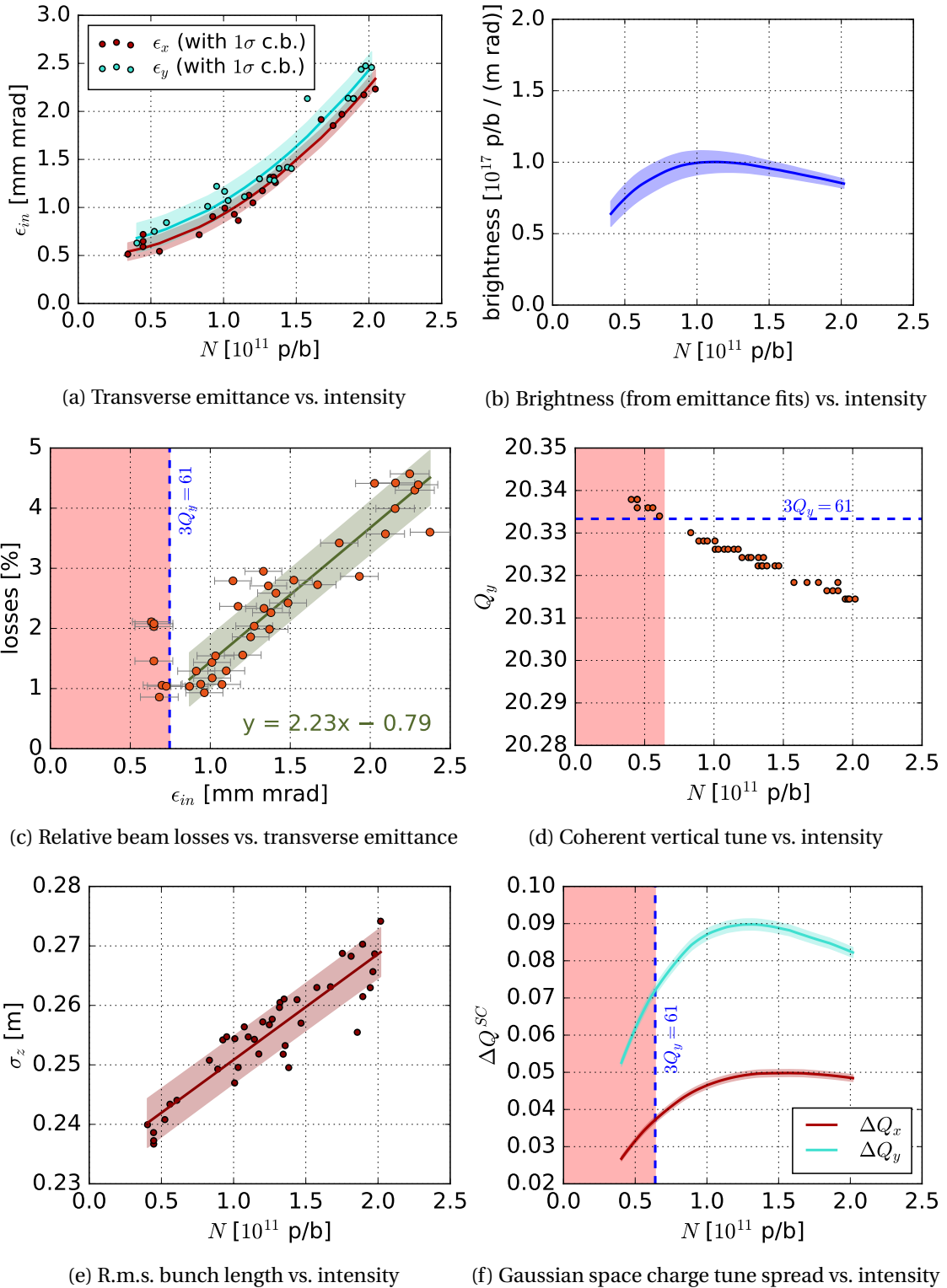
Figure 4.6 – Intensity scan for constant brightness at the $N = 2 \times 10^{11}$ reference coherent dipolar tunes $(Q_x, Q_y) \approx (20.22, 20.31)$.

a low and once a high (ideally constant) space charge tune spread should unveil the respective contribution to the losses by direct space charge and impedance effects.

4.2.2 Constant Emittance

After having analysed the loss behaviour for constant space charge dynamics (for $\epsilon_{in} > 0.75\,\mathrm{mm\,mrad}$), we turn the situation around by keeping the transverse emittances constant while varying the intensity. In this way the brightness is changed in a controlled manner and we investigate to what extent the changing space charge conditions influence the beam losses for a fixed transverse beam size. For this purpose, we cannot modify the PS Booster multi-turn injection as we did before, otherwise the transverse emittances would change. Instead, we make use of a longitudinal acceptance bottleneck: by varying the controlled longitudinal emittance blow-up the beam gets scraped to different extents and we tailor the beam intensity without modifying the transverse beam size.

Figure 4.7a depicts the achieved transverse emittances during the intensity scan. At high intensities we observe a slight emittance increase, otherwise $\epsilon_{x,y}^{in}$ remain nearly constant. The space charge tune spread correspondingly scales directly with the intensity, cf. figure 4.7b. This plot includes 1σ confidence bands considering uncertainties in σ_z and σ_δ and is based on the empirical cubic fit to the measured emittances.

During this experiment, we continuously adjusted the SPS quadrupole currents to keep the coherent vertical tune around $Q_y \approx 20.30$ as shown in figure 4.7d.

This time, the relative beam losses remain well below 2%. An increased scattering on the low intensity side is observed, while the main region within $0.8 \times 10^{11} < N < 1.8 \times 10^{11}$ remains remarkably constant below the 0.5% level. It should be noted that the beam current transformer has a limited resolution for measuring the beam intensity (and hence the losses). When approaching very low intensities, the measurement becomes dominated by this finite resolution to which the observed increased scattering of the data points below $N < 0.8 \times 10^{11}$ can be attributed.

On the other hand, the measurements featuring larger losses above $N > 1.8 \times 10^{11}$ correspond to one fixed machine tune setting, namely the group of points in figure 4.7d with the largest intensities. Extrapolating to $N = 0$ yields a machine tune of $Q_y \approx 20.34$ for this group, i.e. above the $3Q_y = 61$ resonance. The measurement group next to it extrapolates to a machine tune of $Q_y \approx 20.33$ and already belongs to the low loss region. These findings point to an influence of the third-order resonance on the beam loss pattern.

However, in comparison to the previous experiment, the Gaussian tune spreads in figure 4.7b around the high intensities reach much further up to $|\Delta Q_y^{\mathrm{SC}}| \leq 0.22$. Therefore, only the largest transverse amplitudes (with the particles at the lowest incoherent space charge tune shifts) satisfy the incoherent $3Q_y = 61$ resonance condition to excite particles and result in the observed beam loss.

The mere direct space charge argument fails to explain the increasing tendency of the losses with the intensity though. We would rather expect the opposite behaviour of a decreasing loss tendency because at larger intensities, ΔQ^{SC} reaches higher and therefore fewer particles at large transverse amplitudes should be excited and lost. Instead, in line with the findings of the previous experiment, the observed increase of the transverse beam size at these high intensities could account for the increasing loss slope, analogously to figure 4.6.

To sum up, the absence of loss dependency on the intensity for the constant emittances up to $N < 1.8 \times 10^{11}$ again indicates that the transverse beam size influences the amount of beam loss.

4.3 Exciting the $4Q_x = 81$ Resonance

For high-intensity beams in the SPS, the fourth-order $4Q_x = 81$ resonance seems to play a major role besides the third-order $Q_x + 2Q_y = 61$ resonance, as the beam loss measurements from the static tune scan in section 4.1 brought forth in figure 4.4a. Furthermore, the transverse emittance blow-up in figure 4.4b revealed a vertical line of significant emittance growth around $Q_x = 20.28$ in parallel to the $4Q_x = 81$ resonance line. The goal of the following experiment is to understand the influence from direct space charge on these observations, specifically its interaction with the octupolar $4Q_x = 81$ resonance in the vicinity of the proposed optimal betatron tune region around $Q_x = 20.22$ and $Q_y = 20.30$.

Figure 4.8 presents three horizontal sections at $Q_y = (20.30, 20.32, 20.34)$ from the static tune scan to highlight the aforementioned features of the quarter-integer resonance. The relative beam loss rises around the $4Q_x = 81$ line for all three vertical tunes. On a side note, the higher two tunes show the large loss around the previously discussed third-order resonance loss hotspot towards $3Q_x = 61$. In figure 4.8 we observe the significant emittance growth consistently peaking at $Q_x = 20.28$ for all three curves. In the wire scanner profiles we find excessive tail development for the working points $(20.28, 20.30)$, $(20.28, 20.32)$ and $(20.28, 20.34)$ which is not evidently observed for the horizontally adjacent working points. These tails in fact obscure the values of the r.m.s. emittances which are determined via Gaussian fits to the profiles. We will analyse this in more detail in the following. As a last comment on the static tune scan results, we observe the r.m.s. emittance growth at $Q_x = 20.28$ in both the horizontal and the vertical plane – the vertical tune varying between $20.30 \leq Q_y \leq 20.34$ does not have a significant effect on this observation.

In order to quantitatively analyse the influence of space charge on the interaction with the fourth-order resonance, one can increase the strength of the resonance driving term by powering a single octupole magnet which acts like a localised octupolar field error. The SPS is equipped with strong non-linear extraction magnets which are not used in present standard operation. To drive the fourth-order resonance we use the 0.74 m long LOE.10402 extraction
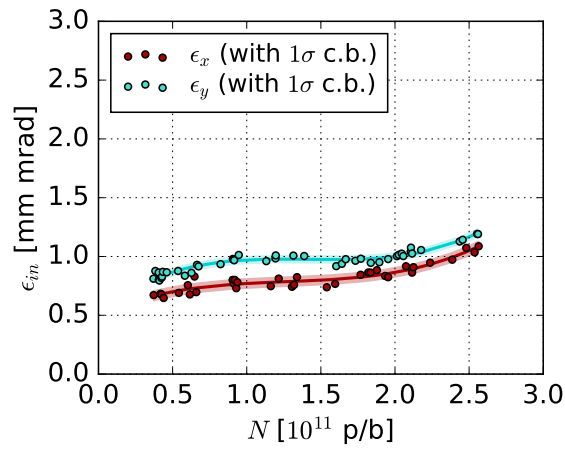
(a) Transverse emittance vs. intensity
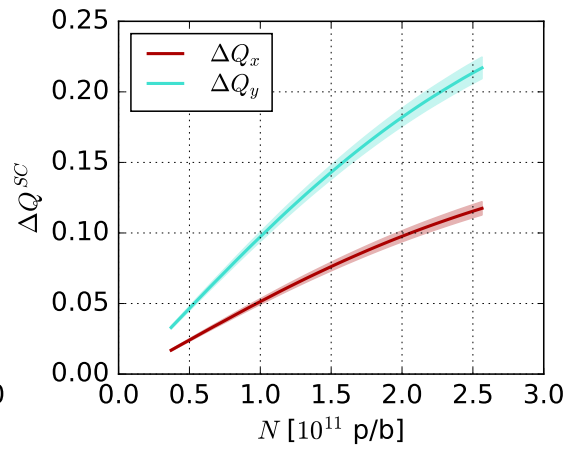
(b) Gaussian space charge tune spread vs. intensity
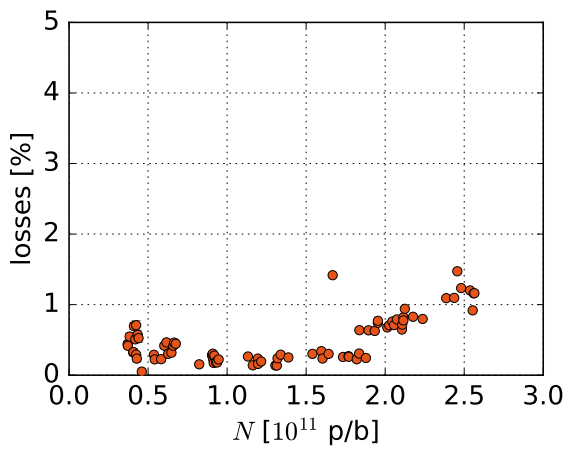
(c) Relative beam losses vs. intensity
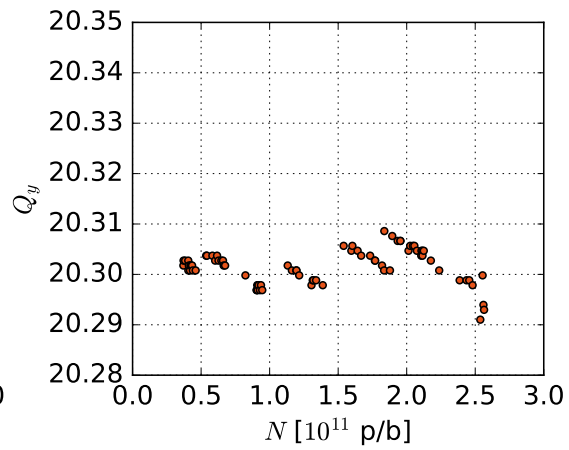
(d) Coherent vertical tune vs. intensity
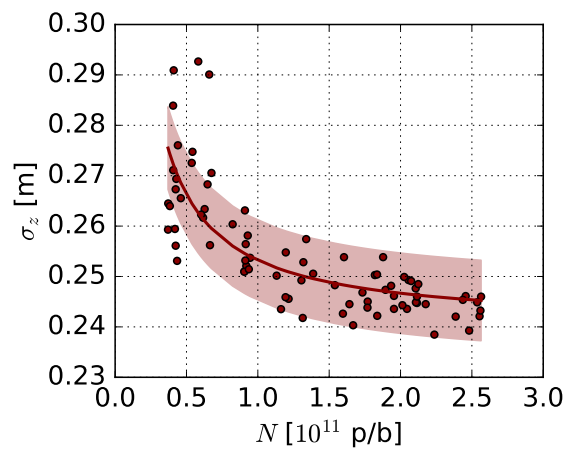
(e) R.m.s. bunch length vs. intensity

Figure 4.7 – Intensity scan for constant emittance keeping the coherent dipolar tunes fixated around $(Q_x, Q_y) \approx (20.22, 20.30)$.

(a) Relative beam losses vs. horizontal tune

(b) Transversely averaged r.m.s. emittance blow-up vs. horizontal tune
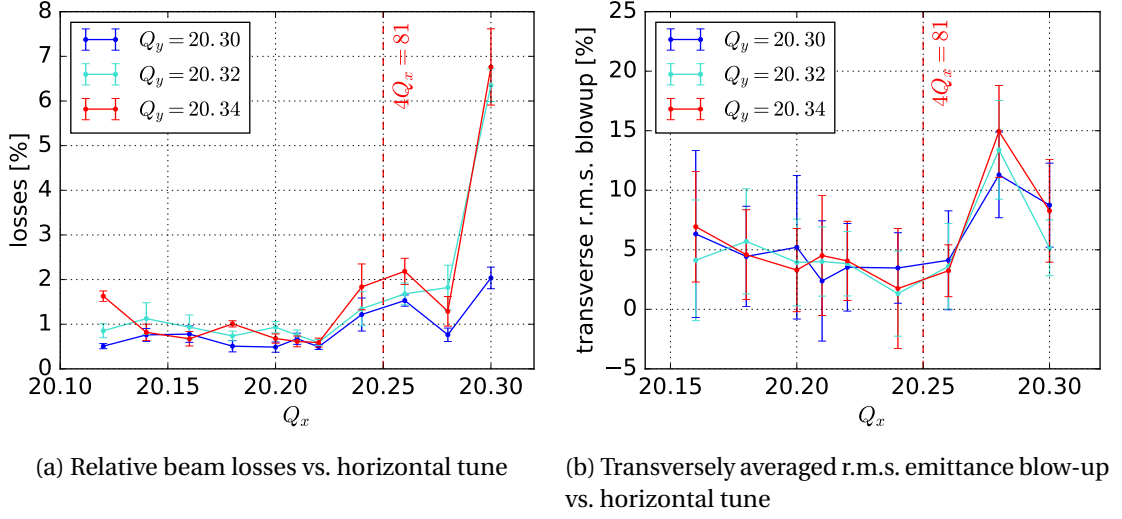
Figure 4.8 – Extracted beam loss and emittance growth from the static tune scan in figures 4.4a and 4.4b.

octupole at a strength of

$$k_3 \doteq \frac{1}{|B\rho|} \frac{d^3 B_y}{dx^3} = 25 \, \text{m}^{-4} \quad . \tag{4.4}$$

The extraction octupole is powered before injection and the current is kept constant during the cycle. The betatron functions for the Q20 optics at the location of LOE.10402 amount to $\beta_x = 98.8\,\text{m}$ and $\beta_y = 34.0\,\text{m}$, i.e. $\beta_x \gg \beta_y$. With the same set-up as in the previous experiments on the SPS injection plateau, we measure the relative beam loss and transverse emittance growth over 3 s. By fixing the vertical coherent dipolar tune and scanning the horizontal one across the $4Q_x = 81$ resonance, the incoherent resonance condition is satisfied for varying transverse amplitudes across the beam. Compare to the simulation experiment by R. Baartman [1998] which we addressed in the introductory chapter 1: instead of varying the intensity N we scan Q_x which leads to an equivalent picture. Notabene, Baartman's simulation varies the intensity dynamically while we statically fix a tune during a set of shots and only then proceed to the next working point.

In fact, for each tested working point, we record three shots per transverse plane, i.e. we have in total six measurements per tune. In order to assess the impact of space charge, we carry out the horizontal tune scan for a high-intensity ($N \approx 2.05 \times 10^{11}$) as well as a low-intensity ($N \approx 0.42 \times 10^{11}$) single-bunch beam variant. Both are produced to have approximately the same transverse beam emittances. However, the different preparation of the beam variants accidentally resulted in larger longitudinal emittances in the high-intensity case: we measured significantly longer bunches and, thus, computed larger values of the momentum spreads assuming again longitudinally matched beams after decease of the quadrupolar injection oscillations. The high-intensity single bunch reached an estimated vertical Gaussian space

charge tune spread of $|\Delta Q_y^{SC}| = 0.158$ which is three times larger than for the low-intensity single bunch. The experimental parameters which differ from the tune scan experiment (cf. table 4.1) are listed in table 4.2.

Table 4.2 – Experimental parameters in the SPS for the driven fourth-order resonance $4Q_x = 81$.

parameter name	symbol	low N beam value	high N beam value
fixed vertical tune	Q_y	20.31	
scanned horizontal tune	Q_x	20.16...20.30	
PS extracted intensity	N	$(0.42 \pm 0.02) \times 10^{11}$	$(2.05 \pm 0.10) \times 10^{11}$
initial horizontal normalised core emittance	ϵ_x	$(0.94 \pm 0.06)\,\text{mm mrad}$	$(0.84 \pm 0.05)\,\text{mm mrad}$
initial vertical normalised core emittance	ϵ_y	$(0.85 \pm 0.06)\,\text{mm mrad}$	$(1.06 \pm 0.04)\,\text{mm mrad}$
r.m.s. bunch length	σ_t	$(0.70 \pm 0.04)\,\text{ns}$	$(0.93 \pm 0.01)\,\text{ns}$
r.m.s. momentum deviation	δ_{rms}	$(1.48 \pm 0.07) \times 10^{-3}$	$(1.94 \pm 0.02) \times 10^{-3}$
Gaussian space charge tune spread	$\Delta Q_{x,y}^{SC}$	$(-0.027, -0.052)$	$(-0.085, -0.158)$
r.m.s. equivalent KV tune shift	$\Delta Q_{x,y}^{KV}$	$(-0.014, -0.026)$	$(-0.043, -0.079)$

From these prepared beam variants we can compute at which bare machine tune the envelope mode responds to the octupolar resonance. With the r.m.s. equivalent KV tune shift of the high-intensity beam given by $\Delta Q_x^{KV} = -0.043$ and the low-intensity beam by $\Delta Q_x^{KV} = -0.014$, we can evaluate the coherent resonance condition (2.137) for the octupolar resonance. The octupolar mode of a 2D isotropic beam (which sufficiently approximates our situation) features three eigenfrequencies [Hofmann 1998]. The matrix coefficient C_{mk} for the betatron resonance with $m = k = 4$ can hence take a value out of $C_{44} \in \{13/16, 7/8, 31/32\}$, cf. table 2.1. The resonance condition theoretically predicts the KV beam to resonate at

$$Q_x = \frac{81}{4} + C_{44}\Delta Q_x^{KV} \approx \begin{cases} 20.261..20.264 & , \text{low } N \\ 20.285..20.292 & , \text{high } N \end{cases} . \tag{4.5}$$

With Sacherer's argument of the r.m.s. equivalence of beams with respect to their space charge dynamics, we therefore expect the r.m.s. emittance blow-up of our beams to peak at these tunes.

During the evaluation of the wire scanner measurements, we found enhanced tails in the beam profiles deviating from a Gaussian distribution. In the low-intensity beams, these tails occurred systematically and without any dependence on the horizontal tune. We extract the normalised emittance in the vertical plane by the following approach: first we fit the whole profile with a Gaussian function to obtain the $(-1.8\sigma, 1.8\sigma)$ interval. Then we restrict a second

Gaussian fit to this bunch core interval to extract the core size σ_y. From this we can readily determine the normalised vertical "core emittance" via $\epsilon_y = \sigma_y^2/\beta_y$ with the betatron function $\beta_y = 60.56\,\text{m}$ at the vertical wire scanner `BWS.52171.V_LIN`. In the horizontal plane, we follow the same approach while additionally taking into account the non-zero dispersion, i.e. we employ equation (2.35) with $\beta_x = 32.55\,\text{m}$ and $D_x \approx -0.5\,\text{m}$ (the exact values depend on the adapted optics model where D_x changes slightly with the horizontal tune, as explained in section 4.1) for `BWS.51731.H_LIN`. The r.m.s. bunch length is extracted by a Gaussian fit to the longitudinal profile and, likewise as in section 4.1, the r.m.s. momentum spread is calculated assuming a longitudinally matched beam (the longitudinal quadrupolar injection oscillations have damped at the point of measurement). As the core region of the beam profile consistently exhibits a Gaussian shape (the residual of the fit vanishes for the core region), the Gaussian assumption for the longitudinal and horizontal plane required to use σ_x (extracted from a Gaussian fit) in equation (2.35) is justified.

For the low-intensity beams, the core beam sizes are indeed consistently $5\% - 6\%$ lower compared to the "general fit" beam sizes based on the full range Gaussian fits. This is the case for both 'in' and 'out' measurements. We therefore exclude any influence of space charge in the SPS as the origin of these tails – they likely arise during the beam preparation further upstream. The high-intensity beams, on the other hand, exhibit clean Gaussian profiles at the 'in' reference. Once the horizontal tune crosses the fourth-order resonance $Q_x = 20.25$, we observe the development of clear tails in the 'out' beam profiles in both transverse planes. Figure 4.9 illustrates the Q_x dependency of these tails for the relevant horizontal tunes around the $4Q_x = 81$ resonance. The three measured beam profiles per tune are plotted on top of each other: note the remarkable reproducibility of the profiles, specifically the tails.

In figures 4.9a and 4.9b we plot the respective core fits in orange and the wire scanner data in blue. All curves are normalised to unity amplitude. The amount of particles in the halos above the core fits increases from $Q_x = 20.25$ to its maximum at $Q_x = 20.27$ after which it declines again. This feature becomes even more apparent in the residual graphs 4.10a and 4.10b, where we plot the measured data points subtracted by the core fit. First of, we note that the Gaussian assumption for the core shape is justified as the residuals vanish until the tails depart. Now for the tails, we observe the maximal area under the residual curve where the tails deviate from the orange Gaussian core fit at the beam profile of $Q_x = 20.27$. Compare this tune with the rise in the r.m.s. emittance blow-up running vertically in parallel to the quarter-integer resonance at around $Q_x = 20.28$ (we scanned in 0.02 steps) in the static tune scan experiment, as explained at the outset of this section.

Another feature of the tails is the point at which they depart from the Gaussian core fit, the halo threshold. In both the horizontal and the vertical plane, the outer reach of the tails is maximal around $Q_x = 20.26\ldots 20.27$. At the same time, the halo threshold moves closer to the centre-of-gravity of the bunch with increasing tune. In figures 4.9a and 4.9b we have added the trace of the $Q_x = 20.24$ beam profile as a dashed red line for each tune. This allows to see that the core remains more or less unaffected by this amplitude dependant emittance growth
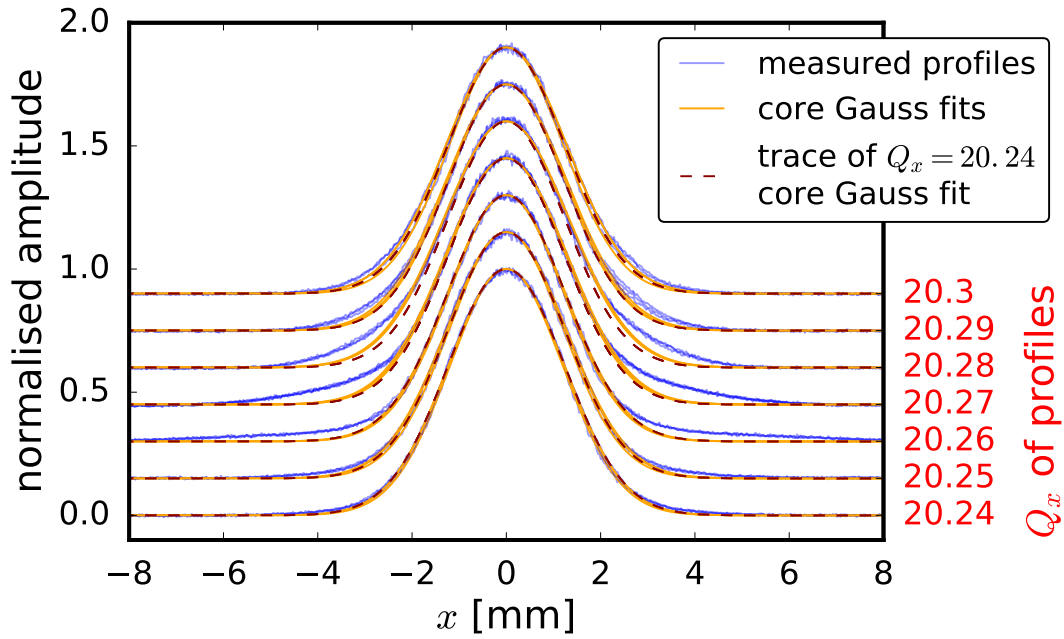
(a) Horizontal beam profiles for various horizontal tunes
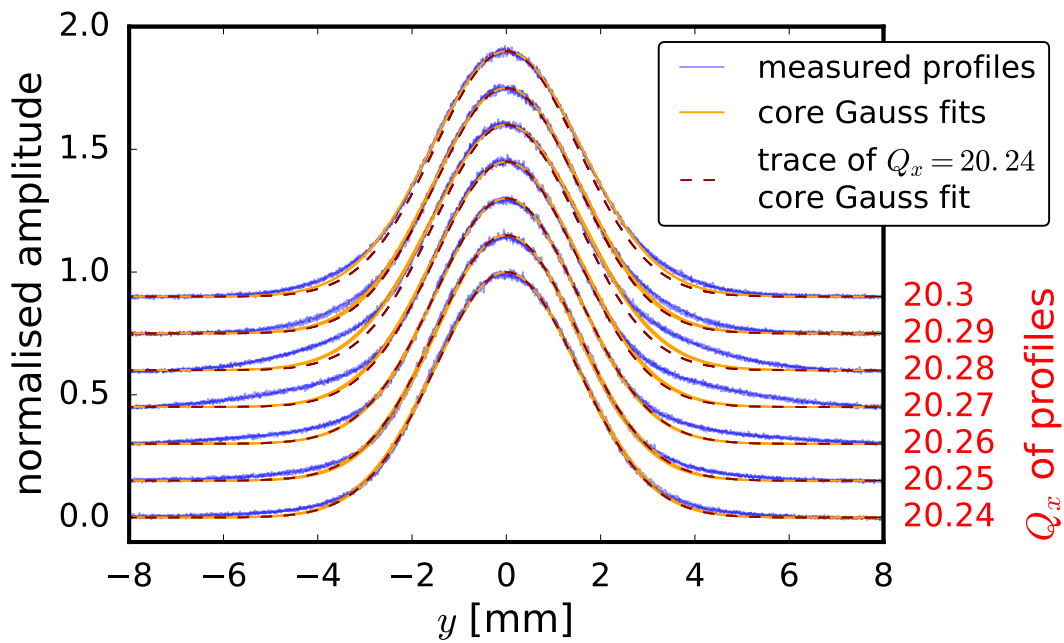
(b) Vertical beam profiles for various horizontal tunes

Figure 4.9 – Beam profiles with clear tails that deviate from the Gaussian core fits.
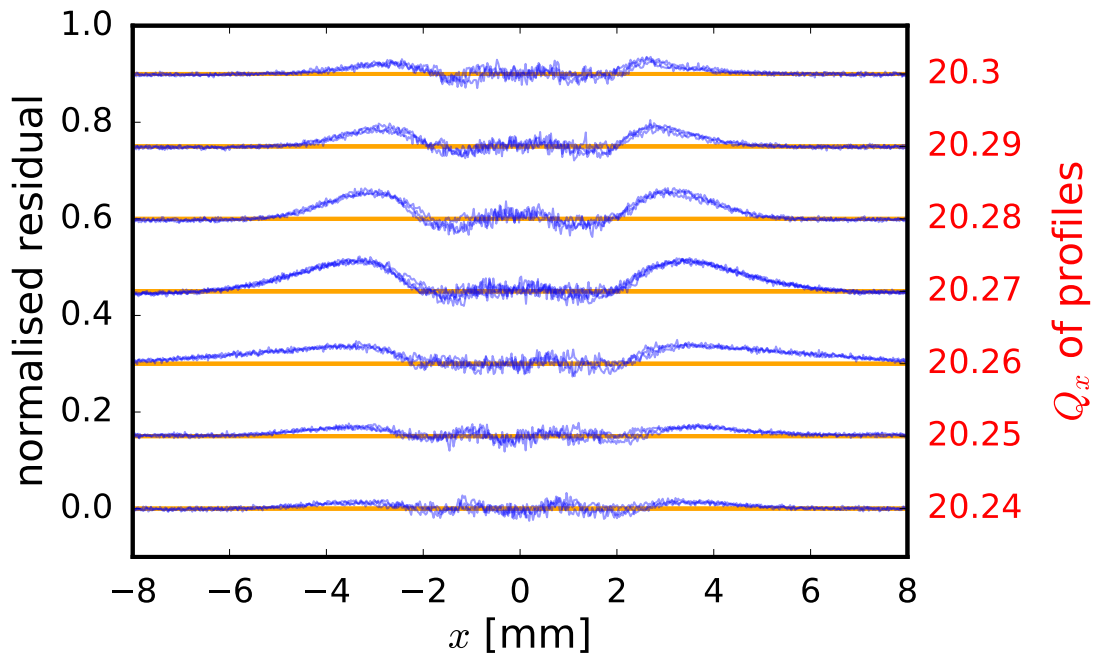
(a) Horizontal residuals for above Gaussian core fits
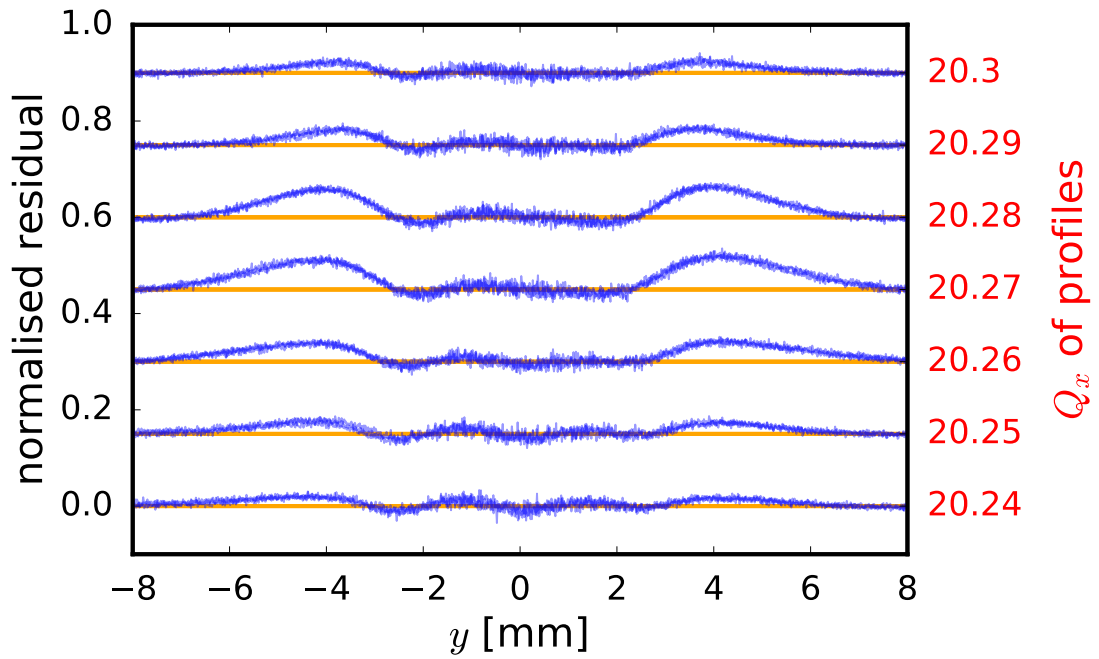
(b) Vertical residuals for above Gaussian core fits

Figure 4.10 – Residuals of the beam profiles from figure 4.9 quantifying the deviation of the tails from the Gaussian core fits.

until $Q_x = 20.27$ from where also the core is blown up: the orange fits here exceed the dashed red $Q_x = 20.24$ line and only return to it at $Q_x = 20.30$ in the horizontal plane.

If the transverse planes were entirely decoupled, we would expect the $4Q_x = 81$ resonance to primarily show an effect in the horizontal plane. We have $\beta_x \approx 2.9\beta_y$ at the extraction octupole which results in a much stronger horizontal driving term for the fourth-order resonance: the stop-band width of the octupole resonance scales with

$$\left(\Delta Q_{\text{stop}}^{(4)}\right)_{x,y} \propto \beta_{x,y}^2 \tag{4.6}$$

[Wiedemann 2007, equation (13.67)] indicating an eightfold stronger excitation in the horizontal plane compared to the vertical plane.

However, we did not correct any coupling in the machine for the low-intensity bunch. What is more, direct space charge introduces a coupling between the planes depending on the space charge perveance. Note that the scanned working points are located in the vicinity of the space charge driven Montague coupling resonance $2Q_x - 2Q_y = 0$ – in fact slightly above, as figure 4.11 indicates. For illustrative purposes, the incoherent space charge tune spreads have been sketched for both beam variants, with the orange one corresponding to the high-intensity and the turquoise one to the low-intensity beam. The mechanism of the Montague difference resonance leads to an exchange of the transverse emittances [Montague 1968]. Therefore, the horizontal emittance growth may be transferred to the vertical plane and consequently the tails can be observed in both planes although the powered octupole mainly drives the horizontal plane.

We can examine this hypothesis by comparing the emittance growth between the strong space charge, high-intensity beam variant and the minimal space charge, low-intensity beam variant. Given that the coupling from direct space charge dominates the lattice coupling, the latter beam should be much less coupled and consequently show the effect of the fourth-order resonance much more in the horizontal than in the vertical plane. In addition, the space charge tune spread is three times smaller which makes the relative tune distance to the Montague resonance large enough not to be affected.

We first evaluate the reference measurement set using the low-intensity beam with the extraction octupole switched off. Figure 4.12a shows the mean values and standard deviation of the respective three horizontal core (solid lines) and general (dashed lines) emittances for each of the scanned horizontal tunes. Both emittance measures reveal no significant dependency on either the tune or the time between the 'in' and 'out' references. Also the relative beam losses in figure 4.12b are consistently below the 2% line and appear independent of the horizontal tune. The previously mentioned tails of the low-intensity beams lead to the systematic constant difference between the core and the general emittances.
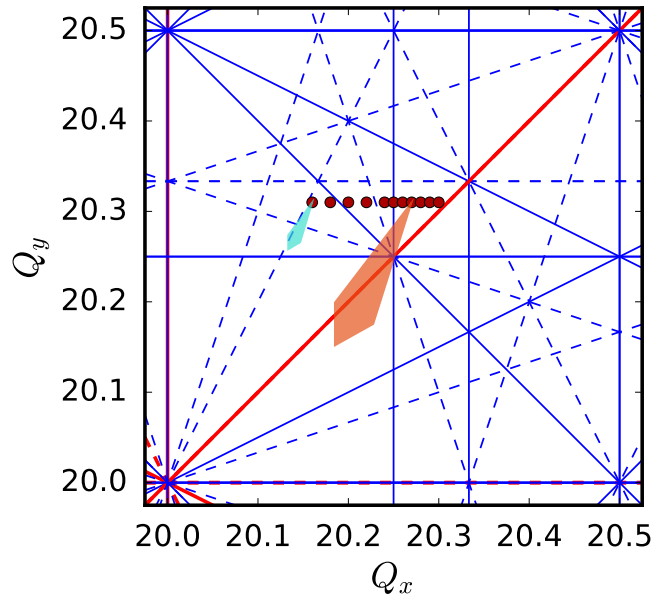
Figure 4.11 – Tune diagram with the scanned coherent dipolar tunes and resonance lines up to 4th order, the high-intensity (orange) and low-intensity (turquoise) incoherent tune foot prints have been sketched.
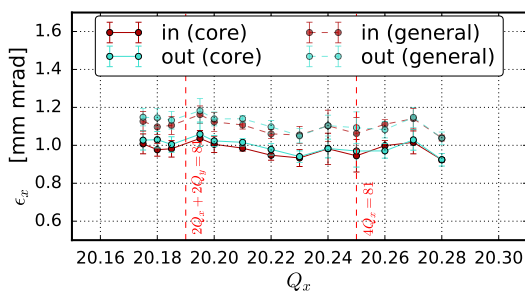
(a) Horizontal emittance from core and general Gaussian fit vs. horizontal tune
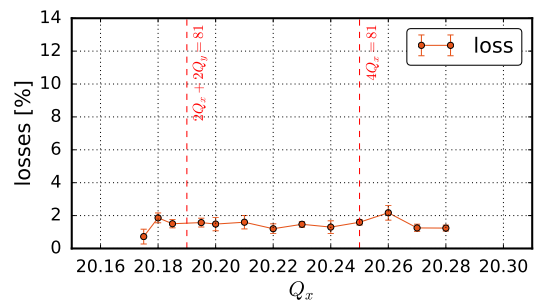
(b) Relative beam losses vs. horizontal tune

Figure 4.12 – Horizontal tune scan for low-intensity beam without the extraction octupole.

The results of powering LOE.10402 are plotted in figure 4.13. Switching on the extraction octupole immediately leads to beam losses far above the 2% line. Besides the obvious peak around the $4Q_x = 81$ resonance in figure 4.13c, we identify another peak at lower tunes. The tune diagram in figure 4.11 indicates the crossing of the fourth order $2Q_x + 2Q_y = 81$ resonance at $Q_x = 20.19$ along our measurement set. This resonance is also driven by the octupolar field error but appears weaker because the large horizontal and the small vertical beta function enter in equal amounts in contrast to the $4Q_x = 81$ resonance.

(a) Horizontal emittance from core and general Gaussian fit vs. horizontal tune

(b) Vertical emittance from core and general Gaussian fit vs. horizontal tune

(c) Relative beam losses vs. horizontal tune

(d) *Horizontal* core emittance blow-up vs. horizontal tune
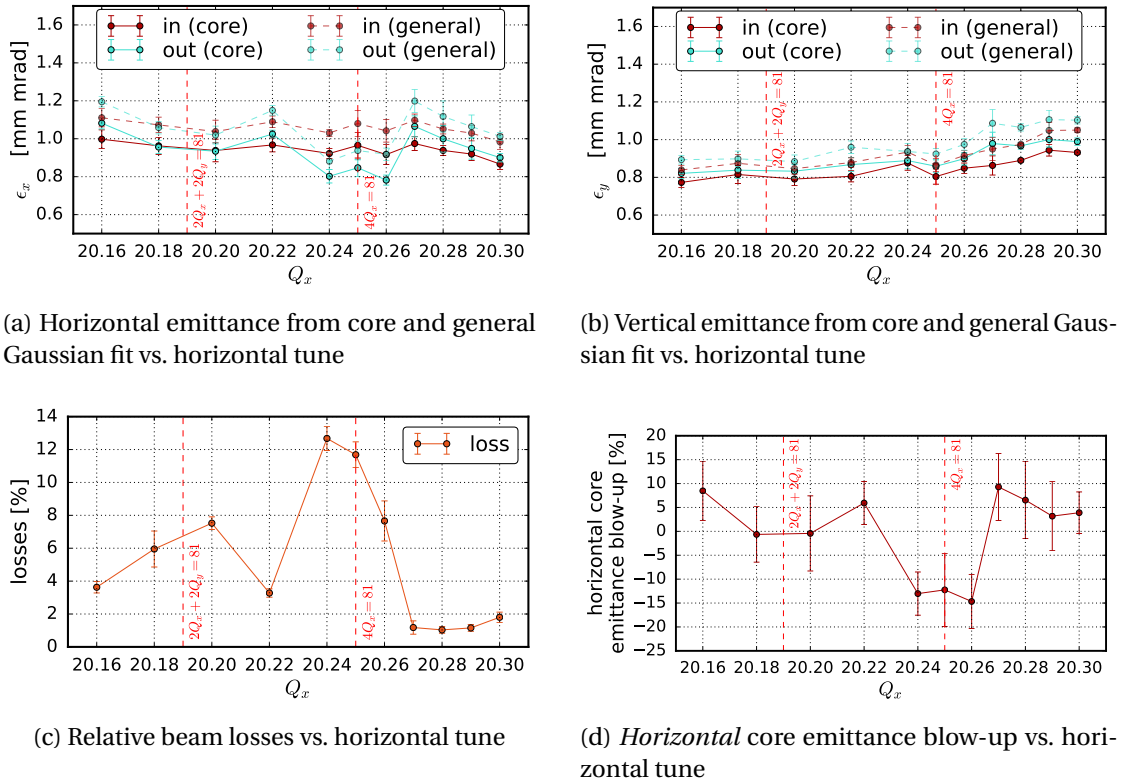
Figure 4.13 – Horizontal tune scan for low-intensity beam with the extraction octupole powered.

The vertical emittances in figure 4.13b remain approximately constant up to a slightly positive slope in both 'in' and 'out' measurements at the upper end of the scanned tunes. In contrast, the horizontal emittances (figure 4.13a) are clearly affected by the $4Q_x = 81$ resonance. The observed beam losses can be attributed to losing particles in the horizontal plane, where the beam profiles shrink by up to 15% as plotted in figure 4.13d. At the same time, we do not observe significant emittance growth above the quarter-integer resonance, if at all at $Q_x = 20.27$ where the error bar excludes zero blow-up. Again, it is noteworthy that the core emittances and the general fit emittances show a consistent difference of about 10% − 12% with the only exception at the horizontal 'out' beam profile for $Q_x = 20.26$: here, we find an indication of a more populated halo with a 18% − 20% larger general emittance compared to the core value (remind that $Q_x = 20.26$ is the theoretically predicted value where the r.m.s.

equivalent KV beam satisfies the space charge depressed resonance condition for the low-intensity beam). As a last remark, the rising horizontal emittance towards small horizontal tunes points to the influence from the integer resonance $Q_x = 20$.

Now let us turn our attention to the high-intensity beam results presented in figure 4.14. The relative beam loss in figure 4.14c shows a similar peak around $Q_x = 20.25$ compared to 4.13c. However, the $2Q_x + 2Q_y = 81$ shows no influence on the loss pattern. Another difference to the low-intensity beams marks the loss increase towards $Q_x = 20.30$. This feature has already been noticed during the systematic tune scan in section 4.1, figure 4.4a exhibits the discussed hotspot around $(Q_x, Q_y) = (20.33, 20.33)$. The extracted loss curve in figure 4.8a at the outset of this section shows these losses to amount to $6 - 7\%$ at $Q_x = 20.30$, while including the octupolar resonance excitation here they slightly rise to $10 - 11\%$. This is far less then the more than fivefold increase of the losses at $Q_x = 20.25$ when driving the octupolar resonance, hence these losses indeed seem independent of the octupole and might rather be attributable to the vicinity of the sextupolar resonance crossing. We conclude from their absence in figure 4.13c (or at least the order of magnitude difference in the losses since there is a slight rising tendency at $Q_x = 20.30$ as well) that these losses are intensity related.
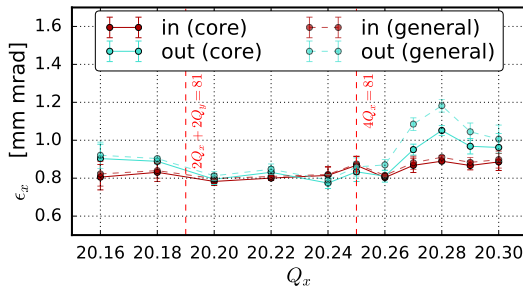
(a) Horizontal emittance from core and general Gaussian fit vs. horizontal tune
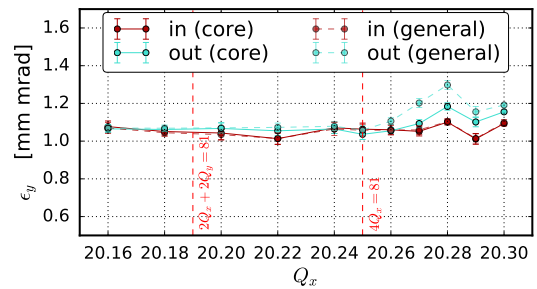
(b) Vertical emittance from core and general Gaussian fit vs. horizontal tune
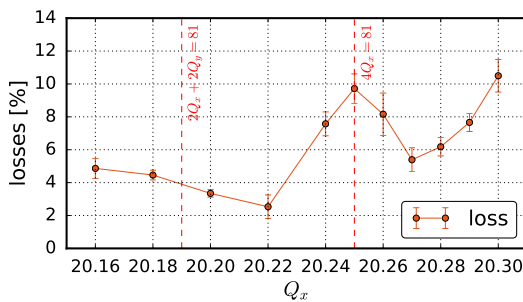
(c) Relative beam losses vs. horizontal tune
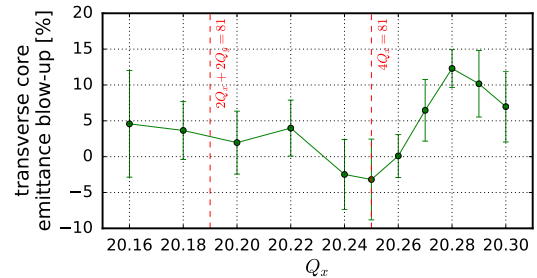
(d) *Transversely averaged* core emittance blow-up vs. horizontal tune

Figure 4.14 – Horizontal tune scan for high-intensity beam with the extraction octupole powered.

Figures 4.14a and 4.14b depict the horizontal and vertical emittances, respectively. This time, the general Gaussian fit coincides with the core fit in both transverse planes below the

quarter-integer resonance or, in other words, there are no significant beam halos. Starting from $Q_x \geq 20.25$, the tails grow as already discussed during the preceding analysis of figure 4.9. Clearly, these tails are attributable to resonance interaction: the 'in' measurements show no tails as opposed to the 'out' measurements, where the general emittances (dashed curves) are much larger compared to the core emittances (solid curves). The peak is reached around $Q_x = 20.28$ which is confirmed by the transverse core emittance blow-up plotted in figure 4.14d with a significant emittance growth of 12%. Recall that $Q_x = 20.28$ also marks the tune where the halo threshold moves closest to the beam centre. The blow-up deviates from zero in a statistically significant manner from $Q_x \geq 20.27$ confirming the finding from the profile analysis. The peak around $Q_x = 20.28$ approximately matches the theoretical prediction from (4.5). Furthermore, it is situated in the same location as originally observed in the static tune scan. In order to compare the amplitude of the emittance growth, it is to be mentioned that the r.m.s. emittance blow-up peak in figure 4.8b reduces to a value of $6 - 8\%$ for the corresponding core emittance. This halving of the emittance growth comparing general to core emittance is also observed in the excited case (cf. the turquoise solid core line and the (twice as far from the red 'in' line located) turquoise dashed line in figures 4.14a and 4.14b). It means that half of the r.m.s. emittance growth is attributable to particles getting excited to transverse amplitudes outside of the 1.8σ radius core region. We conclude that the emittance growth peak along $Q_x = 20.28$ in parallel to the $4Q_x = 81$ resonance line is indeed correlated with the octupolar resonance.

All in all, we indeed see a qualitative difference in the transverse coupling between the low-intensity and the high-intensity beam variants. The observations support the hypothesis stated at the outset that the latter beam variant is affected by emittance exchange from the Montague resonance as opposed to the former. We emphasize the measured tune dependency of the halo threshold whose "moving inward" behaviour fits the incoherent resonance condition being met at decreasing transverse amplitudes in the Gaussian beam towards the centre when increasing Q_x. In general, we conclude that the r.m.s. emittance growth that we noticed in the systematic tune scan from the first section indeed originates from the interaction with the fourth-order resonance: (1.) it is absent for the low-intensity beam without powering the extraction octupole, (2.) it strongly increases for high-intensity beams when the extraction magnet is switched on as compared to when it is off, and (3.) the observed high-intensity beam tails at $Q_x = 20.28$ stated at the outset of the section strongly increase with the additional excitation of the octupole resonance.

Furthermore, space charge is a necessary ingredient to excite the resonance as well as to shift the betatron resonance condition to the higher value, as the comparison between the low and high intensity beam variants shows. In particular, the development of tails depends on intensity: in the low-intensity case, the tails at $Q_x = 20.26$ only occur with the driving octupole; the high-intensity beam in contrast always develops tails at $Q_x = 20.28$ and the excitation only enhances the tails. Hence, space charge also excites the fourth-order resonance. In this context, we remark that it remains an open issue to be clarified for the SPS, why only the horizontal quarter-integer resonance affects beam quality while the vertical one shows no

visible effect in the systematic tune scan from section 4.1, since both $4Q_y = 81$ and $4Q_x = 81$ are regular resonances which are in principle expected to appear on an equal footing.

To understand the location of the r.m.s. emittance growth peak, it is important to use the r.m.s. equivalent KV tune shift in the coherent resonance condition (4.5). This confirms the r.m.s. equivalence of beams established by Sacherer [1971], as the coherent modes of the equivalent KV beam dictate the collective space charge dynamics (in the core) of the Gaussian beam (cf. the discussion by R. Baartman [1998]). It should be added that the theoretical prediction assumes coasting beams while the experiment involves bunched beams. Uesugi et al. [1999] have analysed the 3D envelope equations to address how synchrotron motion influences the prediction for space charge shifted betatron resonances. They conclude that envelope oscillation frequencies (and therefore the C_{mk} factor in (2.137)) in a bunched beam do not differ much from a coasting beam.

Besides the r.m.s. growth associated with the coherent resonance response of the beam, we have observed a five-fold increase of the beam loss at $Q_x = 20.25$ due to powering the octupole. This can be explained by the shrinking of the dynamic aperture due to the strong octupolar non-linearity. The analysis of beam losses due to excitation of halo particles requires the framework of the incoherent space charge dynamics. Previous pioneering work in this direction has been carried out by Franchetti et al. [2003] at CERN's PS in a similar experimental set-up. The authors explain the beam losses with resonance island trapping and detrapping in conjunction with synchrotron motion, which ultimately results in halo particles leaving the dynamic aperture and consequently getting lost at the physical machine aperture at some point. The experimental conditions in the PS are equivalent to the SPS with respect to the necessary parameters to their loss mechanism. The synchrotron motion is orders of magnitude slower than betatron motion allowing for a certain period of resonance island trapping. It is to be mentioned that the (linear) synchrotron period in the SPS of $Q_{S,0}^{-1} \approx 66$ turns is more than an order of magnitude faster as compared to the PS injection plateau. Nonetheless, the betatron tune gives a transverse period of $Q_{x,y}^{-}1 \approx 1/20$ turns, i.e. $Q_{x,y}^{-}1 \ll Q_{S,0}^{-1}$. Therefore the proposed loss mechanism applies to our experiment.

To be more specific, Franchetti et al. propose that particles at large synchrotron amplitudes undergo large betatron tune modulation due to the varying transverse beam self-fields as they traverse the beam between the sparsely populated longitudinal extremities through the dense core. The incoherent tune may hence periodically satisfy the resonance condition. Consequently, this particle gets trapped repeatedly on the resonance islands during a certain period until it reaches a different local line density due to synchrotron motion. During this process the transverse amplitude can slowly increase. Eventually, the particle is lost at the physical machine aperture after exiting the dynamic aperture due to the machine non-linearities (foremost from the strongly powered single octupole magnet). The relevance of large synchrotron and large betatron amplitude particles for the loss mechanism has been confirmed by the findings of Machida [2014] during the analysis of the vertical fourth-order structure resonance in the PS, as we mentioned in the introductory chapter.

4.4 Space Charge Simulations with PyHEADTAIL

The previous experiment provides measurement data with clear features distinguishing low from high intensity beams. We will analyse the driven octupolar resonance results with the aid of the developed space charge tools in our collective effects software PyHEADTAIL. In the simulation model, we take into account the TWISS lattice functions from the MAD-X optics model for the SPS Q20 optics including the horizontal dispersion. Further, we include first-order chromaticity as well as octupolar detuning with amplitude. The goal is to reproduce the previous results in terms of emittance growth and the generation of tails in the otherwise Gaussian distribution due to the resonant excitation of particles.

The non-linear single-particle model for the SPS has been established from measurements [Bartosik, Oeftiger, Schenk, et al. 2016]: the tune variation with momentum offset yields the non-linear chromaticity and the tune variation with transverse amplitude gives the octupolar detuning with amplitude. Second and higher-order chromaticity is observed to contribute to the detuning in the relevant δ momentum range at an order of magnitude below the first order, which is why we only take into account the linear chromaticity in the simulations. Right before the experiment of the fourth-order resonance excitation while using the same super-cycle in the SPS, we scanned the beam momentum (via a radial offset) around the reference p_0 with transversely small low-intensity beams. From the corresponding base-band tune measurements, the chromaticity has been determined to the values $(Q'_x, Q'_y) = (7.5, 3.5)$.

In order to extract the "natural" machine anharmonicities from the detuning with amplitude measurements, two different octupole current configurations are analysed per plane as indicated in figure 4.15. The vacuum tubes around the SPS mostly feature much smaller vertical apertures compared to the horizontal plane. Thus, the accessible vertical amplitude (action J_y) range is smaller which requires stronger octupole currents to see a significant effect over the scanned J_y. From the linear measurement fits with their respective octupole settings for the focusing LOF family and the defocusing LOD family, we obtain that an LOD strength of $k_{3,\mathrm{LOD}} = 0.5$ and vanishing LOF strength would correct the octupolar detuning with amplitude. Therefore, we deduce an equivalent natural machine octupole component amounting to $k_{3,\mathrm{LOD}} = -0.5$ and $k_{3,\mathrm{LOF}} = 0$. The corresponding anharmonicity values $(a_{x,x}^{\mathrm{nat}}, a_{x,y}^{\mathrm{nat}}, a_{y,y}^{\mathrm{nat}})$ are listed in table 4.3, which summarises all relevant simulation parameters in addition to the measurement values from table 4.2.

In order to estimate the anharmonicities inflicted by the powered single extraction octupole LOE.10402 at a strength of $k_3 = 25\,\mathrm{m}^{-4}$, we run simulations with a regular grid of particles uniformly spaced in their transverse action. This set-up has to exclude chromaticity, the natural machine octupole detuning, dispersion as well as synchrotron motion in order to single out the effect from the LOE.10402 on the particles' betatron frequencies. The simulation
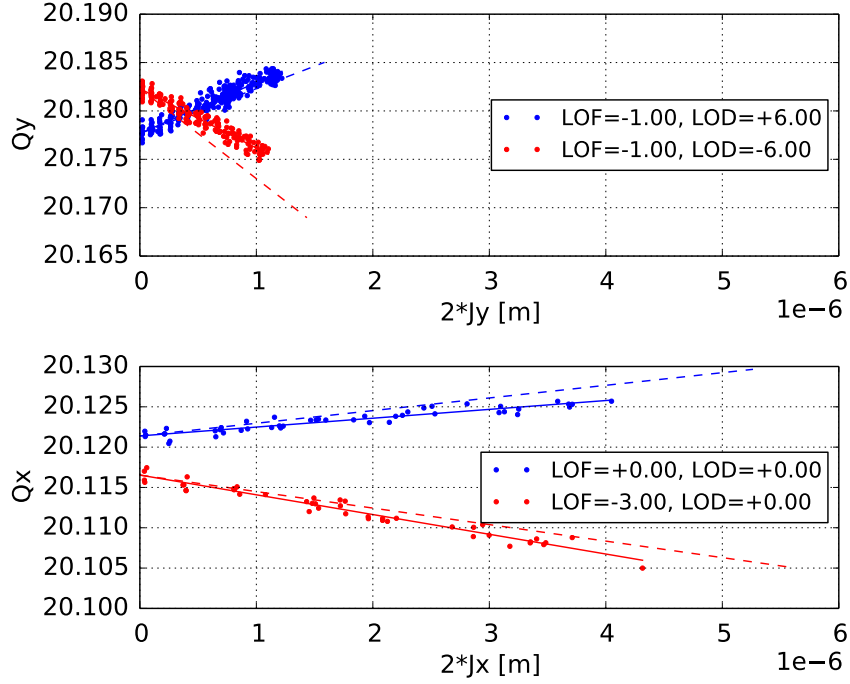
Figure 4.15 – Measurement of octupolar detuning with amplitude in the SPS, the upper plot shows the change of vertical tune versus twice the vertical action (the transverse amplitude in units of single particle emittance) for two configurations for the LOD and LOF octupole families [Bartosik, Oeftiger, Schenk, et al. 2016, figure 3a], the lower plot shows the same for the horizontal plane with two other configurations. The dots indicate measurements with their linear fits given by the solid lines. (The dashed lines refer to the MAD-X model predictions.)

models the effect from the $L = 0.74\,\mathrm{m}$ long LOE.10402 as a thin octupole kick,

$$\Delta x' = -\frac{k_3 L}{3!}\left(x^3 - 3xy^2\right) \quad \text{and} \tag{4.7}$$

$$\Delta y' = -\frac{k_3 L}{3!}\left(y^3 - 3x^2 y\right) \quad, \tag{4.8}$$

at the location of the real LOE.10402 within the linear Twiss lattice used for tracking in Py-HEADTAIL. The non-linear octupolar kick actually limits the dynamic aperture in the otherwise linear simulations in the sense that transverse phase space gets divided into bound and unbound areas. In the unbound area, the amplitude of a particle's trajectory is in principle unlimited and its motion exhibits deterministic chaos. In fact, chaotic motion occurs already around the separatrices between these areas. The dynamic aperture describes the effective limit before the motion of the particles becomes chaotic when arbitrarily close initial conditions lead to exponentially diverging phase space trajectories.

We want to extract the linear frequency in the bound area around the origin within the dynamic aperture. Therefore, we follow the motion of the particles arranged in the regular grid during

Table 4.3 – Simulation parameters for driven octupole resonance.

parameter name	symbol	value
chromaticity	(Q'_x, Q'_y)	$(7.5, 3.5)$
natural anharmonicities	$a_{x,x}^{\mathrm{nat}}$	-72
	$a_{x,y}^{\mathrm{nat}}$	410
	$a_{y,y}^{\mathrm{nat}}$	-580
anharmonicities from LOE	$a_{x,x}^{\mathrm{LOE}}$	1700
	$a_{x,y}^{\mathrm{LOE}}$	-1200
	$a_{y,y}^{\mathrm{LOE}}$	220
macro-particles	N_{mp}	1×10^6
number of segments (space charge kick nodes)	n_{segments}	1200
r.m.s. bunch length	σ_t	$0.77\,\mathrm{ns}$
r.m.s. momentum spread	δ_{rms}	1.45×10^{-3}
Gaussian space charge tune spread	$\Delta Q_{x,y}^{\mathrm{SC}}$	$(-0.12, -0.19)$
r.m.s. equivalent KV tune shift	$\Delta Q_{x,y}^{\mathrm{KV}}$	$(-0.06, -0.1)$

128 turns and obtain their frequencies with a SUSSIX analysis [Bartolini and Schmidt 1998]. The linear slope of the extracted betatron tune depending on the transverse amplitude yields the respective anharmonicity,

$$a_{x,x} = \frac{\partial Q_x}{\partial(2J_x)}, \quad a_{x,y} = \frac{\partial Q_x}{\partial(2J_y)}, \quad a_{y,x} = \frac{\partial Q_y}{\partial(2J_x)}, \quad a_{y,y} = \frac{\partial Q_y}{\partial(2J_y)} \quad . \tag{4.9}$$

If we run at $Q_x = 20.24$, we observe a quite small dynamic aperture due to the proximity to the $4Q_x = 81$ resonance which is excited by the octupole driving term. This can be observed in the extracted frequencies which are plotted in figure 4.16, where the red curves deviate from the linear slope above $2J_x$. For $a_{x,x}$ in graph 4.16a the particles clearly become trapped in the fourth-order resonance around $3J_x$, this is where the non-linearity of the octupole kick dominates the mere linear detuning effect: the dynamic aperture becomes very small. By running the simulations at $Q_x = 20.13$ – i.e. far from the resonant $Q_x = 20.25$ –, we get a nearly perfect linear behaviour within our scanned region. The effective LOE.10402 anharmonicities extracted from these slopes are added to table 4.3. The coupling anharmonicities $a_{x,y}$ and $a_{y,x}$ are equal up to 1% deviation. In general, the quite large LOE.10402 strength of $k_3 = 25\,\mathrm{m}^{-4}$ has a strong impact on the overall octupole component of the machine, as the anharmonicities show directly: the contribution from the extraction octupole is more than an order of magnitude larger than the natural machine octupole component, in particular in the horizontal plane.

(a) Horizontal tune vs. horizontal amplitude.

(b) Vertical tune vs. vertical amplitude.

(c) Horizontal tune vs. vertical amplitude.

(d) Vertical tune vs. horizontal amplitude.
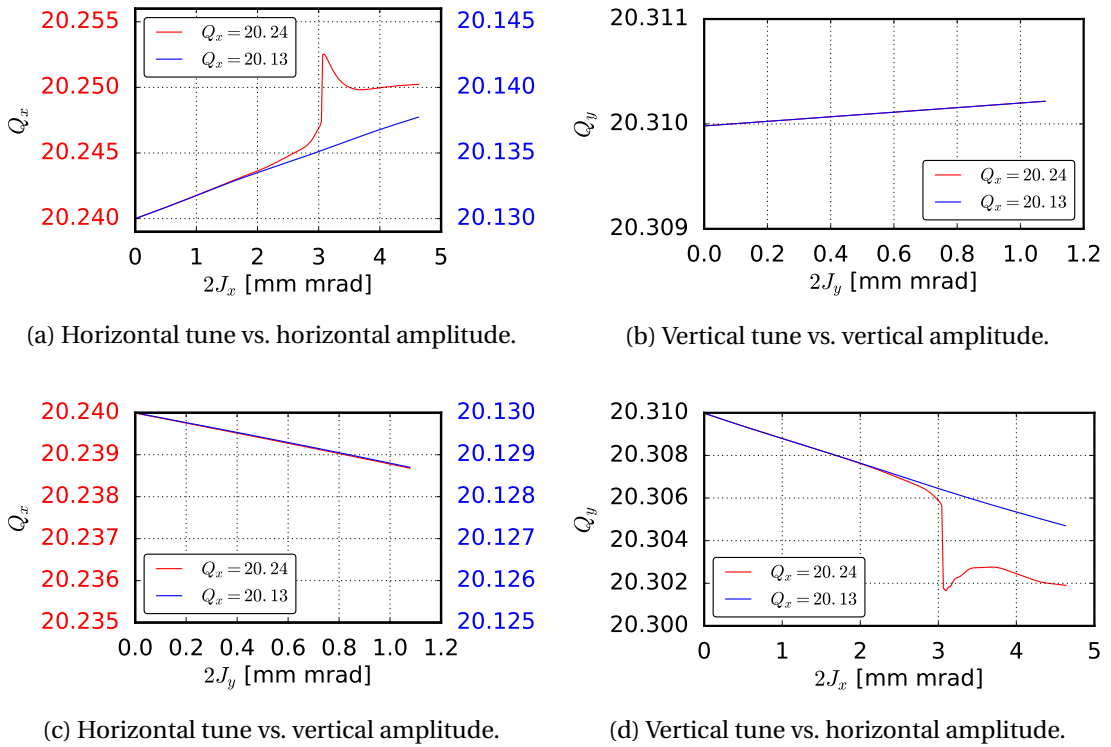
Figure 4.16 – Detuning with amplitude for localised thin octupole kick for two different working points $Q_x = 20.24$ (in red) and $Q_x = 20.13$ (in blue) with fixed $Q_y = 20.31$.

By looking at the Poincaré section for some particles of various horizontal amplitudes at the bare machine tune of $Q_x = 20.24$ from the frequency scan simulation, we can observe the deformation of the single particle phase space due to the extraction octupole in the vicinity of the horizontal fourth-order $4Q_x = 81$ resonance. Figure 4.17 shows the horizontal phase space for particles of three different regions:

1. the blue traces belong to the particles at low horizontal amplitudes $2J_x < 2\,\text{mm mrad}$ which are in the linear detuning region, cf. figure 4.16a;

2. the red traces belong to particles close to the inner separatrix where the detuning behaves non-linear with the amplitude, the individual particle tunes are drawn towards the resonant tune $Q_x = 20.25$ between $2\,\text{mm mrad} \lesssim 2J_x \lesssim 3\,\text{mm mrad}$; and finally

3. the black traces belong to particles outside the inner separatrix which are essentially caught by the four islands generated by the fourth-order resonance.

In fact, the peak in figures 4.16a and 4.16d corresponds to the amplitude of the inner separatrix outside of which the particles in the scanned range are captured within the four resonance islands, jumping clock-wise from one to the next. For horizontal amplitudes further outside one would observe unbound motion and in between more small stable islands – more detailed information can be find in textbooks treating single particle beam dynamics, e.g. in Forest [1998].

117
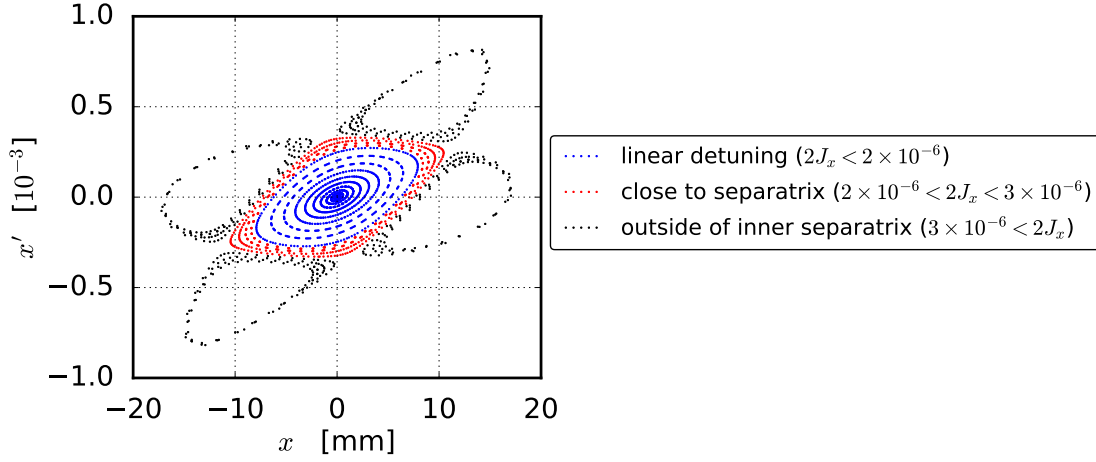
Figure 4.17 – Poincaré section for horizontal phase space (x, x') plotting particles of various amplitudes J_x during 128 turns at the horizontal wire scanner location. The extraction octupole LOE.10402 imprints with resonant islands on the phase space at a bare machine tune of $Q_x = 20.24$.

We observed the beta beating (envelope oscillations due to single-particle effects) caused by the LOE.10402 to remain below 0.5% for both the smooth approximation (with constant betatron functions at $\beta_{x,y} = 54.6\,\mathrm{m}$) and the full SPS Twiss lattice. Therefore we neglect this influence on the linear lattice for our analysis and we always refer to the unperturbed optics functions.

In our PyHEADTAIL simulation we include non-linear synchrotron motion. The beam macro-particle distribution is initialised as a thermal equilibrium inside the RF bucket. We use the correspondingly largest possible longitudinal emittance equivalent to a $\sigma_t = 0.77\,\mathrm{ns}$ r.m.s. bunch length.

First we run simulations without space charge but including all single-particle effects, i.e. chromaticity, octupolar detuning with amplitude (using the natural machine anharmonicities $a_{x,x}^{\mathrm{nat}}, a_{x,y}^{\mathrm{nat}}, a_{y,y}^{\mathrm{nat}}$), non-linear synchrotron motion and the non-linear thin octupole kick while employing the linear Twiss lattice. Figure 4.18 depicts the transverse r.m.s. emittance evolution during the 3 s machine time (equivalent to 130 000 turns). They essentially remain constant for the horizontal tunes $Q_x = 20.24 \ldots 20.30$ (up to very few small spikes when single particles exit the dynamic aperture and increase the r.m.s. emittance until they get lost at the simulated aperture). We find the chromaticity in the model to be a crucial ingredient to the observed beam stability as it provides enough detuning in order to move particles off the resonance such that there is no continuous excitation. If we switch off chromaticity the horizontal emittance immediately grows for $Q_x = 20.25$. If we instead increase the LOE.10402 strength, the size of the resonance stop-band grows. Consequently, one can trap particles long enough on the resonance: from twice the experiment k_3 value on we indeed see the horizontal emittances growing at the resonant bare tune $Q_x = 20.25$. Comparing the observed beam stability for

vanishing intensity in the PyHEADTAIL simulations to the experimentally observed resonance reaction of the low intensity beams (cf. figure 4.13) suggests a notable influence from space charge on the resonance dynamics even at these low intensities.
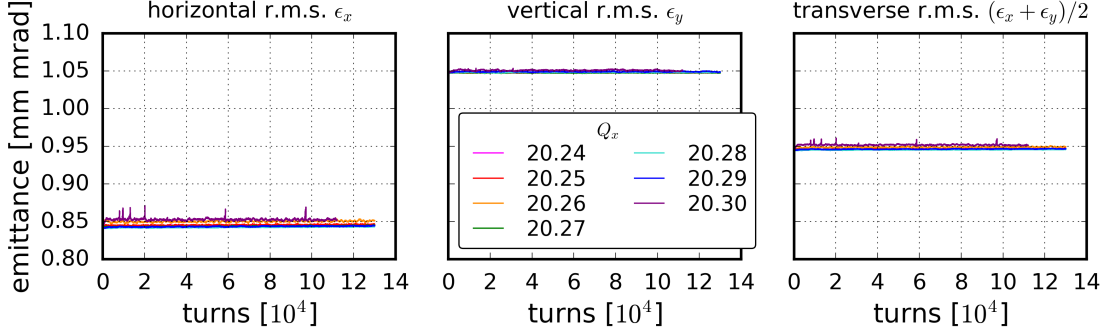
Figure 4.18 – Evolution of the transverse r.m.s. emittances for various horizontal tunes during 3 s at the SPS injection plateau, the PyHEADTAIL simulation includes chromaticity, octupolar detuning with amplitude and the strong octupolar kick at $k_3 = 25\,\mathrm{m}^{-4}$ for beams with vanishing intensity.

After this short discussion of the single particle dynamics contained in our model with the non-linear octupole, we will now turn our attention to the multi-particle effects: we include direct space charge via the Bassetti-Erskine model which does not feature the noise inherent to the PIC model. The beam widths for the semi-analytic formula are continuously updated from the statistical beam standard deviations at each of the $n_{\mathrm{segment}} = 1200$ space charge nodes per turn. We use 1×10^6 macro-particles to resolve the beam along 32 slices in order to obtain solid statistics for the beam quantities such as the statistical r.m.s. emittance. We do not take into account indirect wall effects from image currents due to beam impedances. Moreover, we choose the working points according to the measured coherent tunes from the experiment and hence fix a vertical bare tune of $Q_y = 20.31$ while scanning along $Q_x = 20.24\ldots20.30$ in steps of 0.01.

We simulate the high-intensity beam variant during 10 000 turns. Direct space charge for these high brightness beams entails a quite large tune spread which dominates over the octupolar and chromatic tune spreads. Evaluating expression (2.87) predicts a Gaussian tune spread of $\Delta Q_{x,y}^{\mathrm{SC}} = (-0.12, -0.19)$. Compare this to an r.m.s. chromatic detuning of $Q'_{x,y}\delta_{\mathrm{rms}} = (0.011, 0.005)$ or likewise the even smaller octupolar detuning with amplitude of the order of $a_{x,x}^{\mathrm{LOE}}\epsilon_x/(\beta\gamma) \approx 1.5 \times 10^{-4}$. The incoherent tune spread of the simulated Gaussian beams is depicted in figure 4.19. The tunes of each particle have been determined by switching off synchrotron motion (giving a "momentary" image of the incoherent tune footprint). A SUSSIX analysis then readily provides the particle frequencies from the transverse oscillations during a window of 128 turns. We see that the actual incoherent tune spread reaches about 3/4 from the theoretically predicted value, possibly because of the non-Gaussian horizontal beam distribution (we discussed this non-Gaussian effect in detail in section 3.4: the large ϵ_z leads to a non-Gaussian momentum distribution within the non-linear RF bucket which

distorts the horizontal profile due to dispersion). Using the computed r.m.s. equivalent KV tune shift of $\Delta Q_{x,y}^{\mathrm{KV}} = -0.06$, we obtain a prediction for the r.m.s. emittance growth peak at $Q_x = 20.25 + C_{44} \times 0.06 \approx 20.30$.

Since the RF bucket is very full at the maximum longitudinal emittance for the thermal distribution, we have a certain amount of particles travelling at the largest synchrotron amplitudes at a very low synchrotron tune (compared to the rather rapid linear synchrotron period of $Q_{S,0}^{-1} = 66\,\mathrm{turns}$) due to the strong tune depression from the non-linear RF bucket close to the separatrix. These are also the particles that are found towards the top right end of the tune spread when they are approaching the unstable fix points at the ends of the RF bucket, where the low line charge density entails correspondingly weak local beam self-fields and hence low tune shift.
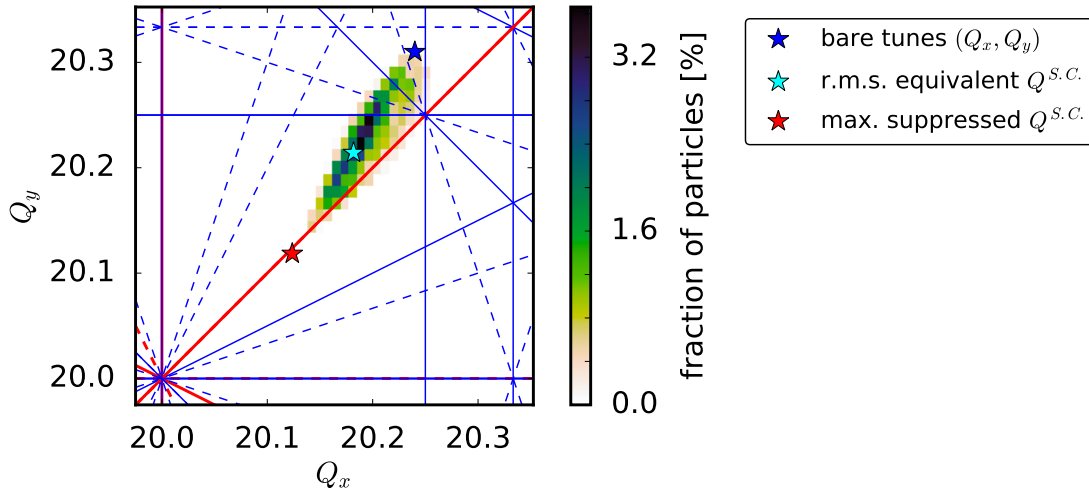
Figure 4.19 – Momentary incoherent tune footprint of the initial Gaussian beam with all included single-particle effects and direct space charge. The bare tunes, the maximally space charge shifted tune from the Gaussian formula and the corresponding r.m.s. equivalent KV tune (shifted by half the Gaussian spread) are indicated as stars.

The halo is made up of particles travelling also at large transverse amplitude in addition to large synchrotron amplitudes. These halo particles experience the least incoherent betatron tune depression from space charge. We observe that they reach very close to the bare machine tune in the tune footprint. According to the core-halo model, the halo particles experience the beam core as an external source of electromagnetic fields and therefore their stability depends on whether they satisfy the incoherent resonance condition (with the C_{44} factor multiplied to the incoherent KV tune shift) for the fourth-order $4Q_x = 81$ resonance, in analogy to expression (4.5). As the halo particles' incoherent tunes are situated so close to the bare tune, we consequently expect them to become resonantly excited to very large transverse amplitudes (and eventually lost at the aperture) around bare tunes of $Q_x = 20.25$. Therefore, the tune spread reaching so close to the bare tune can account for the losses in the experiment from figure 4.14c, similarly to what we previously discussed based on the PS experiment results

[Franchetti et al. 2003].

We record the r.m.s. emittance growth over 10 000 turns: the final transverse emittance growths are plotted in figure 4.20. During the experiment in the previous section, we measured the emittance growth over 3 s and therefore $\approx 13\times$ more turns. The absolute values of the resulting emittance growths are therefore not to be compared, nonetheless, we can draw conclusions from the location of the peak when comparing to figure 4.14d. The transverse emittance exchange owing to the Montague coupling resonance dynamics leads to an enhancement of the horizontal emittance growth due to the octupole resonance excitation effect. The green diamond marked curve shows a strong horizontal emittance growth. On the other hand, the orange star marked curve shows a slight emittance decline in the vertical plane during the 10 000 turns – however, it is to be noted that the vertical emittance remained larger than the horizontal emittance within this simulation window. Overall, we observe the peak of the transversely averaged r.m.s. emittance growth to be located around $Q_x = 20.28$ to 20.29 which is 0.015 lower the theoretical prediction while the curve overall matches the experimental observation.
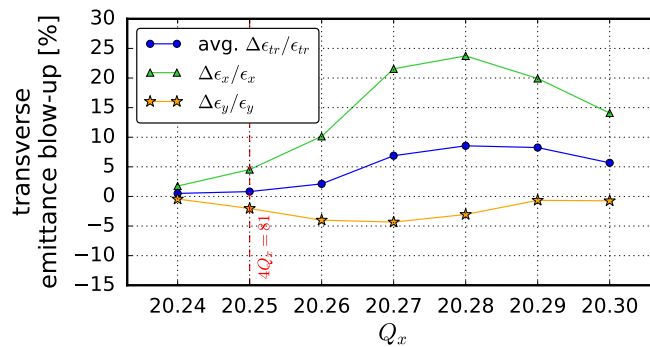
Figure 4.20 – Transverse emittance growth after 10 000 turns.

Let us now turn our attention to the generated tails in the distribution. We recorded the beam profiles during the simulation at the Twiss lattice start where the optics parameters read $\beta_x = 104\,\mathrm{m\,rad}$, $\alpha_x = -1.87\,\mathrm{rad}$, $D_x = 7.96\,\mathrm{m}$, $\beta_y = 32.3\,\mathrm{m\,rad}$, $\alpha_y = 0.626\,\mathrm{rad}$. We average the betatron profiles during 200 turns and fit them with a Gaussian function within the $(-1.8\sigma, 1.8\sigma)$ region in analogy to the measurement procedure. The horizontal betatron profile is obtained by subtracting the dispersive contribution for each particle via $x_\beta = x - D_x\delta$ before calculating the histogram for the beam profile. The residuals of the Gaussian fits (i.e. the profile subtracted by the fit) after 3500 turns and after 10 000 turns are shown in figure 4.21 for both transverse planes in order to single out the tails and the depopulation of the core.

The magnitude of the tails after these simulation times is on the one-percent level as opposed to the measurement values in figure 4.10 where we observe tails of up to 10% of the Gaussian fit amplitude. At 3500 turns, we observe more dominant tails in the horizontal plane from $Q_x \geq 20.27$ to higher tunes (figure 4.21a) while the vertical plane shows the tails mostly below $Q_x \leq 20.27$ (figure 4.21b). Moreover, the residual shapes around the centre in the vertical plane
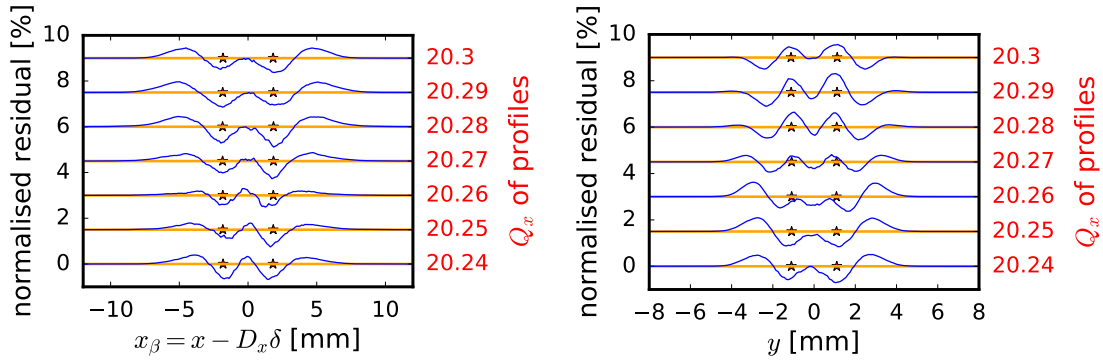
(a) Horizontal normalised residual for the betatron part after 3500 turns.

(b) Vertical normalised residual after 3500 turns.
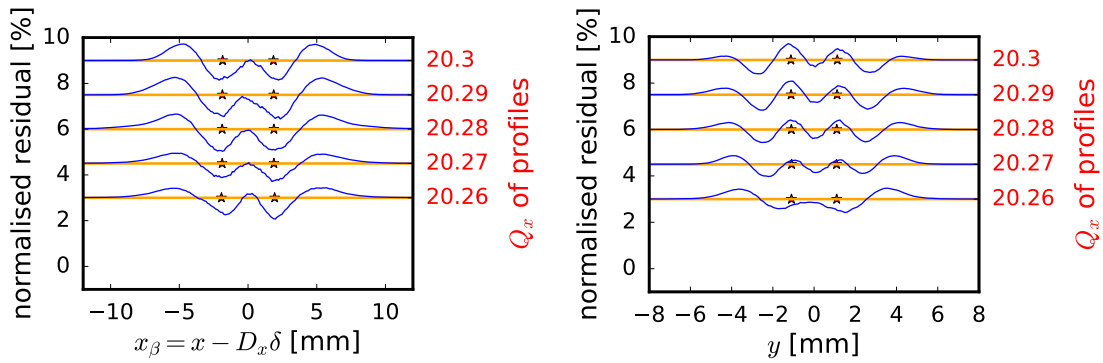
(c) Horizontal normalised residual for the betatron part after 10 000 turns.

(d) Vertical normalised residual after 10 000 turns.

Figure 4.21 – Residuals of the transverse beam profiles via subtraction of the Gaussian fits show the created tails. The red stars indicate the Gaussian 1σ widths.

above $Q_x \geq 20.26$ show a dip, i.e. a relative decline of the local density with respect to the flanks at 1σ (cf. the red star indications) in comparison to the Gaussian reference. This feature persists until 10 000 turns as can be seen in figure 4.21d for the profiles above $Q_x \geq 20.27$.

In general, we note that the horizontal profiles consequently depopulate around the 1σ value indicated by the red stars compared to the Gaussian reference while the initial macro-particle distribution was exactly Gaussian distributed (up to numerical noise). The particles move out to higher horizontal amplitudes and generate tails. In contrast, the vertical profiles show increased densities around 1σ for $Q_x \geq 20.27$ – the higher the tune the more pronounced the effect – while this feature inverts towards the other end below $Q_x \leq 20.26$ and the 1σ amplitude also depopulates (here there are also prominent tails which are absent at higher horizontal tunes).

In the measurement, the profiles around the centre would have enough time until the 3 s 'out' wire scan to thermalise to a Gaussian equilibrium distribution around the core and we

are only left with the pronounced tails. In the resonantly excited horizontal plane, we have found the tails in the experimental beam profiles to reach farthest at $Q_x = 20.26$ and the highest deviation from the Gaussian reference at $Q_x = 20.27$, after which the halo threshold moved back inside the beam (cf. figure 4.10a). In comparison, the simulation results at 10 000 turns (figure 4.21c) exhibit the farthest tail reach at $Q_x = 20.28$ and the highest deviation at $Q_x = 20.29$. At $Q_x = 20.30$ the halo threshold moves back towards the core.

Longer simulation studies could provide evidence whether the bunch core will thermalise to a Gaussian equilibrium. Also the imprinting of the horizontal tails on the vertical plane which we observed in the experiment might take longer than the simulated 10 000 turns.

To summarise, we observe the qualitative generation of tails in the simulation but the smaller duration as compared to the experiment does not allow yet to make a concluding quantitative comparison between beam profiles in the experiment and the simulation. The simulations show the same r.m.s. behaviour in the averaged transverse emittance growth as in the experiment and both are consistent with the coherent resonance condition of the r.m.s. equivalent KV beam.

5 Mitigation: Hollow Bunches

The electric self-fields of a particle beam become stronger with higher intensity (i.e. the total charge) and denser spatial concentration. At the same time, both variables are usually sought to be maximised for the final application of the beam. For a transversely Gaussian distributed bunch of particles, the effect of the self-fields is quantified by the space charge tune spread:

$$\Delta Q_{x,y}^{\mathrm{SC}}(z) = -\frac{q}{8\pi^2 \epsilon_0 m_p c^2} \frac{\lambda(z)}{\beta^2 \gamma^3} \oint ds \frac{\beta_{x,y}(s)}{\sigma_{x,y}(s) \left(\sigma_x(s) + \sigma_y(s)\right)} \quad . \tag{2.87}$$

From the formula above we can deduce that:

(i.) space charge scales with the inverse energy $(\beta\gamma^2)^{-1}$, hence the most critical cycle time for an accelerator is around the injection,

(ii.) a decrease of the peak line charge density $\lambda_{\max}$ leads to a smaller tune spread extent, and

(iii.) a broader momentum distribution leads to larger horizontal beam sizes and hence a smaller tune spread extent (increasing δ_{rms} correspondingly translates to larger $\sigma_x = \sqrt{\beta_x \epsilon_x/(\beta\gamma) + D_x^2 \delta_{\mathrm{rms}}^2}$, cf. equation (2.35)).

We suppose given constraints on the normalised emittance (i.e. transverse beam size), intensity and bunch length: a common strategy to mitigate space charge impact is to reshape the longitudinal distribution of the usually quasi-parabolic / Gaussian bunches. The common approach to reshape the bunch is to adiabatically add a second RF harmonic during the critical cycle times. The relative phase of the higher harmonic with respect to the fundamental can be adjusted such as to reduce, or even cancel, the phase focusing at the centre of the bucket. This results in a lower peak line density and a longer bunch as illustrated in figure 5.1a. In this "bunch lengthening" mode the bucket separatrix becomes wider around the bucket ends and flatter in the bucket centre, which results in both a larger bucket area (longitudinal acceptance) and flatter iso-Hamiltonian contours at the bucket centre (and therefore bunch distributions with depressed line densities). Correspondingly, the strongest transverse electric fields in

vicinity of the dense bunch centre decrease and the space charge tune spread shrinks: the beam becomes less prone to resonances and stop-bands located near the nominal working point in the tune diagram.

Using higher harmonics to mitigate space charge requires additional RF systems or multiple broad band modules that can be efficiently tuned on the required higher frequencies. Besides, double-harmonic shaped bunches may need to be transferred between subsequent accelerators (e.g. from the CERN PS Booster to the PS). This however requires a precise alignment of the relative phase between RF harmonics of both the sending and the receiving machine to avoid longitudinal mismatch (in the case of bunch-lengthening mode for second harmonics).

An alternative to reshaping the longitudinal profile indirectly via a modified Hamiltonian is to alter the phase space distribution directly. This consideration leads us to the concept of *"hollow bunches"*.
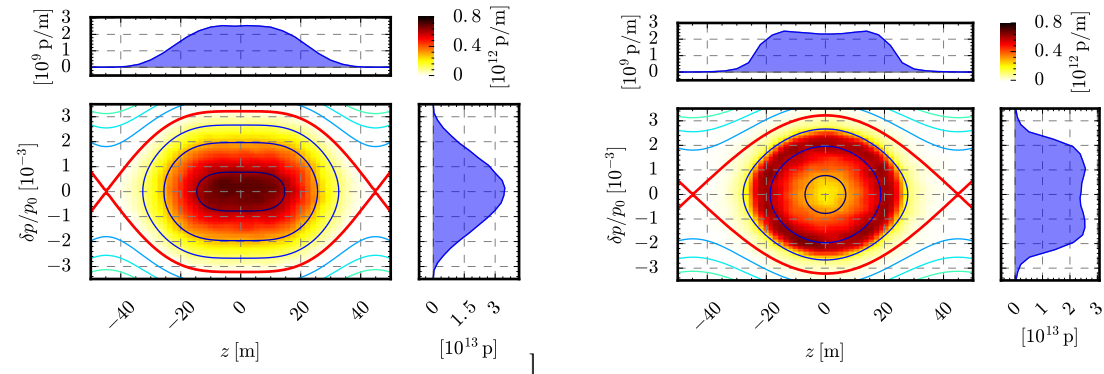
(a) Double-harmonic bucket in bunch lengthening mode (i.e. 180° relative phase and $V_{h=2} = V_{h=1}/2$) populated with a matched distribution (note the quasi-Gaussian distribution in the momentum projection).

(b) Single-harmonic bucket at the same fundamental RF voltage populated with a hollow distribution. The spatial projection is flat equivalent to the second harmonic case, but additionally also the momentum projection becomes flat.

Figure 5.1 – Longitudinal phase space (z, δ) is presented in a tomography-typical layout. The lower left shows the momentum δ versus the coordinate z, the separatrix in red encloses the RF bucket. The density of the particle distribution is given by the colour scale in the upper right corner, yellow to red to black depicts increasing density. In addition, the equi-Hamiltonian contours indicate the particle trajectories. The upper plot shows the spatial projection and the plot to the right the momentum projection.

A bi-Gaussian longitudinal phase space distribution (i.e. a multivariate Gaussian normal distribution in both the momentum $\delta = (p - p_0)/p_0$ and the spatial coordinate z) exhibits the largest density at its centre. In contrast, a hollow distribution features the highest phase space density at a non-zero synchrotron amplitude, making it look like a ring, cf. figure 5.1b. Consequently, the spatial projection is much flatter compared to the Gaussian counterpart. Tuning correctly the ring thickness versus the depletion of the core, the longitudinal profile can be made flat without line density peaks at the bunch ends. An additional advantage of

hollow distributions over double-harmonic reshaping is the broader momentum distribution, cf. figure 5.1.

A hollow bunch can in principle be transferred between machines with the usual single harmonic RF synchronisation. With its intrinsic flattened profile geometry, such a beam is expected to accommodate for more intensity at fixed transverse normalised emittances and bunch length due to its better transverse space charge behaviour.

5.1 Creation Variants

Numerous methods to create hollow distributions have been proposed and experimentally tested over the past decades, to name some significant approaches in the literature:

1979: second-harmonic debunching in the Linac [Delahaye et al. 1980]

1979, 1999: deposition of empty buckets into a debunched beam and subsequent adiabatic RF capture of the coasting hollow beam [Delahaye et al. 1980; Lindroos et al. 2000],

1993: excitation of a parametric dipolar resonance via phase modulation [Cappi, Garoby, et al. 1993; Huang et al. 1993; Lee 2004],

2001: insertion of empty phase space into the bunch centre via second harmonic RF gymnastics [Carli 2001],

2001: inversion of phase space contours turning the centre of a Gaussian bunch outward via second harmonic RF gymnastics [Carli 2001; Carli and Chanel 2002], and

2004: RF phase jump of 90° [Wei et al. 2005].

In the framework of the LIU project, the LHC will have to be provided with beams having double intensity N but approximately the same transverse emittances $\epsilon_{x,y}$ compared to present operation (LIU Technical Design Report, Damerau et al. [2014]). The increase of the PS injection energy from $E_{\mathrm{kin}} = 1.4\,\mathrm{GeV}$ to $2\,\mathrm{GeV}$ envisaged in the baseline of the LIU programme is aimed at relaxing the expected space charge impact, as the tune spread (2.87) shrinks with $\Delta Q_{x,y} \propto 1/(\beta\gamma^2)$ (one $\beta\gamma$ factor is absorbed by the geometric emittances due to adiabatic damping).

Hollow bunches have the potential to provide an additional tool against space charge to reach the required goals. The present study has been tailored to the characteristics of LHC beams. The idea is to create hollow bunches in the PS Booster and subsequently transfer them into the PS to overcome the brightness limits given by the affordable emittance blow-up (cf. table 1.1) during the PS injection plateau.

Among the techniques for the creation of hollow bunches listed above, only three options have been retained and investigated in numerical simulations: the insertion of empty phase space, the inversion of a Gaussian bunch, and the parametric dipolar resonance. The starting point in

our simulation study is a stationary thermal (i.e. time-independent exponential) distribution in the PS Booster RF bucket at extraction energy. The results are presented in the following subsection.

5.1.1 Longitudinal Simulations with PyHEADTAIL

The PS Booster parameters used for this study are displayed in table 5.1. As a starting point, the three schemes have been analysed under non-accelerating conditions. In fact, most of the aforementioned experimental efforts to create hollow bunches have been carried out keeping the beam at constant energy.

Table 5.1 – Beam parameters in the PS Booster for the hollow bunch creation simulation studies.

kinetic energy	E_{kin}	1.4 GeV
initial longitudinal emittance	ϵ_z^{norm}	1.3 eV s
initial bunch length	$B_L \doteq \dfrac{4\sigma_z}{\beta c}$	180 ns
fundamental harmonic	h	1
RF $h = 1$ voltage	V_{rf}	8 kV
synchroton period (at 1.4 GeV)	Q_S^{-1}	3924 turns
PS Booster circumference	C	$2\pi \cdot 25$ m
transition energy	γ_{tr}	4.05

Insertion of Empty Phase Space

Figure 5.2a shows the programmed evolution of the parameters of the two main PS Booster RF systems ($h = 1$ and $h = 2$), i.e. voltage and phase of the $h = 1$ system (V_1, ϕ_1) as well as of the $h = 2$ system (V_2, ϕ_2). These functions were originally proposed by Carli [2001]. Schematically, the second harmonic is exploited to open a second empty bucket, wrap the core of the bunch around it and finally combine it with the first bucket. Figure 5.3 depicts the corresponding intermediate states.
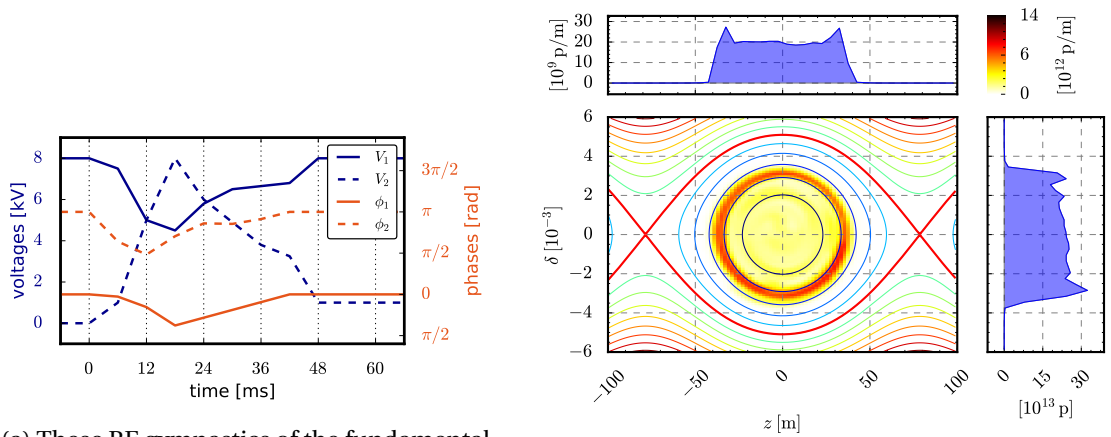
(a) These RF gymnastics of the fundamental and the double harmonic system (with voltages $V_{1,2}$ and phase offsets $\phi_{1,2}$)...

(b) ... create this hollow distribution when neglecting the influence of longitudinal space charge.

Figure 5.2 – Insertion of empty phase space into the longitudinal distribution.

This method creates a thin ring in phase space which leads to peaks towards the ends of the profile projection. The thickness is not easily controllable in order to create a more even, flat-topped profile. Moreover, the success of the hollow bunch creation proved extremely sensitive to RF parameter deviations in the experiments conducted by Carli [ibid.].

Inversion of Phase Space Distribution

In the same paper, the author proposes less complex RF parameter functions (figure 5.4a) which essentially achieve a redistribution of phase space contours. Figure 5.5 illustrates how the dense Gaussian bunch core is exchanged with the sparsely populated exterior part, essentially turning the bunch distribution inside out. Varying the initial longitudinal emittance between $\epsilon_{z,\mathrm{rms}} = 0.5\,\mathrm{eVs}$ and $1.2\,\mathrm{eVs}$ revealed that the resulting bunch length B_L of this scheme is independent of ϵ_z.

(a) 1 turn equivalent to 0 ms

(b) 3×10^4 turns equivalent to 17.2 ms

(c) 4.5×10^4 turns equivalent to 25.8 ms

(d) 5.3×10^4 turns equivalent to 30.6 ms

(e) 6.2×10^4 turns equivalent to 35.5 ms

(f) 7.2×10^4 turns equivalent to 41.4 ms

(g) 8.4×10^4 turns equivalent to 47.8 ms

(h) 10.5×10^4 turns equivalent to 60 ms
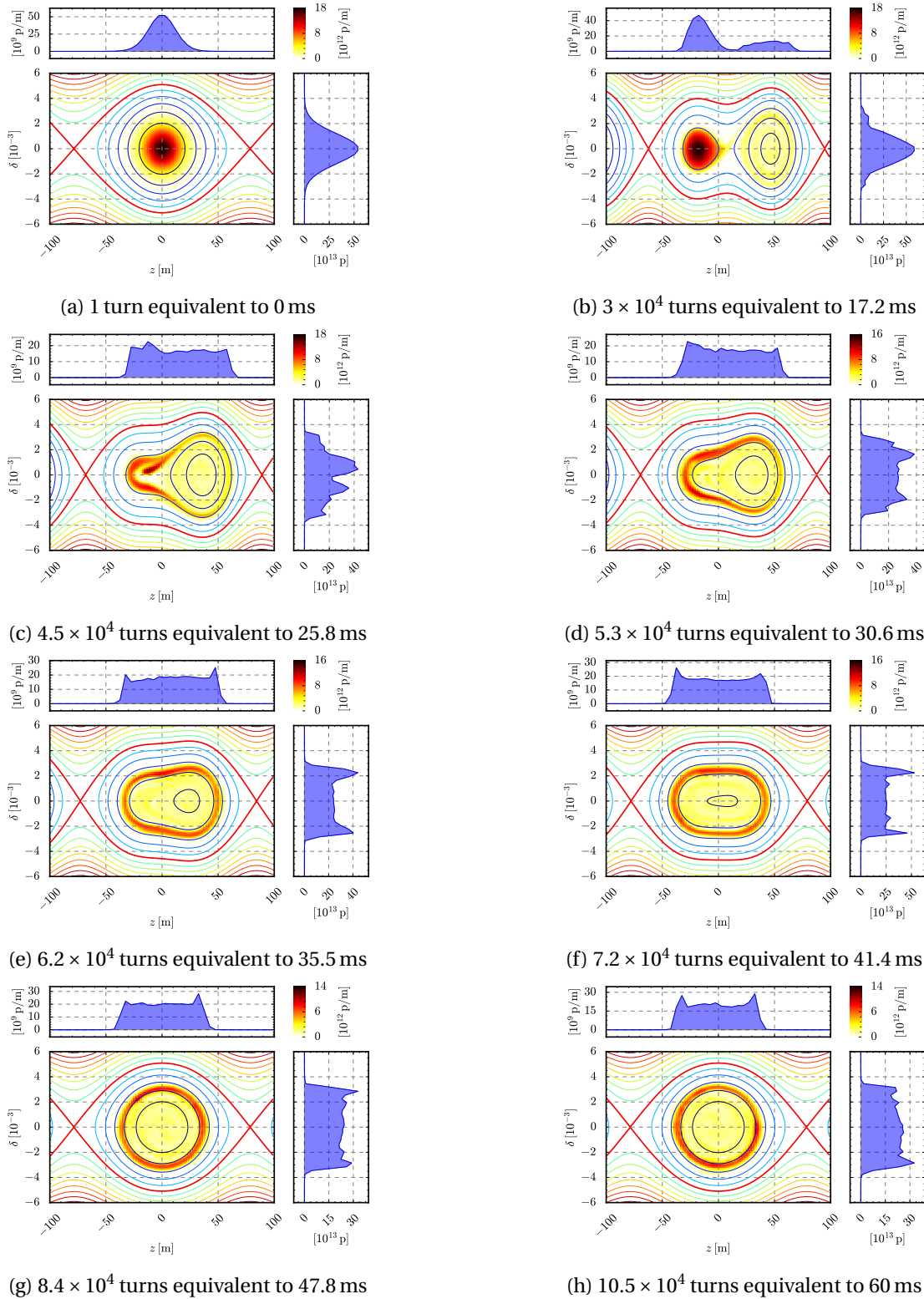
Figure 5.3 – Longitudinal phase space (z, δ) during the RF gymnastics depicted in figure 5.2a. Starting from a Gaussian distribution, an empty second-harmonic bucket is adiabatically opened and recombined with the other full bucket during a controlled blow-up. The simulation includes longitudinal space charge effects.

(a) These RF gymnastics of the second-harmonic system (voltage $V_{1,2}$ and phase offset $\phi_{1,2}$)...

(b) ... create this hollow distribution when neglecting the influence of longitudinal space charge.
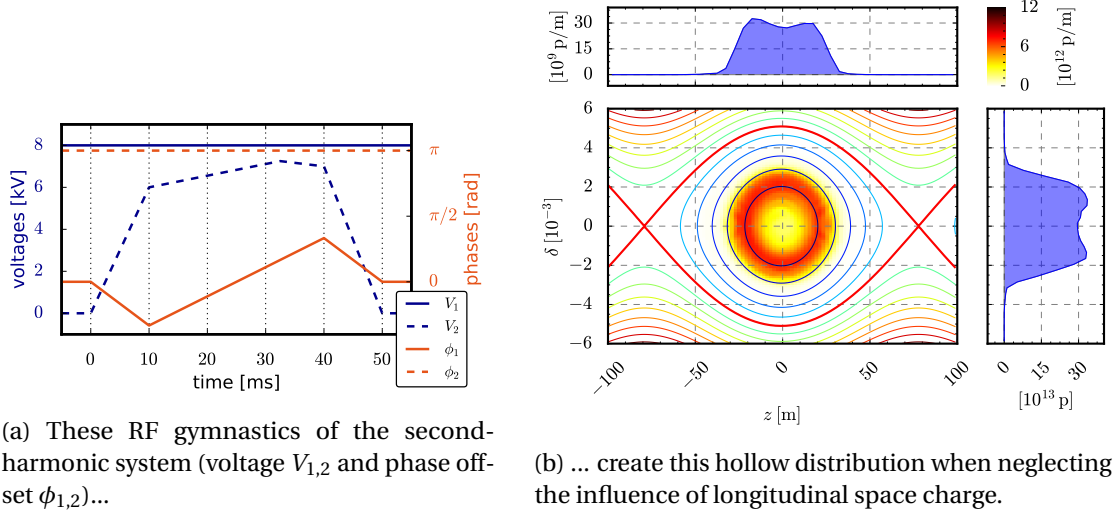
Figure 5.4 – Inversion of the longitudinal phase space distribution.

Dipolar Parametric Resonance

The previous two strategies rely on the use of a double harmonic RF system. The following approach turns out to be quite flexible and works for a single harmonic system. In 1993 the idea emerged to deliberately drive the bunch onto a *parametric resonance* [Cappi, Garoby, et al. 1993]. To this end the phase loop feedback system is used, which aligns the RF reference phase ϕ_{rf} with the centre-of-gravity of the bunch. The dipole mode of the longitudinal parametric resonance is excited by phase modulation [Lee 2004]. Doing so, the central particles can be excited to higher synchrotron amplitudes during only a few synchrotron periods T_S and consequently the bunch core depletes. We modulate the phase loop offset around the synchronous phase φ_s:

$$\phi_{\mathrm{rf}}(t) = \varphi_s + \hat{\phi}_{\mathrm{drive}} \sin(\omega_{\mathrm{drive}} t) \quad . \tag{5.1}$$

To excite the beam, the driving frequency ω_{drive} needs to satisfy the resonance condition

$$m\omega_{\mathrm{drive}} \simeq n\omega_S \quad , \tag{5.2}$$

where ω_S denotes the angular synchrotron frequency. The integer numbers m and n characterise the $m : n$ parametric resonance. The $m = 1$, $n = 1$ resonance proves most useful for our purposes – higher harmonic resonances deplete the bunch centre less as they produce two or more filaments pointing outwards from the core (instead of just one). Figure 5.6 illustrates such a measured phase space distribution resulting from driving the $1 : 2$ resonance.

In fact, in order to optimally hollow out the Gaussian distribution one needs to excite at a slightly lower frequency than the linear synchrotron frequency $\omega_{S,0}$ in the centre, $\omega_{\mathrm{drive}} \lesssim 0.95\omega_{S,0}$. This corresponds to the frequency at a synchrotron amplitude equivalent to a third

(a) 1 turn equivalent to 0 ms

(b) 2.5×10^4 turns equivalent to 14.4 ms

(c) 3.8×10^4 turns equivalent to 21.5 ms

(d) 4.5×10^4 turns equivalent to 25.6 ms

(e) 5.2×10^4 turns equivalent to 29.6 ms

(f) 6.0×10^4 turns equivalent to 34.5 ms

(g) 7.0×10^4 turns equivalent to 39.9 ms

(h) 8.75×10^4 turns equivalent to 50 ms
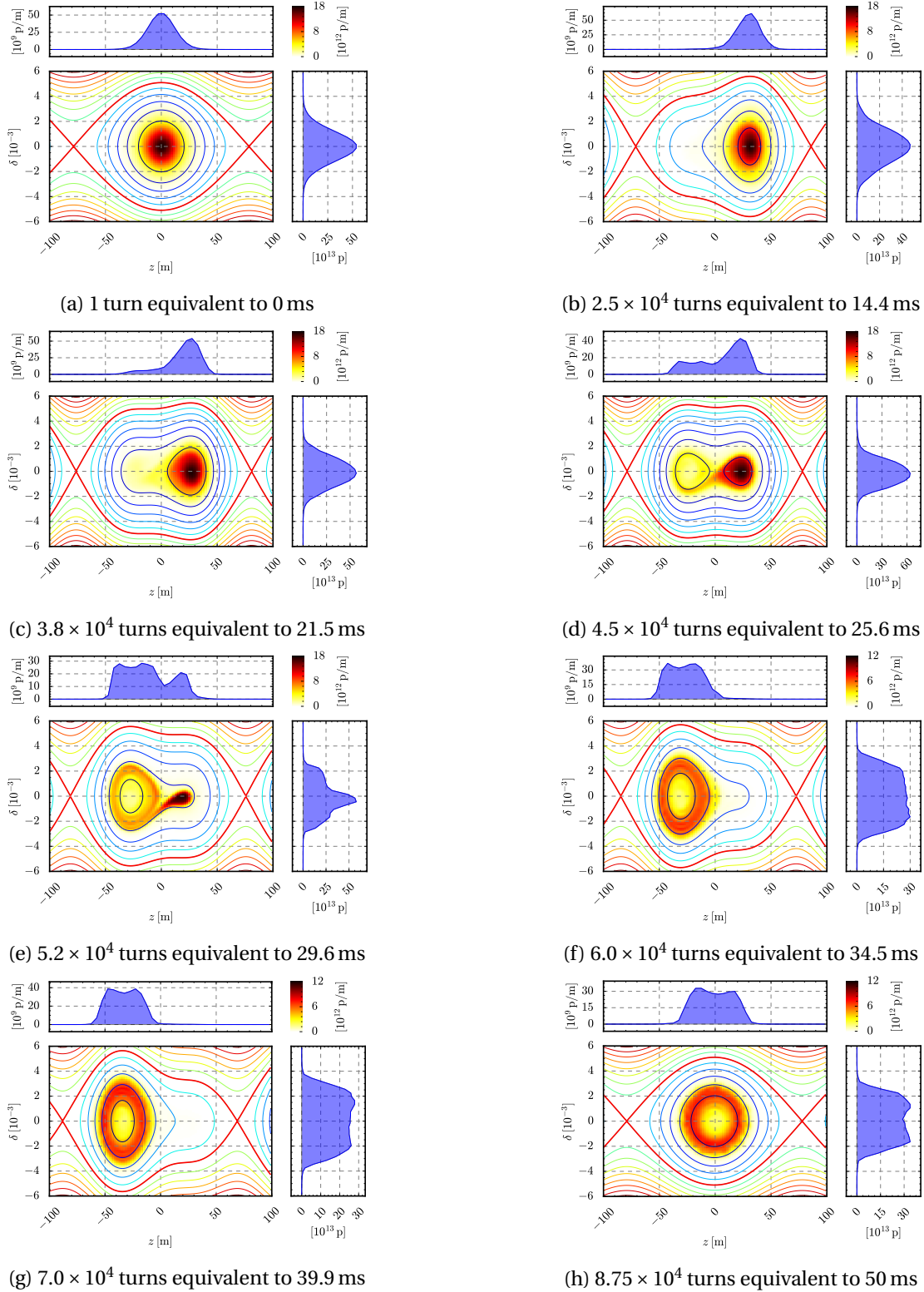
Figure 5.5 – Longitudinal phase space (z, δ) during the RF gymnastics depicted in figure 5.4a. The dense centre of the Gaussian is exchanged with the sparse exterior. The simulation includes longitudinal space charge effects.
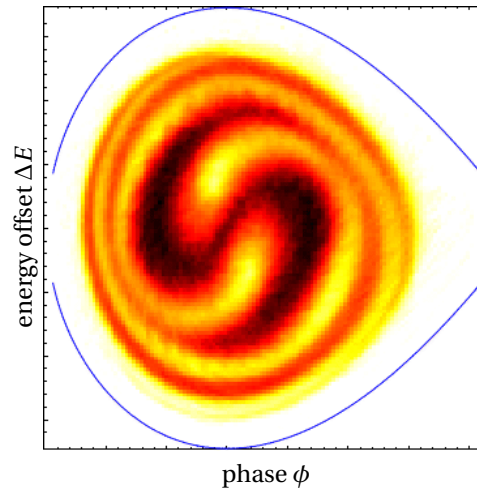
Figure 5.6 – Longitudinal phase space $(\phi, \Delta E)$ via phase space tomography measured in the PS Booster (with $\phi = -hz/R$ and $\Delta E = \delta p_0 c/\beta$ to relate to the variables used in the simulations). The distribution resulted from a $1:2$ dipolar parametric resonance which has been excited during seven synchrotron periods. The corresponding two filaments spiralling outwards from the core are clearly visible.

of the separatrix value.

Figure 5.7 shows the effect for a small ratio of the longitudinal emittance to the bucket acceptance ($1.3\,\mathrm{eVs}$ to $7.3\,\mathrm{eVs}$): the whole bunch is hit by the resonance. All particles initially move within the bucket centre in the linear regime at $\omega_{S,0}$ and are driven to much higher synchrotron amplitudes.

The azimuthal angular spread in phase space directly follows from the synchrotron frequency spread due to the non-linearities of the sinusoidal bucket: particles on inner contours close to the bucket centre move at higher synchrotron frequencies and rapidly leave the particles on the outer contours behind. The modulation duration determines the azimuthal span to which the excited particles surround the depleted bucket centre. The optimal duration distributing the particles as evenly as possible depends on both the excitation amplitude $\hat{\phi}_{\mathrm{drive}}$ and the ratio between longitudinal emittance and bucket acceptance.

After this short excitation period the distribution needs to be smoothed: either by filamentation or, to speed up the process, by high-frequency phase modulation.

(a) 1 turn equivalent to 0 ms

(b) 8.6×10^3 turns equivalent to 4.9 ms

(c) 1.3×10^4 turns equivalent to 7.6 ms

(d) 1.8×10^4 turns equivalent to 10.3 ms

(e) 2.3×10^4 turns equivalent to 13.0 ms

(f) 2.7×10^4 turns equivalent to 15.7 ms

(g) 3.2×10^4 turns equivalent to 18.4 ms

(h) 3.5×10^4 turns equivalent to 20.2 ms
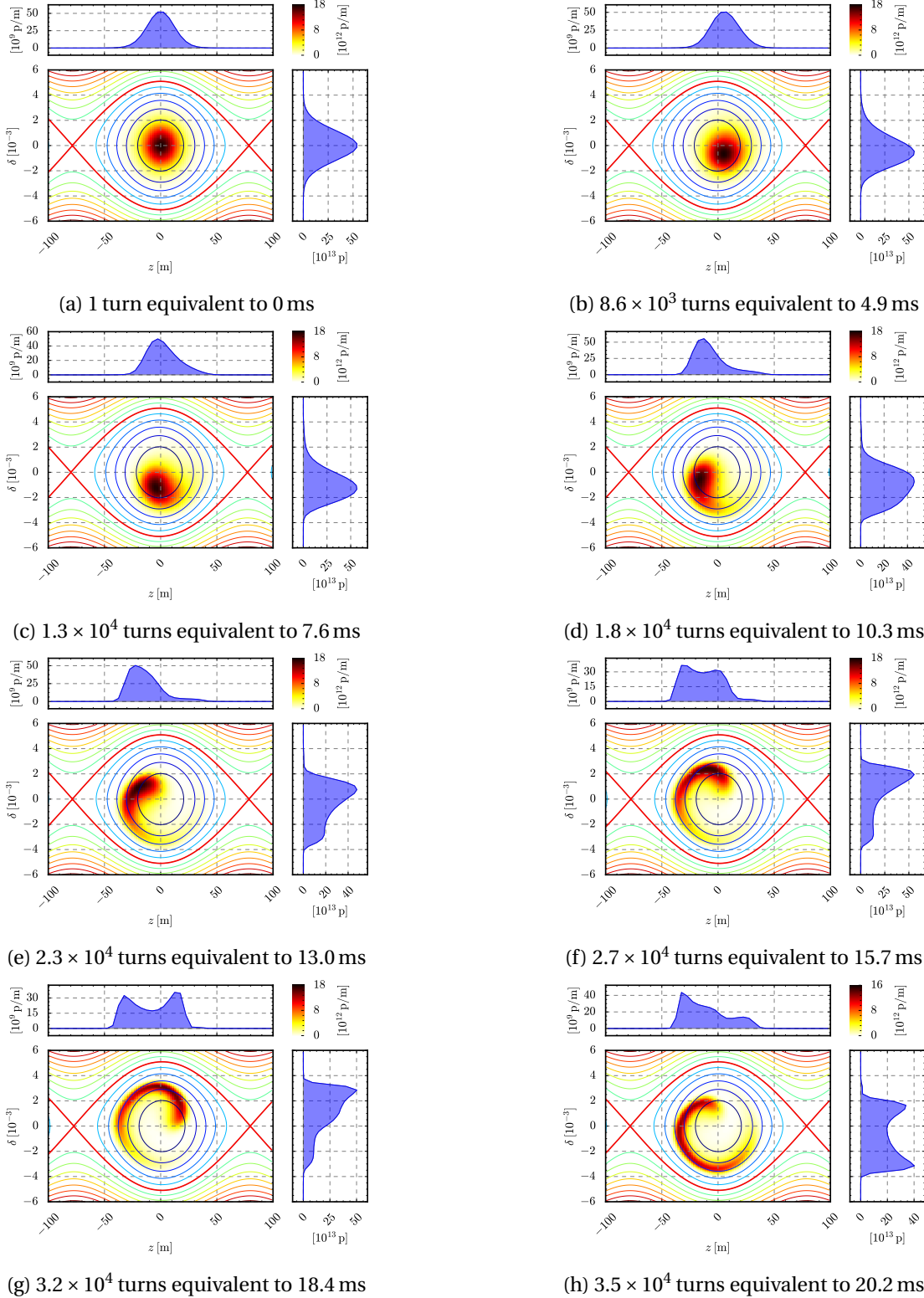
Figure 5.7 – Longitudinal phase space (z, δ) during the RF phase modulation. The excitation of a longitudinal dipolar parametric resonance at $\hat{\phi}_{\text{drive}} = 18°$ is shown for a duration of nine synchrotron periods. The simulation includes longitudinal space charge effects.

5.1.2 Hollow Bunches on the Ramp

In principle, the idea is to add the depletion process involving minimal changes to the operational LHC beam cycles. In the usual PS Booster cycle for LHC beams, the pulse coming from LINAC2 is injected over a certain number of turns while the PS Booster dipole magnetic B-field is ramped (cf. figure 5.8). The RF frequency is kept constant during this process and the beam slowly spirals horizontally inwards [Hancock 2016]. When the injection process is ended, the radial position of the beam is fixed by the fixed RF frequency, which now has to catch up with the canonical revolution frequency programme determined by the dipolar B-field. From this point on the beam momentum $\dot{p} = e\rho\dot{B}$ increases as typical for a synchrotron with radial feedback. This acceleration ramp continues until extraction energy, which is currently at $E_{\text{kin}} = 1.4\,\text{GeV}$. The time derivative of the dipolar magnetic field strength rises up to a maximum of $\dot{B} = 2.27\,\text{T/s}$.
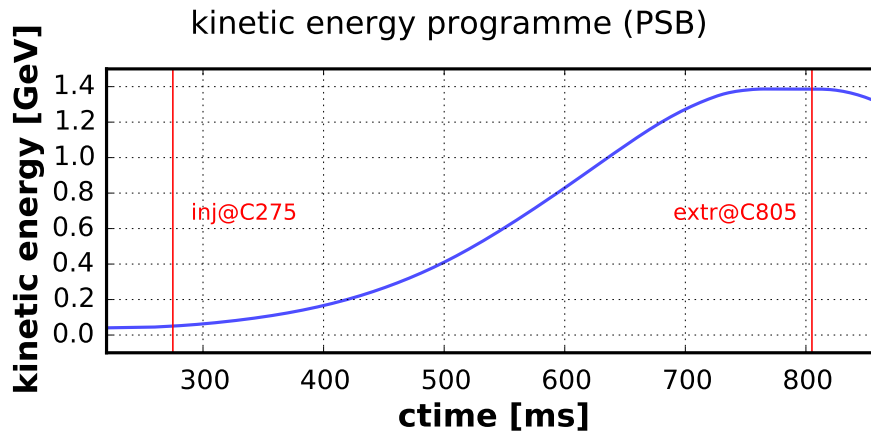
Figure 5.8 – Kinetic energy along the PS Booster cycle [Hanke 2013].

As emphasized before, the first two hollow bunch creation schemes, namely the insertion of empty phase space as well as the inversion of the phase space distribution, rely on the double harmonic RF systems. Adapting the described necessary voltage and RF phase programmes to the acceleration ramp would require detailed fine-tuning. Tailoring the resulting hollow bunches to varying requirements regarding e.g. longitudinal emittance involves non-trivial adaptations of the RF gymnastics for each setting.

The excitation of the $1:1$ dipolar parametric resonance appears more straightforward regarding these concerns. Therefore we decided to study this scheme as a simple add-on during acceleration. Simulations indeed proved the scheme to work fine on the ramp. This means, one can apply this hollow bunch creation scheme in a flexible way to the existing LHC beam cycle in the PS Booster without modifying the magnetic ramp – which all previous efforts to experimentally create hollow distributions did.

There are only two adaptations necessary: on the one hand, the driving frequency ω_{drive} needs to be adapted to the decrease of the synchrotron frequency $\omega_{S,0} \propto \sqrt{\cos(\varphi_s)}$. On the

other hand, we change to a single harmonic bucket during the excitation by switching off the double harmonic RF systems. Present operation uses them for bunch shaping during the entire acceleration ramp.

5.1.3 Longitudinal Space Charge Effects

We have conducted intensity scans up to $N = 6.4 \times 10^{12}$ for all three hollow bunch creation schemes to analyse the impact of longitudinal space charge on the mechanism.

For the two double harmonic based schemes, the depletion of the bunch does not significantly depend on the intensity. The bunch profiles feature local spikes during the creation process. As the PS Booster operates below transition, longitudinal space charge acts in a defocusing manner and these spikes dilute slightly. This results in wider rings in the final hollow product. In the (academic) case above transition, however, space charge focuses these spikes, which are especially pronounced in the 'insertion of phase space' strategy. Consequently, we see microwave instabilities developing at higher intensities.

The parametric resonance mechanism, however, depends on the beam intensity. For a constant driving amplitude $\hat{\phi}_{\mathrm{drive}}$, the obtained depletion decreases with increasing N. To analyse this, we excite the resonance very weakly at a driving amplitude of $\hat{\phi}_{\mathrm{drive}} = 0.025\sigma_z/R \approx 0.7°$. Without space charge, the bunch needs about 25 synchrotron periods to spread around the bucket centre. Figure 5.9 illustrates the influence from longitudinal space charge: for increasing N the core resists to spread azimuthally. The lower amplitude particles appear to follow their orbits at the same frequency as the outer higher amplitude particles. This means that the frequency spread due to the non-linear sinusoidal bucket is counteracted by the local space charge forces.

(a) $N = 0.16 \times 10^{12}$ (b) $N = 0.64 \times 10^{12}$ (c) $N = 1.6 \times 10^{12}$ (d) $N = 3.2 \times 10^{12}$
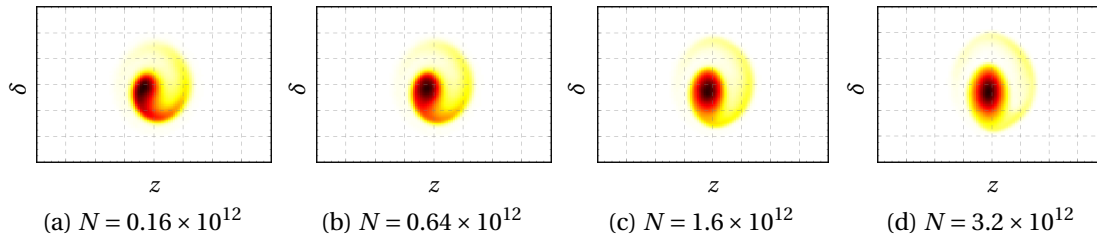
Figure 5.9 – Longitudinal phase space (z, δ) for different intensities N after $25\,T_S$ of excitation at a very weak driving amplitude of $\hat{\phi}_{\mathrm{drive}} \approx 0.7°$. The simulation shows for increasing intensities how the bunch core ceases to decohere during the resonant centroid motion. Longitudinal space charge prevents the azimuthal spreading and hence works against the hollowing mechanism. The numeric experiment is conducted at 2 GeV, the future PS Booster extraction energy where space charge is expected to play a minor role compared to lower energies.

The linearised space charge force for a longitudinally Gaussian beam profile,

$$Q_S^2 = Q_{S,0}^2 + \frac{1}{\sqrt{2\pi}\sigma_z^3} \frac{N r_0 \eta R^2 g}{\beta^2 \gamma^3} \quad , \tag{2.89}$$

shows the synchrotron tune depression below transition as $\eta < 0$. To compare this space charge tune depression with the effect from the non-linear bucket, we ran longitudinal simulations during 100 synchrotron periods in the PS Booster ($\eta < 0$) for various intensities. All simulation runs start from the same initial Gaussian distribution with $\sigma_z = 15\,\text{m}$ r.m.s. bunch length. We fix particles at synchrotron amplitudes across the whole bunch and extract their synchrotron tune by Fourier transforming their longitudinal motion. These values are plotted in figure 5.10 versus the respective initial synchrotron amplitudes, which are expressed as the maximal spatial amplitude z_{max} of the particle's trajectory.
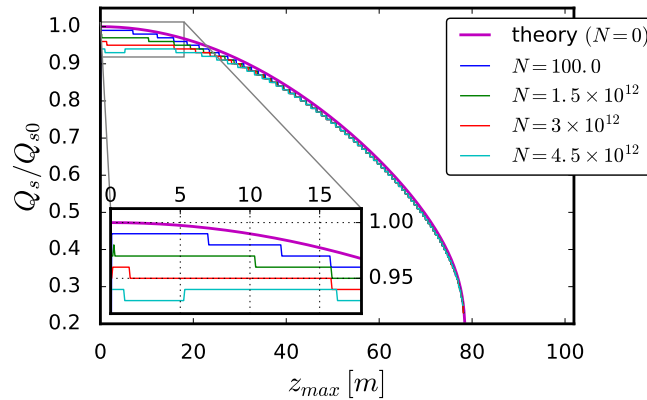
Figure 5.10 – The ratio of actual synchrotron frequency Q_S to linear synchrotron frequency $Q_{S,0}$ versus the synchrotron amplitude expressed as z_{max} (in maximal coordinate amplitude units). The influence of longitudinal space charge from the Gaussian bunch with $\sigma_z = 15\,\text{m}$ bunch length below transition adds to the synchrotron tune depression due to the non-linear bucket.

At $z_{max} = 0$ one can directly observe the tune depression given by equation (2.89). Then, for larger synchrotron amplitudes towards the bucket separatrix, the non-linear sinusoidal bucket additionally reduces the linearised synchrotron tune.

Without space charge for $N = 0$, one obtains a certain tune spread across the bunch comparing the bucket centre $z_{max} = 0$ to the bunch ends at $z_{max} = 2\sigma_z = 30\,\text{m}$. This effect becomes even more pronounced if one would move the bunch centre to non-zero z. The closer we shift the bunch centre towards the separatrix, the larger the synchrotron tune spreads across the bunch. This is precisely the mechanism that leads to the angular spreading of the bunch in longitudinal phase space during the parametric resonance depletion procedure.

Now, adding the space charge effect, figure 5.10 reveals that at larger intensities N the tune spread across the bunch diminishes (compare again between $z_{max} = 0$ and $z_{max} = 30\,\text{m}$). For $N = 4.5 \times 10^{12}$, the Gaussian bunch imprints a nearly constant plateau onto the parabolically decreasing $N = 0$ synchrotron tune curve: space charge makes the bunch resist phase focusing. (At yet larger intensities or smaller σ_z the tune around the origin would even turn into a local dip.) This effect is known as suppression of decoherence by space charge [Rumolo, Boine-Frankenheim, et al. 2003].

In the same way, the bunch deforms the violet synchrotron frequency curve when the bunch centre is moved to larger $z > 0$. This leads to a reduction of the synchrotron tune spread across the bunch core. Consequently, the core does not spread out azimuthally in longitudinal phase space after it has been excited to non-zero z_{max} by the dipolar parametric resonance, which explains the previously mentioned findings presented in figure 5.9.

The analysis in terms of frequency spread also provides a possible remedy: the absolute tune spread ΔQ_S per Δz due to the bucket non-linearities (i.e. the derivative of the magenta curve in figure 5.10) evidently increases towards the separatrix. Therefore, exciting the particles to higher synchrotron amplitudes by means of a larger driving amplitude $\hat{\phi}_{\text{drive}}$ may restore a sufficient synchrotron tune spread across the bunch in order to surround the bucket centre with particles.

Large-scale parameter scans for the driving frequency ω_{drive}, the excitation duration $T_{\text{excitation}}$, the driving amplitude $\hat{\phi}_{\text{drive}}$ and the bunch intensity N simulated for various PS Booster cycle times (which correspondingly influence the bucket size, the beam momentum and the impact strength of longitudinal space charge) revealed optimal regions for the experimental production of hollow bunches in the PS Booster. The modulation duration determines the azimuthal span to which the excited particles surround the depleted bucket centre. The optimal duration distributing the particles as evenly as possible depends in descending importance on the excitation amplitude $\hat{\phi}_{\text{drive}}$, the ratio between longitudinal emittance and bucket acceptance, and the beam intensity. Good values lie between $T_{\text{excitation}} = 4 T_S \dots 7 T_S$.

5.2 Implementation in the Proton Synchrotron Booster

In order to apply the phase modulation concept to the real machine, one needs to make use of the RF phase feedback systems in the PS Booster. The situation is a bit more involved than in the simulation model, as there are competing RF feedback systems: the radial position of the beam is steered via the "radial loop" controlling the RF frequency while the beam phase is regulated via the "phase loop". Both beam variables are therefore interlinked and modulating the RF phase will necessary involve both loops. Already during normal operation (without any "exotic" attempts to drive resonances) the gains for the two systems need to be carefully balanced to achieve the wanted behaviour in both beam variables.

As the whole low-level RF (LLRF) system has been digitised recently, the phase loop reference phase was initially controlled via a fixed register value. Our first attempts to drive the parametric longitudinal resonance hence operated with the radial loop [Oeftiger, Bartosik, A. J. Findlay, et al. 2016]. The resonant motion was indeed observed but, since the resistance of the phase loop could not be sufficiently suppressed, the resonance appeared to be severely damped. This approach produced rather disturbed hollow distributions and was therefore not followed up.

Instead, the reference phase steering has been set up to directly exploit the phase loop in place

of the radial loop. Experiments with varying bucket acceptances – by choosing different cycle times the bucket size changes due to acceleration – and initial longitudinal beam emittances lead to determining the optimal excitation time: we established a reliable procedure to create hollow bunches on the acceleration ramp via driving the parametric resonance at $E_{\mathrm{kin}} = 0.71\,\mathrm{GeV}$ which is reached at cycle time C575. Figure 5.11 exhibits the longitudinal phase space distribution at relevant cycle times until injection into the Proton Synchrotron. Appendix A explains the details of the process in terms of the low-level RF parameters.

We start exciting the parametric resonance from a parabolic distribution, cf. figure 5.11a. At this point, the bunch has been blown up to a matched emittance of $\epsilon_{z,100\%} \approx 1.1\,\mathrm{eVs}$. The separatrix indicates the accelerating single-harmonic bucket featuring an acceptance of $1.8\,\mathrm{eVs}$.

Figure 5.11b depicts the long filament into which the bunch has been turned during the six synchrotron periods long excitation. The lower plot in the right panel shows phase space density averaged over an iso-Hamiltonian orbit around the stable fixed point (at the origin) versus synchrotron amplitude, with the latter represented by the intercept of that orbit on the negative energy half-axis. The upper plot then plots the cumulated particle density versus synchrotron amplitude, correspondingly represented on the upper energy half-axis. At the separatrix we find an accumulated 100% of the distribution. Both graphs clearly demonstrate the central depletion of the distribution: below, the local density vanishes towards zero energy corresponding to the yellow hole in the left phase space graph. Above, the cumulated density remains at zero until the filament begins.

After smoothing by means of a controlled longitudinal blow-up we finally obtain a matched hollow distribution, as illustrated in figure 5.11c, 5 ms before extraction to the PS. During the smoothing, the bunch centre has intentionally been slightly refilled with particles, which thus flattens the longitudinal projection and prevents spikes at both ends of the bunch profile. The lower right graph shows the correspondingly increased central density, which is approximately two thirds of the maximum density within the ring.

Driving frequency scans for the parametric resonance revealed a broad and sharply defined resonance window. The beam turned out to be correctly excited for frequencies in the range

$$649\,\mathrm{Hz} \leq f_{\mathrm{drive}} \leq 734\,\mathrm{Hz} \quad .$$

At the same time, the beam features a synchrotron frequency of $f_{S,0} = 775\,\mathrm{Hz}$ at C575 when the excitation begins, which decreases to $f_{S,0} = 730\,\mathrm{Hz}$ at C590 (after seven synchrotron periods of excitation). The limits of this resonance window are sharply defined on the level of 1 Hz, as figure 5.12 clearly indicates.

Careful adjustments of the phase loop feedback systems allowed to minimise the non-linear interaction of the beam with the damping mechanisms during the resonance driving period. For a too strong gain, the phase loop continuously realigns the phase of the main C02 cavities

(a) PS Booster cycle time C573, 2 ms before the excitation

(b) PS Booster cycle time C591, directly after the excitation

(c) PS Booster cycle time C800 (5 ms to extraction)

(d) PS cycle time C171, directly after injection.
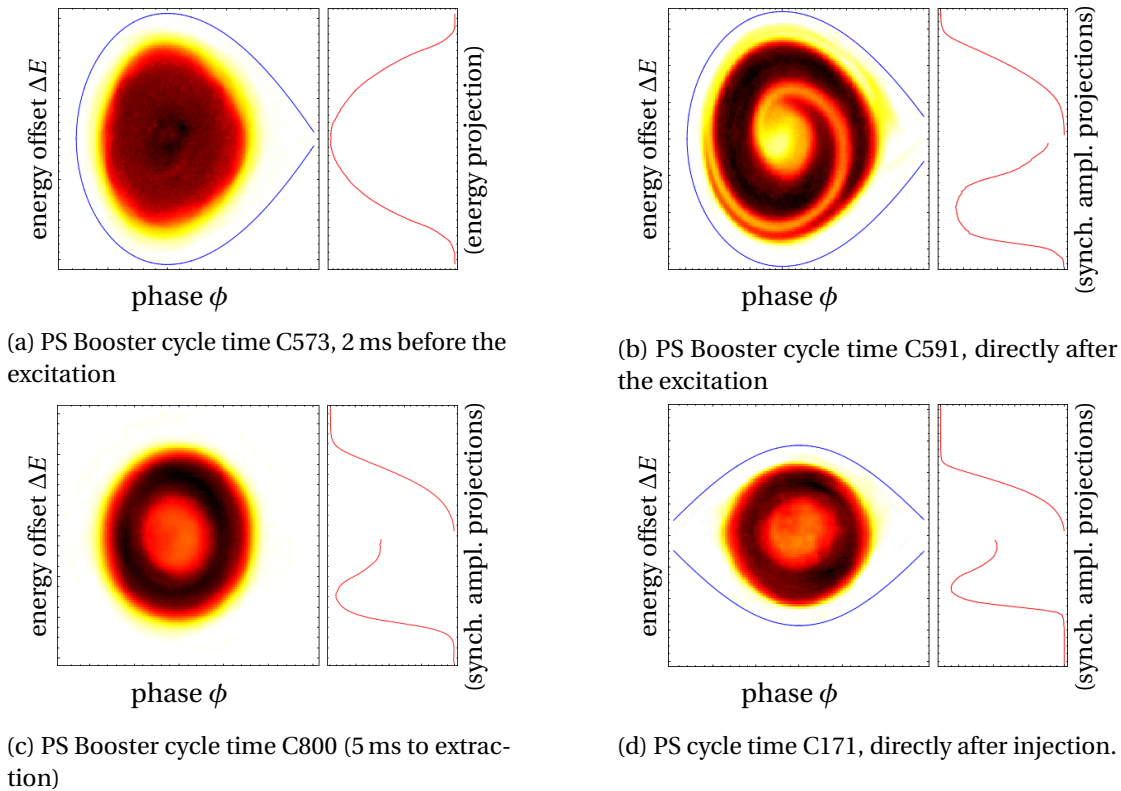
Figure 5.11 – Longitudinal phase space ($\phi, \Delta E$) and projections (cf. text) at different stages during the hollow bunch creation process in the PS Booster. The density (colour) scales differ across the plots.

with the beam. This counteracts the excitation and leads to severely perturbed distributions. On the other hand, too weak gains lead to beam loss as the RF systems detach from the beam signal reference. Observing the beam centre-of-gravity signal during the excitation enabled us to find a phase loop gain which achieves a clean 90° delay of the resonating beam phase in response to the sinusoidal phase modulation. Also the amplitude of the beam phase signal shows whether the beam gets damped by the phase loop. We exploited this to minimise the damping impact which corresponds much closer to the simulation model.

Figure 5.13 shows the match between simulated and measured phase space distribution for the same parameters at the same time after the excitation. This match was not achieved when the impact of the feedback systems significantly damped the resonance, as the major part of the distribution would not blow up while peripheral particles appeared violently shaken around the bucket in the tomographically reconstructed phase space measurements.

The beam distributions created with the established process proved to be reliably depleted: repetitive tomography [Hancock, Lindroos, and Koscielniak 2000] measurements on many consecutive pulses (each directly after the excitation) consistently provided the same phase space distribution.

(a) $f_{\text{drive}} = 648\,\text{Hz}$ (b) $f_{\text{drive}} = 649\,\text{Hz}$ (c) $f_{\text{drive}} = 734\,\text{Hz}$ (d) $f_{\text{drive}} = 735\,\text{Hz}$
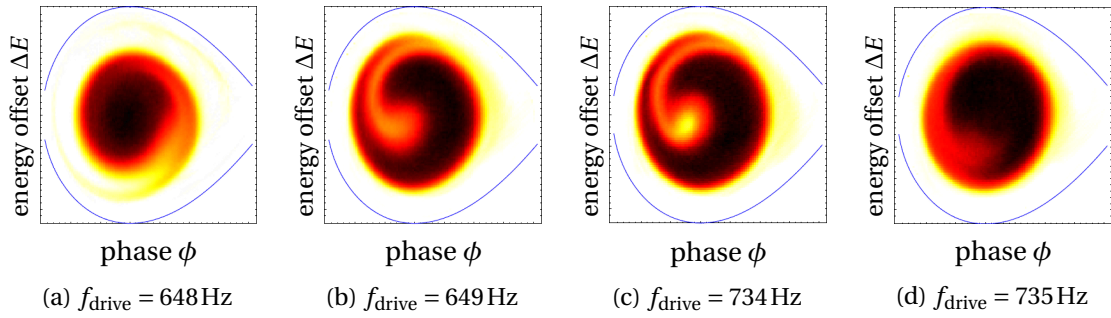
Figure 5.12 – Longitudinal phase space $(\phi, \Delta E)$ at cycle time C590 after the dipolar parametric resonance at various driving frequencies ω_{drive}. The beam response to the excitation reveals a sharply defined driving frequency window between 649 Hz and 734 Hz.
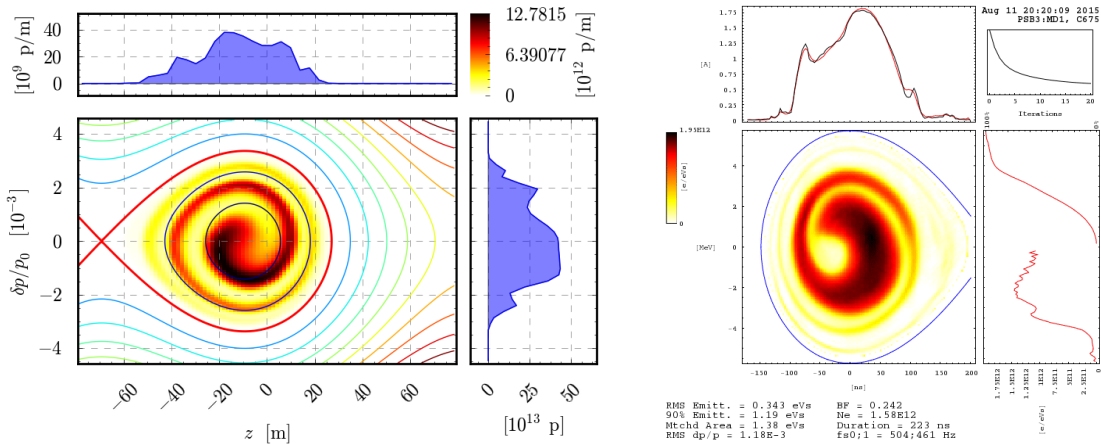
(a) PyHEADTAIL with longitudinal space charge, the longitudinal coordinate z relates to the phase via $z = -\phi R$.

(b) PS Booster measurement for the same time.

Figure 5.13 – Simulation and measurement in the PS Booster agreed quite well, as these snapshots taken at the same time after the excitation show, given the same parameters for both set-ups. PyHEADTAIL simulations including longitudinal space charge facilitated the machine implementation process by enhancing the understanding of the dynamics (as continuous observation of the phase space is possible) for a given set of parameters.

During these reproducibility assessments, we observed high-frequency modifications in the filaments, cf. figure 5.14. Varying the injected turns in the PS Booster revealed a clear dependency on the beam intensity which is a hint to an evolving instability at around 40 MHz. While these dynamics did not influence the resulting hollow bunches in any obvious way, it nevertheless showed that exotic distributions such as ours may provide an interesting tool to visualise and analyse such high-frequency influences.
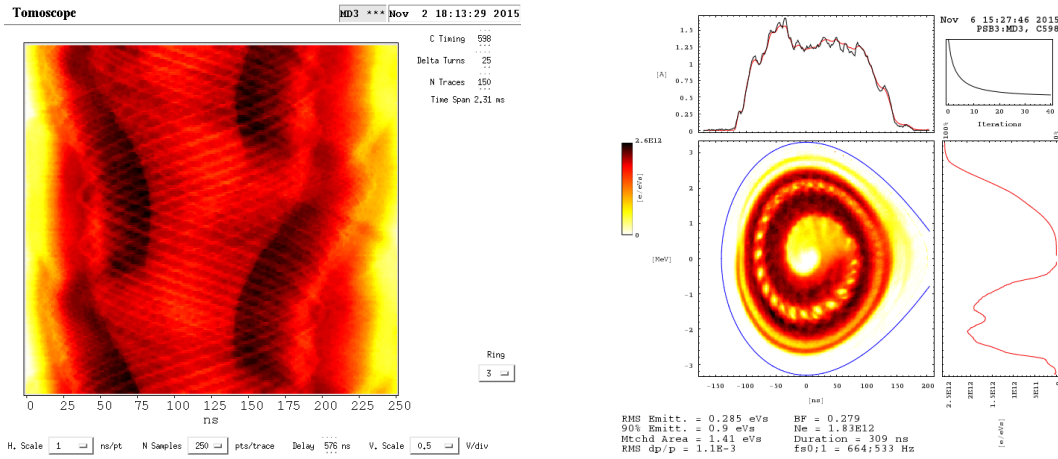
(a) Longitudinal waterfall plot showing empty phase space droplets interspersing the oscillating distribution during the excitation.

(b) Phase space tomography clearly reproduces the empty droplets which occur at a high frequency of roughly 40 MHz.

Figure 5.14 – During the driven oscillation, the phase space distribution is sensitive to high-frequency influences seen with high intensity bunches.

5.3 Behaviour in the Proton Synchrotron

Transverse space charge simulations in the PS over 2000 turns provide the incoherent particle tune footprint of the hollow distribution (generated in the PS Booster simulations). The flat profile of a hollow bunch reduces the extension of the tune spread: the usual wide tune spread from Gaussian profiles is strongly compressed as the line charge density in the front and the tail of the bunch becomes closer to the level of the bunch centre, cf. figure 5.15. This entails that most particles feature an incoherent tune around the same value. The remaining spread comes from the transverse Gaussian nature of the beam as well as the longitudinal flanks (the profile is not perfectly rectangular).

5.3.1 Bunch Splitting for Hollow Bunches

The 72 bunch production scheme in the PS is mainly used for LHC type beams [Damerau 2011]. To reach large intensities, two subsequent batches spaced by one basic cycle of 1.2 s are injected into the PS. For the first batch, all four PS Booster rings provide one bunch each, then the second batch arrives with two more bunches. The six bunches are received by the PS at

(a) Gaussian footprint with $\Delta Q_y^{SC} \approx 0.31$.

(b) Hollow footprint for the same parameters.

Figure 5.15 – Tune footprints for both a Gaussian and a hollow distribution in the PS with the same beam characteristics (intensities, transverse emittances and total bunch lengths) [Wasef 2013].

fundamental $h = 7$. Then the PS accelerates from the present injection energy at $E_{kin} = 1.4\,\text{GeV}$ to an intermediate plateau at $E_{kin} = 2.46\,\text{GeV}$, cf. figure 5.16. In order to reach the final 72 bunches, RF gymnastics split the initial 6 bunches into 3, then 2 and again 2 bunchlets during the PS cycle.

The first adiabatic change to a fundamental of $h = 21$ between cycle times C1830 and C1890 essentially constitutes the "triple splitting". It is set up on the intermediate energy plateau and is preceded by two controlled longitudinal blow-ups (one during 15 ms at C1375 and the second during 25 ms at C1480).
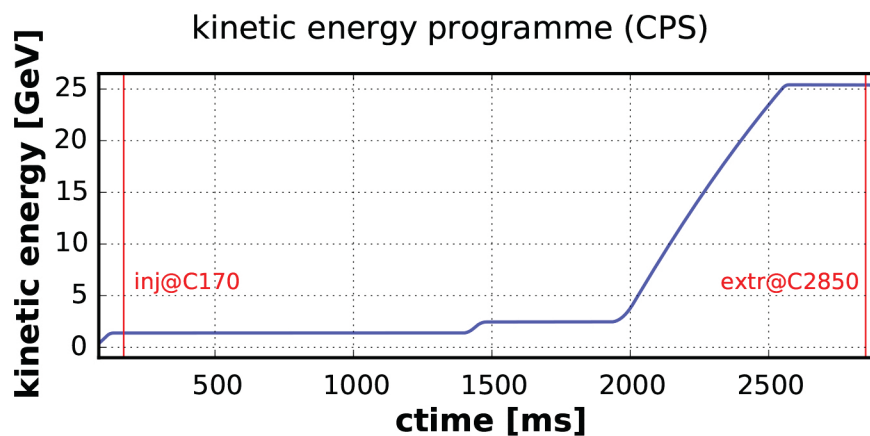
Figure 5.16 – Kinetic energy along the double batch injection PS cycle [Damerau 2011].

We continue to work with the single hollow bunch injected as a first "batch". In order to observe how the triple splitting process affects the longitudinal phase space distribution, we

switch off the two canonical blow-ups which would otherwise disrupt the hollow distributions. Figure 5.17a shows the evolution of the line density as the flat bunch is split into three. Indeed, tomographic reconstruction of the phase space after the splitting reveals the lasting hollowness of the central bunchlet. The outer bunchlets remain flat (flatter than for the usual Gaussian distributions). The ratio of depletion between the outer and central bunch might depend on the thickness of the initial phase space ring: a hollow bunch with a deep dip in the profile might leave a hollow trace in the outer bunches as well – instead, our ring is quite thick as it is tailored to a flat projection.
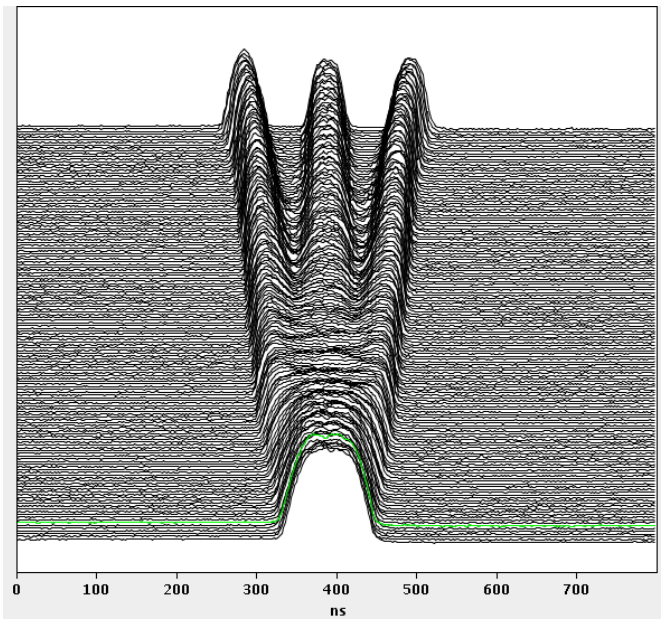
(a) Mountain diagram from C1830 to C1890, each contour represents a longitudinal profile with a step of 185 turns. The horizontal axis is plotted in time units $t = -\beta c z$.

(b) First (left) triplet bunch.

(c) Second (central) triplet bunch.

(d) Last (right) triplet bunch.
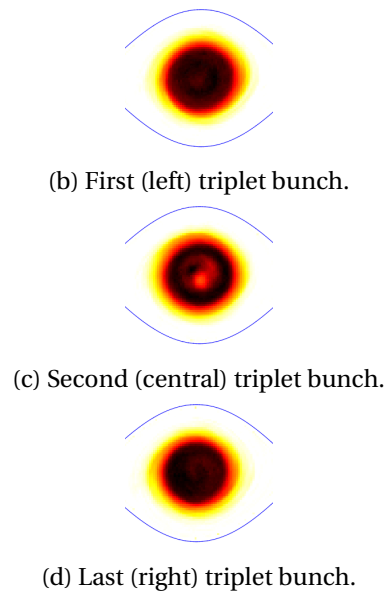
Figure 5.17 – Triple splitting process in the PS for a hollow distribution. The central bunch remains slightly hollow while the outer bunches become flat, as the longitudinal phase space plots on the right illustrate.

After the acceleration ramp at the extraction plateau, the RF fundamental is twice increased by a factor 2 – the so-called "double splitting" to produce $6 \times 3 \times 2 \times 2 = 72$ bunches, going from $h = 21$ to $h = 42$ and then to $h = 84$. Garoby and Hancock [1994] already reported the double splitting to work for hollow distributions: the longitudinal distribution remains intact at a longitudinal blow-up of less than 10%.

5.4 Space Charge Mitigation in the Proton Synchrotron

To assess the impact of direct space charge during the PS injection plateau, we measure transverse emittance blow-up and beam loss under various space charge conditions. The goal is to compare space charge effects between hollow bunches and the usual parabolic bunches. Typical examples of each beam type are shown in figures 5.18a and 5.18b. Since hollow distributions are tailored to reduce the maximum line charge density, one expects a better behaviour under strong space charge conditions. The parabolic LHC type bunches have been further blown up than to the usual $\epsilon_{z,100\%} = 1.3\,\text{eVs}$ (corresponding to a bunch length of $B_L = 180\,\text{ns}$) in order to match the hollow bunch length.

Two different experiments have been conducted to examine possible improvements when deploying hollow bunches:

1. **scanning the bunch length**:
   by compressing the bunch, the maximal line density increases entailing stronger space charge forces. Our strategy is to compare the emittance blow-up between the two longitudinal distributions for a given parameter set of bunch length, transverse emittance and intensity. The space charge detuning (2.87) combines these parameters in a well-defined quantity. The formula assumes a Gaussian distribution in the longitudinal plane, which allows to study the question: "Do hollow bunches lead to less emittance blow-up for a given bunch length, transverse emittance and intensity?"

2. **decreasing the vertical tune**:
   when approaching the integer tune $Q_y = 6$ starting from below the octupole resonance $4Q_y = 25$, the space charge depressed beam will start to resonate and blow up the transverse emittance. The goal is to compare the resonance dynamics between the two beam types. In contrast to the previous scenario where the RF voltage varies, the bunch length and also the synchrotron tune remain constant here. We investigate: "Do the hollow bunches behave better (in terms of emittance blow-up and beam loss) than the parabolic bunches at a given tune distance from the integer resonance?"

These results have partly been reported in Oeftiger, Bartosik, A. Findlay, et al. [2016] and presented in Oeftiger, Hancock, and Rumolo [2016].

5.4.1 Experimental Set-up

The properties of a single injected bunch are measured directly after the first injection from the PS Booster and directly before the second injection takes place. The first four bunches from the PS Booster are injected into the PS at cycle time C170. Correspondingly, the first emittance measurement (labelled 'in') is set to C185. These 15 ms allow injection oscillations to be damped as well as the adjustment of certain RF settings (such as the total RF voltage for the bunch length scan). After a basic cycle period of 1.2 s, a second batch would be transferred from the PS Booster. The second emittance measurement (labelled 'out') is hence taken at C1350, 20 ms before the second injection. Interferences from the transfer preparation systems (e.g. the PS Booster–PS synchronisation loop) can be avoided. The beam and machine parameters are listed in table 5.2.

Table 5.2 – The relevant Proton Synchrotron machine and beam parameters.

parameter	symbol	value
long. 100% emittance hollow	$\epsilon_{z,100\%}$	$1.43 \pm 0.15\,\text{eVs}$
long. 100% emittance parabolic	$\epsilon_{z,100\%}$	$1.47 \pm 0.11\,\text{eVs}$
PS Booster extracted horizontal r.m.s. emittance	ϵ_x	$\approx 2.23\,\text{mm\,mrad}$
PS Booster extracted vertical r.m.s. emittance	ϵ_y	$\approx 2.12\,\text{mm\,mrad}$
injection plateau energy	E_{kin}	$1.4\,\text{GeV}$
synchrotron period ($V = 25\,\text{kV}$)	Q_S^{-1}	$725\,\text{turns}$
fundamental harmonic (flat-bottom)	h	7
PS circumference	C	$2\pi \cdot 100\,\text{m}$
transition energy	γ_t	6.09

At both reference times, the three-dimensional spatial beam distribution is reconstructed along with the longitudinal momentum distribution. At two different locations in the ring, flying wires scan the horizontal and vertical bunch profile. A wall current monitor records the longitudinal beam profile repeatedly over many turns equivalent to half a synchrotron period. The momentum distribution can thus be reconstructed via offline phase space tomography [Hancock, Lindroos, McIntosh, et al. 1999]. In order to ensure a valid comparison between the 'in' and 'out' references, any shots featuring a longitudinal r.m.s. emittance variation of more than 5% are disregarded. Most measurements feature a stable longitudinal r.m.s. emittance though.

(a) Reconstructed parabolic longitudinal distribution.

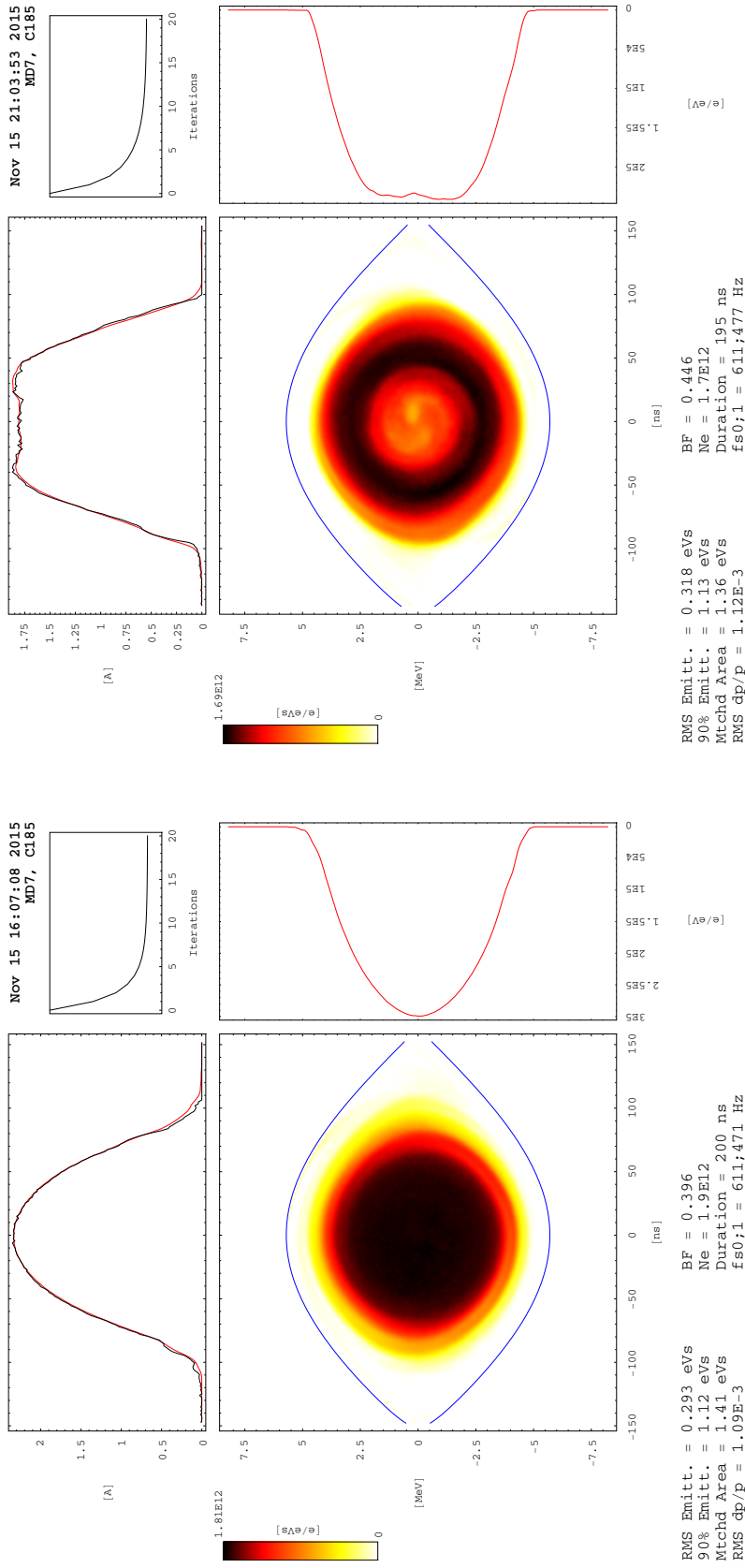(b) Reconstructed hollow longitudinal distribution.

Figure 5.18 – Tomograms of typical candidates for the two compared beam types show the charge density in phase space (t, ΔE) along with the projected beam profile and energy distribution. Both measurements have been taken in the PS at cycle time C185.

5.4.2 Transverse Emittance Determination

Vertical Plane

In order to determine the transverse emittances from wire scans, one needs to account for the shape of the profile. Especially in the vertical plane the beam is affected by the onset of the vertical integer resonance. The vertical profile therefore exhibits pronounced tails: especially at early cycle times a halo emerges as shown in figure 5.19a. If one simply fits the whole profile $p(y)$ with a Gaussian function $g(y)$ via a least squares algorithm, the standard deviation of $g(y)$ will under-represent the tails (see the green curve labelled "general fit" in the figure).

The residual of this general fit, $g(y) - p(y)$, is depicted in figure 5.20. Given the standard deviation σ_{pre} and the mean value y_0 of the general fit, we see a systematic negative deviation from about $1.8\sigma_{\text{pre}}$ on outwards. This feature is present for almost all vertical wire scans. We conclude that the Gaussian fit does not represent the tails. Consequently, we define a "core region" of the bunch within $-1.8\sigma_{\text{pre}} < y - y_0 < 1.8\sigma_{\text{pre}}$ and establish two alternative approaches to determine the transverse emittance.

The 'core emittance' refers to fitting only the core region with a Gaussian function and extracting the vertical emittance from the standard deviation $\sigma_{y,\text{core}}$. To this end, we determine the core region for each wire scan via a first 'general' fit over the whole profile to obtain the estimated σ_{pre}. The measurement set roughly agrees with the Gaussian within the previously defined core region. A subsequent second Gaussian fit constrained to the core domain then yields the core emittance

$$\epsilon_{y,\text{core}} = \sigma_{y,\text{core}}^2 \beta\gamma/\beta_y \quad , \tag{5.3}$$

with β_y denoting the vertical beta function at the wire scanner location.

Alternatively, the 'r.m.s. emittance' $\epsilon_{y,\text{rms}}$ refers to evaluating the statistical standard deviation of the entire measured profile $p(y)$ within a radius of $\sigma_{\text{pre}} < 4$,

$$\sigma_{y,\text{rms}}^2 = \int\limits_{-4\sigma_{\text{pre}}}^{4\sigma_{\text{pre}}} dy \, (y - y_0)^2 p(y) \quad \implies \quad \epsilon_{y,\text{rms}} = \sigma_{y,\text{rms}}^2 \beta\gamma/\beta_y \quad . \tag{5.4}$$

This approach takes into account the tails in an r.m.s. equivalent manner as opposed to the core emittance approach.

The two approaches lead to significantly larger r.m.s. emittances with up to 30% difference to the core emittance. The ratios between the two at both reference cycle times are listed in table 5.3.
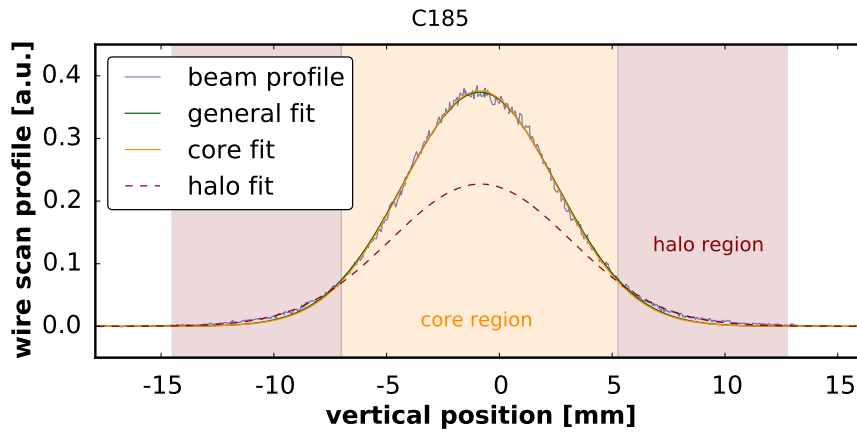
(a) PS wire scan at C185. The distribution shape deviates from a Gaussian profile on the tails due to space charge dynamics: the onset of the vertical integer resonance drove particles from the core to the tails. The core itself (within $\sim 1.8\sigma$) remains more or less Gaussian, as the orange fit shows. The dashed red line shows a separate Gaussian fit to the tails (within $1.8 < \sigma < 4$). The corresponding offset is not reflected in the Gaussian fit to the whole profile shown in green (which essentially matches the orange core fit).
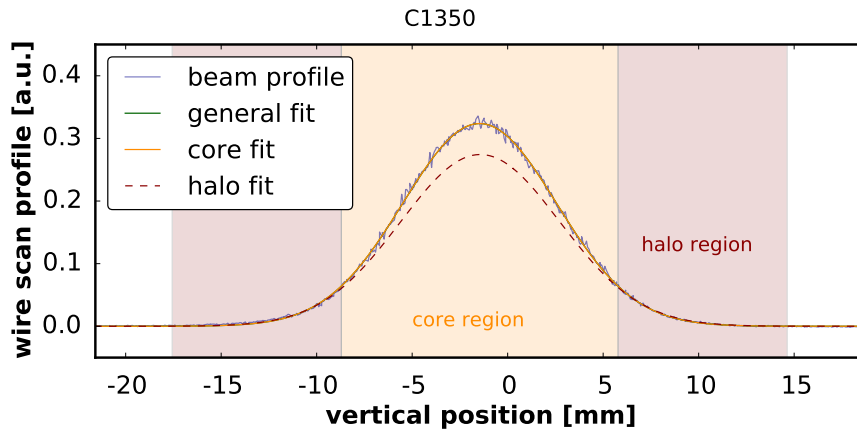
(b) PS wire scan at C1350. The distribution is much broader as the core has blown up significantly. Note that the profile resembles a Gaussian shape much more than at C185, the halo fit approaches the core fit.

Figure 5.19 – Typical vertical beam profiles from wire scans at the beginning and end of the 1.2 s long Proton Synchrotron injection plateau.

Table 5.3 – Significantly different results for core and r.m.s. emittance evaluation in the vertical plane. The data for the hollow and parabolic longitudinal distributions are taken from the bunch length scan.

$\epsilon_{\mathrm{rms}}/\epsilon_{\mathrm{core}}$	C185	C1350
parabolic	1.236 ± 0.024	1.148 ± 0.035
hollow	1.294 ± 0.042	1.215 ± 0.059
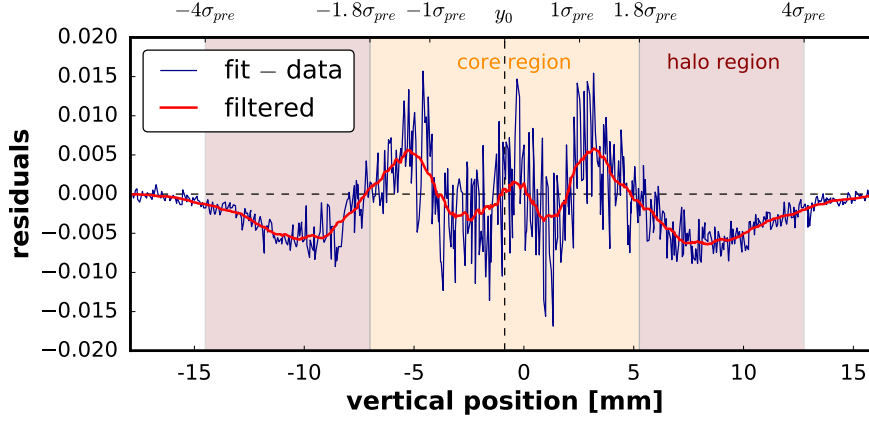
Figure 5.20 – The residual of the general Gaussian fit to the wire scan of figure 5.19a (i.e. the difference between the blue and the green curve). This plot defines the core and the halo regions.

Horizontal Plane

In the horizontal plane, one also needs to account for the dispersive contribution to the beam profile. The horizontal position of a particle is given by a sum of two independent random variables,

$$x = x_\beta + x_{\text{disp}} \qquad \text{with} \qquad x_{\text{disp}} = D_x \delta \quad , \tag{2.23}$$

where x_β denotes the betatron motion and D_x the dispersion function at the wire scanner location. The corresponding horizontal distribution $p(x)$, i.e. the measured wire scanner profile, is hence expressed as a convolution of the betatron distribution $f_\beta(x)$ with the dispersive distribution $f_{\text{disp}}(x) = f_\delta(x/D_x)/|D_x|$:

$$p(x) = \int_{-\infty}^{\infty} dx' \, f_\beta(x - x') f_{\text{disp}}(x') \quad . \tag{2.33}$$

In order to extract the horizontal beam emittance, we are interested in determining the standard deviation of the betatron part x_β of the profile. The standard approach is to fit the profile with a Gaussian distribution with least-squares regression analysis. Consequently, the fit standard deviation σ_x is used with the r.m.s. momentum deviation δ_{rms} (obtained via longitudinal phase space tomography) in the emittance expression (2.35). For the present case this approach is no longer valid, especially in the hollow configuration where the momentum distribution differs from a Gaussian normal distribution by construction. Therefore, the resulting profile is not Gaussian normal and the extracted σ_x does not represent the r.m.s. value of the horizontal distribution. We shall get much more accurate results for the horizontal emittance by manual convolution.

For each horizontal wire scan an instantaneous momentum profile f_δ has been reconstructed

with the aid of tomography. A wire scan takes up to a synchrotron period for traversing the up to 4 cm wide beam at a wire speed of 15 m/s. The recorded horizontal profile therefore consists of a convolution of the pure betatron distribution with the momentum distribution during its temporal evolution over the whole synchrotron period.

Now, some shots (especially at C185 which is 15 ms after injection) exhibit slightly non-stationary momentum distributions such as the blue curve in figure 5.21. This can be traced e.g. to quadrupolar longitudinal mismatch, the impact of the synchronisation loop (especially for the hollow distributions) and recombination kicker rise time overlaps with the beam pulse. Consequently, the momentum distribution will oscillate during the wire scan which in principle results in changing dispersion contributions for each point of the measured profile.

As an approximation, we replace the measured momentum distribution by a stationary estimate, which we then use for the further convolution processing. In longitudinal action-angle variables, we integrate out the angle for each synchrotron amplitude. Mapping this synchrotron amplitude projection back into momentum space yields a good stationary estimate for the filamented equivalent momentum distribution, as figure 5.21 depicts.
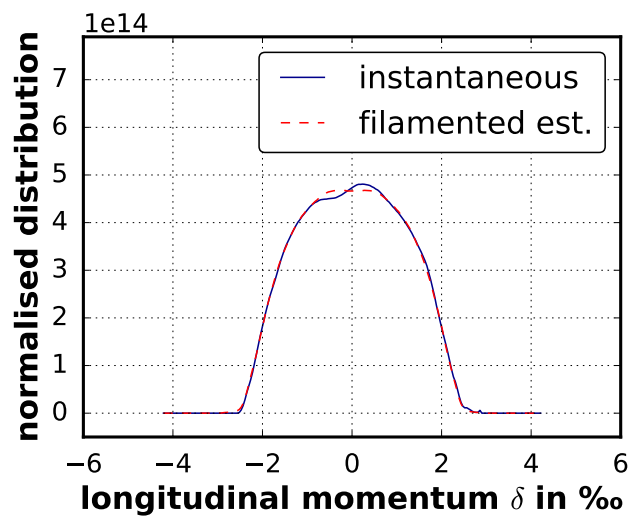
Figure 5.21 – A non-stationary momentum distribution (bound to filament) and its filamented estimate by means of integrating out the angle along the synchrotron amplitude and mapping back onto longitudinal momentum space.

The contributions to the measured wire scanner profile from the betatron motion f_β and from the dispersion f_{disp} are of the same magnitude.

Various approaches to deconvolve $p(x)$ with the measured f_{disp} to obtain f_β have been followed. Polynomial division (via SciPy's `signal.deconvolve`) did not lead to useful results as it requires f_{disp} to be of smaller extent than $p(x)$. The division of the Fourier transforms of $p(x)$ and f_{disp} turned out to be heavily affected by high frequency noise in the profile. Gaussian fits

to the corresponding Fourier spectrum featured large uncertainties.

The finally adopted approach assumes x_β to be Gaussian distributed and leads to reasonable results. Instead of deconvolving, we reverse-engineer $p(x)$ by convolving f_{disp} with a Gaussian profile of some estimated standard deviation σ_{x_β}. As both are normalised to integrate to unity and convolutions are translation invariant, the amplitude and mean value of the Gaussian function are fixed. The only remaining free variable is hence the standard deviation σ_{x_β}. A least squares algorithm is employed to find the optimal σ_{x_β} by comparing the convolution result to the actual wire scanner measurement data $p(x)$. Figure 5.22 shows the various distributions for a hollow case (and hence rectangular-like momentum distribution).
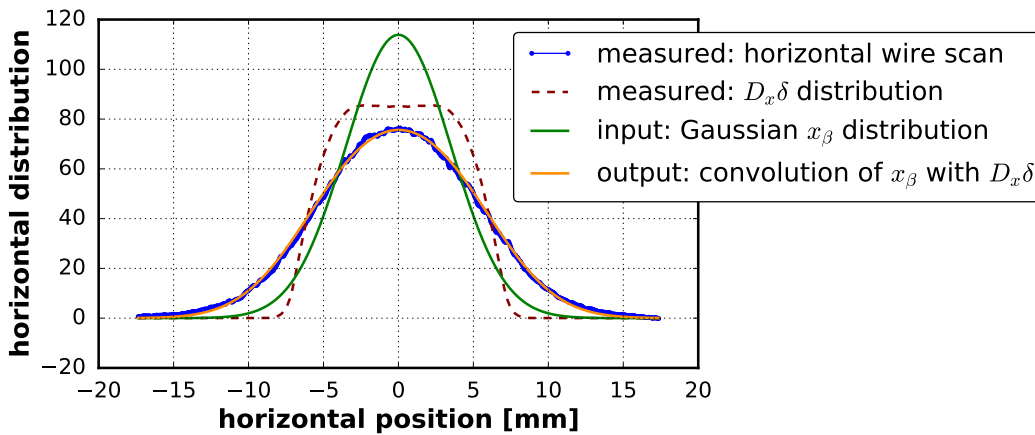
Figure 5.22 – The convolution output of the measured dispersive distribution (consisting of the stationary momentum distribution projection multiplied by the dispersion D_x at the location of the wire scanner) with a Gaussian function as an estimate for the betatron distribution reconstructs the measured horizontal wire scanner profile data. The variable betatron standard deviation σ_{x_β} can then be determined by least-squares-fitting the convolution to the wire scan.

This approach serves for more accurate emittance estimates taking into account the present longitudinal beam geometries and may well be a suitable algorithm for future space charge studies on the CERN low-energy rings. Table 5.4 summarises the overestimation of up to 35% by using the usual formula for the emittance that assumes a Gaussian momentum distribution. In the horizontal case, the pronounced tails found in the vertical plane are less significant but they still contribute to the factor.

5.4.3   Bunch Length Scan

The PS Booster cycles to produce the longitudinally quasi-Gaussian and hollow bunches are set up such that the longitudinal matched ("100%") emittances and therefore the compared bunch lengths are the same. Indeed, the recorded shots had a ratio of $\epsilon_{z,100\%}^{\text{hollow}}/\epsilon_{z,100\%}^{\text{parabolic}} = 0.992 \pm 0.182$. Correspondingly, the geometry of hollow bunches makes their longitudinal r.m.s. emittance consistently larger at a ratio of $\epsilon_{z,\text{rms}}^{\text{hollow}}/\epsilon_{z,\text{rms}}^{\text{parabolic}} = 1.085 \pm 0.052$. The hollow phase space

Table 5.4 – The usual dispersive emittance $\epsilon_{\text{usual-Gauss}}$ formula (2.35) for the Gaussian fit extracted σ_x (assuming perfectly Gaussian profiles) strongly overestimates the horizontal emittance: the present momentum distributions are broader than a perfect longitudinal bi-Gaussian distribution. Consequently, when their contribution is removed, a smaller betatron residual should remain. Also a weakly pronounced halo (similarly to table 5.3) contributes $\sim 10\%$ to these numbers. The $\epsilon_{\text{convolution}}$ emittance results from the convolution and least-squares fitting algorithm. The data for the hollow and parabolic longitudinal distributions are taken from the bunch length scan.

$\epsilon_{\text{usual-Gauss}}/\epsilon_{\text{convolution}}$	C185	C1350
parabolic	1.303 ± 0.061	1.248 ± 0.062
hollow	1.348 ± 0.067	1.280 ± 0.074

distributions in our experiment could potentially be further optimised at creation time in the PS Booster in order to achieve higher r.m.s. emittances at a given matched emittance – this would further improve the presently reported results below.

During the experiment, the bunch length has been scanned over the full available range of 140 to 210 ns. The upper bound is determined by the recombination kicker rise time window. The bunch has been compressed during the initial window of 15 ms by ramping up the total RF voltage from 25 kV to higher values up until the maximally achievable 80 kV. The latter determines the lower bound for the bunch length (for our fixed longitudinal matched emittance).

Adiabatic bunch compression depends on the increase of the RF voltage: the initial bunch length can be decreased by

$$B_{L,\text{final}} = \left(\frac{V_{RF,\text{initial}}}{V_{RF,\text{final}}} \right)^{\frac{1}{4}} B_{L,\text{initial}} \tag{5.5}$$

[Garoby 2011]. Correspondingly, a transferred initial bunch length of $B_L = 200$ ns can be reduced to 150 ns by ramping up to the maximum RF voltage. However, due to the fluctuating shot-to-shot efficiency of the controlled longitudinal blow-up, the bunch lengths transferred to the PS varied roughly between 190 ns and 210 ns, allowing us to cover a global range of total bunch lengths between 130 ns and 210 ns when applying adiabatic bunch shortening. Table 5.5 lists some further specific parameters besides table 5.2.

Table 5.5 – Relevant experiment beam parameters for the bunch length scan.

parameter	value
hollow N	$(1.66 \pm 0.05) \times 10^{12}$
parabolic N	$(1.84 \pm 0.03) \times 10^{12}$
Q_x, Q_y	$(6.23, 6.22)$
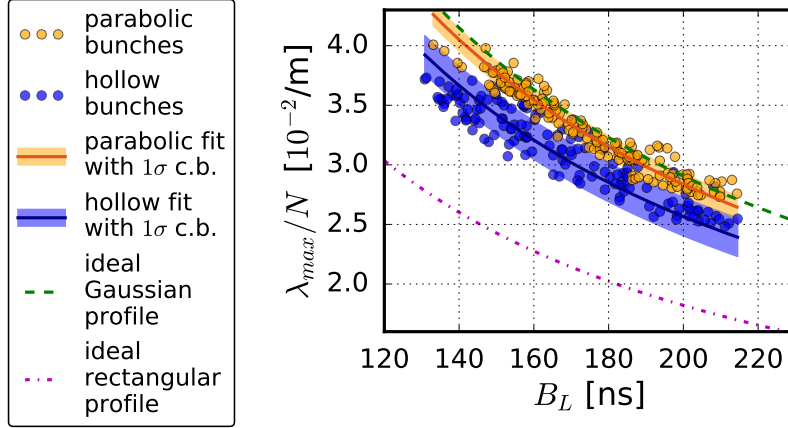
Figure 5.23 – Intensity normalised peak line charge density versus total bunch length. Hyperbolic fits $\lambda_{\max} \propto 1/B_L$ with their 1σ confidence bands yield a significant factor of 0.9 between hollow and parabolic bunches at a given bunch length.

Evaluating the reached ratios of peak line density to bunch length of the hollow and parabolic distributions, figure 5.23 shows a 10% depression of the maximal line density for hollow distributions as compared to parabolic ones for any given bunch length. A theoretically ideal rectangular profile of $4\sigma_z$ bunch length would yield a $\sqrt{2\pi}/4 \approx 0.63$ depression factor compared to a perfect Gaussian. Both extremal cases are plotted in figure 5.23 for comparison. It shows that our parabolic bunches resemble the ideal Gaussian case with their ratio of peak line density to bunch length. The flattened profile of the hollow bunches, however, shows room to improve towards an ideal rectangular profile (which by itself is impossible to achieve in a single-harmonic RF bucket).

Beam losses are small, they lie below the 2% level until C1350 and do not show any significant dependency on the space charge detuning. This coincides with the findings of Wasef et al. [2013] during a similar experimental set-up: losses in this tune region only start when increasing the vertical coherent tune from $Q_y = 6.245$ to $Q_y = 6.255$ as the beam hits the $4Q_y = 25$ octupole resonance. The coherent tune in our experiment lies slightly lower around $Q_y = 6.22$ for $N = 1.7 \times 10^{12}$.

To address the outstanding question whether hollow bunches lead to less emittance blow-up for a given intensity N, bunch length B_L and transverse emittance $\epsilon_{x,y}$, we choose to evaluate $\Delta Q_{x,y}^{\max}$ assuming a 6D Gaussian distributed beam in equation (2.87). Hence we apply the emittance relation (2.35) as well as using the Gaussian peak line density $\lambda_{\max} = N/(\sqrt{2\pi}\sigma_z)$ where we set $\sigma_z = B_L/4$.

Figure 5.24 shows how hollow bunches provide statistically significantly lower vertical emittances for the same unified reference tune shift $\Delta Q_{x,y}^{\max}$. The real tune shift of the hollow bunches is a factor 0.88 lower due to their reduced $\lambda_{\max}$ and the larger σ_x. In contrast, the parabolic bunches are rather well represented by the Gaussian approach (factor 0.97 lower

real tune shift).
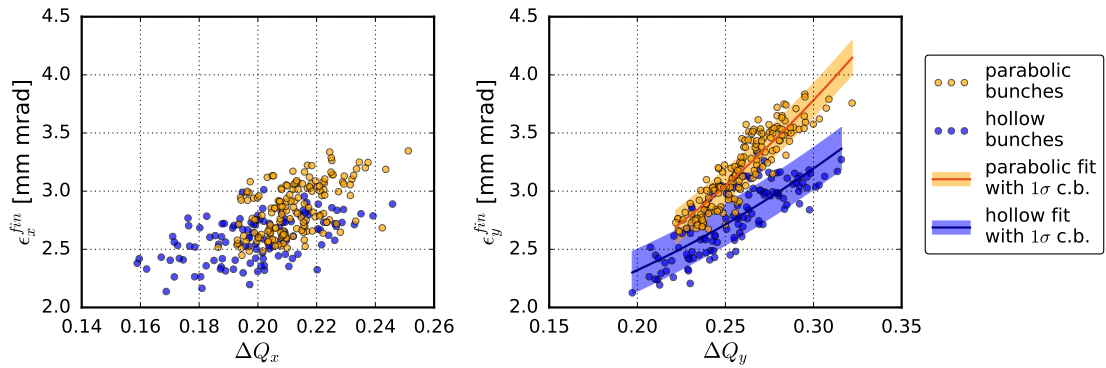
Figure 5.24 – Final core emittances versus Gaussian reference space charge detuning (based on assuming a 6D Gaussian distributed bunch). A quadratic fit is superimposed with its 1σ confidence band.

5.4.4 Vertical Tune Scan

The PS essentially offers two knobs to control the machine tune at injection energy: the low energy quadrupole magnets (LEQ) and the pole face windings (PFW) along with the figure-of-eight loop. In general, small currents in the PFW especially in the narrow windings add to the non-linear behaviour of the PS and drive betatron resonances, as analysed in detail by Huschauer [2012]. It has been shown that the width of the stop-band is effectively increased as well as the strength of the resonance driving.

The 10 A maximum current of the linear LEQ allowed us to decrease the vertical tune from the nominal value of $Q_y = 6.22$ until $Q_y = 6.11$, while steadily keeping the horizontal tune at $Q_x = 6.23$. Below this value, we made use of the PFW while keeping the figure-of-eight loop fixed (calculating the needed settings with the 4CM matrix approach [Freyermuth et al. 2010]) to further decrease the vertical tune until $Q_y = 6.07$. Further experimental parameters besides table 5.2 are listed in table 5.6.

Table 5.6 – Relevant experiment beam parameters for the vertical tune scan.

| parameter	value
hollow N	$(1.66 \pm 0.06) \times 10^{12}$
parabolic N	$(1.84 \pm 0.04) \times 10^{12}$
V_{RF}	25 kV

For both beam types, we injected the bunch into the PS on the respective vertical tune and keep the tune settings fixed until the end of the injection plateau. The coherent transverse beam tunes are measured with the short pick-up of the Base Band Tune system [Gasior and R. Jones 2005]. Figure 5.25 shows that the first 15 ms from injection until the C185 measurement

are sufficient to already considerably blow up the transverse core emittances below $Q_y < 6.20$.
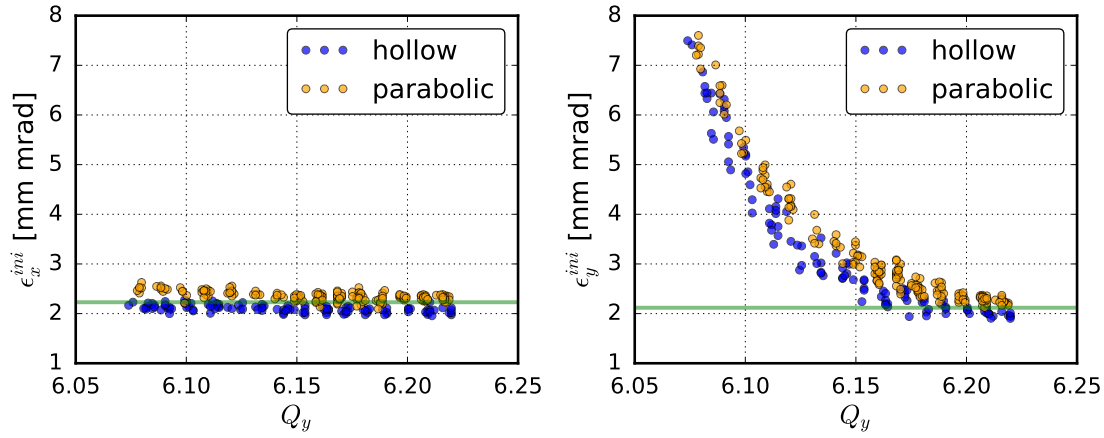
(a) Core emittances at cycle time C185.
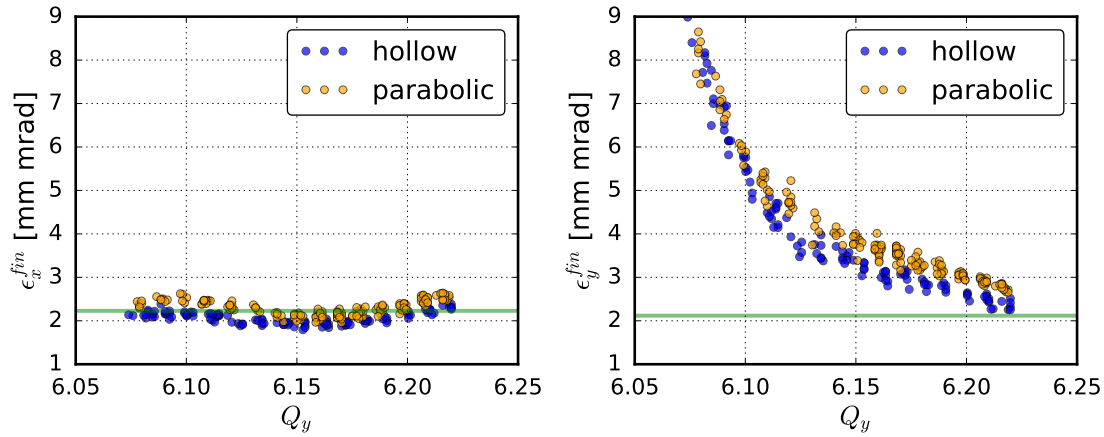
(b) Core emittances at cycle time C1350.

Figure 5.25 – Measured transverse core emittances versus the vertical tune. The green line shows the PS Booster emittance measured for a parabolic bunch at extraction using expression (2.35).

The measured emittance curve increases its slope below $Q_y = 6.11$ which may be a straightforward indicator of the additionally used PFW. This feature is more visible in the measurements at C1350 in figure 5.25b. At the same time, the loss patterns of both beam types in figure 5.26 show a decrease as soon as the PFW are used. For the emittance calculation, we assumed constant $\beta_{x,y}$ at the wire scanner locations. In reality, $\beta_{x,y}$ change with the corresponding tune settings. Since the LEQ and the PFW are situated at different locations in the ring, respectively, they also have a different influence on the local beta functions when changing the tune. Varying beta functions can then lead to losses at different positions and with different magnitude as well as to overestimated emittances.

Another possible influence might come from the increased non-linear behaviour of the machine when using only the LEQ because the PFW are then forced to vanishing currents (which

in the case of the narrow windings is problematic as previously mentioned). These two aspects can result in the behaviour observed in the emittance and loss plots at $Q_y = 6.11$.
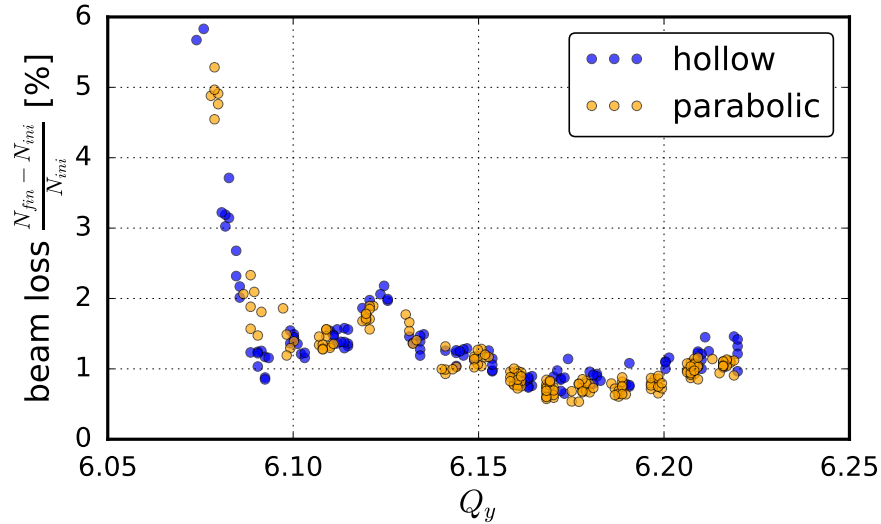
Figure 5.26 – Beam loss for hollow and parabolic bunches versus the vertical tune.

The received intensity in the PS differs by 10% between the two beam types, which approximately matches the difference between the two emittance curves exhibited in figure 5.25. Also the beam loss is equivalent in both cases. Therefore, our data do not allow to identify a significant difference between the two beam types when approaching the integer tune in the vertical plane.

6 Conclusion

The goals of this Ph.D. project comprise firstly the development of a self-consistent numerical simulation tool to model space charge dynamics in CERN's low-energy machines, secondly measurements of space charge effects at the accelerators to benchmark the developed models as well as understand the present limits, and thirdly the investigation of mitigation techniques to counteract the impact of space charge where it leads to beam quality degradation. Throughout the course of this thesis, the space charge issues with high brightness beams in the Large Hadron Collider (LHC) injector chain are analysed with the aid of the implemented space charge models in our collective effects simulation software, PyHEADTAIL. The future beams in the context of the High Luminosity LHC (HL-LHC) upgrade project are foreseen to feature twice the number of particles per bunch and exhibit slightly lower transverse normalised emittances compared to present operation. To enable the injectors to provide this increased intensity per transverse emittance (beam brightness), two identified bottlenecks in terms of strong space charge impact during the Proton Synchrotron (PS) and Super Proton Synchrotron (SPS) injection plateau need to be alleviated. In the framework of the mitigation approaches examined in this thesis, we have established reliable production of a novel Proton Synchrotron Booster (PS Booster) beam type with a hollow longitudinal phase space distribution. We quantitatively assessed the relaxation of space charge constraints in the PS by using these flattened bunches in order to extract beams of higher brightness. An extensive investigation of the downstream SPS space charge situation during the long injection plateau paves the way for the future high brightness beams. We have identified an optimal working point region, where the produced beams are minimally affected by emittance growth and beam losses hence complying with the tight LHC Injectors Upgrade (LIU) requirements. Major efforts also went into accelerating PyHEADTAIL on Graphics Processing Unit (GPU) architectures. The space charge suite has greatly benefitted from this, in particular, GPU acceleration has made beam dynamics studies with full 3D particle-in-cell (PIC) models feasible.

In the following, we go through the detailed results of this Ph.D. thesis and discuss the implications for CERN's circular accelerators and possible future studies.

6.1 PyHEADTAIL and its Space Charge Suite

The GPU acceleration of PyHEADTAIL is a crucial ingredient to long-term space charge simulations with the PIC 3D model running more than $\mathcal{O}(1000\,\text{turns})$. The 3D model allows treatment of the circular low-energy machines at CERN without neglecting the longitudinal correlation of the space charge forces along slices of the beam. Many tools used at CERN to model space charge in ring accelerators (such as PyORBIT or MAD-X with space charge) employ 2D or at best 2.5D (transverse slice-by-slice) approximations. In this case only the transverse plane is solved for the space charge forces (which are possibly weighted with the local longitudinal line charge density for the 2.5D slice model) while the shape of the beam self-fields are assumed to be independent of the longitudinal distribution. Consequently, the real space charge forces can be wrongly estimated for beam velocities considerably lower than c, i.e. $\beta < 1$. The developed 3D model is readily applicable for in-depth simulation studies in particular for the PS Booster or CERN's Low Energy Ion Ring (LEIR), where recent experimental studies have identified severe space charge impact to limit machine performance [Bartosik, Hancock, et al. 2016].

The high performance computing version of the 2.5D PIC model in PyHEADTAIL also profits from the GPU acceleration, as the longitudinal beam slices can be solved in parallel. The computational complexity of the employed GPU algorithms often scales less rapidly than on a scalar CPU for many numerical parameters (such as the number of macro-particles) which is beneficial for exploring the parameter space during resolution and convergence studies. The better scaling behaviour can become very interesting for upcoming studies of the interplay of collective effects, among them being the influence of space charge on beam-electron-cloud interaction in the arcs of the LHC at injection energy.

The employed combination of macro-particle and PIC simulation techniques originates from plasma physics, where it is widely employed to study collective modes and plasma instabilities e.g. for fusion reactors. Analogous models are used for N-body simulations in astrophysics and cosmology, where e.g. the creation of solar winds or even the structure formation of galaxies and galaxy clusters in the universe are investigated.

Simulations with PyHEADTAIL's space charge suite have been extensively compared with analytic formulae (as in the case of the Quadrupolar Pick-up (QPU)) and measurements (as in the SPS high brightness studies).

6.2 Quadrupolar Pick-Ups to Measure Space Charge

QPU set-ups provide a means to measure the incoherent Kapchinskij-Vladimirskij (KV) tune shift of a beam as a quantity to estimate the space charge impact. This approach provides a promising alternative to measuring the brightness using the wire scanners (for the transverse emittances) in conjunction with the beam current transformer (for the intensity). It would be advantageous to determine the emittances directly from the space charge tune shift, as this

avoids using the optics model of the machine which is known to introduce large uncertainties on the emittance values e.g. when using the wire scanners (the uncertainty is on the order of the allocated emittance growth budget for the LHC operation). For space charge purposes, the envelope mode measurement method appears more natural than the beam profile measurement via wire scanners. The observables (the envelope mode frequencies) are closely related to space charge dynamics on which they are to give quantitative information.

The theory for the quadrupolar coherent modes has been worked out in section 2.2 taking into account the regime of the CERN machines which mostly operate at nearly equal tunes close to the coupling resonance. For certain relevant beam intensities, beam sizes and tunes, the coupling strength $D \approx 1$ lies somewhere between the two often employed approximations in either the far off-coupling or the fully coupled case. This has to be accounted for when relating the envelope mode frequencies to beam parameters. Simulations based on the PIC space charge model in section 3.5 showed the space charge depressed coherent modes and confirmed the derived theoretical relation to the incoherent KV tune shift.

Experiments to be done in the near future with a quadrupolar pick-up in the PS will reveal to what extent the bunching of the beam play a role in the brightness determination. Sacherer's treatment of the space charge depressed envelope modes [Sacherer 1971] includes a 3D derivation for bunched beams, which has been followed up by Uesugi et al. [1999]. The extended theoretical model may provide further insight into this matter.

6.3 Hollow Bunches for the PS Injection Plateau

For sufficiently high brightnesses, beams residing at constant energy at the PS injection plateau suffer from r.m.s. emittance growth. The frequency of the collective motion of the beam core is strongly depressed by space charge, consequently the integer resonance excites the particles in the beam core to higher transverse amplitudes. The synchrotron motion in the longitudinal plane plays an important role in this process – in this spirit the peak line charge density determines the maximal electromagnetic fields. Consequently, the bunch core tune depression by space charge can be reduced by modifying the longitudinal bunch profile as to decrease the peak line charge density. This strategy offers to accommodate more particles per bunch for a given transverse emittance.

We have set up a reliable process in the PS Booster to reduce the peak line charge density by shaping the longitudinal phase space distribution into a ring. The excitation of a dipolar parametric resonance in the longitudinal plane results in the depletion of the radio frequency (RF) bucket core, where the usual parabolic or Gaussian bunch distributions feature the highest phase space density of particles. This approach to create such longitudinally hollow phase space distributions (or simply hollow bunches) in the PS Booster involves minimal changes to the presently operational LHC beam cycle (cf. appendix A) which is a considerable advantage of the developed method in comparison to other mechanisms. Accepting hollow bunches in the PS does not require any additional adaptation of the PS cycle nor further

synchronisation measures between the machines.

The flattened longitudinal projection of the hollow bunches indeed relaxes the space charge impact on the PS injection plateau: for a given bunch length (which is usually sought to be maximised within the 205 ns window of the recombination kicker rise time in the PS Booster), intensity and emittance, the hollow bunches were subject to significantly less emittance blow-up than the usual parabolic bunches in the region of the operational machine tunes. We emphasize that, in comparison to the usual strategy to flatten the line charge density by using a second-harmonic RF system in anti-phase (i.e. bunch lengthening mode), hollow phase space distributions also feature a wider momentum spread. The correspondingly increased dispersive contribution leads to larger horizontal beam sizes hence providing an additional factor suppressing space charge. We conclude that hollow bunches are a viable tool to extract higher beam brightness from the PS to comply with the LIU parameters.

The triple splitting process in the PS is required to provide three bunchlets of approximately the same intensity per bunchlet. We found this to apply also to hollow parent bunches – the resulting inner bunchlet even persists to have a ring-like phase space distribution while the outer bunchlets are simply flat with a large patch of constant phase space density in the centre. Nevertheless, any controlled longitudinal blow-up procedure inserted before the triple splitting would considerably distort the original hollow distribution and restore a parabolic-type distribution which would then result in the usual triple splitting with equal phase space distributions. Converting the hollow bunches back to parabolic ones does not pose a problem as the hollow bunches are mainly required for the injection plateau itself (at the end of which the triple splitting takes place).

6.4   High Brightness Beams in the SPS

Building on a preliminary SPS working point study below the quarter-integer resonance $Q_y < 20.25$ [Bartosik, Argyropoulos, et al. 2014], we have carried out a systematic static tune scan with high brightness beams across the lower left tune diagram half-integer quadrant. The extensive study revealed two relevant resonances, the third-order $Q_x + 2Q_y = 61$ and the fourth-order $4Q_x = 81$. As opposed to the PS, the regular vertical quarter-integer resonance does not degrade the beam quality, which entails the accessibility of working points above $Q_y > 20.25$. We have identified an optimal working point region around $(Q_x, Q_y) = (20.22, 20.30)$ for high brightness beams. Here, the beam loss is bounded by 1% while the emittance growth remains below 4% over the 3 s constant injection energy plateau. These figures appear in line with the allocated LIU budgets from table 1.1. We conclude that the working point optimisation based on the Q20 optics alleviates the impact of space charge and, therefore, any related bottleneck issue at the SPS.

Our detailed analysis of the beam losses within this optimal working point region revealed a clear scaling with the transverse beam size. Keeping the same transverse emittances while varying the beam brightness and hence the space charge tune shift did not lead to a considerable

effect on the beam loss. Thus, we exclude any impact of the vertical quarter-integer resonance on the high brightness beams. During this study, the third-order resonance $3Q_y = 61$ has been observed to produce losses at low intensities while it does not appear at high intensities in the systematic tune scan (cf. figure 4.4a). The losses coincide with the coherent vertical tune crossing $Q_y = 20.\overline{3}$ while at the same time the incoherent tune spread also shrinks in this low intensity area. We propose an incoherent loss mechanism where the halo particles being shifted to higher tunes (for lower intensities as compared to higher intensities) interact with the third-order resonance. Future studies could include an experiment with several sets of intensity scans for different fixed vertical bare machine tunes around $Q_y = 20.\overline{3}$. The coherent dipolar tune would then cross the resonance at different intensities for the different bare tunes. This experimental set-up should uncover the dependency on the coherent dipolar tune as well as the incoherent tune spread. The respective loss patterns should then allow to distinguish the influence of impedance effects from direct space charge.

Finally, we investigated the identified fourth-order $4Q_x = 81$ resonance by powering a single strong octupole magnet which acts like an octupolar error contributing with a significant resonance driving term. The set-up follows a similar experiment carried out for the PS [Franchetti et al. 2003] where the incoherent nature of the losses and halo population due to octupole resonance islands has been shown. In the SPS we observe the same phenomenon with a tune dependent generation of tails in the beam distribution. The halo threshold – defined by the location where the enriched tails deviate from the Gaussian core fit – moves outwards from the centre as the bare machine tune approaches the resonance from above. The collective response of the beam core to the resonance exhibits the maximal r.m.s. emittance growth at the tune where the r.m.s. equivalent KV distribution satisfies the octupolar mode resonance condition in accordance with the predictions from Sacherer's theory on the r.m.s. equivalence of beams. These findings coincide with the picture of the halo-core model which we discussed in the introductory chapter by reference to the work of R. Baartman [1998] who reviewed space charge dynamics when interacting with betatron resonances.

6.5 Ready for the High Luminosity LHC Era

The present thesis project has contributed to the understanding and mitigation of space charge aspects in view of the LIU requirements. The mitigation strategies developed in the framework of this Ph.D. thesis have the potential to alleviate the brightness limitations at CERN's PS and SPS in conjunction with all the other elaborate machine upgrades taking place to reach the future HL-LHC beam parameters. We are eagerly looking forward to what bright future and exciting discoveries these bright beams will bring for the LHC experiments in the HL-LHC era.
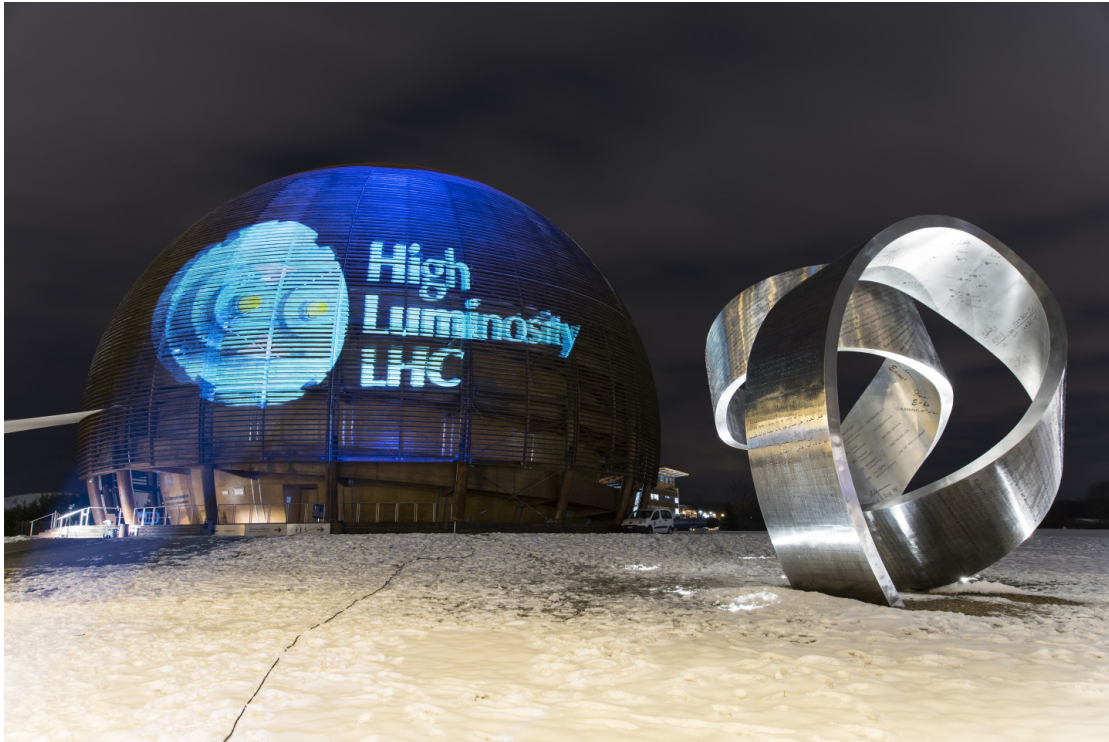
Figure 6.1 – The globe of science and innovation at CERN celebrating the year of light [Brice 2015].

# A Setting Up Hollow Bunches in the Proton Synchrotron Booster

This appendix explains the procedure leading to a reproducible production of hollow bunches in the PS Booster. As discussed in chapter 5, the approach relies on exciting a 1 : 1 dipolar parametric resonance during the PS Booster acceleration ramp. The following paragraphs aim to provide the interested reader with the concrete implementation details.

The set-up is based on the `LHC1A` cycle providing the first batch to the PS (which leads to 48 out of the 72 bunches at PS extraction) for the 25 ns scheme [Damerau 2011]. The goal was to robustly produce hollow bunches with a minimalistic set of changes to the canonical settings in order to ease possible operational implementation in the future. The creation procedure has been tested in ring 3, which is located at the same height as the PS ring so that any unwanted effect from spurious vertical dispersion in the PS can be ruled out in the experiments.

The parametric resonance is excited at cycle time C575. The starting point is a typical bunch blown up to a matched 100% emittance of about 1.1 eVs. This blow-up happens during a 50 ms window from C500 on, it marks the last intentional longitudinal modification during the conventional `LHC1A` cycle. At C575, the bunch has been accelerated to a kinetic energy of about $E_{kin} = 0.714$ GHz (cf. the magnetic cycle in figure 5.8).

Usually, the second harmonic system is kept on almost until extraction to the PS. Instead, we essentially switch off the C04 second harmonic RF system by ramping it down to the minimal voltage of 0.5 kV between C550 and C575: therefore, we practically have a single-harmonic bucket available to work with at the start of the excitation, cf. figure A.1.

The acceptance of this bucket is about 1.8 eVs at C575. Figure A.2 shows how scans revealed an optimal angular distribution of the particles for a excitation duration of 6 synchrotron periods. The lower right plot shows the synchrotron amplitude projection for each phase space distribution. For 5 synchrotron periods, the plot increases monotonically towards the centre (the vertical centre of the surrounding box), the bunch is not yet sufficiently depleted. 7 synchrotron periods excitation duration show more density at lower synchrotron amplitudes than 6 synchrotron periods, i.e. the bunch tends again to occupy the bucket centre.
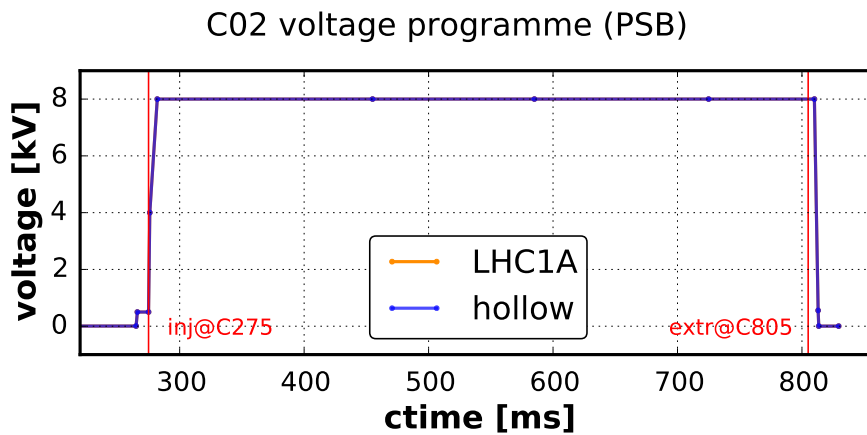
(a) The fundamental RF system C02 features the same settings at 8 kV as for the canonical cycle.
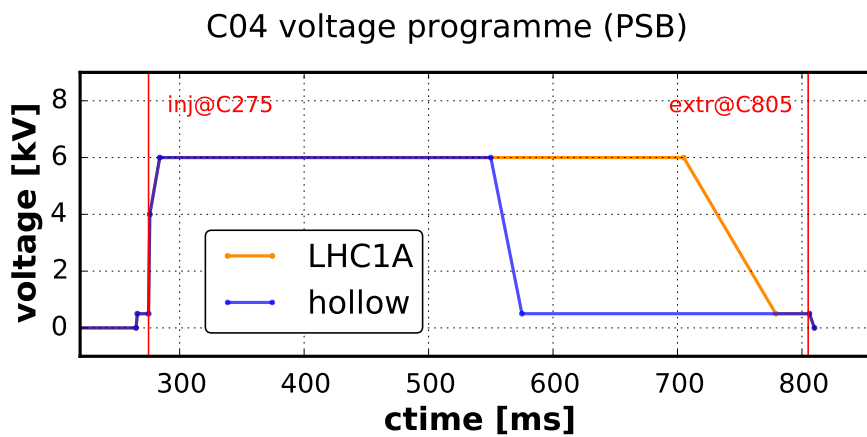
(b) The second harmonic RF system C04 is adiabatically ramped down after the blow-up at C550 during a 20 ms window.

Figure A.1 – Ramping down the second harmonic RF voltage yields a quasi-single-harmonic at C575 at the beginning of the excitation.

(a) 5 synchrotron periods
(2× higher phase loop gain lead
to smaller matched emittance)

(b) 6 synchrotron periods

(c) 7 synchrotron periods

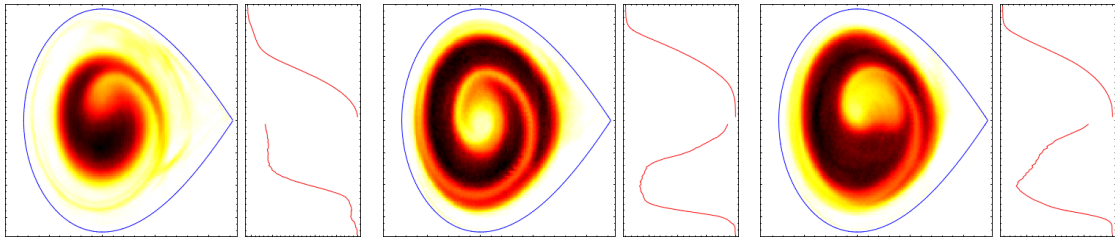Figure A.2 – While the parametric resonance depletes the bunch centre, the outer particles move slower than the inner particles due to the synchrotron frequency spread (coming mainly from the bucket non-linearities). Scanning the excitation duration yields 6 synchrotron periods as the optimal value. Below, the bunch is not yet sufficiently depleted, while above, the inner particles overtake the outer particles and the distribution collapses again.

This behaviour comes from the fact that the phase loop feedback system plays a significant role the longer the excitation takes. The feedback gain hence needs to be carefully adjusted. If it is too strong, the phase loop non-linearly compensates for the phase modulation and strongly affects the resulting distribution in a destructive manner. On the contrary, if the phase loop gain is too low, the RF systems couple too weakly to the beam phase to align their reference phase, which results in severe beam losses. Figure A.3 shows the adjustments made for hollow bunches. Three relevant phases have been optimised:

1. During the (few ms lasting) excitation after C575 the gain needs to be low to allow for a large blow-up of the emittance during the resonance. (E.g. in figure A.2a, the phase loop gain was twice as high as in the other two samples, correspondingly the blow-up effect of the resonance is suppressed due to the feedback system.)

2. Directly after the excitation, the phase loop gain needs to be relatively high to tightly fix the beam's centre of gravity, otherwise the distribution continues to slightly oscillate within the bucket and widens the well-defined steep flanks.

3. During the synchronisation to the PS RF systems after C760, the revolution frequency and the beam phase are readjusted. The latter process disrupts the hollow distribution and fills in the depleted centre if both the phase loop and the synchronisation loop gains are too high.

The shaken distribution needs to be smoothed after the resonance. Two subsequent 50 ms long high-frequency phase modulation blow-ups are employed at C600 and C700 (figure A.4a). The C16 RF system is used for this purpose operating on the ninth harmonic. A particle is then

phase loop offset (PSB)
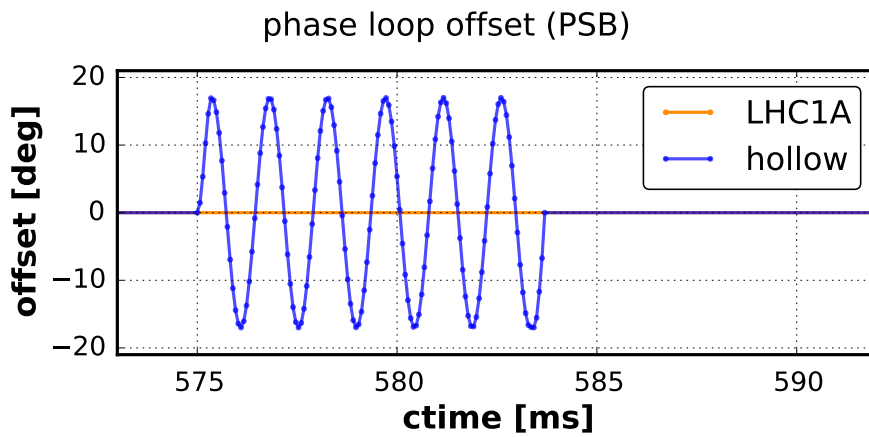
(a) 6 synchrotron periods of phase modulation.
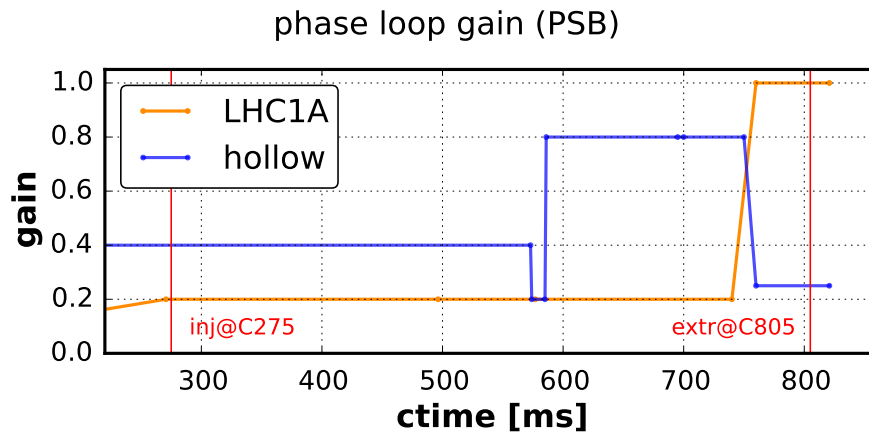
phase loop gain (PSB)

(b) The carefully adjusted phase loop gain function.

Figure A.3 – Settings for the phase loop offset showing the phase modulation which creates the hollow bunches and the adapted phase loop gain function.

exposed to a total RF voltage function

$$V(t) = V_{h=1}\sin(\phi) + V_{h=9}\sin\big(9\phi + \theta_1 + \underbrace{\hat{\psi}\sin(\omega_{HF}t + \theta_2)}_{\text{high frequency phase modulation}}\big) \quad, \tag{A.1}$$

depending on the phase ϕ with which it arrives at the main RF cavity. Due to software restrictions, the modulation amplitude is fixed during a cycle and therefore determined by the setting of the first blow-up, $\hat{\psi} = 120°$.

The high-frequency phase modulation blow-up is a parametrically resonant process (equivalent to the 1:1 resonance we exploit for the hollowing). The resonate condition determines which particle synchrotron amplitudes are excited to gain energy; it not only depends on the modulation frequency but also on the angle offset θ_1 of the modulation [Cappi, Shaposhnikova, and Garoby 1992]. At the time of the experiment, the PS Booster did not trivially allow a determination of the relative phase between the C16 and the C02 RF systems. This essentially left us to empirically optimise the blow-up frequencies to work on the relevant phase space contours. The baseline for the modulation frequency is set to $\omega_{HF} = 0.91\omega_{S,0}$ directly after the excitation, which aims to hit the synchrotron amplitude of the ring to blow it up to larger emittances as well as to smooth it. The last blow-up operates at $\omega_{HF} = 0.93\omega_{S,0}$ aiming to flatten the slightly convex density profile by filling the central hole with particles from the inner part of the ring.

This procedure provided a reasonably stable mechanism to create stationary (i.e. filamented) hollow phase space distributions and transfer them to the PS.

C16 voltage programme (PSB)
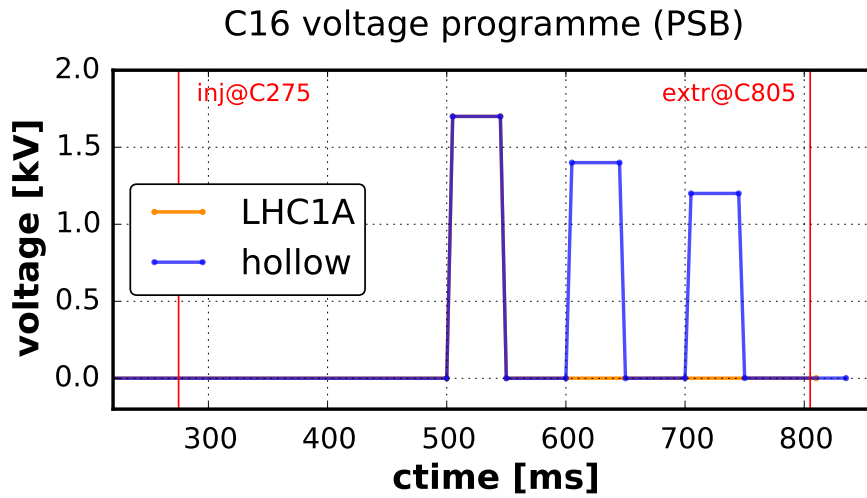
(a) The first blow-up at C500 produces the $\epsilon_{z,100\%} \approx 1.1\,\mathrm{eVs}$ bunch. The second one at C600 smooths the irregular non-stationary distribution after the excitation. Finally, the third blow-up at C700 redistributes particles to the bunch centre to flatten the longitudinal bunch profile.

C16 frequency programme (PSB)
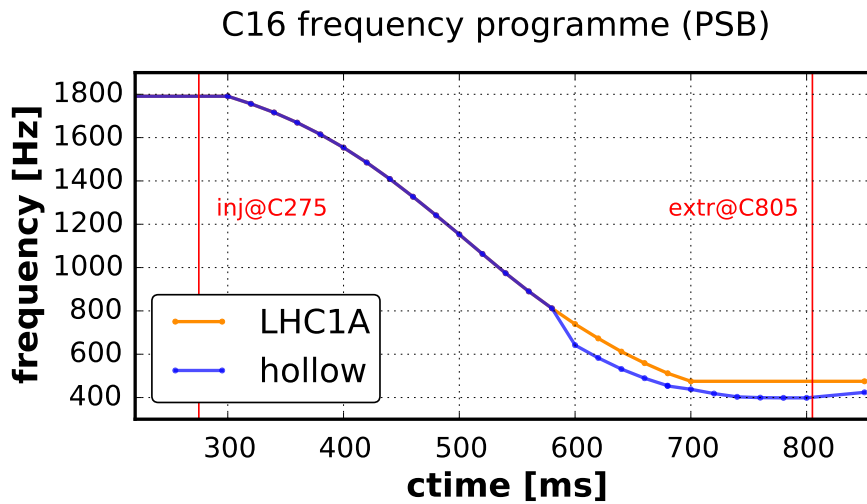
(b) The frequency baseline for the high-frequency phase modulation. The first (canonical) blow-up runs at the linear synchrotron frequency, the second at $0.91\omega_{S,0}$ and the third at $0.93\omega_{S,0}$.

Figure A.4 – High-frequency phase modulation with the C16 cavities provides longitudinal blow-up.

Bibliography

Aad, G. et al. (2012). "Observation of a new particle in the search for the Standard Model Higgs boson with the ATLAS detector at the LHC". In: *Phys. Lett. B* 716.arXiv:1207.7214. CERN-PH-EP-2012-218, 1–29. 39 p.

Aaij, R. et al. (2013). "First observation of CP violation in the decays of B_s^0 mesons". In: *Phys. Rev. Lett.* 110.22, p. 221601. arXiv: 1304.6173 [`hep-ex`].

Aaij, R. et al. (2015). "Observation of $J/\psi p$ Resonances Consistent with Pentaquark States in $\Lambda_b^0 \to J/\psi K^- p$ Decays". In: *Phys. Rev. Lett.* 115 (7), p. 072001.

Accelerator Beam Physics Group, C. (2016). *MAD-X, Methodical Accelerator Design.* http://cern.ch/madx/.

Ade, P. A. R. et al. (2015). "Planck 2015 results. XIII. Cosmological parameters". In: arXiv: 1502.01589 [`astro-ph.CO`].

Ahnert, K., D. Demidov, and M. Mulansky (2014). "Solving Ordinary Differential Equations on GPUs". In: *Numerical Computations with GPUs*, pp. 125–157.

Apollinari, G. et al. (2015). *High-Luminosity Large Hadron Collider (HL-LHC): Preliminary Design Report.* Geneva: CERN.

Arduini, G. et al. (2014). "How to maximize the HL-LHC performance". In: *RLIUP: Review of LHC and Injector Upgrade Plans*, pp. 81–94.

ATLAS Collaboration and CMS Collaboration (2015). "Combined Measurement of the Higgs Boson Mass in pp Collisions at $\sqrt{s} = 7$ and 8 TeV with the ATLAS and CMS Experiments". In: *Phys. Rev. Lett.* 114 (19), p. 191803.

Baartman, R. A., M. D'yachkov, and F. W. Jones (1999). "Modeling of space-charge phenomena in multi-turn tracking". In: *IEEE Particle Accelerator Conference (PAC 1999)*. Vol. 1. IEEE, pp. 128–130.

Baartman, R. (1998). "Betatron Resonances With Space Charge". In: *Space Charge Physics in High Intensity Hadron Rings*. Vol. 448. AIP, pp. 56–72.

Bartolini, R. and F. Schmidt (1998). *A Computer Code for Frequency Analysis of Non-Linear Betatron Motion.* Tech. rep. SL-Note-98-017-AP. Geneva: CERN.

Bartosik, H., T. Argyropoulos, et al. (2014). "Can we ever reach the HL-LHC requirements with the injectors?" In: *RLIUP: Review of LHC and Injector Upgrade Plans*, pp. 95–104.

Bartosik, H., S. Hancock, et al. (2016). "Space Charge Driven Beam Loss for Cooled Beams and Mitigation Measures in the CERN Low Energy Ion Ring". In: *ICFA Advanced Beam Dynamics Workshop on High-Intensity and High-Brightness Hadron Beams (HB 2016)*, TUAM5X01.

Bibliography

Bartosik, H. (2013). "Beam dynamics and optics studies for the LHC injectors upgrade". Presented on 13 Nov 2013. PhD thesis. TU Vienna.

Bartosik, H., G. Iadarola, et al. (2014). "TMCI Thresholds for LHC Single Bunches in the CERN-SPS and Comparison with Simulations". In: *International Particle Accelerator Conference (IPAC 2014)*, TUPME026.

Bartosik, H., A. Oeftiger, M. Schenk, et al. (2016). "Improved Methods for the Measurement and Simulation of the CERN SPS Non-linear Optics". In: *International Particle Accelerator Conference (IPAC 2016)*, THPMR036.

Bartosik, H., A. Oeftiger, F. Schmidt, et al. (2016). "Space Charge Studies with High Intensity Single Bunch Beams in the CERN SPS". In: *International Particle Accelerator Conference (IPAC 2016)*, MOPOR021.

Bassetti, M. and G. A. Erskine (1980). "Closed Expression for the Electrical Field of a Two-dimensional Gaussian Charge". In: *CERN ISR TH 80-06*.

Blewett, J. P. (1952). "Radial Focusing in the Linear Accelerator". In: *Phys. Rev.* 88 (5), pp. 1197–1199.

Brice, M. (2008). "Aerial View of the CERN taken in 2008." CERN-MI-0807031. Copyright 2008 by CERN under the CC BY-SA 4.0 license.

– (2015). "Images projected on the Globe of Innovation 'Light & Luminosity'." CERN-PHOTO-201502-026-5. Copyright 2015 by CERN.

Burnet, J.-P. et al. (2011). *Fifty years of the CERN Proton Synchrotron: Volume 1*. Geneva: CERN.

Cappi, R., R. Garoby, et al. (1993). "Measurement and Reduction of Transverse Emittance Blow-up Induced by Space Charge Effects". In: *IEEE Particle Accelerator Conference (PAC 1993)*. IEEE, pp. 3570–3572.

Cappi, R., E. Shaposhnikova, and R. Garoby (1992). "Experimental Study of Controlled Longitudinal Blow-up". In: *CERN PS 92-40-RF*.

Carli, C. (2001). "Creation of Hollow Bunches Using a Double Harmonic RF System". In: *CERN PS 2001-073-AE*.

Carli, C. and M. Chanel (2002). "Creation of Hollow Bunches by Redistribution of Phase Space Surfaces". In: *European Particle Accelerator Conference (EPAC2002)*, WEBGB001.

Chanel, M. (1996). "Study of beam envelope oscillations by measuring the beam transfer function with quadrupolar pick-up and kicker". In: *European Particle Accelerator Conference (EPAC 1996)*, pp. 1015–1017.

Chao, A. W. (1993). *Physics of collective beam instabilities in high energy accelerators*. Wiley.

Chatrchyan, S. et al. (2012). "Observation of a new boson at a mass of 125 GeV with the CMS experiment at the LHC". In: *Phys. Lett. B* 716.arXiv:1207.7235. CMS-HIG-12-028. CERN-PH-EP-2012-220, 30–61. 59 p.

Chen, C. and R. C. Davidson (1994). "Nonlinear properties of the Kapchinskij-Vladimirskij equilibrium and envelope equation for an intense charged-particle beam in a periodic focusing field". In: *Phys. Rev. E* 49 (6), pp. 5679–5687.

Christofilos, N. (1956). *Focussing System for Ions and Electrons*. US Patent 2736799.

Courant, E. D., M. S. Livingston, and H. S. Snyder (1952). "The Strong-Focusing Synchroton – A New High Energy Accelerator". In: *Phys. Rev.* 88 (5), pp. 1190–1196.

Damerau, H. (2011). *RF Aspects for LHC Type Beam in the PS*. BE/OP Shutdown Courses.

Damerau, H. et al. (2014). *LHC Injectors Upgrade, Technical Design Report, Vol. I: Protons*. Tech. rep. CERN-ACC-2014-0337. Geneva: CERN.

Davis, T. A. and E. Palamadai Natarajan (2010). "Algorithm 907: KLU, a direct sparse solver for circuit simulation problems". In: *ACM Transactions on Mathematical Software (TOMS)* 37.3, p. 36.

De Melis, C. (2016). "The CERN accelerator complex. Complexe des accélérateurs du CERN". OPEN-PHO-ACCEL-2016-009. Copyright 2016 by CERN.

Delahaye, J. P. et al. (1980). "11th International Conference on High-Energy Accelerators: Geneva, Switzerland, July 7–11, 1980". In: Basel: Birkhäuser Basel. Chap. Shaping of Proton Distribution for Raising the Space-Charge of the CERN PS Booster, pp. 299–304.

Forest, E. (1998). *Beam dynamics*. Vol. 8. CRC Press.

Franchetti, G. et al. (2003). "Space Charge and Octupole Driven Resonance Trapping Observed at the CERN Proton Synchrotron". In: *Physical Review Special Topics-Accelerators and Beams* 6 (12), p. 124201.

Freyermuth, P. et al. (2010). "CERN Proton Synchrotron Working Point Matrix for Extended Pole Face Winding Powering Scheme". In: *International Particle Accelerator Conference (IPAC 2010)*, THPE019.

Frigo, M. and S. G. Johnson (2005). "The design and implementation of FFTW3". In: *Proceedings of the IEEE* 93.2, pp. 216–231.

Garoby, R. (2011). "RF gymnastics in synchrotrons". In: *Proceedings, CAS - CERN Accelerator School: RF for Accelerators, Ebeltoft, Denmark, 8 - 17 Jun 2010*. arXiv: 1112.3232 [physics.acc-ph].

Garoby, R. and S. Hancock (1994). "New techniques for tailoring longitudinal density in a proton synchrotron". In: *European Particle Accelerator Conference (EPAC 1994)*.

Gasior, M. and R. Jones (2005). "The Principle and First Results of Betatron Tune Measurement by Direct Diode Detection". In: *CERN LHC Project Report 853*.

Geist, G. A. and C. H. Romine (1988). "LU factorization algorithms on distributed-memory multiprocessor architectures". In: *SIAM Journal on Scientific and Statistical Computing* 9.4, pp. 639–649.

Gilardoni, S. et al. (2014). "Long-term Beam Losses in the CERN Injector Chain". In: *ICFA Advanced Beam Dynamics Workshop on High-Intensity and High-Brightness Hadron Beams (HB 2014)*, THO1LR01.

Givon, L. (2016). *scicit-cuda, Python interface to CUDA device / runtime, cuBLAS, cuFFT and cuSOLVER*. http://scikit-cuda.readthedocs.io/.

Gluckstern, R. L. (1970). "Oscillation Modes in Two Dimensional Beams". In: *Proton Linear Accelerator Conference*. Vol. C700928, p. 811.

Hancock, S., M. Lindroos, and S. Koscielniak (2000). "Longitudinal Phase Space Tomography with Space Charge". In: *Physical Review Special Topics-Accelerators and Beams* 3.12, p. 124202.

Hancock, S., M. Lindroos, E. McIntosh, et al. (1999). "Tomographic Measurements of Longitudinal Phase Space Density; 1999 ed." In: *CERN PS 99-002-OP*.

Bibliography

Hancock, S. (2016). "Tomography at Injection in the PSB". In: *CERN ACC NOTE 2016-0040.*

Hangst, J. S. (2014). "Fundamental Physics with Antihydrogen". In: *Springer Tracts Mod. Phys.* 256, 203–221. 19 p.

Hanke, K. (2013). "Past and Present Operation of the CERN PS Booster". In: *International Journal of Modern Physics A* 28.13, p. 1330019.

Hardt, W. (1966). "On the Incoherent Space Charge Limit for Elliptic Beams". In: *CERN ISR-INT-300-GS-66-2.*

Hegglin, S. (2016). "Simulating Collective Effects on GPUs". MA thesis. D-MATH/D-PHYS Dep., ETH Zürich.

Heuer, R. (2012). "CERN Press Release: CERN Experiments Observe Particle Consistent with Long-sought Higgs Boson". In: *CERN Bulletin* (28-29).

Hockney, R. W. and J. W. Eastwood (1988). *Computer Simulation Using Particles.* CRC Press.

Hofmann, I. (1998). "Stability of anisotropic beams with space charge". In: *Phys. Rev. E* 57 (4), pp. 4713–4724.

Hofmann, I., R. Bar, et al. (1998). "Observation and interpretation of space charge phenomena for high intensity". In: *Space Charge Physics in High Intensity Hadron Rings.* Vol. 448, pp. 15–25.

Hofmann, I., G. Franchetti, et al. (2003). "Space charge resonances in two and three dimensional anisotropic beams". In: *Physical Review Special Topics-Accelerators and Beams* 6.2, p. 024202.

Hofmann, I., L. Laslett, et al. (1983). "Stability of the Kapchinskij-Vladimirskij (KV) distribution in long periodic transport systems". In: *Particle Accelerators* 13.3-4, pp. 145–178.

Huang, H. et al. (1993). "Experimental determination of the Hamiltonian for synchrotron motion with rf phase modulation". In: *Phys. Rev. E* 48 (6), pp. 4678–4688.

Huschauer, A. (2012). "Working point and resonance studies at the CERN Proton Synchrotron". MA thesis. Vienna, Tech. U.

Iadarola, G. et al. (2015). "PyECLOUD for PyHEADTAIL: Development Work". Presented at Electron Cloud Meeting.

Jansson, A. (2001). "Non-Invasive Measurement of Emittance and Optical Parameters for High-Brightness Hadron Beams in a Synchrotron". Presented on 9 May 2001. PhD thesis. Geneva: Stockholm U.

Kapchinsky, I. M. and V. V. Vladimirsky (1959). "Limitations of proton beam current in a strong focusing linear accelerator associated with strong space charge". In: *International Conference on High Energy Accelerators*, pp. 274–288.

KEK, Japan (2013). "Final Focus at the ATF2 test facility". Newsline, Linear Collider Collaboration.

Kesting, F. and G. Franchetti (2015). "Propagation of numerical noise in particle-in-cell tracking". In: *Physical Review Special Topics-Accelerators and Beams* 18 (11), p. 114201.

Khachatryan, V. et al. (2015). "Evidence for Collective Multiparticle Correlations in p-Pb Collisions". In: *Phys. Rev. Lett.* 115 (1), p. 012301.

Kishek, R. A. et al. (2000). "Errors, Resonances, and Corrections in the Space-charge-dominated Beam of the University of Maryland Electron Ring (UMER)". In: *ICFA Advanced Accelerator Workshop, The Physics of High Brightness Beams*, pp. 297–308.

Klöckner, A. et al. (2012). "PyCUDA and PyOpenCL: A scripting-based approach to GPU run-time code generation". In: *Parallel Computing* 38.3, pp. 157–174.

Lapostolle, P. M. (1971). "Possible emittance increase through filamentation due to space charge in continuous beams". In: *IEEE Transactions on Nuclear Science* 18.3, pp. 1101–1104.

Lee, S. (2004). *Accelerator Physics*. World Scientific.

Li, K. et al. (2016). "Code Development for Collective Effects". In: *ICFA Advanced Beam Dynamics Workshop on High-Intensity and High-Brightness Hadron Beams (HB 2016)*, WEAM3X01.

Lindroos, M. et al. (2000). "Hollow Bunch Distributions at High Intensity in the PS Booster". In: *European Particle Accelerator Conference (EPAC 2000)*, p. 1528.

Linglin, D. et al. (1983). "Experimental observation of isolated large transverse energy electrons with associated missing energy at $\sqrt{s} = 540$ GeV". In: *Gluons and Heavy Flavours*, pp. 611–636.

Lu, Q. and J. Amundson (2014). "Synergia CUDA: GPU-accelerated Accelerator Modeling Package". In: *Journal of Physics: Conference Series* 513.5, p. 052021.

Lund, S. (2015). *Beam Physics with Intense Space Charge*. US Particle Accelerator School.

Lund, S. M., T. Kikuchi, and R. C. Davidson (2009). "Generation of initial kinetic distributions for simulation of long-pulse charged particle beams with high space-charge intensity". In: *Physical Review Special Topics-Accelerators and Beams* 12 (11), p. 114801.

Machida, S. (2014). "Space Charge Simulation for 4th Order Resonance". Presented at Space Charge Collaboration Meeting 2014, CERN.

Métral, E., T. Argyropoulos, et al. (2016). "Beam Instabilities in Hadron Synchrotrons". In: *IEEE Transactions on Nuclear Science* 63.2, pp. 1001–1050.

Métral, E., G. Rumolo, et al. (2007). "Simulation study of the horizontal head-tail instability observed at injection of the CERN Proton Synchrotron". In: *IEEE Particle Accelerator Conference (PAC 2007)*. IEEE, pp. 4210–4212.

Montague, B. W. S. L. (1968). *Fourth-order coupling resonance excited by space-charge forces in a synchrotron*. Geneva: CERN.

N. Bell and J. Hoberock (2011). "Thrust: A productivity-oriented library for CUDA". In: *GPU computing gems Jade edition* 2, pp. 359–371.

Ng, K.-Y. (2006). *Physics of intensity dependent beam instabilities*. World Scientific.

Nickolls, J. et al. (2008). "Scalable parallel programming with CUDA". In: *Queue* 6.2, pp. 40–53.

NVIDIA (2016a). *cuFFT, Fast Fourier Transform library, CUDA Toolkit*. https://developer.nvidia.com/cufft/.

– (2016b). *cuSOLVER, collection of dense and sparse direct solvers, CUDA Toolkit*. https://developer.nvidia.com/cusolver/.

– (2016c). *cuSPARSE, Sparse Matrix library, CUDA Toolkit*. https://developer.nvidia.com/cusparse/.

Bibliography

Oeftiger, A. (2015). "Development And Benchmarking of Space Charge Modules for PyHEAD-TAIL". Presented at EUCARD2/XBeams Workshop on Space-charge Effects in Particle Accelerators, Oxford.

– (2016). "Parallelisation of PyHEADTAIL, a Collective Beam Dynamics Code for Particle Accelerator Physics". In: arXiv: 1610.05801 [`physics.comp-ph`].

Oeftiger, A., A. Aviral, et al. (2016). "Space Charge Studies with High Intensity Single Bunch Beams in the CERN SPS". In: *International Particle Accelerator Conference (IPAC 2016)*, WEPOY044.

Oeftiger, A., H. Bartosik, A. J. Findlay, et al. (2016). "MD210 Note: Creation of Hollow Bunches in the PSB". In: *CERN ACC NOTE 2016-0045*.

Oeftiger, A., H. Bartosik, A. Findlay, et al. (2016). "Flat Bunches with a Hollow Distribution for Space Charge Mitigation". In: *International Particle Accelerator Conference (IPAC 2016)*, MOPOR023.

Oeftiger, A., S. Hancock, and G. Rumolo (2016). "Space Charge Mitigation with Longitudinally Hollow Bunches". In: *ICFA Advanced Beam Dynamics Workshop on High-Intensity and High-Brightness Hadron Beams (HB 2016)*, MOPR026.

Oeftiger, A. and S. Hegglin (2016). "Space Charge Modules for PyHEADTAIL". In: *ICFA Advanced Beam Dynamics Workshop on High-Intensity and High-Brightness Hadron Beams (HB 2016)*, MOPR025.

Papaphilippou, Y. et al. (2013). "Operational Performance of the LHC Proton Beams with the SPS Low Transition Energy Optics". In: CERN-ACC-2013-0124, 3 p.

Perlmutter, S. et al. (1999). "Measurements of Omega and Lambda from 42 high redshift supernovae". In: *Astrophys. J.* 517, pp. 565–586. arXiv: astro-ph/9812133 [`astro-ph`].

Pogorelov, I., K. Amyx, and P. Messmer (2011). "Accelerating Beam Dynamics Simulations with GPUs". In: *IEEE Particle Accelerator Conference (PAC 2011)*. WEP164, pp. 1800–1802.

Pogorelov, I., K. Amyx, J. Balasalle, et al. (2012). "CUDA Kernel Design for GPU-based Beam Dynamics Simulations". In: *International Particle Accelerator Conference (IPAC 2012)*. MOPPC089, pp. 343–345.

PS Staff (1999). "40 Years of CERN's Proton Synchrotron". In: *CERN Courier* 39.10.

Qiang, J., M. A. Furman, and R. D. Ryne (2004). "A parallel particle-in-cell model for beam–beam interaction in high energy ring colliders". In: *Journal of Computational Physics* 198.1, pp. 278–294.

Qiang, J. et al. (2006). "Three-dimensional quasistatic model for high brightness beam dynamics simulation". In: *Physical Review Special Topics-Accelerators and Beams* 9 (4), p. 044204.

Qiang, J. et al. (2007). "Erratum: Three-dimensional quasistatic model for high brightness beam dynamics simulation [Phys. Rev. ST Accel. Beams 9, 044204 (2006)]". In: *Physical Review Special Topics-Accelerators and Beams* 10.12, p. 129901.

Qin, H. et al. (2015). "Canonical symplectic particle-in-cell method for long-term large-scale simulations of the Vlasov–Maxwell equations". In: *Nuclear Fusion* 56.1, p. 014001.

Reiser, M. (2008). *Theory and Design of Charged Particle Beams*. Wiley Series in Beam Physics and Accelerator Technology. Wiley.

Riess, A. G. et al. (1998). "Observational Evidence from Supernovae for an Accelerating Universe and a Cosmological Constant". In: *The Astronomical Journal* 116.3, p. 1009.

Rumolo, G., O. Boine-Frankenheim, et al. (2003). "Effects of Space Charge on Decoherence in Ion Beams". In: *IEEE Particle Accelerator Conference (PAC 2003)*. Vol. C030512, p. 2607.

Rumolo, G., H. Bartosik, et al. (2014). "Expected performance in the injectors at 25 ns without and with LINAC4". In: *RLIUP: Review of LHC and Injector Upgrade Plans*, pp. 17–24.

Sacherer, F. J. (1971). "RMS envelope equations with space charge". In: *IEEE Transactions on Nuclear Science* 18.3, pp. 1105–1107.

Sadoulet, B. et al. (1983). "Experimental observation of lepton pairs of invariant mass around 95 GeV/c^2 at the CERN p$\overline{p}$ collider". In: *11th International Symposium on Lepton and Photon Interactions at High Energies*, pp. 27–52.

Salvant, B. (2010). "Impedance model of the CERN SPS and aspects of LHC single-bunch stability". Presented on 4 Mar 2010. PhD thesis. Switzerland: Ecole Polytechnique, Lausanne.

Schindl, K. (1999). "Space Charge". In: *CERN PS 99-012-DI*, 26 p.

Schmidt, F. et al. (2016). "Code Bench-marking for Long-term Tracking and Adaptive Algorithms". In: *ICFA Advanced Beam Dynamics Workshop on High-Intensity and High-Brightness Hadron Beams (HB 2016)*, WEAM1X01.

Schoch, A. (1958). *Theory of linear and non-linear perturbations of betatron oscillations in alternating-gradient synchrotrons*. Geneva: CERN.

Singh, R. et al. (2014). "Observations of the quadrupolar oscillations at GSI SIS-18". In: *International Beam Instrumentation Conference*.

Uesugi, T. et al. (1999). "Observation of quadrupole mode frequency and its connection with beam loss". In: *IEEE Particle Accelerator Conference (PAC 1999)*. Vol. 3. IEEE, pp. 1821–1823.

Wasef, R. (2013). *private communication*.

Wasef, R. (2014). "PS Experiments and Simulations". Presented at Space Charge Collaboration Meeting 2014, CERN.

Wasef, R. et al. (2013). "Space Charge Effects and Limitations in the CERN Proton Synchrotron". In: *CERN ACC 2013-0176*.

Wei, J. et al. (2005). "Intra-beam Scattering Theory and RHIC Experiments". In: *AIP Conference Proceedings* 773.1, pp. 389–393.

Wiedemann, H. (2007). *Particle accelerator physics*. Springer.

Wiese, U.-J. (2010). "Particle Physics of the Early Universe". Lecture Notes, Institute for Theoretical Physics, University of Bern.

Zannini, C. (2013). "Electromagnetic Simulation of CERN accelerator Components and Experimental Applications". Presented on 15 Apr 2013. PhD thesis. Ecole Polytechnique, Lausanne.

Zotter, B. W. (1998). "Early work on space charge effects in particle accelerators". In: *Space Charge Physics in High Intensity Hadron Rings*. Vol. 448, pp. 26–37.

Acronyms

AGS Alternating Gradient Synchrotron. 1, 7

ALICE A Large Ion Collider Experiment. 4

ATLAS A Toroidal LHC ApparatuS. 2, 5

BNL Brookhaven National Laboratory. 1, 7

CIC cloud-in-cell. 63, 74

CMS Compact Muon Solenoid. 2, 4, 5

FFT Fast Fourier Transform. 65–67, 69–71, 81–83, 91

GPU Graphics Processing Unit. 18, 68–72, 159, 160

HL-LHC High Luminosity LHC. 15, 17, 90, 92, 159, 163

KV Kapchinskij-Vladimirskij. 8–10, 12–15, 18, 34–39, 41, 42, 47–51, 68, 76, 77, 79, 81–83, 85, 87, 92, 104, 110, 113, 116, 120, 123, 160, 161, 163

LEIR Low Energy Ion Ring. 160

LHC Large Hadron Collider. 1–7, 15, 17, 38, 89, 94, 127, 159–161, 163

LHCb Large Hadron Collider beauty. 3

LINAC Linear Accelerator. 7

LIU LHC Injectors Upgrade. 15, 17, 90, 127, 159, 162, 163

NGP nearest-grid-point. 56, 73, 74

ODE ordinary differential equation. 23, 24, 26, 31

PIC particle-in-cell. 10, 18, 57, 63, 68–75, 81, 83, 119, 159–161

PS Proton Synchrotron. 1, 7, 8, 12, 13, 15–17, 19, 76–78, 80, 81, 84, 86, 89–94, 97, 113, 120, 126, 127, 139, 140, 142–147, 149, 153, 155, 157, 159, 161–163, 165, 167, 169

PS Booster Proton Synchrotron Booster. 7, 8, 15–17, 19, 60, 97, 100, 126–129, 133, 135–138, 140–142, 146, 152, 153, 156, 159–162, 165, 169

QPU Quadrupolar Pick-up. 32, 47, 75, 76, 84, 160

RF radio frequency. ii, 15, 21, 28–32, 56, 57, 60, 61, 72, 92, 118–120, 125–132, 134–136, 138, 139, 143–146, 153, 154, 161, 162, 165–167, 169

SM Standard Model of particle physics. 1–6

SPS Super Proton Synchrotron. 10, 15, 17, 18, 53, 54, 68, 72–75, 77–79, 84, 89–94, 97, 98, 100, 101, 103–105, 112–115, 118, 119, 159, 160, 162, 163

Adrian Oeftiger

Curriculum Vitæ

address: *Emilia Noyeres*
10, chemin des Noyères
1217 Meyrin, Switzerland
✉ *a.oeftiger@gmx.net*
born 17.06.1990 in Hagen, Germany

Education

May 2013 – Dec 2016 — **Doctoral Student in Accelerator Physics**, *CERN and École polytechnique fédérale de Lausanne (EPFL)*, Switzerland.
Thesis: "Space Charge Effects and Advanced Modelling for CERN Low Energy Machines"

CERN scholarship for three-year doctoral student programme

PhD graduation

Sep 2011 – Apr 2013 — **Master Student in Theoretical Physics**, *University of Bern*, Switzerland.
Thesis: "On the Effect of Global Cosmological Expansion on Local Dynamics"

MSc diploma awarded, graduated *summa cum laude*

Sep 2007 – Jun 2010 — **Bachelor Student in Physics**, *University of Bern*, Switzerland.
Thesis: "Supersymmetric Quantum Mechanics"

BSc diploma awarded, graduated *magna cum laude*

Jun 2007 — **Abitur Graduate**, *Otto-Hahn-Gymnasium Gifhorn*, Germany.
○ bilingual (English) classes in biology, history, geography, politics, sports
○ student exchange to Lima, Perú in 2004 during ten weeks

German secondary education diploma, graduated *1.6 (magna cum laude equivalent)*

Professional Experience

Sep 2014 – Jan 2015 — **Teaching Assistant**, *EPFL*, Switzerland.
Introduction to Particle Accelerators

Feb 2011 – Apr 2011 — **Collaborator**, *Brookhaven National Laboratory*, U.S.
Collider-Accelerator department: development and evaluation of numerical simulations for eRHIC (high energy electron-ion collider) project.

cf. proceedings of International Particle Accelerator Conf. 2012, New Orleans, U.S.: W. Fischer, C. Montag, and A. Oeftiger, *Ion Bunch Length Effects on the Beam-beam Interaction and its Compensation in a High-luminosity Ring-ring Electron-ion Collider*

Jun 2010 – Dec 2010 — **Summer Student and Collaborator**, *CERN*, Switzerland.
CERN scholarship for three-month summer student programme and subsequent collaboration with Beams department.
Topic: vacuum and beam physics for CLIC (Compact Linear Collider) project.

cf. CERN CLIC-Note-930 (2011): A. Oeftiger and G. Rumolo, *Fast Beam-ion Instabilities in CLIC Main Linac, Vacuum Specifications*

2009 – 2013 — **Teaching Assistant**, *University of Bern*, Switzerland.

Sep 2012 – Jan 2013	Statistical Thermodynamics II
Sep 2011 – Jan 2012	Quantum Mechanics I
Feb 2010 – Aug 2010	Physics with Mathematical Methods II
Sep 2009 – Jan 2010	Physics with Mathematical Methods I

Schools

Jan 2015	**U.S. Particle Accelerator School**, *Hampton, Virginia*, U.S. two-week school on "Beam Physics with Intense Space Charge"
Aug 2013	**CERN Accelerator School**, *Trondheim*, Norway. two-week school on "Advanced Accelerator Physics"

Languages

German	*native speaker*		French	*fair*
English	*fluent*		Latinum	*extended*
Spanish	*very good*			

Scholarships

2008 – 2013	**German National Academic Foundation**. ○ 5 year financial grant ○ two-year workshop on "Learning How To Walk", construction of walking robots in close collaboration with the Locomotion Lab of the University of Jena, Germany. ○ one-week spring school on "Bose-Einstein Condensates" in Papenburg, Germany. ○ one-week summer school on "Analyzing of Matter in XFELs" in Überlingen, Germany.

Skills

Languages	C, C++, CUDA, Java, Python, Shell/Bash	**Web**	CSS, HTML/XHTML, Javascript, PHP
Scientific	Matplotlib, SciPy, Maple, Mathematica, AVS Express	**Office**	LaTeX, Microsoft Office, LibreOffice, LaTeX beamer
Operating Systems	Linux, Windows	**Source Management**	Git, Github

Volunteer Work

2015 – 2016	**S-TEAM, international Scout project**, Switzerland and Poland. 1 year of international project leadership and workshop organisation, `http://s-team.kno3.ch/`
2013 – 2014	**ScoutingTrain, international Scout project**, Germany, Poland and Russia. 1.5 years of international team leadership and workshop organisation, `http://scoutingtrain.org/`
2008 – 2010	**Board Member of Student Association**, *University of Bern*, Switzerland. 2 years of board membership, organisation of physics student association
2003 – 2007	**Active Scout team leadership**, *Gifhorn*, Germany. 4 years of Scout team organisation on local level, representative on state level

Hobbies & Interests

Travelling, funk band (keys and guitar), sports (martial arts and table tennis)

References

Prof. Dr. Leonid Rivkin
Supervisor Doctoral Thesis
Accelerator Physics
Large Research Facilities Dep., PSI
Particle Acceler. Physics Lab, EPFL
Switzerland
✉ leonid.rivkin@epfl.ch
☎ +41 21 693 04 76

Dr. Giovanni Rumolo
Co-supervisor Doctoral Thesis
Accelerator Physics
Accelerator and Beam Physics Group,
Beams Dep., CERN
Switzerland
✉ giovanni.rumolo@cern.ch
☎ +41 22 767 32 64

Prof. Dr. Matthias Blau
Supervisor Master Thesis
Theoretical Physics
Gravity & String Theory Group,
University of Bern
Switzerland
✉ blau@itp.unibe.ch
☎ +41 31 631 86 26